Microscale spatiotemporal evolution of multi-species electroactive biofilms towards the development of a microfluidic device

Lucila Martínez Ostormujof

THÈSE

En vue de l'obtention du

DOCTORAT DE L'UNIVERSITÉ DE TOULOUSE

Délivré par :

Institut National Polytechnique de Toulouse (Toulouse INP)

Discipline ou spécialité :

Génie des Procédés et de l'Environnement

Présentée et soutenue par :

Mme LUCILA MARTINEZ OSTORMUJOF

le mardi 7 mars 2023

Titre :

Etude spatiotemporelle des biofilms électroactifs multi-espèces à l'échelle microscopique par une approche microfluidique et optique

---

Ecole doctorale :

Mécanique, Energétique, Génie civil, Procédés (MEGeP)

Unité de recherche :

Laboratoire de Génie Chimique (LGC)

Directeur de Thèse :

M. BENJAMIN ERABLE

Rapporteurs :

M. ERIC TRABLY, INRAE NARBONNE

MME NELLY HENRY, UNIVERSITE SORBONNE

Membres du jury :

MME ELISABETH NEUHAUSER, UNIVERSITE TOULOUSE 3, Présidente

M. BENJAMIN ERABLE, TOULOUSE INP, Membre

M. SEBASTIEN TEYCHENE, TOULOUSE INP, Membre

M. STÉPHANE ARBAULT, UNIVERSITE DE BORDEAUX, Membre

Microscale spatiotemporal evolution of multi-species electroactive biofilms towards the development of a microfluidic device

Multi-species electroactive biofilms (EABs) are able to exchange electrons with an electrode surface. EABs are mainly used in bioelectrochemical systems (BES), where the generation of electricity is difficult to sustain over the long term. Generally, EAB electroactivity reaches a maximum (J_{max}) that declines gradually after a few tens of days of BES operation. In this context, the typical use of macroelectrodes for testing the hypotheses related to the loss in the EAB electroactivity difficults the setting and control of homogeneous conditions, coupled to the single-point destructive analyses techniques, where the EAB spatio-temporal evolution is clearly lost.

The first part of this thesis was devoted to work with stainless steel (SS) microelectrodes (Ø=50µm), as to ensure more homogeneous experimental conditions at the electrode surface. Initially, the formation of salt marsh EABs on microelectrodes was standardized, where the distinctive electroactivity observed in macroelectrodes was successfully reproduced. Subsequently, four main temporal stages of biocolonization and electroactivity were thoroughly described. High viability, maximum biofilm growth rate and high extracellular polymeric substances (EPS) protein content favoured the increasing electroactivity up to J_{max}. Then, the gradual decline in the electroactivity became irreversible, where biofilm growth rate decreased with dead cells accumulation and the increase of EPS polysaccharides content. In addition, a shift in the EAB microbial population occurred from *Marinobacterium* spp. to *Desulfuromonas* spp. Lastly, further studies focusing in the role of the EPS in the EAB electroactivity showed consistently high EPS protein and low EPS polysaccharides content when the electroactivity was enhanced.

The second part of this thesis focused in the development of a transparent microBES (V=0.3 mL) with a SS integrated microelectrode, for the in situ real-time observation of the microelectrode/EAB and EAB/planktonic cells interfaces. The dynamics of biofilm formation were correlated with the EAB electroactivity, where the discovery of an active dense layer of planktonic bacteria in the proximities of the microelectrode/EAB interface opens new research directions in the biofilm formation and electron transfer mechanisms.

Etude spatiotemporelle des biofilms électroactifs multi-espèces à l'échelle microscopique en vue du développement d'un outil microfluidique

Les biofilms électroactifs (EABs) multi-espèces sont capables d'échanger des électrons avec la surface d'une électrode. Les EABs sont principalement utilisés dans les systèmes bioélectrochimiques (BES), où la production d'électricité est difficile à maintenir à long terme. En général, l'électroactivité des EABs atteint un maximum (J_{max}) qui diminue progressivement après quelques dizaines de jours de fonctionnement du BES. Dans ce contexte, l'utilisation typique de macroélectrodes pour tester les hypothèses liées à la perte d'électroactivité des EABs rend difficile la fixation et le contrôle de conditions homogènes, couplées à des techniques d'analyses destructives ponctuelles, où l'évolution spatio-temporelle des EABs est clairement perdue.

La première partie de cette thèse a été consacrée au travail avec des microélectrodes (Ø=50µm) en acier inoxydable (SS), afin d'assurer des conditions expérimentales plus homogènes à la surface de l'électrode. Dans un premier temps, la formation des EABs provenant des marais salants sur les microélectrodes a été standardisée, où l'électroactivité distinctive observée dans les macroélectrodes a été reproduite avec succès. Par la suite, quatre étapes temporelles principales de la biocolonisation et de l'électroactivité ont été détaillées. Une viabilité élevée, des taux de croissance maximaux du biofilm et une quantité importante de protéines de substances polymériques extracellulaires (EPS) ont favorisé l'augmentation de l'électroactivité jusqu'à J_{max}. Ensuite, le déclin progressif de l'électroactivité est devenu irréversible, alors que la vitesse de croissance du biofilm à diminué avec l'accumulation de cellules mortes et l'augmentation de la quantité de polysaccharides d'EPS. En outre, la population microbienne des EABs a évolué de *Marinobacterium* spp. à *Desulfuromonas* spp. Enfin, d'autres études portant sur le rôle de l'EPS dans l'électroactivité des EABs ont montré une quantité constamment élevée de protéines d'EPS et une faible proportion de polysaccharides d'EPS lorsque l'électroactivité a été augmentée.

La deuxième partie de cette thèse s'est focalisée sur le développement d'une microBES transparente (V=0.3 mL) avec une microélectrode intégrée en SS, pour l'observation in situ et en temps réel des interfaces microélectrode/EAB et EAB/cellules planctoniques. La dynamique de la formation du biofilm a été corrélée à l'électroactivité du EAB, où la découverte d'une couche dense active de bactéries planctoniques à proximité de l'interface microélectrode/EAB ouvre de nouvelles voies de recherche sur la formation du biofilm et les mécanismes de transfert d'électrons.

Acknowledgements

The work presented in this thesis was developed at the Laboratoire de Génie Chimique (LGC) within the BioSyM department of the Institut National Polytechnique de Toulouse (INPT).

First of all, I would like to express all my genuine gratitude to my thesis supervisors: Benjamin Erable and Sébastien Teychené, for having entrusted me with this innovative and interdisciplinary subject. Benjamin, thank you for your great availability, your patience and above all your enthusiasm. Sébastien, thank you for your encouraging spirit, your advice and for the interest brought to this work. All the discussions we have had allowed me to advance not only in my thesis but also grow as a researcher. I thank you both for your investment, your innovative ideas and especially for having guided me, advised me and reassured me throughout these three years.

Furthermore, I would like to thank the reviewers: M. Eric Trably and Mme. Nelly Henry and the examiners: Mme. Elisabeth Girbal-Neuhauser and M. Stéphane Arbault for accepting the responsibility of being part of my thesis jury and dedicating your time to provide your critical point of view and enrich my thesis work.

This thesis was developed within the framework of the MICROBE project, for which I would like to sincerely thank the various partners involved: Wafa Achouak and her team at LEMIRE, Mohamed Bakarat and Sylvain Fochesato for the DNA analyses and the numerous enriching discussions. Stéphane Pinck for your help with experimentation in my early thesis days. Emmanuel Cid for your precious aid with image processing and optical flow algorithms. I would also like to give special thanks to Juan Diego Carvajalino Olave, whom I had the pleasure of working together during his Master 2 internship.

A special thought and gratitude for all the people of the LGC (and close laboratories) who contributed to the realization of this work. To Issac and Raj for your enormous help and patience in the development of the microfluidic devices. To Marie-Line De Solan for the interesting discussions in front of the SEM and the ICP analyses. In addition, many thanks to Cécile Pouzet and Yves Martinez from FRAIB for the training on the use of the confocal microscope. I would also like to thank the administrative staff of the LGC: Dany Bouscary, Claudine Lorenzon, Patricia Uliana and Alain Phillip for all your kind help over the years.

These three years in the lab have been a great opportunity to meet some incredible people. I would like to thank the rest of the Biofilm team. Thank you Luc for your contagious good humor, unfailing help in the technical side and for the provision of salt marsh for my experiments. Thank you Régine for your positive energy and daily enthusiasm. Thank you Alain for your dry humor and wise knowledge, and thank you Marie-Line for your kindness and your good advice.

I would like to thank my colleagues and also friends, PhD-students, post-docs and interns. I have the feeling of having been part of two generations of young researchers. Thank you to the first generation: Morgane, Julien, Emma and Cedric, for welcoming me in the lab and integrating me into the group, even when I did not speak a word of French. I would also like to thank Mexican gang: Silvia, Lauren, Isaura and Marco. Thank you very much for the fun moments, I was very glad to meet you at the beginning of my PhD. I would especially like to thank my colleague and roommate Sabine. Thank you for being a great friend and for the support in the sometimes-difficult times of Covid and confinement. To the second generation: Sirine, Silvia de los Santos, Anthony, Laura, Lorenzo, Paul. Thank you for the (not very) scientific discussions, the UNO tours at lunchtime, the four o'clock coffee break, and all the funny times, worthy of tears of laughter, shared outside the lab. I feel very grateful of having met you and thank you for your encouragement in the final times of my PhD.

Last, but not least, I would like to thank my family, who despite the distance always knew how to be present during these three years of PhD. To my parents, for all their unconditional support in order to pursue my dreams and to my brother, who had a key role in taking the decision to do a PhD in France. Finally, to my closest friends, who have always stood by me and motivated me to move forward in difficult times.

Table of Acronyms

BES: Bioelectrochemical Systems

EAB: Electroactive Biofilm

TRL: Technology Readiness Level

MFC: Microbial Fuel Cells

MEC: Microbial Electrolysis Cells

EPS: Extracellular Polymeric Substances

EET: Extracellular Electron Transfer

DET: Direct Electron Transfer

MET: Mediated Electron Transfer

QS: Quorum Sensing

AHL: Acyl Homoserine Lactone

WWTP: Wastewater Treatment Plant

AS: Activated Sludge

SMS: Salt Marsh Sediments

COD: Chemical Oxygen Demand

SS: Stainless Steel

CC: Carbon Cloth

WE: Working Electrode

CE: Counter Electrode

REF: Reference Electrode

SCE: Saturated Calomel Electrode

ITO: Indium Tin Oxide

PDMS: Polydimethylsiloxane

OCP: Open Circuit Potential

CV: Cyclic Voltammetry

CA: Chronoamperometry

CE: Coulombic Efficiency

CP: Chronopotentiometry

CLSM: Confocal Laser Scanning Microscopy

SEM: Scanning Electron Microscopy

HDMS: Hexamethyldisilazane

DIC: Differential Interference Contrast Microscopy

PMT: Photomultiplier Tubes

ASV: Amplicon Sequence Variant

SRS: Scaling with Ranked Subsampling

ANOVA: Analysis Of Variance

J_{max}: Maximum Current Density

HS: High Salinity

LS: Low Salinity

ICP: Inductively Coupled Plasma

OTU: Operational Taxonomic Unit

EDX: Energy Dispersive X-Ray Analysis

PCA : Principal Component Analysis

PS : Polysaccharides

Prot : Proteins

C12: N-(3-Oxododecanoyl)-L-homoserine lactone

C6: N-Hexanoyl-L-homoserine lactone

C4: N-Butyryl-DL-homoserine lactone

PQS: Pseudomonas Aeruginosa Signal

Table of contents

General introduction

The rapid growth of the world population and economy has led to a significant energy consumption, where fossil fuels have been dominantly employed as a main resource, accounting for more than 80% of the entire energy production globally in 2019[1]. Nevertheless, the massive use of fossil fuels inevitably contributes to global warming and climate change, which has boosted the investigation of alternative energy sources (Jung et al., 2020).

A renewable energy source is a way of producing energy that is able to exploit naturally renewable resources. It is also referred to as decarbonated energy, which includes nuclear and biogas, in addition to the classics: wind energy, solar energy, biomass, geothermal energy, i.e. energy that emits few emissions into the atmosphere, from design to energy production itself. Renewable energies have been growing progressively for several years and in 2021 represent 13.0% of primary energy consumption and 19.3% of gross final energy consumption in France.

As an alternative energy source to fossil fuels, waste-to-energy can also be an important instrument in the energy and ecological transition. The incineration, pyrolysis and methanisation processes are technologically mature processes and the so-called bioelectrochemical processes or bioelectrochemical systems (BES) are still under development but are gradually gaining in maturity.

BES have the ability of transforming organic waste streams into energy, positioning these promising technologies for a circular bioeconomy and for reducing the environmental footprint. The central operating principle of a BES is based on a microbial electroactive biofilm (EAB), usually hosting a diverse microbial community, i.e. a multi-species biofilm, formed on the surface of an anode that catalyzes the oxidation of several organic substances to produce electric current. Therefore, the unit formed between the EAB and the surface of an anode, which is generically referred to as a microbial anode or bioanode, represents the functional core of the BES.

Although the first demonstration of BES technologies was demonstrated more than 20 years ago, the transition from laboratory work to full industrialization is still on struggle, with a maturity level stagnating in a Technology Readiness Level (TRL) between 4 and 6. Problems related to the scaling up of BES or to the low current densities achieved are widely recognized and documented in the literature (Borole et al., 2011; Leicester et al., 2020; Tan et al., 2021). Less highlighted but critical to the technological development of BES is the long-term stability of EAB electroactivity, which is unfortunately difficult to maintain. In general, multi-species EABs have a maximum electroactivity that gradually declines after a few tens of days of BES operation.

[1] https://www.iea.org/reports/world-energy-balances-overview/world

The hypothetical reasons for this loss of electroactivity are mainly related to the spatio-temporal evolution of multi-species EABs, where:

- The dynamics of the biofilm microbial population evolves in time, where electroactive bacteria co-habits with non-electroactive species that do not contribute with current production.
- The biofilm thickness increases over time, reaching a restrictive active biofilm thickness. This means that the biofilm is mainly electroactive at low thicknesses and then its electroactivity gradually decreases as the biofilm grows. This can be due to a change in the main electron transfer mechanism when the biofilm reaches a threshold thickness or whether electron transfer is at some point limited far from the electrode.
- The production of extracellular polymeric substances by the biofilm, and more specifically its accumulation, can negatively affect the generation of current in the bioanode.
- Depletion of nutrients and/or substrates over time within or around the EAB can inhibit microbial growth.
- The progressive creation of chemical gradients (nutrients, substrates, inhibitory metabolites) within the biofilm generated over time create more or less inactive regions that do not contribute to its electroactivity. The inactive regions may be also due to a change in the redox potential within the biofilm as the distance between the bacterial cells and the anode increases, as well as local acidification, due to the production of protons when the substrate is oxidized.

Some of these hypotheses have already been raised by some authors, but in all cases the studies have been only partial and the dynamics are still unknown. Also, until this day, most of the experimental studies carried out have used macroscopic reactors (at least a few tens of milliliters), where the physicochemical, spatial and microbial conditions of the biofilm environment are difficult to access and control. Furthermore, analytical measurements of biofilm are performed at a single point in time, usually at the end point. This failure to take into account the temporal and spatial evolution of the biofilm contributes to a great loss of valuable information to explain the progressive decline of its electroactivity.

Therefore, this thesis aims to investigate the spatio-temporal evolution of multi-species EABs on anodes at all-time scales, from the initial stages of biofilm formation to its long-term operation, as to prove the mentioned hypotheses related to the loss of their electroactivity with an original methodological approach. The downscaling of the anode-EAB interface, coupled with microscopic and electrochemical techniques permits the spatio-temporal real-time study of biofilms on the scale of bacterial cells.

The main challenge that was a major issue throughout my thesis was related to obtaining an experimental instrument to investigate the biofilm at the microscopic scale: this involved reducing the size of the anode and developing a transparent microBES to form and study multi-species EABs in situ directly under an optical microscope field.

The work described in this thesis is part of the MICROBE project supported by the ANR. The project brings together the Laboratory of Chemical Engineering (LGC, UMR 5503) where the BioSyM (Microbial Systems and Bioprocesses) and GIMD (Interfacial and fluid engineering) departments were mainly implicated. The Laboratory of Microbial Ecology of the Rhizosphere and Extreme Environments (LEMiRE UMR 7265) and the Electronics and Information Technology Laboratory of the CEA were also a project partner mainly in charge of biological analyses.

The manuscript of this thesis work is divided into six chapters. Chapter I starts with a detailed description of bioanodes. EAB basics and the main parameters for bioanodes formation and operation are discussed in depth. Then the focus sets into describing the causes that explain limitations in the electroactivity of multi-species EABs. The chapter closes with a state of the art of the tools to study multi-species EABs in bioanodes: microelectrodes and microBES.

Chapter II gathers the materials, techniques and protocols used for the experiments described in Chapters III to VI. This chapter contains a description of the culture media and microbial inocula, the experimental set-ups in the macro and micro scale and the analytical techniques implemented. In addition, certain special protocols that were developed for microscopy techniques and for post-processing microscope images were also included.

Chapters III to V describe the experimental results obtained during the course of the thesis when only the size of the anode was scaled down to the microscale. In these chapters, microelectrodes were implemented as the anode in macroscopic electrochemical reactors.

Chapter III is devoted to standardize the formation of a multi-species EAB on an anode with the size of a microelectrode (Ø=50µm). Different microelectrode materials, sources of microbial inoculum and culture media were tested.

Chapter IV studies the spatio-temporal evolution of multi-species EABs on microelectrodes regarding biocolonization, cell viability, microbial and chemical composition as to correlate these variables with the EAB electroactivity.

Chapter V follows a research hypothesis put forward at the end of Chapter IV. The role of multi-species EAB extracellular proteins and polysaccharides in the biofilm electroactivity is studied in depth as well as the optimization of the EABs electroactivity.

Chapter VI is divided into two parts. First, Part A describes in detail the step-by-step protocol using microfluidic techniques as to obtain a viable microBES. Part B integrates the microBES with optical microscopy and electrochemical techniques in simultaneous as to study in real-time the spatio-temporal evolution of multi-species EAB and its electroactivity.

The work described in this thesis has been valorized by:

One published review article:

- **S. Pinck, L. Martinez Ostormujof, S. Teychené, B. Erable.** *Microfluidic Microbial Bioelectrochemical Systems: An Integrated Investigation Platform for a More Fundamental Understanding of Bacterial Biofilms* published in "*Microorganisms"* journal (December 2020) and inserted in Chapter I.

One submitted research article:

- **L. Martinez Ostormujof, S. Teychené, W. Achouak, S. Fochesato, M. Bakarat, I. Rodriguez Ruiz, A. Bergel, B. Erable.** *Systemic Analysis of the Spatiotemporal Changes in Multi-Species Electroactive Biofilms to Clarify the Gradual Decline of Current Generation in Microbial Anodes* submitted in "*ChemElectroChem*" journal (November 2022) and inserted in Chapter IV.

Six oral conferences in international congresses:

- **Martinez Ostormujof L., Teychené S., Erable B.** *Micro-scale and real time investigation of multi-species electroactive biofilms in microfluidic bioelectrochemical chips.* 1st International Bioenergy and Environment Congress (I-BE-C) "From Photosynthesis to Biotechnology" *(16-18 février 2021, Cités des Energies, Cadarache, France, On-Line).*
- **Martinez Ostormujof L., Teychené S., Erable B.** *Unravelling Performance Limitations of Microbial Anodes: A Real-time Microscale Approach.* XXVIth International Symposium on Bioelectrochemistry and Bioenergetics of the Bioelectrochemical Society on «Bioelectrochemistry for improved Life Quality *(10-15 Mai 2021, Cluj-Napoca, Roumanie, On-Line).*
- **Martinez Ostormujof L., Teychené S., Erable B.** *Real-time microscale investigation of microbial anodes in bioelectrochemical systems (BES) for the organic waste conversion.* 8th International Conference on Engineering for Waste and Biomass Valorisation *(31 Mai – 04 juin 2021, Toronto, Canada, On-Line*).
- **Martinez Ostormujof L., Teychené S., Erable B.** *In situ and non-destructive real time microscopic investigation of multi-species electroactive biofilms on transparent microfluidic BES.* 5th European Meeting of the International Society for Microbial Electrochemistry and Technology *(13-15 Septembre 2021, Girona, Espagne, On-Line).*
- **Martinez Ostormujof L., Teychené S., *Erable B.*** *Exploring structuration, heterogeneity and chemistry gradients in multi-species electroactive biofilms using microfluidic bioelectrochemical chips.* Keynote lecture - Regional Meeting of the International Society of Electrochemistry (*15-19 août 2022, Prague, République Tchéque)*

- **Martinez Ostormujof L., Teychené S., Cid E., Erable B.** *Clarifying the early stages of microbial anode formation using real-time optical microscopy and image processing.* 8th International Meeting of the International Society for Microbial Electrochemistry and Technology (*19-23 septembre 2022, La Canée, île de Crète, Grèce).*

Chapter I : State of the Art

I.1. Microbial bioelectrochemical systems (BES)

In the early 2000s, the discovery that bacterial cells can transfer electrons directly to insoluble electron donors and acceptors, i.e. to electrode, without mediators (Bond and Lovley, 2003), has given birth to a number of practical applications assembled under the title of Bioelectrochemical Systems (BES). These technologies respond to the interest of several fields such as energy generation, substrate degradation, synthesis of value-added products (H_2, ethanol, and biogas) and environmental concerns. The latter includes wastewater treatment of several types, soil remediation, water desalination and depollution of contaminated environments (Ramírez-Vargas et al., 2018).

Classification of BES comprises two main groups: whether they are designed to produce power, or if energy is required to provide a product or other output. The core of their functioning lies in the properties of electroactive bacteria to attach to the electrode surface, form an electroactive biofilm (EAB) and convert the chemical energy that is stored in organic compounds. In the case of microbial fuel cells (MFC), energy will be converted directly to electric current. For microbial electrolysis cells (MEC), energy will be transformed to hydrogen or other compounds. Other technologies also exist under the classification of BES, such as microbial electrochemical snorkel for wastewater treatment, microbial electrosynthesis for producing chemical products (alcohols, organic acids) from CO_2 reduction, microbial electrofermentation for obtaining fermentation products (ethanol, butanol, propionate), microbial electroremediation and microbial remediation cells for depollution and biodegradation of contaminants.

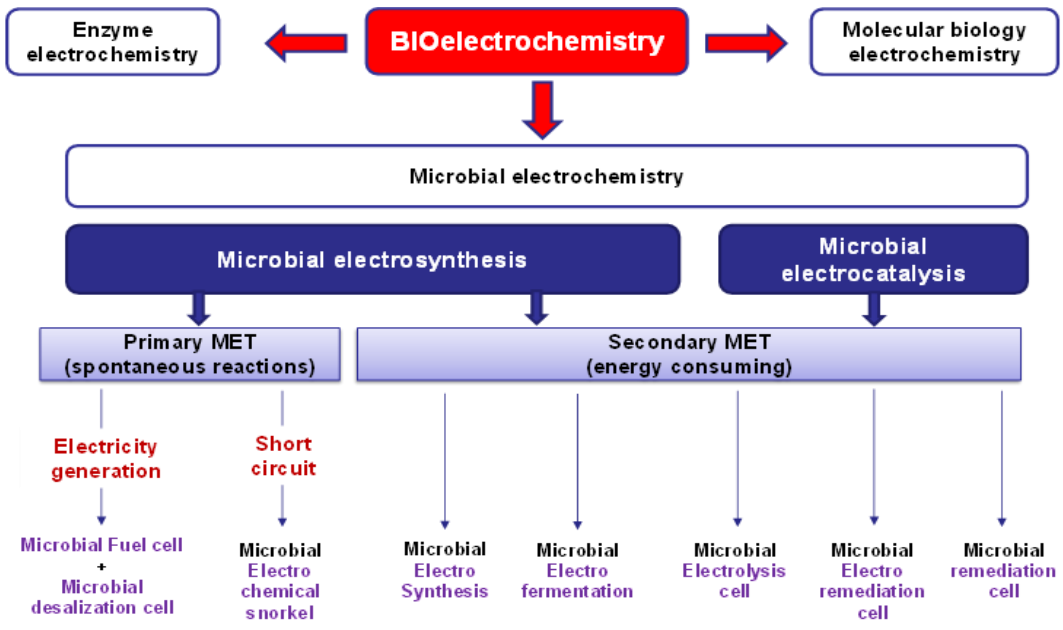

Figure I-1: Applications of bioelectrochemical systems. Modified from (Ramírez-Vargas et al., 2018).

I.2. Microbial anodes (or bioanodes) of BES

This section focuses on the anode compartment of the BES where the microbial anode is located. The microbial anode is the anode electrode colonized by a microbial biofilm, which acts as an electrocatalyst. The formation of a biofilm on the anode is a natural spontaneous process; the mechanisms and time frame of this process are explained in detail in the following subsection. Next, the focus is put on the particularities of EABs, including a detailed description of the fine mechanisms of exogenous electron transfer in electroactive microorganisms. The parameters or effectors related to the electrode-microorganism-electrolyte tryptic affecting the design and operation of microbial anodes are then discussed. Finally, the major physical and chemical phenomena limiting the electroactivity of anode biofilms are reviewed.

I.2.1. Biofilm basics

Bacteria can exist in a planktonic form, where suspended free cells float in a liquid medium, or they can group together in a structured way, surrounded by a matrix made of polymeric substances, to constitute what is known as a biofilm.

I.2.1.1. Stages of biofilm formation

The formation of a biofilm is a complex process, yet it occurs in a few common steps. First, bacterial cells reach a surface and adhere themselves to it. Subsequently, cell multiplication and division form micro-colonies, which eventually grow and mature. Finally, dispersion from the biofilm matrix takes place, returning bacteria into the planktonic form.

A- Adhesion: reversible and irreversible - The process of biofilm formation starts with the adhesion of a small number of cells to a surface. In order to do so, bacteria needs to sense the proximity of a surface and elaborate behavior patterns to approach the latter (Costerton, 1999). In this manner, planktonic bacteria displace due to its motility or hydrodynamic forces present in the medium and attaches themselves to the identified surface. The attachment of the bacterial cells into the surface is known as adhesion, ruled by physical forces such as Van der Walls or electrostatics (Jamal et al., 2018). Since the covalent-type bonds involved in these forces are weak, cells can suffer a reversible adhesion, detaching themselves from the surface and returning to the planktonic state. Nevertheless, cells can synthetize proteins and polysaccharides, which enhance adhesion, making it irreversible.

B- Growth: Formation of microcolonies and maturation - Once cells are irreversibly attached to the surface, there is an augmentation of microbial population by cell division and cells are able to communicate within each other through auto-induced signals. These microcolonies remain anchored to the surface due to the secretion of extracellular polymeric substances (EPS). Cell aggregations coordinate between each other for the exchange of substrate and metabolic products. In this stage, the

biofilm presents multiple layers and can reach a thickness of 10 µm (Thormann et al. 2004; Gupta et al. 2016). As the microcolonies keep on growing, due to the access of surrounding nutrients and substrate in the medium, the synthesis of EPS also continues. This increases the size of the biofilm, where thickness can reach up to 100 µm. At this point, the biofilm is at its maturity state (Gupta et al., 2016).

C- Decline - As the biofilm increases in size, cells can be detached returning to the planktonic state and colonize a new surface. This can happen due to nutrient deficiencies or stress conditions. In addition, detachment can occur also by physical forces, such as erosion created by fluid shear at the biofilm-bulk interface (Donlan, 2002).

I.2.1.2. Multi-species biofilms

Biofilms can be formed by a single bacterial species, however most nature biofilms are formed by several ones. In multi-species biofilms, bacterial cells compete, cooperate and communicate with each other, where these interactions can often change the physiology as well as the function of the whole biofilm bacterial species (Yang et al., 2011). The cooperation and competition among the microbial populations can improve current production of a multi-species biofilm formed on the anode of a BES. Y. Liu et al. (2015) compared current production in a *G.Sulfurreducens* biofilm and a multi-species biofilm, where the synergetic interaction between bacterial species in the multi-species biofilm enhanced current production. On the other hand, interactions between bacterial cells can also affect current production, such as substrate oxidation for methanogenesis routes (Sleutels et al., 2011) or the production of inhibitory metabolites (Bourdakos et al. 2014).

I.2.1.3. Extracellular polymeric substances (EPS)

Bacterial cells that conform the biofilm possess the ability of secreting extracellular material, such as exopolysaccharides, nucleic acids, proteins, and to a lesser extent, lipids. These self-produced substances that surround and encase the bacterial cells form a matrix of different types of biopolymers that can account for more than 90% of the biofilm volume (Sutherland, 2001). As a primary function, extracellular polymeric substances (EPS) promote the irreversible adhesion of microorganisms to surfaces, allowing the cohesion among bacterial cells and the development of micro-colonies. Progressive in situ production of EPS drives the formation of a tridimensional polymer matrix presenting voids and channels. Voids in the matrix are pores containing water, providing the cells with a hydrated environment. Channels distribute nutrients to the inner regions of the biofilm and remove waste products from microbial activity (Flemming and Wingender, 2010).

Among the physical properties by the once-stablished EPS, providing stability, resistance to mechanical removal against fluid shear stress and its role as diffusional barrier are mainly described. The latter can lead to the creation of all kinds of nutritional and chemical gradients in the matrix such as pH, oxygen, metabolites, ions and other soluble molecules that create a heterogeneous local environment within the

biofilm. The role of EPS as a local nutrient reservoir of biomolecules and signaling compounds is also highlighted (Karygianni et al., 2020).

I.2.2. Electroactive biofilms (EABs)

These biofilms, formed on a conductive surface, have the peculiarity of accepting or receiving electrons from the conductive surface, therefore producing electric current. For bioanodes, electroactive bacteria are able to transfer electrons stored in organic compounds to a solid electrode, thus acting the latter as the terminal electron acceptor (Schaetzle et al., 2008). How bacteria exchange electrons with the anode has been widely described in the literature and seems well understood up to today. The possible mechanisms of electron transfer are presented below:

I.2.2.1. Electron transfer mechanisms (EET)

Due to the microbial diversity present in multi-species biofilms, and the presence or coexistence of multiple EET, the understanding of these mechanisms has been mostly examined for model systems involving single-species electroactive bacteria, being cells from the genus *Shewanella* and *Geobacter* the two most well studied ones. In this field, mechanisms of EET are depicted in Figure I-2 and classified in two large groups: mediated and direct.

- Mediated electron transfer

In this case, electroactive bacteria exploits a redox molecule that acts as a shuttle for electron transport. In a cyclic process, the redox mediator gains an electron from the bacterial cell and transfers it to the electrode, therefore returning to the original oxidized state and set to be reused. The redox mediators can be classified in endogenous (if they are produced by bacteria) or exogenous (if they are externally added compounds).

Before acknowledging the existence of endogenous mediators, the addition of soluble redox mediators was the chosen strategy to boost electron transfer from the electroactive bacteria to the electrode. The use of exogenous mediators comprised organic dyes (Park et al., 1999; Rahimnejad et al., 2011), thionine and quinone derivatives (Allen and Bennetto, 1993; Ieropoulos et al., 2005), among others. Thereby, bacteria unable to perform direct electron transfer or to produce their own redox mediators were gifted with an electroactive capability. However, this method presented disadvantages since toxicity of the compounds and the necessity of regular addition in order to enhance electron transfer, could lead to environmental and practical issues.

Endogenous mediators are metabolites produced by the bacterial cells, which can be reused in several redox cycles. In the case of *S. Oneidensis MR-1*, it has been demonstrated that cells secreted molecules of riboflavins, which participated in the mechanism of electron transfer. The removal of the riboflavins in the *Shewanella* biofilms reduced the production of electric current to more than 70% (Marsili et al.,

2008). Another example of flavins as endogenous mediators is pyocyanin, which is a secondary metabolite produced by *Pseudomonas Areuginosa*. The improvement of pyocyanin production in biofilms showed a four-time increase on the current production of the bioanode compared to the control experiment (Shen et al., 2014).

- Direct electron transfer

As the name indicates, this type of electron transfer involves a physical contact between the membrane of the electroactive bacterial cells and the electrode surface. *S.Putrefaciens* and *G.Sulfurreducens* were the first bacterial species that demonstrated the performance of electron transfer without the addition of an electron mediator (B. H. Kim et al. 1999; Bond and Lovley 2003).

Direct electron transfer (DET) can be achieved by protein intermediates known as c-type cytochromes present in the outer surface of the bacterial membrane. These proteins are redox compounds containing heme groups, which can either be in an oxidized or reduced state. This type of DET was observed for thin biofilms of *G.Sulfurreducens* (Busalmen et al., 2008). However, as the thickness of the biofilm increased, only the first monolayer of bacteria in contact with the electrode contributed with electron transfer. Yet, it was discovered that there was no deficiency in current production as the *Geobacter* biofilms got thicker (Reguera et al., 2006). This introduces the discovery of the second mechanism of direct electron transfer, related to the growing of conductive pili across the outer membrane of bacterial cells. It was found that the pili showed a current response when applying a voltage, forming a network of conductive pili or nanowires within the biofilm (Reguera et al., 2005). These two mechanisms are not exclusively independent of each other. In *Geobacter* biofilms, for a thickness less than 10 µm, the pili network works cooperatively with the cytochromes in the biofilm matrix, in order to ensure the electron discharge to the electrode. However, when the thickness of the biofilm increases, the reversible oxidation-reduction of the cytochromes becomes rate limiting in the cells further from the electrode, with an accumulation of reduced species in the external layers. At this point, the mediation by nanowires becomes dominant since the pili appendages are able to discharge electrons at micrometer distances, therefore connecting the cells in the upper layers of the biofilms to the oxidized cytochromes in the closest regions of the electrode (Steidl et al., 2016).

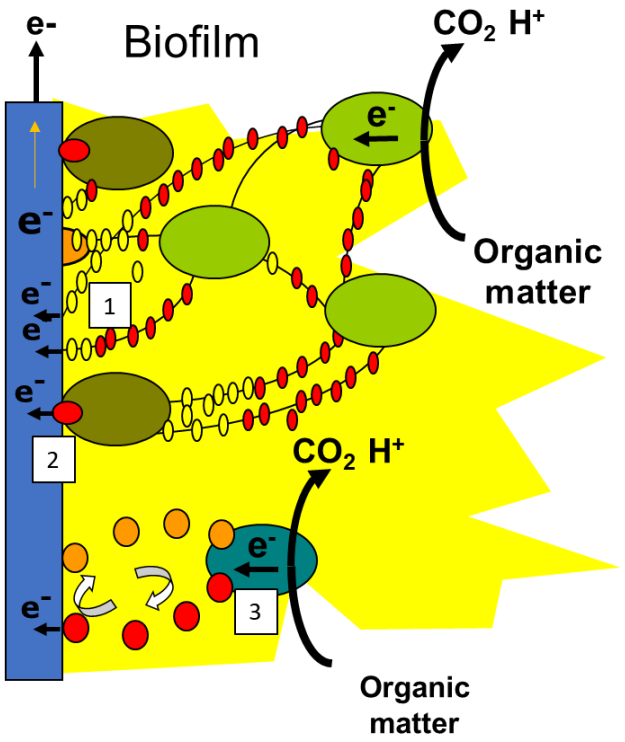

Figure I-2 : Schema of the different EET mechanisms. (1) EET by pili. (2) EET by direct physical contact between the cell and the electrode. (3) EET by redox mediators. Modified from Santoro et al., 2017.

I.2.3. Bioanode formation

The functioning of a BES is intrinsically linked to the colonization of the anode by electroactive bacteria. The process of EAB formation on the anode surface consists of a few steps. An inert electrode is immersed in an anolyte composed by a liquid culture medium that contains a substrate and is inoculated with a source of electroactive microorganisms (inoculum). Generally, the solution is devoid of oxygen or other soluble acceptors, as to favor the anode as the sole electron acceptor. The anode is then polarized at a fixed potential relative to a reference electrode by the use of a potentiostat (Figure I-3 (A)), or coupled to a cathode via a simple electrical resistance (Figure I-3 (B)), assuring that the cathode potential is greater than the anode potential. The electroactive bacteria present in the anolyte degrade the substrate, which serves as their source of carbon and electrons, and evacuate the electrons resulting from oxidation to the anode via the mechanisms already described in section I.2.2.1. In other words, bacteria respires on the anode, which they use as the final electron acceptor.

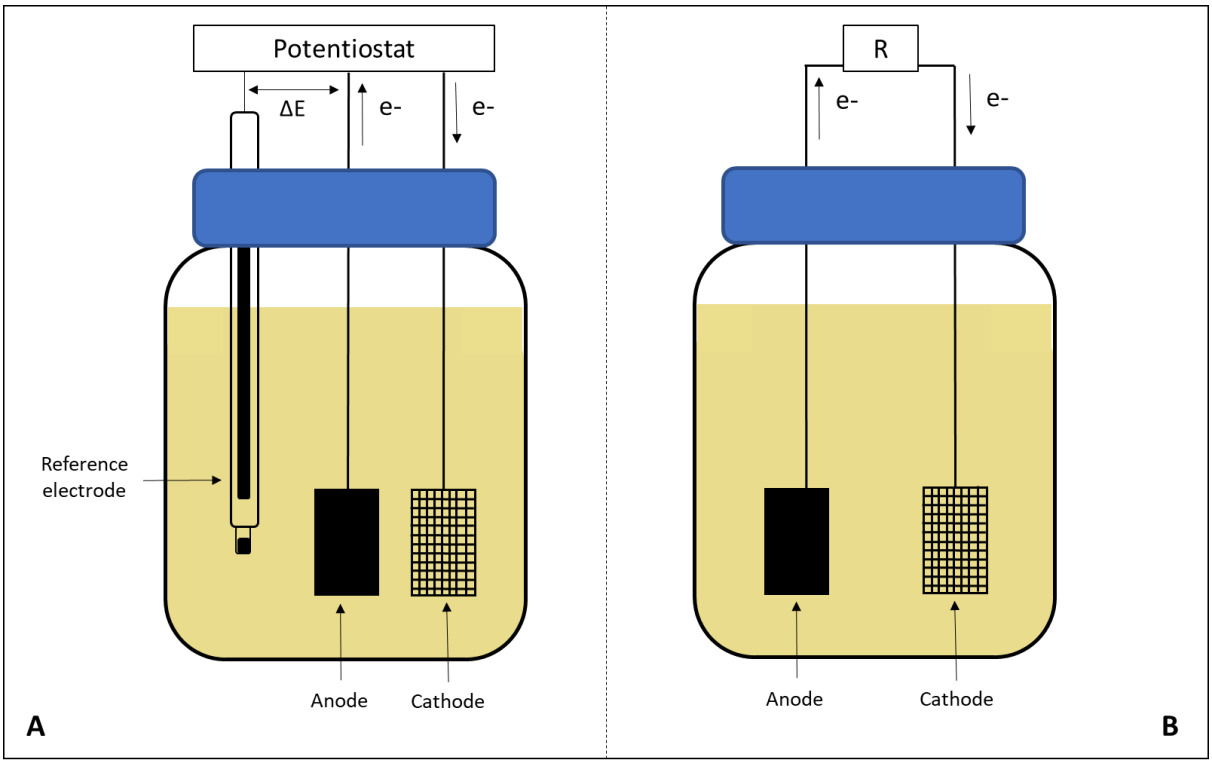

Figure I-3 : Schemes of BES reactors. (A) Three-electrode system connected to a potentiostat. (B) Two-electrode system connected to an external resistance.

For the bioanode formation, some parameters are fixed before EAB formation and are not modifiable. Others parameters can be set before biofilm formation and later changed. This section aims at describing the main parameters to form an EAB on the anode of a BES, as indicated in Table I-1.

Table I-1 : Relevant parameters to form bioanodes in bioelectrochemical systems.

Fixed before EAB formation and non-modifiable	Fixed before EAB formation and modifiable
• Anode material • Source of electroactive microorganisms (inoculum)	• Type and concentration of substrate • Supply of the culture medium, substrate and inoculum • Temperature • Anode potential

I.2.3.1. Anode material

Selecting anode material is an important challenging decision when designing a bioanode, since it is a non-modifiable parameter during the formation of an EAB. In order to have a well performing bioanode, the chosen material must be biocompatible (for allowing the development of the EAB over its surface, but at the same time being resistant to biological degradation) and electrically conductive (for ensuring the electron flow between the biofilm and the electrical collector). In addition, it should be resistant to mechanical changes and corrosion. For industrial applications, low-cost and durability are also required (Mier et al., 2021). Metallic and carbon based are the most suitable materials for the characteristics

required for a bioanode, and are therefore the most widely used. In the case of carbon materials, a wide range of configurations is commercially available, which also include carbon derivatives such as graphite or amorphous carbon. Carbon based electrodes can be classified whether the structure is plane, packed or brush-shaped (Wei et al. 2011). Plane electrodes include carbon paper, carbon cloth, carbon mesh and planar graphite. Roubaud et al. (2019) tested industrial planar graphite, carbon felt and carbon cloth as anode materials in a MEC fed with domestic wastewater, where graphite doubled current production in comparison to carbon felt and carbon cloth, probably due to the higher conductivity of graphite and its strong hydrophilicity. Subsequently, packed-structured carbon anodes can increase the available colonization surface for bacteria. In this group, carbon felt, graphite felt and granules, and granular activated carbon are found. However, not always the use of a tridimensional electrode increases the performance of the bioanode, as in some cases bacteria is not able to colonize the internal volume of the tridimensional electrode and only form a biofilm in the external surface (Blanchet et al., 2016). Finally, brushed-shaped carbon electrodes were also used as bioanodes of MFC (Logan et al. 2007; Shahid et al. 2021) however fiber agglomeration can hamper bacterial and substrate diffusion into the internal fibers of the brush when working in macroreactors. To conclude, carbon based electrodes are low-cost versatile biocompatible options for bioanodes. However, as their conductivity is of two to three orders of magnitude lower than that of metallic materials, they are at a disadvantage for industrial applications. BES electric performance can decrease with a low conductive electrode. The performance loss may be small in a lab-scale reactor, yet in a reactor of industrial dimensions, the loss can be more important.

In the field of metallic materials, gold and platinum were used only for fundamental studies in small sized electrodes, since its elevated price prevents its use as macroelectrodes (Y. Liu et al. 2010; Pocaznoi et al. 2012). Less expensive metals can be used as electrodes if there is a conductive passivation layer that protects the metal from its oxidation. This is the case of stainless steel, of which its reasonable cost, resistance to corrosion, and large industrial availability in different compositions and morphologies, suggest it as a suitable option for the development of bioanodes. Our research group at LGC is pioneer in the use of stainless steel anodes in BES. Dumas et al. (2008) formed *G.sulfurreducens* biofilms over stainless steel anodes catalyzing acetate oxidation up to current production of 2.4 A/m^2. The following year, Erable and Bergel (2009) used a natural marine biofilm as inoculum to form the first EAB under constant polarization over stainless steel plates and grids, reaching current production values of 5.9 and 8.2 A/m^2 respectively. Later, Pocaznoi et al. (2012) used stainless steel electrodes with different surface topographies to form bioanodes from soil leachate. The surface topography did not considerably affect the current production, and maximal values of 20.6 A/m^2 where obtained when polarizing the anode at -0.2 V/SCE. Stainless steel was also used as a foam design. Ketep et al. (2014) tested this material configuration and carbon cloth in the same operational conditions. The production of current was of 80 A/m^2 when using stainless steel foam in comparison to the 33 A/m^2 obtained for carbon cloth.

Other metallic materials, such as copper and silver, have been generally discarded as anode materials due to their antimicrobial properties, since they release metal ions into the medium that can be detrimental for the growth, development and/or activity of bacteria. Baudler et al. (2015), however, succeeded at polarizing metals at a potential lower than its electrochemical oxidation potential, avoiding the release of metal ions to the bulk. This was proved for copper, nickel, silver, gold and stainless steel, where the higher current density values of the study were for copper and silver reaching 15.1 A/m^2 and 11.1 A/m^2 respectively.

I.2.3.2. Inoculum or source of electroactive bacteria

Once the anode material is selected, the next step in forming a bioanode is choosing the source of electroactive bacteria. Chabert et al. (2015) revisited the electroactivity of natural, anthropogenic and extreme environments, determining that a wide variety of electroactive bacteria is present in several ecosystems.

Electroactive bacteria grow in natural environments such as aquatic, beach and marine sediments. Bond et al. (2002) were pioneers in harvesting energy from marine sediments by implementing a benthic MFC. In addition, Rousseau et al. (2013) worked with salt marshes to inoculate MECs for biohydrogen production. Soils and composts enriched in organic matter are also a prolific source of electroactive bacteria. Cercado-Quezada et al. (2011) profited from the microbial community present in garden compost leachate to treat dairy waste in the bioanode of a MFC. Later, garden compost leachate was used to form EABs for implementing more fundamental studies, such as the investigation of the temperature effect on bioanodes and the mechanisms of biofilm formation (Oliot et al. 2017; Chong et al. 2018). Besides natural environments, electroactive bacteria can also be found in several types of industrial wastewaters such as dairy, brewery, tannery, paper-plant wastes, among others (Aghababaie et al., 2015). Activated sludge is also used as a source of electroactive bacteria for wastewater treatment in different BESs configurations (Yoshizawa et al. 2014; Hoareau et al. 2021).

Certain electroactive bacteria can thrive in extreme environments, such as hypersaline, acidic environments, or at high temperatures. As examples, Askri et al. (2019) inoculated BESs with hypersaline sediments providing from lake sediments where NaCl concentration reached 200 g/L. Ni et al. (2016) operated a MFC with acidophilic microorganisms enriched at a pH of 2.5 to treat wastewater providing from an underground mine containing inorganic sulfur compounds. Parameswaran et al. (2013) grew microbial bioanodes with a thermophilic bacterium usually found in marine sediments, at a temperature of 60°C. In a more extreme case, Yilmazel et al. (2018) operated MEC at a temperature of 80°C with electroactive strains isolated from hydrothermal systems. Apparently, thermophiles are rich in multi-heme c-type cytochromes, which are later involved in EET to solid electron acceptors.

Figure I-4 : Diverse natural environments source of electroactive bacteria: a) salt marsh sediments, b) soil sediments, c) wastewater, d) activated sludge from water treatment plant, e) hypersaline sediments, f) deep marine sediments.

Regarding the diversity of electroactive bacteria, an extensive literature review reported 94 species comprising bacteria and archaea able to perform EET. From the 94 species, 65 were identified to perform anodic EET (Koch and Harnisch, 2016). Logan et al. (2019) identified that electroactive bacteria mainly belonged to the *Proteobacteria* and *Firmicutes* phylum. Within *Proteobacteria*, in the class of *Gammaproteobacteria*, there was a predominance of the *Shewanella* genus, whether for *Deltaproteobacteria*, there was a majority of the *Geobacter* genus with the presence of *Desulfuromonas.* This is not surprising, since the best-characterized electroactive species in bioanodes until this day are *Geobacter* and *Shewanella spp.* (Hu et al., 2021).

From a practical point of view, bioanodes can be formed using single-species or multi-species inoculum. Single-species inoculum is useful for an in-depth study of electron transfer mechanisms, as their complexity is reduced to a single bacterial species. In addition, the control over the parameters of anode formation can be more finely tuned since the bacterial specie is unique and known. However, working with a multi-species inoculum, which leads to the formation of a multi-species EAB, is closer to the real conditions of implementation of a bioanode in a BES.

I.2.3.3. Substrate: source of electrons and carbon

The following step for the formation of the bioanode is the choice of the substrate. The latter acts as the source of energy and carbon (nutrient) for bacteria. Bacteria are capable of oxidizing a wide variety of organic molecules in order to collect energy for growth and metabolic functions. The choice of substrate and its concentration does not only influences the selection of electroactive bacteria from a multi-species inoculum, but also impacts on the biofilm electroactivity. Substrates used in the anode of a BES include

simple substrates, such as carbohydrates, fatty acids and amino acids. More complex substrates, comprising all-types of wastewater streams, such as urban food, livestock, textile and paper industry effluents, can also work as substrate for improving waste valorization. In this case, the consortium of bacteria is able to degrade complex molecules in order to provide electroactive microorganisms with simple substrates (Pandey et al., 2016).

Acetate represents the most commonly used simple substrate in the BES anode (Pant et al., 2010). Its popular choice is based in the fact that acetate does not follow alternative microbial conversions, such as methanogenesis and fermentation at room temperature, being widely available for oxidation in the Krebs cycle. The oxidation of acetate follows the equation:

$$CH_3COO^- + 4H_2O \rightarrow 2HCO_3^- + 9H^+ + 8e^- \quad \text{Eq. I-1}$$

As indicated before, acetate can also be obtained as a product of several metabolic pathways for longer carbon compounds, as for example glucose. However, fermentative bacteria must first degrade the glucose molecule into simpler molecules, such as acetate, to be available for electroactive bacteria (Freguia and Rabaey, 2008). The problematic that this could entail is the creation of electron sinks due to fermentation. The production of hydrogen from fermentation could serve as an electron donor to methane, diverting electron flow away from the bioanode (Lee et al., 2008). Later, the rapid utilization of fermentation end products by electroactive bacteria, (i.e. lactate, formate and butyrate) was described as a synergistic requirement of the bacterial consortium when fermentative substrates are used (Kiely et al., 2011). In another study, Flayac et al. (2018) used acetate, lactate, propionate and butyrate as substrate in wastewater inoculated MECs. They found out that the biofilms were mainly dominated by the *Geobacter* genus but there were differences at the species level. Therefore, they proposed a degradation pathway of complex substrates into acetate, which appeared to induce syntrophic interactions between acetate producing and consuming bacteria. This seems to indicate that in order to choose a suitable substrate, the nature of the microbial population present in the inoculum must be taken into account, as this consequently have an impact on the microbial community of the bioanode.

I.2.3.4. Supply of the anolyte, substrate and inoculum

The anodic chamber or compartment of a BES can be operated in batch, fed-batch or continuous mode. If the anolyte is not changed, the system works in batch mode. However, as this can lead to the depletion of nutrients or substrate, in addition to the generation of by-products that can inhibit cell development, operation in fed-batch mode is a viable alternative. This operation mode is the most widely used so far. In a fed-batch mode the whole anolyte can be completely renewed at strategic stages of the experiment, mainly when current production decreases (Blanchet et al. 2015; Oliot et al. 2017). In other cases, only a part of the anolyte can be renewed (Carmona-Martínez et al., 2013), or the suspended biomass eliminated to favor preferentially the growth of electroactive bacteria (Ahn and Logan, 2010).

Replacement of the anolyte can also be helpful to understand if bacteria uses molecules as electron shuttles for EET (Bond and Lovley, 2003; Marsili et al., 2008) or if the anolyte contains soluble electron acceptors that could compete with the anode, preventing electrons from being used by the bioanode for current production. Conversely, the BES can be operated in continuous mode. Typically, the EAB formation starts in batch mode (for a few days) and then is switched to continuous by feeding the reactor with fresh anolyte. Continuous mode allows control of the anolyte composition and improves electroactive reaction pathways. However, a proper residence time inside the reactor must be set. If shear stress created inside the reactor is too high, it can detach cells from the biofilm. Residence times are in general between 12 to 20 hours (Santoro et al., 2017).

The culture medium of a BES can be a synthetic liquid medium of a known composition containing electrolytes, minerals and vitamins, or a real, environmental one inoculated with a microbial inoculum. In some cases, when working with a real medium, this one can work as the microbial inoculum as well. In order to obtain reproducible results when working with BES, the environmental inoculum sampling site should be as precise as possible. In addition, the concentration of the inoculum should not exceed 10% v/v with respect to the anolyte, as to avoid large deviations in the inoculum microbial population that could lead to poor reproducibility of the EABs electroactivity (Rimboud et al., 2014).

Substrate concentration is another operating parameter to be fine-tuned. For acetate, it was observed that current production in EABs generally increases proportionally to acetate concentration at low concentration values and then current production either tends to a maximum plateau or is inhibited, when acetate concentration is at high values. Pocaznoi et al. (2012) demonstrated this in bioanodes formed from soil leachate at different acetate concentrations of 10, 20, 50 and 100 mM. In this case, acetate was added in pulses; this means that acetate was re-added to the reactors when current dropped to zero and no current limitations in the range from 10 to 50 mM were seen. However, at 100 mM, the electroactivity of the EAB was reduced to its half. Ter Heijne et al. (2015) observed a similar trend in MFCs with current increasing from 0 to 1.1 A/m^2 with acetate concentration ranging from 0 to 1 mM, and a later current stabilization at 1.4 A/m^2 at acetate concentration values from 1 to 20 mM. The mode of acetate addition can also play a role in the electroactivity of EABs. For salt marsh sediments, Rousseau et al. (2013) determined that regular addition of acetate on a daily basis at 40 mM yielded better results than pulse addition when acetate dropped to values close to 5 mM.

I.2.3.5. Temperature

In general, the bioanode is operated in a range of between 20°C to 45°C, which are the values for mesophilic optimal bacterial activity. Temperatures higher than 50°C were probed to inhibit the anodic performance, inactivating microbial metabolism and decreasing the production of current (Li et al., 2013). In addition, temperature has a direct impact in the kinetics of the anode. Y. Liu et al. (2010) increased the temperature from 30°C to 40°C in wastewater biofilms formed over graphite-rod anodes

and yielded a current increase of 80%. Oliot et al. (2017) also determined a two times faster start-up time for EABs formed from soil-type inoculum at 40°C compared to those formed at 25°C. However, the strategy of raising the temperature can also stimulate the growth of non-electroactive bacteria which could compete for the consumption of the substrate resulting in low coulombic efficiencies (Michie et al., 2011).

I.2.3.6. Anode potential

The voltage between the anode and the anolyte with respect to a reference electrode is called the anode potential. If the potential is not controlled, and no current flows through the electrodes, the anode is at open circuit potential. On the other hand, the potential can be controlled by the use of a potentiostat. In general, potentiostats are connected to the anode and to a computer, where a software allows the control of the potentiostat by the user. A defined potential can be applied to the anode and controlled at a fixed level (constant polarization). Conversely, the anode can be polarized constantly at some periods, and be left at a free, open circuit potential, at others (intermittent polarization).

- Constant polarization

The tuning of the anode potential plays a key role in the electroactivity of bioanodes. Thermodynamically speaking, the ideal would be to implement bioanodes that yield the highest achievable current at the lowest workable potential. Following the laws of electrochemistry, as higher the potential, higher current densities should be harvested by bioanodes. However, this is not always the case. In some bioanodes, an enhanced electroactivity at higher potentials was reported (Rousseau, 2016), whereas bioanodes polarized at more negative potentials showed higher current production (Torres et al., 2009). In addition, no correlation between polarization potential and current production was also described (González-Muñoz et al., 2018). These discrepancies lie in various experimental factors, such as the anode material, the nature of the inoculum and culture medium, the timescale of biofilm formation, among others.

For single-species biofilms, the effect of anode potential was mainly investigated for the model bacteria of *G.Sulfurreducens* (Dumas et al. 2008) and *S.Oneidensis* (Cho and Ellington 2007) species. In the case of *G.Sulfurreducens*, this anaerobic electroactive specie effectively grew with low anode potentials in the range between -0.41 V/SCE to +0.11 V/SCE, showing a peak of current production at 0 V/SCE. For higher potentials, from 0.4 V/SCE to 0.6 V/SCE, current production decreased and it was thought that bacteria was under stress conditions, since they activated the production of extracellular polysaccharides for cell protection (Yang et al., 2019). For *S.Oneidensis*, Kitayama et al. (2017) formed biofilms over graphite electrodes at the potentials of -0.24 V/SCE and 0.16 V/SCE. Higher current density values were observed for the biofilm formed at 0.16 V/SCE. This biofilm presented a compact morphology and the absence of EPS polysaccharides. In contrast, biofilm formed at -0.24 V/SCE, showed a random

distribution of cells, an increased polysaccharides production and low current values. Pinto et al. (2018) worked in a larger potential range from -0.34 V/SCE to 0.46 V/SCE, confirming the logical trend of higher current production at higher potentials for *Shewanella* species.

For multi-species EABs, the observation of a trend is more complex than for single-species biofilms. In the case of wastewater as inoculum, Zhu et al. (2014) run MECs with domestic wastewater, observing a decrease in current production at higher potentials. They also reported that the microbial population of the bioanode was unaffected by the anode potential, in where biofilms were dominated by bacteria similar to *G. Sulfurreducens.* In a later study, Guo et al. (2021) operated three-electrode system chamber BES with brewery wastewater at different anode potentials, finding out that the highest current production was at 0 V/SCE, and then decreasing with the raising potential. Dennis et al. (2016) operated a stack of MFC with a mixture of anolytes from anaerobic reactors, and observed a decline of the EABs electroactivity at very high potentials (0.56 V/SCE) with the formation of thinner biofilms. At all potentials, microbial population was closely related to *G. Sulfurreducens*, but with an enrichment of a different *Geobacter* population at 0.56 V/SCE. For the case of marine sediments, Rousseau et al. (2016) showed an increase in current production with more positive applied potentials on graphite felt electrodes. *Marinobacter spp* and *Desulfuromonas spp* dominated the bioanodes after 15 days of polarization, and the ratio of these two species depended on the anode potential. Later, González-Muñoz et al. (2018) tested hypersaline sediments in a potential range from -0.4V/SCE to 0.1 V/SCE, reporting that the polarization potential had no effect in the maximum current production.

- Intermittent or delayed polarization

Furthermore, some authors have worked under periods of no polarization control. This means that the formation of the bioanode takes place at some periods at a free, or open-circuit, potential where no current is recorded. At other periods, constant potential is imposed by a potentiostat and current is measured in time by a chronoamperometric technique. Pocaznoi et al. (2012) showed the benefits of delayed polarization when forming EABs from compost leachate over carbon cloth electrodes. For biofilms formed under delayed polarization, current density values of 9.4 A/m^2 were obtained after 3 to 9 days of polarization, whereas for biofilms formed at constant polarization, the same current values were obtained after 36 days of polarization. This strategy also affected the biofilm morphology, obtaining more compact and homogeneous biofilms when working at constant polarization, while biofilms with a more dispersed and heterogeneous structure were formed by delayed polarization. Later, Zhang et al. (2018) studied the effect of shorter intermittent applied polarization periods (from 1s to 300s) in multi-species EABs mainly dominated by *Geobacter*. They found that intermittent polarization enhanced current production, having an impact in the morphology of the biofilm, linking these facts with the regulation of redox proteins and c-type cytochromes within the biofilm matrix. In order to understand these phenomena from a more fundamental point of view, Ter Heijne et al. (2020), reviewed

the phenomenon of electron storage in EABs, stating that during open circuit potential, electrons can be stored in the biofilm and consequently released when the circuit is closed. If intermittent polarization is carried out at short-time scales, electron storage should be expected to happen in reduced cell components, such as cytochromes. On the other hand, if it occurs at longer timescales, electrons should be stored in the form of polymeric substances. However, the integrated understanding and identification of electron flows in EABs is so far at its very early stages.

I.2.4. Limitations on the electroactivity of bioanodes

The electroactivity or electrochemical performance of bioanodes is generally assessed by the anode current density J (A/m^2). In multi-species bioanodes, current density severely drop after a few days or tens of days of operation, sometimes losing even more than 50% of their maximum electrochemical performance (J_{max}). Table 1 from Research Article 2 resumes bibliographic studies where this phenomena is observed. Among the possible causes that can explain these limitations in the electroactivity of bioanodes, the ones described in this section are acknowledged from a point of view of the EAB.

I.2.4.1. Metabolic spatial variability

In the initial moments of bioanode formation, the biofilm cells attached to the anode have access to both the nutrients and substrate present in the anolyte, as well as the anode. Consequently, as the biofilm grows in thickness, the cells in the outer layer of the biofilm should have a better access to the nutrients and substrate, whereas the cells placed in the inner layers should have the electron acceptor (anode) more available. This can make the metabolic activity of the biofilm spatially and temporally heterogeneous, thus affecting its electrochemical properties. The main causes that can affect the metabolic activity on EABs are related to transport phenomena and redox-states of molecules that are implicated in electron transfer:

- Biofilm acidification: When electroactive bacteria oxidize organic substrate, protons are produced. As the biofilm plays the role of physical barrier, limiting the diffusion of chemical compounds, accumulation of protons can occur within the biofilm and local acidification can take place.
- Substrate and nutrient gradients: To ensure the viability of the biofilm, nutrients and substrate must reach all the biofilm bacterial cells. If diffusion is limiting, probably activity is likely to occur in the external layers of the biofilm. Therefore, the deprived areas may not contribute to current production.
- Variation of the redox potential: EET within the biofilm occurs via the reduction of cytochromes (DET) or mediators (MET), which must be in their oxidized state. If the potential is not

homogeneous throughout the biofilm, where in some areas the cytochromes or mediators are in their reduced state, these areas will be less active than others will.

To this day, there is a discrepancy between the results of the metabolic variability of the biofilm. Certain authors describe a bioanode with active cells in the outer layers, and an inactive inner core. On the other hand, others describe that cells closest to the electrode are the most active, and then the activity is reduced as they approach the limit with the liquid bulk. The main theories of these two approaches are described below:

i) Inactive inside, active outside

Renslow et al. (2013) formed 400 μm *G. Sulfurreducens* biofilms to prove why they become less effective at producing current with an increasing thickness. They found that the electron donor, acetate, was not detectable in the range of 0 to 170 μm. In addition, the external layers of the biofilm were metabolically more active than the bottom ones. For measurement, they used uranium as a redox-active probe and X-ray absorption spectroscopy to determine the uranium oxidation state. In this study, they proposed that a metabolically active region has access to the electron donor, and the base, which is deprived, only functioned as a conductive network. Researchers from the same group, Babauta et al. (2013) determined that pH, measured with a pH microelectrode, was not a limiting factor and confirmed the metabolic variability by measuring the redox gradient inside the biofilm with a redox microelectrode.

Sun et al. (2015, 2016) grew EABs from *G. Anodirreducens SD-1*, *G. Sulfurreducens* and domestic wastewater inoculum. To determine the metabolic state of the cells they detected their viability by cell staining coupled with confocal microscopy. Regardless of the inoculum, in all cases the trend in the biofilm viability was similar. In the initial moments of biofilm formation, the cells were mostly viable (live). Then, after the peak current (reached at day 8 for *G. Sulfurreducens*, at day 15 for *G. Anodirreducens SD-1* and at day 18 for domestic wastewater), non-viable (dead) cells were detected by microscopy close to the anode and growing with the biofilm thickness. This trend of dead cells inside, live cells outside was linked with the decrease of charge resistance inside the biofilm after J_{max} and the increase of diffusional resistances. Sun et al. (2017) also discovered that when increasing the potential applied to a MEC multi-species bioanode, current raised after 18 days. In addition, the inner dead layer that they had already described was diminished. Oppositely, when decreasing the potential, current dropped and the dead layer was again present. Cai et al. (2022) also observed these same phenomena after 27 days of biofilm formation when working at low potentials.

Acidification of the biofilm can be another cause for the drop of the electroactivity. The most used strategy to avoid proton accumulation is the use of an anolyte based on a buffer solution, i.e. phosphate or bicarbonate buffer. Torres, et al. (2008) demonstrated that when working with a mixed culture enriched of *G. Sulfurreducens*, current production was directly proportional with phosphate buffer

concentration. Later, Pocaznoi et al. (2012) added different concentrations of bicarbonate buffer to compost leachate bioanodes, where in this case, the buffering effect on current production was not relevant in comparison to the previous study. Ranjan et al. (2017) studied the buffer effect in more detail. They observed that when forming *Geobacter*-enriched bioanodes with a 100 mM phosphate buffer medium the pH within the biofilm was stable. When gradually lowering the buffer concentration from 100 to 50 mM in the medium after 35 days of operation, current production decreased together with an internal pH gradient measured with a pH microelectrode. Microscopic observations showed an internal dead layer for the biofilms that had internal acidification. The same metabolic spatial variability results and the same correlation of the electroactivity with buffer concentration were observed by G. Yang et al. (2021) when growing bioanodes with different buffer concentrations for brewery wastewater treatment. In addition, the presence of a buffer also influenced bacterial community of the biofilm, being the latter enriched with *Geobacter* at high buffer concentrations (50 to 100 mM) and with *Methanobacteria* at low buffer concentrations of 5 mM.

ii) Inactive outside, active inside

Read et al. (2010) reported that for EABs formed in a period of six days from *G. Sulfurreducens* and *S.Oneidensis* MR-1, a decrease in viability was associated with an increase in biofilm thickness using confocal microscopy. Later, Schrott et al. (2014) observed the active cells close to the anode and less active cells far from the anode in thick *G. Sulfurreducens* biofilms, proposing that current was mainly produced by the cells that were closed to the anode surface. As the biofilm developed, cells that grew far from the electrode were limited in terms of respiration rates. Chadwick et al. (2019) also determined that for *G. Sulfurreducens* biofilms, the highest metabolic activity was in the electrode surface, regardless of the applied anodic potential or the biofilm thickness by using isotope probing coupled to nanoscale mass spectroscopy. They suggested that electron transfer over distance, in spite of substrate, pH and/or redox potential gradients could be the cause of performance limitations.

In summary, it is very likely that the discrepancy between the two theories is due to the different experimental techniques to detect the metabolic variability (i.e. confocal microscopy coupled with cell staining for viability, redox-active probes, and isotope probes) and the time scales over which the experiments were run. As an example, for *G. Sulfurreducens*, depending on the biofilm thickness at the measuring interval and the technique used, different results were obtained. Additionally, a remark should be made in the cases that cells stains coupled with microscopic techniques were used to determine viability. It was reported that in some cases, viable bacterial cells could be permeable to Propidium Iodide, which stains dead cells. In addition, Syto 9, which stains live cells, might have issues to cross the cell membrane of Gram-negative bacteria (Davey and Hexley, 2011; Kirchho and Cypionka, 2017; Stiefel et al., 2015).

I.2.4.2. Microbial heterogeneity

In addition to the metabolic spatial variability, it is also possible to find a spatial and/or temporal heterogeneity of the microbial community within the EAB. Tejedor-Sanz et al. (2018) found a microbial spatial stratification in a four months old EAB where an inner cluster of *Geobacter* species surrounded by another type of bacteria in the outer layers. Temporal stratification was likewise studied. Whether the EAB is young, i.e. 15 days (Pepè Sciarria et al., 2019) or much more mature, i.e. 2 months, (Chang et al. 2022) the majority of the microbial populations that compose the EAB evolved over time.

I.2.4.3. EPS production and composition

The spatio-temporal evolution of the EPS production and composition can affect the EAB electroactivity in two ways. On one hand, the growing EPS matrix can act as a barrier to the diffusion of substances, creating substrate, pH, oxygen, metabolites, ions and other soluble molecules gradients within the biofilm. On the other hand, the relationship in the composition between EPS proteins and EPS polysaccharides can influence the EAB electroactivity.

Proteins and polysaccharides represent the largest portion of the biofilm matrix where they fulfil different functions (Sheng et al. 2010). On one hand, proteins in the EPS contain the redox machinery for electron transfer. Heme-binding proteins (containing an iron atom in their structure) such as cytochrome-c were found in the EPS of *S. Oneidensis* and *G. Sulfurreducens* (Cao et al., 2011; Inoue et al., 2011; Li et al., 2016). On the other hand, polysaccharides are critical to anchor c-type cytochromes between bacterial cells in the matrix, and serve as protection when the biofilm is under stress conditions (Rollefson et al., 2011). However, the insulating nature of polysaccharides can decrease the electrical conductivity of the biofilm matrix, therefore affecting the EABs electroactivity (Borole et al., 2011).

The ratio between EPS proteins and EPS polysaccharides in the EAB matrix started to gain interest in the very recent years in terms of electron conduction within the biofilm. G. Yang et al. (2019) grew *G. soli* bioanodes at different polarization potentials and stopped them after the maximum current point, i.e. after 3 to 4 days of experiment, for EPS analysis. Guo et al. (2021) performed a similar experiment with multi-species inoculum retrieving the EPS after 9 days of inoculation. T. Li et al. (2020) studied the effect of acetate concentration on current density analyzing the exopolymeric matrix after 3 days of operation when current reached the maximum value. For all these studies, a positive correlation was found between current production and protein content in EPS. In contrast, a negative correlation was determined between current production and polysaccharide content in EPS.

Others authors investigated on how to modify the amount of polysaccharides in the matrix by exposing the EAB to compounds known to be toxic for the cells. Zakaria and Dhar (2020) exposed the bioanode of a glucose-fed MFC to silver nanoparticles. Current production declined up to 30% in comparison to the control experiment (non-exposed) and the ratio of polysaccharides to proteins raised from 40% to

70%. In another study, multi-species EABs were grown in anodes with different chlorine concentrations. The concentration of polysaccharides augmented 18 times in comparison to the control experiment when chlorine concentration was the higher of the tested range (0.5 mg/L). The protein content decreased significantly. Current production felt by more than 60% (Dong et al., 2021). In these cases, polysaccharides become the dominant component of the EPS, playing their role as a protective barrier against the transfer of external agents.

It is then assumed that if polysaccharides reach a concentration where their non-conductive nature hinders electron transfer between the redox-active proteins and the electrode, the electroactivity of the biofilm will be clearly affected.

I.2.4.4. Quorum sensing

In the process of biofilm formation, cell aggregation is controlled by quorum sensing (QS). This mechanism refers to an intercellular communication through self-produced molecules, generally acyl homoserine lactones (AHLs) for Gram-negative bacteria. When cell density increase, the concentration of the self-produced molecules reaches a threshold value, or quorum, activating the cell-cell communication mechanism (Paquete et al., 2022).

AHLs were detected in the exopolymeric matrix of four bacterial species from the halophilic *Halomonas* genus. Synthesis of the self-produced molecules was dependent of the biofilm growing phase and the maximum value was reached during the late exponential phase (Llamas et al., 2005). Jing et al. (2019) demonstrated that *Geobacter* sp. were able to secrete AHLs as well. Another QS sensing mechanism is also possible for bacteria that execute indirect electron transfer. *Pseudomonas Aeruginosa* uses phenazine mediators for indirect electron transfer. QS molecules control the production of phenazine, which mediate electron transfer to the anode (Venkataraman et al., 2010). A similar mechanism was recently described for the model electroactive bacteria of *S. Oneidensis*, where biofilm formation was induced by low concentrations of riboflavin (37 nM), also serving as electron shuttles (Edel et al., 2021).

The use of QS in BES was tested by Monzon et al. (2016) adding QS molecules to the anode inoculated with an hypersaline strain of *Halanaerobium praevalens.* A 95% augmentation in biofilm mass and a 30% increase in current generation compared to the control experiment was described. Chen et al. (2017) working with a multi-species bioanode confirmed the activity of QS processes through an AHL-sensing bacterium. However, as the concentration of AHLs molecules was low, their precise identification was not possible. Nevertheless, when adding three very common commercial AHLs, the electrochemical activity of the biofilm was improved. The relative abundances of *Geobacter* spp. were boosted by the addition of QS molecules and the amount of EPS and redox activity was improved. More recently Z. Liu et al. (2021), used QS molecules to shape the microbial consortia of the EAB of a MEC fed with

waste activated sludge. The biofilm microbial community was enriched in certain electroactive species because of the addition of AHLs molecules.

Apparently, the application of QS molecules in a concentration range of 0.1 to 10 μM for the bioanode of BES is a feasible approach to boost current density. However, it remains to be investigated whether the benefits are short-termed or not.

I.3. Tools for studying multi-species EABs in bioanodes

Multi-species EABs represent a complex subject of study. As described before, the use of a multi-species inoculum implies that electroactive bacteria coexist with non-electroactive, that the mechanisms of EET can be different from one species to the other, that the mechanisms of biofilm formation and the EPS synthesis and composition can be diverse within the biofilm. In addition, the EAB is a living system that evolves spatially and temporally, where its electroactivity is affected in the course of time. The usual methodologic approaches to investigate multi-species bioanodes are typically conducted at the global scale of the biofilm, by using macroelectrodes as the anode, in BES of hundreds of milliliters to several liters. In these configurations, the physicochemical conditions at the anode-EAB-anolyte interface are difficult to determine and control. Biofilm sampling and post-treatment analyses, such as chemical, microscopic, genetic or functional affect the original properties of the biofilm and are generally done at one point of the experiment, usually at the end. To not consider the biofilm dynamics contributes to a great loss of precious information in relation to its electroactivity.

Miniaturizing BES is an alternative way to study multi-species bioanodes at the scale of the biofilm and bacterial cells. The use of microelectrodes and/or microBES allows to access, control and study the local phenomena occurring at the anode-EAB-anolyte interface. The integration of microBES with other techniques, i.e. microscopic, electrochemical, genetic, enables in situ and non-destructive EAB investigation, thus considering its spatio-temporal evolution.

In this section, as a preliminary step in the miniaturizing process, microelectrodes for applications in macroBES will be presented. Subsequently, the benefits of miniaturize the complete BES and their integration with other techniques for biofilm studies will be described in a review article.

I.3.1. Microelectrodes

In terms of definition, a microelectrode is an electrode with at least one dimension being on the micron scale. Common microelectrode shapes can include disk, cylinder, band, sphere and wire type, where in general, the critical dimension falls in the micrometer range of 0.1 to 50 μm (Pletcher, 1991). The most remarkable property of microelectrodes is the enhancement of diffusional mass transport in comparison to macroelectrodes. At very short times, when the thickness of the diffusion layer of the reactant is much smaller than the radius of the electrode (considering a spherical geometry), the microelectrode appears

to be planar to a molecule reaching the edge of the diffusion layer. However, when time is long enough and stationary state is reached, the micro-dimension of the electrode becomes relevant and mass transport is inversely proportional to the radius of the microelectrode (Forster, 1994). This means that as smaller the dimension, the shorter the time to reach stationary state.

In EABs, the use of microelectrodes (in theory to their enhanced mass transport property) is useful to quantify the changes in local phenomena in both the biofilm and the bulk solution surrounding it. As microelectrodes do not affect the biofilm environment, they are widely used as measuring probes to evaluate pH, substrate and redox gradients inside the biofilm as well as for detecting composition and/or hydrodynamic changes in the liquid bulk. In practice, lab-made stainless steel microelectrodes were used as oxygen probes for monitoring oxygen reduction in biofilms submerged in drinking water (Dulon et al., 2007). More sophisticated microelectrodes were developed with a built-in reference electrode to measure pH gradients and redox potential changes in *S. Oneidensis* and *G. Sulfurreducens* bioanodes (Babauta et al. 2013; Babauta et al. 2011). For cathodes, conductivity and sulfide content were measured in wastewater fed microbial fuel cells by using homemade microelectrodes built in platinum and silver microwires (Guerrini et al., 2014).

Another promising use of microelectrodes is as an anode support for EABs. By directly forming a biofilm on the microelectrode, it is possible to enhance mass transfer and biocolonization with respect to macroelectrodes. To our understanding, the only reported use of microelectrodes in macroBES to grow microbial EABs was carried out using platinum microelectrodes in the range of 25 to 50 µm to form garden compost biofilms under constant polarization and with acetate as substrate. Microelectrodes of 25-µm diameter reached a maximum current density of 66 A/m^2, whereas microelectrodes of 50 µm attained 19 A/m^2. Larger diameter of platinum wires of 500 and 1000 µm provided only 7 A/m^2 and thinner biofilms were formed, indicating that the dimensions of the microelectrode enhanced mass transfer (Pocaznoi et al. 2012). As other features, the small size of microelectrodes as bioanodes allows an easy manipulation prior to microscopic analysis. In general, the bioanode can be observed in its entirety, without the need to reduce the size of bioanode sample. Microscopy pretreatment protocols, such as cell staining, labeling, dehydration and/or fixation are less time consuming than in macro-scale bioanodes since diffusion phenomena are enhanced.

I.3.2. Microfluidic BES (Article 1)

The miniaturization of BES is conceivable thanks to the benefits of microfluidics, which allow the creation of microfluidic BES (microBES) in different geometries and materials. The possible access to cell-cell and cell-anode interactions, the fine-tuning of electrolyte hydrodynamic conditions and the coupling with real-time analysis techniques show the great potential of these devices as a valuable tool for EAB study and investigation.

The following review article gives a comprehensive overview of microBES as an integral investigation platform. First, the complexity of the object of study is presented. Then, the idea of downscaling BES is introduced along with the available microfluidic techniques and the different existing microBES designs and configurations. The main advantages and limitations of microfluidic techniques are described. Consequently, the contributions of microfluidics to the fundamental knowledge of EAB are discussed together with promising perspectives for multi-species EABs.

microorganisms

MDPI

Review

Microfluidic Microbial Bioelectrochemical Systems: An Integrated Investigation Platform for a More Fundamental Understanding of Electroactive Bacterial Biofilms

Stéphane Pinck, Lucila Martínez Ostormujof, Sébastien Teychené and Benjamin Erable *

Laboratoire de Génie Chimique, Université de Toulouse, CNRS, INPT, UPS, 31432 Toulouse, France; stephane.pinck@ensiacet.fr (S.P.); lucila.marinezostormujof@toulouse-inp.fr (L.M.O.); sebastien.teychene@ensiacet.fr (S.T.)

* Correspondence: benjamin.erable@ensiacet.fr

Received: 14 October 2020; Accepted: 19 November 2020; Published: 23 November 2020

Abstract: It is the ambition of many researchers to finally be able to close in on the fundamental, coupled phenomena that occur during the formation and expression of electrocatalytic activity in electroactive biofilms. It is because of this desire to understand that bioelectrochemical systems (BESs) have been miniaturized into microBES by taking advantage of the worldwide development of microfluidics. Microfluidics tools applied to bioelectrochemistry permit even more fundamental studies of interactions and coupled phenomena occurring at the microscale, thanks, in particular, to the concomitant combination of electroanalysis, spectroscopic analytical techniques and real-time microscopy that is now possible. The analytical microsystem is therefore much better suited to the monitoring, not only of electroactive biofilm formation but also of the expression and disentangling of extracellular electron transfer (EET) catalytic mechanisms. This article reviews the details of the configurations of microfluidic BESs designed for selected objectives and their microfabrication techniques. Because the aim is to manipulate microvolumes and due to the high modularity of the experimental systems, the interfacial conditions between electrodes and electrolytes are perfectly controlled in terms of physicochemistry (pH, nutrients, chemical effectors, etc.) and hydrodynamics (shear, material transport, etc.). Most of the theoretical advances have been obtained thanks to work carried out using models of electroactive bacteria monocultures, mainly to simplify biological investigation systems. However, a huge virgin field of investigation still remains to be explored by taking advantage of the capacities of microfluidic BESs regarding the complexity and interactions of mixed electroactive biofilms.

Keywords: microfluidics; microfabrication; bioelectrochemical systems; microbial fuel cell; electroactive biofilms; extracellular electron transfer

1. Introduction

The ability of bacteria to transfer electrons from or to a solid material (i.e., extracellular electron transfer (EET)) has long been known in the domains of microbial corrosion or biogeochemistry [1,2] but it is only during the last twenty years that it has been used to harvest energy or to catalyze specific electrochemical reactions in bioelectrochemical systems (BESs) [3–6]. In such engineering systems, bacteria considered as electrochemically active (or electroactive) are able to exchange electrons with electrodes, which they can use as extracellular electron donors or acceptors. The detailed mechanisms allowing the passage of

electrons between the bacterial cells and the surface of the solid material of the electrodes are diverse [7] (Figure 1).

Microorganisms **2020**, *8*, 1841; doi:10.3390/microorganisms8111841 www.mdpi.com/journal/microorganisms

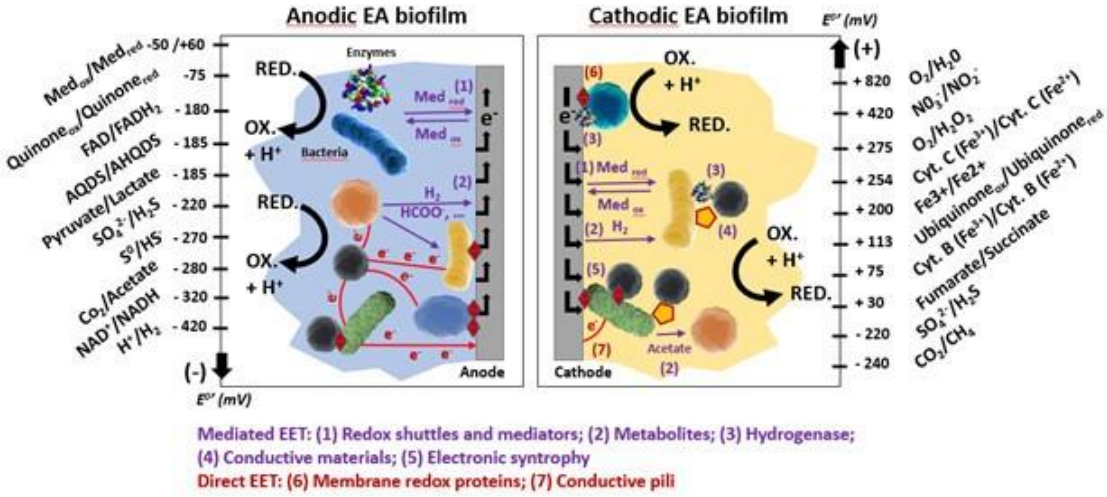

Figure 1. Overview of the bacterial external electron transfer (EET) mechanisms described in the literature and operating individually or in combination in anodic and cathodic biofilms. This figure was adapted from Aghababaie et al. 2015 [8], Santoro et al., 2017 [9], and Blasco-Gomez et al., 2017 [10].

EET may occur either by direct physical contact between bacteria and the electrode [11], through redox proteins attached to the bacterial outer membrane [12], or by bacterial nanowires [13,14]. It can also be mediated by electron shuttles [15,16]. Most of these very sophisticated mechanisms are still being investigated by electrochemical, microscopic, genetic and molecular engineering approaches [14,17]. These EET mechanisms are expressed in a very heterogeneous way at the scale of a bacterial consortium, given the species-dependent nature of EET mechanisms. For example, the nanowires and cytochromes of the outer membranes are not universally expressed, synthesized or induced by the same bacterial species [13,14,18,19]. However, the wide variety of micro-organisms within a microbial community permits the cohabitation of various EET strategies that ultimately improve the electrocatalytic activity of bacterial consortia, allowing a wider range of applications of BESs in the fields of bioenergy, biorefineries, biomass, wastewater and organic waste treatment.

Electroactive bacteria (*Geobacter sulfurreducens*, *Shewanella oneidensis*, *Desulfuromonas acetoxidans*, *Pseudomonas aeruginosa*, *Geothrix fermentans*, *Geobacter metallireducens*, *Geobacter bremensis*, *Geoalkalibacter* sp., *Lactococcus lactis*, *Rhodobacter capsulatus*, *Thermincola ferriacetica*, etc.) [20] can collect electrons from a wide range of soluble substrates [3,4] and transfer them to an electrode in the anodic compartment of a BES. In addition, some of the electroactive bacteria (*Geobacter sulfurreducens* again, but also *Clostridium scatologenes*, *Clostridium ljungdahlii*, *Escherichia coli*, *Sporomusa ovata*, etc.) can collect electrons from solid electrodes, i.e., at the biocathodes of microbial fuel cells (MFCs) [21,22], microbial electrosynthesis systems (MESs) [23–26], microbial electrolysis cells (MECs) [27] or other specific BESs for pollutant remediation [28,29]. Regardless of whether they are anodic or cathodic, electroactive bacteria organize themselves as a biofilm on the surface of the electrode. Their growth dynamics and electrochemical activity on the electrode surface are continuously evolving according to the microbial community populations and the physicochemical conditions of the interface formed between the electrode and the bulk solution; (i) the source of electroactive bacteria (pure culture, synthetic cocktails, consortia), (ii) the properties of the electrode, such as the nature of the material, its topography, its potential, or (iii) the parameters of the bulk, such as temperature, pH, salinity, hydrodynamics and concentrations of soluble nutrients, strongly affect the development of biofilms of electroactive bacteria on the electrodes, and the nature and performance of the EET mechanisms that predominate, mainly within the biofilm. Among the series of parameters described in the literature as having a demonstrated influence on the electrochemical activity of the electrode-electroactive biofilm interfaces (Figure 2), some are fixed and others are modifiable during the formation of electroactive biofilms.

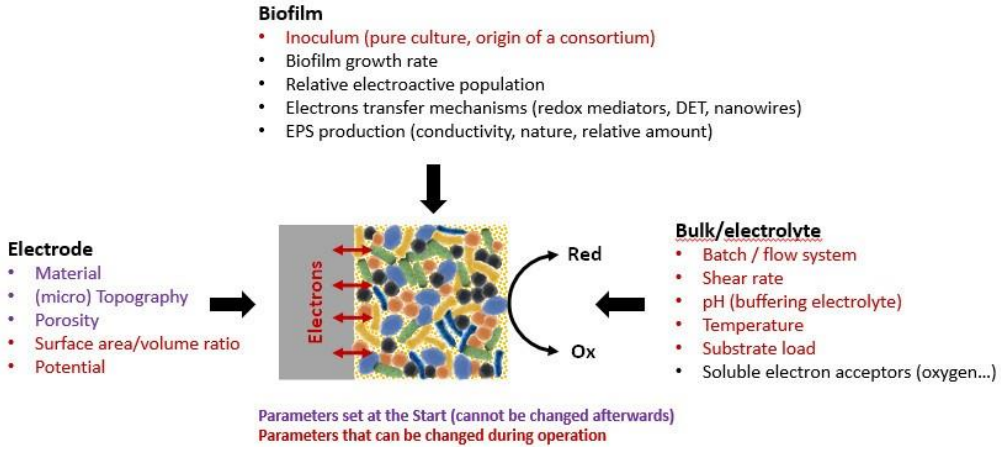

Figure 2. Electrode, biofilm, or electrolyte-related parameters known to have a significant impact on the formation and performance of microbial electrocatalytic systems.

Therefore, the investigation of electroactive biofilms is a multiscale challenge (molecules → cells → biofilm) with a living electrocatalytic interface in evolution as the object of study. However, in the literature, most of the work is conducted at the global scale of a biofilm, i.e., at a rather macroscopic scale of understanding of the phenomena with the implementation of macro electrodes and macro BES. Miniaturizing experimental systems is, however, a very interesting alternative way to study local phenomena at the scale of internal biofilm or even of individual bacterial cells. Thus, the combined or individual use of microelectrodes [30,31] and/or BES microreactors [32–34] are dedicated experimental tools giving access to these phenomena of interest at a deeper scale than that of the whole electroactive biofilm. The scale-down of BESs, thanks to microfluidic reactor concepts, allows the experimental systems to be further miniaturized by also ensuring precise control of the electrolyte flow. The latter would be an important parameter because shear stress [35], concentration gradient [36,37] and interaction with planktonic bacteria [35] have an impact on the colonization and formation of biofilm on electrode surfaces.

The idea of using microfluidics to miniaturize BESs was born from their compatibility with easy microfabrication technologies, such as photolithography and soft-photolithography, which are lowcost fabrication methods. Regardless of the manufacturing processes, microfluidic BESs can be classified into two categories. A first category would be the two-electrode set-ups, which are either scaled down macro MFCs with a reactor volume between milliliters and the microlitre [38–43] or colaminar microfluidic MFCs [44–49]. A second category would be the three-electrode set-ups that have often been used in more fundamentally oriented studies [50–53] in reactors where at least one of the dimensions (height, length, or width) is micrometric.

Microfluidic BESs are used as model experimental systems to develop larger scale MFCs, e.g., to test a new electrode material for a microbial fuel cell, or to design proper microfluidic MFCs, whether single [38,39,41,48] or stacked [43] in order to generate energy. Since they make it possible to control the experimental conditions more sensitively at the interface of the electrode and the bulk solution, microfluidic BESs are also used for the rapid detection of electroactive microorganisms [54,55] and as biosensors for environmental monitoring [44,56–59]. The unique properties of microfluidic systems make them useful in the field of fundamental research, as precise control over the flow would be a critical tool for promoting mass transport or for changing the interfacial conditions at the biofilm– electrolyte interface in electroactive biofilm studies. Microfluidic microbial systems are also described in the study of EET involving nanowires [60] or energy taxy [61], for example.

Some recent reviews [62–65] have already described the functioning and limitations of microfluidic BESs. However, they have mainly focused on microfluidic MFCs and related energy efficiency issues. Beyond this much investigated field, microfluidic BESs also have many implications and uses in the more fundamental arena of understanding. The present review proposes to focus on the results and fundamental insights that microfluidic BESs have brought to the fundamental understanding of the field of electroactive biofilms. First, the different microfluidic BES systems are presented with their individual limitations and

advantages. Then, attention is drawn to the knowledge that microfluidic systems have brought to the field of electroactive biofilms. Finally, perspectives for how microfluidic systems could be used to investigate parameters influencing electroactive bacteria in an electrochemical system are proposed.

2. Microfluidic Microbial BES

2.1. Scaling Down the BES

Macro sized BESs are well-studied systems [3,9,66–70] but, as they are multiscale devices with biological micro objects as catalysts, they are complex and our understanding of them on the macroscale is hindered by the numerous elements involved. Scaling down the BES reactor volume would ensure a more precise and better-defined understanding of the interaction between them, especially between the electroactive bacteria and the electrodes inside the electrolyte. These systems would be simplified, as it would be easier to obtain accurate control over the parameters and the elements involved. However, just scaling down the dimensions would do little to simplify the system. To gain an accurate and precise understanding of the interaction between electroactive bacteria or biofilms and electrodes, controlling the flow inside the BES would also be necessary, as it is a key parameter of the sheer stress, concentration gradient and interaction between the bacteria and the electrode, which acts as support material for the biofilm formation [43–45].

Microfluidic technology contributes greatly to these aspects, as a technology that allows submillimetric working volumes to be used while keeping precise control of the flow [19,48,50,52] . The devices designed with the aim of achieving these parameters are called microfluidic BESs. They are BESs with dimensions around a milliliter and less, where the flow is precisely controlled.

2.2. A Wide Range of Designs and Materials

The design and construction techniques used to obtain a microfluidic BES are various [32,38– 41,43–53]. The materials used depend on the technique applied to design the cell. They could be of the same nature as in macroscale BESs, i.e., non-conductive plastic, silicon, glasses, nafion proton exchange membranes [38,39,71,72] in scaled down, milliliter sized BES [42,49,53,73–77].

Most widely used approaches for the fabrication of microfluidic chips rely on soft photolithography techniques and cast molding of a polymer or hot embossing. Molds for microfluidic manufacturing using soft lithography techniques have traditionally been made using SU-8 technology [78] (Figure 3A). This liquid photoresist is spin-coated on a silicon wafer. Then, a series of long processes are combined: baking to dry the deposited layer of liquid photoresist, UV exposure through a mask to print the design patterns on the resin, post-exposure baking, slow cooling to room temperature to avoid cracking in the layer due to temperature stress, and then repetition of the entire process to add additional layers if necessary. Finally, the fabrication is completed by etching the microfluidic structures in the resin layer with a suitable solvent (propylene glycol methyl ether acetate), thus completing the definition of the master mold. Similarly, and for specific applications, microfluidic structures can be fabricated directly using the SU-8 photoresist as the building material, following equivalent fabrication schemes [79]. In any case, due to the uneven distribution of the photoresist during the centrifugal coating step, the manufacturing process can lead to up to 10% thickness variation in the microfluidic structures. Given the special requirements of SU-8 technology and the long lead times for mold making, lower cost processes based on the use of dry film photoresist have been proposed for mold making without the need for clean room facilities or hazardous chemicals [80]. These dry film-based processes (Figure 3A route 1b) are less expensive and up to 10 times faster than the standard SU-8 technology and, in addition, allow more precise control of the thickness of the structures [79].

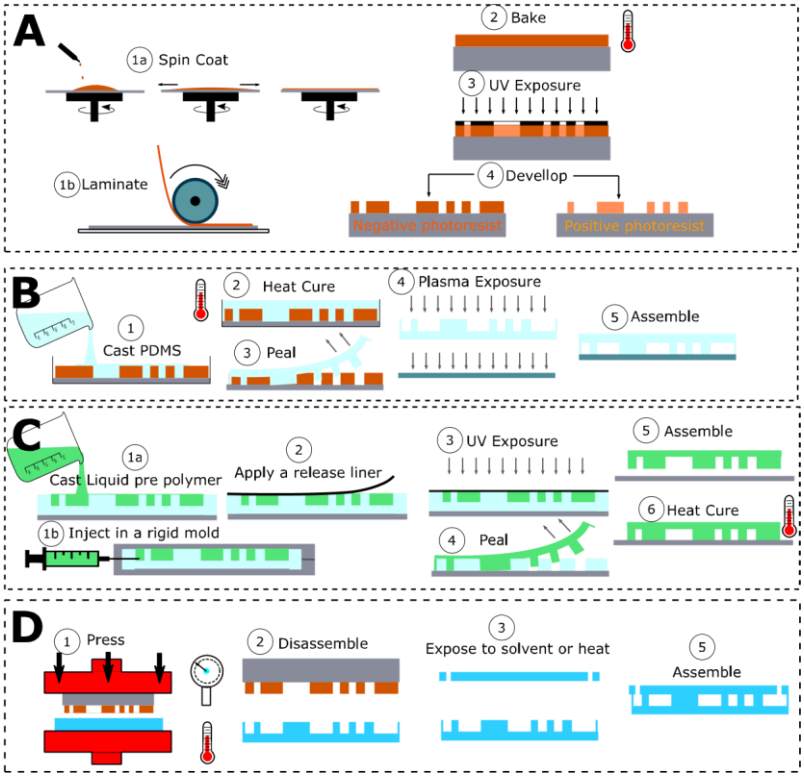

Figure 3. Overview of the most widely used techniques for master-mold and microfluidic chip fabrication. (**A**) Mold fabrication technique using liquid photoresist (1a) or dry film photoresist (1b). (**B**) Microfluidic chip fabrication using polydimethylsiloxane (PDMS). (**C**) Microfluidic chip fabrication using dual cure liquid-prepolymer (Epoxy, OSTEMER, NOA, thiolene, etc.) by cast molding technique (1a) or reactive injection molding (1b). (**D**) Microfluidic chip fabrication using thermoset polymers by hot embossing.

From this master mold, several types of materials can be used to replicate the microfluidic chips. Polydimethylsiloxane (PDMS) [42,49,53,73–77] is one of the most widely used materials for microchip fabrication by the classical casting technique [81]. Once cast, it is thermally cross-linked on the microfluidic master mold. Subsequently, the structures are peeled off and bonded to a substrate (e.g., a glass slide) to seal the microfluidic channels (Figure 3B). As an alternative to PDMS for the fabrication of casting chips, OSTEMER [82], a thiol-alkene-epoxy copolymer, should be mentioned. OSTEMER is optically transparent, less porous than PDMS, less permeable, and has high chemical resistance. This material has two independent curing steps, allowing a first cross-linking of the liquid mixture by means of UV exposure, which leads to a solid but flexible material that can be bonded to almost any type of surface by means of the remaining free epoxy groups, which are then cross-linked by a thermal process (Figure 3C).

As an alternative, some optically transparent, thermoplastic materials have also been used for chip fabrication by different manufacturing techniques [83]. Among these techniques, hot embossing (Figure 3D), which also requires a master mold for fabrication, is probably the most widely used to date [84], but there are also techniques allowing direct fabrication (and thus accelerating the step from initial design to prototyping), such as laser engraving and micro-milling [75,85], spark erosion wire cutting [42,48,76], and new additive fabrication processes applied to 3D printing technologies [86]: stereolithography, laminate fabrication and, more recently, melt deposition modeling [87].

In the last five years, paper-based microfluidic devices have gained in popularity [46,88–91]. As for PMMA, micromachining and laser printing are often used to design micro patterns and structures on paper-type materials [46,90]. Casting wax is generally used during those steps to harden and form the micropattern of such devices [88,89,91].

Gold is commonly used as electrode material in microfluidic BESs as it is conductive and compatible with most of the microfabrication process used in microfluidics [39], even though bare gold could possibly

have an altering effect on the redox proteins of the bacterial membrane implied in EET [92]. More typical materials basically used in macro BESs, such as carbon base electrodes, are essentially used in microfluidic BESs with reactors having above-milliliter volumes [39,40] but their minimum sizes are not compatible with the process used to design microliter scale systems [38,41,74]. However, during the last decade, several attempts have been made to use such materials; as in the works of Qian et al. with carbon cloth [72], Nath et al. with carbon nanotubes [46], or Ren et al. with a film of polymer-CNT [92]. Lately, other, metallic materials, such as a Ni-based electrodes have been tested as electrode material in order to improve the microfluidic set-up [75].

2.3. The Different Types of BES

Microfluidic microbial BESs can be separated into two categories based on the number of electrodes present inside the set-up. In the first category, microfluidic BESs with two electrodes are based on the operation of MFCs. These microfluidic BESs are either scaled down batch MFCs [38–43] or co-laminar flow BESs designed to address the transport limitations of scaled down MFCs [32,44– 49]. A second category of microfluidic BESs are set-ups with three electrodes, which focus on a more analytical aim, with the incorporation of an additional reference electrode [50–53].

2.3.1. Scaled Down MFC: Membrane Microfluidic MFC

Membrane microfluidic MFCs are MFCs designed with a reactor volume in the 7 mL to 1.5 µL range [38,39,41,46,73,93,94]. They are basically regular microscale MFCs in which the volume of the reactor is easily lowered from liters to several dozen milliliters to a few microliters in the smallest system [41]. They function in the same way as macroscale MFCs. In a typical MFC, the anode is inoculated with electroactive bacteria (Figure 4A). The bacteria oxidize organic substrates in the electrolyte (anolyte) and then provide electrons to the anode surface, either directly or indirectly. The electrons are then transferred to the cathode through an external resistance, where oxidants (oxygen or ferricyanide are major examples) are electrochemically reduced by an abiotically catalyzed reaction. A proton exchange membrane (PEM) or, more broadly, an ionic exchange membrane (IEM) separates the two chambers to prevent mixing of their electrolytes, while ions including protons can still be exchanged between them. In a membrane microfluidic MFC, the organization is basically the same, except that the electrodes are generally produced directly with microfabrication techniques in order to match the scale of the micro reactor system (Figure 4A).

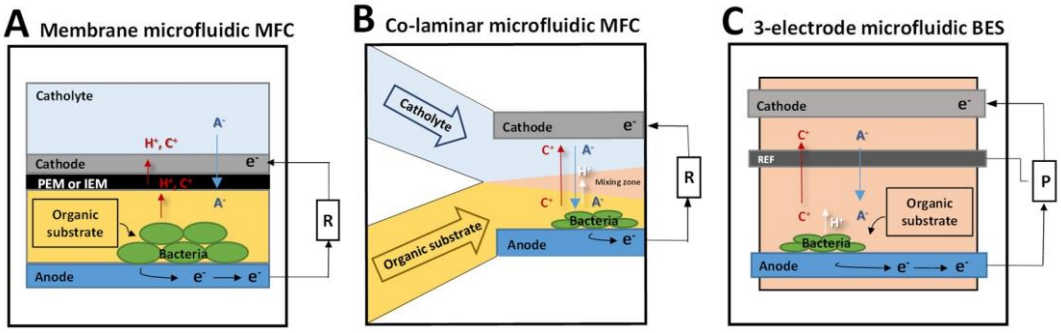

Figure 4. Presentation of the three categories of microfluidic bioelectrochemical system (BES). (**A**) small-scale membrane microbial fuel cell, (**B**) co-laminar electrode microfluidic, (**C**) BES with the incorporation of an additional reference electrode.

Initially, a milliliter scale microfluidic membrane MFC and a microliter scale one were differentiated by the fact that the first generated considerable power density whereas the second was shown to provide a better current density but a low power density [63]. For example, a power density up to 10 mW m^{-2} and a current density of 32 mA m^{-2} were obtained with a graphite felt electrode in the work of Ringeisen et al. [39] with a monoculture of *S. oneidensis* MR-1 in a 1.2 mL microfluidic MFC. The authors considered that their milliliter scale MFC produced 160 times more current density and 1960 times more power density than a

regular MFC when the real electrode area surface used was taken in account. Microliter scale membrane MFCs [41] produced power densities of up to 1.5 mW m^{-2} and current densities of 130 mA m^{-2} at that time with the same species and a gold electrode.

Nonetheless, microliter scale membrane microfluidic MFCs have been the object of much research during the last decade. Performances have risen to a maximum recorded power density of 830 mW m^{-2} and a current density of 2.59 A m^{-2} when using a mix of polymer and carbon nanotubes as electrode, and inoculating a bacterial consortium enriched with *Geobacter* species [93] in the anodic chamber of 12.5 µL. In contrast, a work with *Shewanella oneidensis* MR-1 in a milliliter scale membrane microfluidic MFC, presenting one of the highest performances to date, displayed a power density of around 661 mW m^{-2} and a current density of 0.4 A m^{-2} with a 3D graphene nickel foam anode [94].

Miniaturizing MFCs to the micro scale is thus far more efficient, as the main advantage of scaling down MFCs is to improve the surface area-to-volume (SAV) ratio. The smaller the reactor volume, the higher the SAV ratio. Improving the SAV ratio has an impact on several aspects of the BES system. Firstly, the ratio between the quantity of bacterial cells adhering to the electrode and the quantity of planktonic bacterial cells tilts more in favor of sessile bacterial cells, which leads to a decrease in interfering biochemical reactions and competition for the biological oxidation of the pool of organic substrates. Secondly, the electrolyte flow at the electrode surface can be modulated upwards since mass transfer limits the overall reaction rate, i.e., as measured by current density. DominguezBenetton et al. have shown that the mass transfer coefficient increases when the characteristic electrode length decreases [94]. Assuming that a microscale membrane MFC differs from a macroscale one only by the length of its electrode, miniaturizing the system would forcibly improve the surface maximum flux. Finally, miniaturizing MFC to microscale also leads to a reduction in the internal resistances, by shortening the inter-electrode distance [9,65,67–70,72,73,95–97] or increasing the IEM surface area relative to the smaller size of the electrodes [98]. Microfluidic membrane MFCs are, however, actually considered as low energy output systems, classified among the low power density production systems, because of the presence of the membrane inside the MFC set-up [64].

Oxygen penetration problems related to the gas permeability of the materials used in the microfabrication processes is critical, especially with PDMS, which is entirely permeable to oxygen. Alternative ways to address this issue are to coat the PDMS [74] or to use anodic facultative anaerobic bacterial strains or consortia, less affected by the presence of oxygen.

2.3.2. Membraneless Microfluidic MFC: The Co-Laminar Microfluidic MFC

Taking advantage of the short characteristic length of the microreactor and the high SAV ratio, the fluidic Reynolds number (*Re*), which is the ratio of the inertial forces to viscous forces, is low (less than 100) [99]. When the Reynolds number is low, the flow is laminar rather than turbulent [100]. The mass transport of soluble compounds and ions is then determined by phenomena of diffusion rather than convection. In a co-laminar microfluidic MFC, as two parallel inlets would allow the cathodic and the anodic electrolytes to be injected separately, the fluid flow dynamics would prevent the two electrolytes from mixing (Figure 4B). The implementation of a physical separator such as an IEM membrane (i.e., as in the membrane microfluidic MFC) then becomes irrelevant [101]. Using this idea, Li et al. developed the first membraneless microfluidic MFC in 2011 [49], reaching current densities of 25.4 mA m^{-2} and 18.4 mA m^{-2} with *S. oneidensis* MR-1 and *G. sulfurreducens* electroactive model bacterial strains, respectively, on a gold anode.

Since then, different models of membraneless co-laminar MFCs have been designed with different types of configurations, which can be succinctly divided into Y/T shaped co-laminar MFCs [48,49,77] and membraneless MFCs with exotic geometries [47,75]. The highest performing system reported to date, with carbon cloth electrodes, generated a power density of 3200 W m^{-3}, i.e., 1.18 W m^{-2} when the dimension of the limiting electrode was considered, and a current density of 35.5 A m^{-2} [48]. These performances are 1.3 (power density) and 14 times (current density) higher than in the most efficient microfluidic MFC [93].

Like the microfluidic membrane MFCs, co-laminar microfluidic MFCs take advantage of a short response time and a high SAV ratio. In addition, they present a simplified structure, as they do not need a separator membrane. Therefore, they have a lower internal resistance [64] than the membrane microfluidic MFC. The absence of membrane allows the faster transfer of ionic charges in the electrolytes. The precisely controlled laminar flow helps to enhance the system as the stable shear force generated sweeps away weakly

adhered cells and favors the formation of a robust anodic biofilm [102]. At the same time, the controlled laminar flow helps to preserve stable concentrations of nutrients in the diffusion layer around the biofilm and participates in a better evacuation of the anodic reaction products, especially protons [103].

Even though this co-laminar microfluidic system presents many advantages, it has some limitations. Due to the laminar flow, which authorizes the transfer of mass through diffusion only, a boundary layer effect, where bacteria accumulate at the entrance of the microfluidic channel, is often observed. The biofilm develops more at the entrance of the channel than it does farther along the electrode, resulting in a thicker biofilm at the entrance and a thinner one at the end. To counter this effect, special architectures with multiple anolyte inlets have been proposed by Yang et al. [33]. A second issue for membraneless microfluidic BESs is the shear rate induced by the flow. A low flow rate would induce a low shear rate, so the boundary layer discussed previously would be thicker and supplying the biofilm with nutrients would be slower, resulting in less effective formation of the biofilm [102]. Conversely, if the flow rate were too high, the high shear stress would alter the biofilm formation on the anode. Partial or total detachment of the electroactive biofilm accompanied by a considerable loss of power density [76] could also occur due to hydrodynamic instability.

2.3.3. Three-Electrode Microfluidic BES

Three-electrode microfluidic BES set-ups are characterized by the presence of a reference electrode to normalize the results recorded with the working electrode (Figure 4C). Such a system allows reliable information to be collected and electrochemical reaction kinetics to be recorded independently on anodes and cathodes. To date, only a few types of three-electrode systems have been elaborated in microfluidic BESs [50,51,53].

One of the solutions proposed to obtain a valid electrode reference is the use of a gold pseudoreference. The potential versus standard hydrogen electrode (SHE) of the pseudo reference is calculated by evaluating the shift between the redox peak of ferricyanide recorded in voltammetry with the gold pseudo reference and a commercial Ag/AgCl reference in the same bacterial growth media [51,53].With such a set-up, a study by Zarabadi et al. has shown that the bio resistance and bio capacitance of an electroactive biofilm, measured by impedance, is greatly modified by the shear rate applied to it [53]. Another study, using a similar set-up, has demonstrated that increasing the flow rate could mitigate the acidification of *G. sulfurreducens* biofilm but only in starvation conditions [51]. A solution proposed to obtain a reference electrode usable in a microfluidic BES set-up with three electrodes consists of designing a particular architecture with co-laminar fluid specifically selected for the reference electrode. In this system, an Ag/AgCl electrode is fabricated by electroplating Ag on a gold substrate and then oxidizing it in saturated KCl solution. This integrated reference electrode would then be circulated with a saturated KCl solution as the co-laminar fluid. As the mass transfer is assured only by diffusion and not by convection in this co-laminar system, the Ag/AgCl reference electrode would be calibrated and stable for this concentration of KCl [50]. Such a set-up was proven to be stable for over 30 days and demonstrated the precise correlation between the electroactive behavior of *G. sulfurreducens* and the presence of two substrates: ferric citrate and formaldehyde [50].

A major limitation of the three-electrode micro set-up is the necessity to possess a stable reference microelectrode. The Ag/AgCl pseudo references [104–106] often used in microfluidic analytical electrochemical cells generally have too short a life span, no more than a few days, when used in a microfluidic three-electrode BES. As it is difficult to design functional pseudo references that form an integral part of the system, some set-ups use commercial references at the electrolyte outlet to characterize their system [52]. In theory, this option is strictly limited to highly conductive electrolytes, i.e., electrolytes highly charged with ions.

Considering the situation described in this overview, the design of easy to fabricate integrable microreferences would be a major advance in this field.

3. Contribution of Microfluidic Investigations to the Fundamental Knowledge of Electroactive Biofilms

Fluid flow control and working in microchannels offer the advantages of temporal and spatial control of the physical–chemical conditions of the electrolytes, application of hydrodynamics, and combination with real-time analytical techniques of spectroscopy, microscopy, and electrochemistry to study the many characteristics (Figure 5) that profoundly affect the formation and electrochemical performance of electroactive biofilms. The ability to precisely control and monitor the flow rate in the microfluidic set-up makes it possible to accurately adapt the shear rate applied to the biofilm as well as the concentration of nutrients and substrates. The micro construction techniques also enable exotic dedicated architectures of microchannels to be elaborated and different types of micro sized electrodes to be used to investigate bacterial cell adhesion and EET mechanisms. Inherent in microfluidic systems, such abilities have helped to disentangle some fundamental mechanisms that are particular to electroactive biofilms. They are discussed in the following sections.

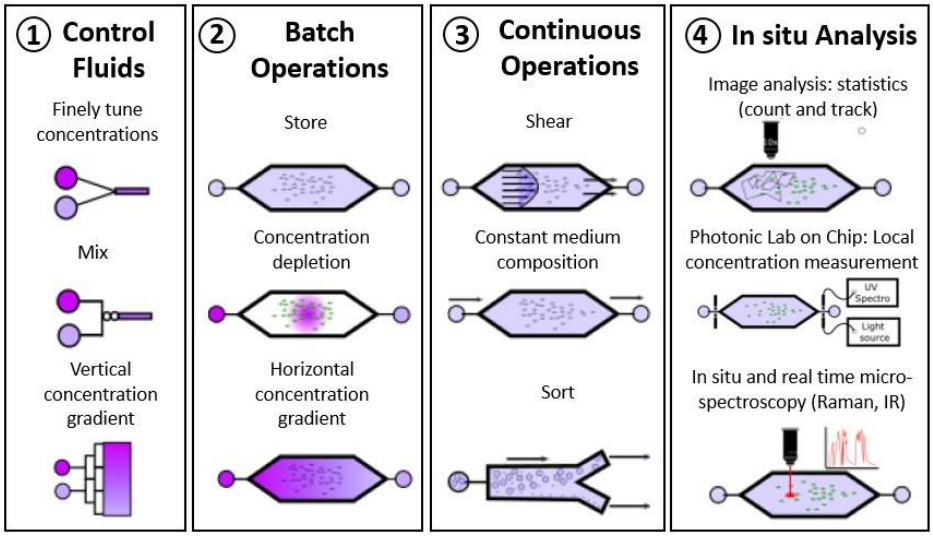

Figure 5. Advantages offered by microfluidic set-up for studying cells. The microfluidic set-up takes advantage of a fine control of hydrodynamics, (**1**) on the way that the microfluidic device is operated (batch (**2**) or continuous mode (**3**)) and on the opportunity to perform local and in-situ analyses (**4**).

Most of the local characterizations aimed at elucidating the relationships between the electronic transfer mechanisms in biofilm and the physical structuring of biofilm on the electrodes have been carried out ex situ by removing the microbial anodes for microscopic imaging or spectroscopic analytical methods. A microbial microfluidic BES, because of its small size and the transparency of its materials (transparent polymers, glass, transparent electrodes), offers a resolutely innovative solution for performing coupled analyses of optical microscopy, spectrometry or electroanalysis (impedance, potentiometry, voltammetry) in situ, in real time and non-invasively.

3.1. Contributions to Disentangle the EET Mechanisms

Direct or indirect bacterial EET mechanisms have been widely studied [107,108] and microfluidic tools have aided the investigation of such mechanisms during the last 15 years. Basically, macrosystems allow EET mechanisms to be extensively studied with a wide range of exploration strategies from electroanalytic methods to microscopy investigations and genetic engineering [52]. However, in experimental or analytical macrosystems, it is difficult to be certain whether the result of the observation is attributable to the mechanism itself, or to an assembly of several mechanisms or combined phenomena, or to an artefact due to the myriad of chemical molecules and bacterial species present in the macrosystem. Microfluidics provides significant help in this respect, by allowing more localized interrogation of the system under investigation, by limiting interference reactions, and by applying precisely controlled conditions to

the bioelectrocatalytic interfaces. Benefiting from these advantages, Ringeisen et al. proved that microfluidic BESs are proficient tools to discriminate between the direct electron transfer part alone and the total EET driven by *S. oneidensis* [39]. In their work, the current generation obtained in the microfluidic BES was markedly lower, by 30 to 100% depending on the situation, than the current obtained following the addition of an electron shuttle molecule. It is an interesting tool since *S. oneidensis* is known to have an EET resulting essentially from mediated electron transfer [16]. The importance of the mediated EET for *S. oneidensis* is also precisely pictured and studied by combining microfluidic approaches with the implementation of nanoelectrodes in microfluidic BESs. Jiang et al. were among the first to observe that mediated EET was the predominant EET mechanism within *S. oneidensis* [106]. Allying microscopy with microfluidics, they demonstrated that the number of cells attached to the electrode was not directly correlated with current generation, supporting the theory of a main EET based on mediated electron transfer. They also demonstrated that replacing the bacterial growth medium with a new, fresh batch after 48 h would reduce the current by around 95%, which could be recovered to about 80% by switching back to the old medium. This result again strongly supports the predominance of mediated EET for this specific species of electroactive bacteria. Recently, microfluidics has also been used to clarify the mechanistic operation of the EET performed by *Geobacter* nanowires. In their study, Michelson et al. state that nanowires can effectively transfer electrons up to 15 μm from the bacterial cell but they need a bound redox cofactor to work efficiently [60], a result which is consistent with the model theorized by Steidl et al. one year earlier [14]. Another interesting example demonstrating, once again, the contribution of microfluidics to the fundamental field of EET is the discovery of the correlation existing between the polarizability of the bacterial cells and their ability to perform EET. Allying microfluidics and electrophoresis, Wang et al. demonstrate that the faculty to perform EET is directly correlated with the polarizability of the bacterial cells [109]. In their work, the deletion of bacterial genes coding for cytochromes, crucial to the mechanism of direct EET, diminished the polarizability of the genetically engineered cells, whereas the polarizability of cells modified to express a new EET pathway increased. Apart from its high involvement in the rapid screening of electroactive species, this information is of great interest as it could be directly related to relevant mechanisms linked to the formation of electroactive biofilm on electrodes.

3.2. Contributions to Our Understanding of Electroactive Biofilm Formation

Biofilm formation is an extensive field of research, which is of great interest beyond the scope of electroactive biofilms, since it is the subject of numerous industrial strategies aimed at increasing or decreasing the adhesion capacity of bacteria. Its relevance to electroactive species is of prime importance, as success in producing a robust electroactive biofilm should allow efficient, sustainable EET. Nevertheless, studies on the impact of the ability to perform EET from electroactive bacterial species during the dynamics of electroactive biofilm formation are scarce. Currently, microfluidic approaches have helped to distinguish several mechanisms that could be involved in this specific topic.

The first mechanism, based on the polarization of the bacterial cell, is not unique to electroactive species but rather is common to all bacteria [109,110]. As the bacteria would aggregate to form a biofilm, the succession of polarization and depolarization of cells synchronizes and leads counter ions such as K^+, Na^+, Cl^- to accumulate around the biofilm creating a concentration gradient of ions [109]. It could be imagined that the gradient of such ions could drive the planktonic bacterial cells to the biofilm by chemotaxis-like mechanisms. Using microfluidics, Humphries et al. demonstrate that the planktonic bacteria, whatever their species, direct themselves to the biofilm at a rate directly correlated with the oscillation of the polarization of the membranes of bacteria in the biofilm [107]. The formation of the biofilm is then greatly impacted by the electric communication thus generated. This phenomenon is especially interesting in electroactive species, which have high polarizability since they are able to perform EET [111,112].

A second mechanism was demonstrated with *S. oneidensis* based on an energetic chemotaxis called “energy taxy” by the authors [61]. In their work, they successfully showed that bacterial cells moved to follow a gradient of oxidized riboflavin artificially created in a microfluidic BES set-up. In electroactive biofilms, oxidized riboflavin would be self-secreted by the bacterial cells and accumulated around the biofilm as the cell aggregates and the reduced riboflavin would be reoxidized when in contact with the anode. The

planktonic cells would then direct themselves to the biofilm by going from one oxidized riboflavin to another, using them as final electron acceptors, following an "energy" gradient.

The last mechanism was based on an electric field gradient. Although this mechanism has not been demonstrated with a microfluidic set-up nor with a millifluidic set-up, the same advantages and properties of microfluidics were used here to carry out the demonstration. Du et al. have pointed out that electroactive bacterial species from wastewater actually respond to an electric field to form a biofilm [110]. Flowing across the electric field, the bacteria from wastewater form a biofilm, centered on the electric field, with a thickness of 88 μm, which is reduced to 30 μm at the edge of the electric field. Metagenomic community investigations performed on this particular biofilm showed that the concentration of *Geobacter* species inside the biofilm was 25% higher at the center of the biofilm than at its edge, implying that, for electroactive species, electric forces could be involved in the formation of the biofilm.

3.3. Contributions to Spatial Probing of the Electrochemical Activity of Biofilms

Electroactive biofilms have structural and chemical organizations directly attributable to the bacterial populations from which they originate, their stage of development or maturity, and the local hierarchical organization and co-occurrence of EET mechanisms, all of which depend on the polarization of the electrode on which the biofilm develops [113]. The literature describes patterns of mature biofilms with very different morphologies according to the experimental conditions of electrode potential, the production or absence of polymeric matrix for electron storage [114], monoculture or mixed populations, bioanodes or biocathodes [115,116].

The question has been raised as to whether the electrochemical activity of bacterial cells is homogeneous or not in electroactive biofilms depending on the stage of development of the biofilm, i.e., mainly in connection with its thickness in relation to the electrode surface. The vast majority of investigations have been undertaken with *Geobacter sulfurreducens* model electroactive biofilms, although alternative work conducted with mixed biofilms has shown that the conclusions are not entirely transposable from the single species model system to more realistic multispecies systems [117]. Nevertheless, this *Geobacter sulfurreducens* species is highly represented in mixed anodic biofilms with percentages of representativeness sometimes exceeding 90% [20,118,119]. Blanchet et al. have even demonstrated a strong direct correlation between the maximum current density provided by bioanodes and the relative abundance of *Geobacteriaceae* [118,120]

Geobacter sulfurreducens is, therefore, a model of anodic electroactive bacteria capable of forming biofilms with a homogeneous structural appearance and a homogeneous thickness that can exceed 100 μm. The biofilms of *Geobacter sulfurreducens* are conductive and express two coexisting types of direct EET mechanisms: conductive pili and c-type cytochromes. Gene expression of these mechanisms has been reported to be homogeneous throughout the thickness of *Geobacter sulfurreducens* biofilms. This observation was made in real time and in situ, in a transparent chamber equipped for confocal laser scanning microscopy. The fluorescence signal monitored was based on a genetic construction allowing the expression of the reporter gene coding for a short half-life fluorescent protein [121]. Despite this uniform expression of the direct mechanisms of EET, several groups of authors have nevertheless demonstrated that the electrochemical activity of *Geobacter sulfurreducens* biofilms is limited when the biofilms exceed a thickness of 10 μm [14,122,123], i.e., a stratification of about 20 layers of bacterial cells.

The hypotheses put forward to explain why these *Geobacter sulfurreducens* biofilms fail to produce current densities proportional to the biofilm thickness or its biovolume are:

- Chemical gradients in protons [124,125] or substrates [126] that directly impact cell physiology, viability, and metabolic and respiratory activity. The basal zone closest to the anode is, in principle, the most impacted zone.
- Redox potential gradients that condition the redox state of the c-type cytochrome, with a higher proportion of reduced cytochromes in the layers more distant from the anode surface [127–130].
- A stratification of the coexisting direct mechanisms of EET: pili become the main electron discharge mechanism in the upper region far from the anode (> 10 μm), where the c-type cytochromes are mainly in the reduced state [14].

These explanations and validated experimental demonstrations are often contradictory. For example, some studies report increased cell mortality in the proximity of the anode, while others claim that the biofilm zone in contact with the bulk electrolyte is the zone most affected by mortality. Questions arise as to the possibility of methodological bias or bias related to the sampling and post treatment of samples before their observation by confocal laser microscopy scanning. To discriminate between these models, the metabolic activity in *Geobacter sulfurreducens* biofilms was measured in a z-profile from stable isotope probes incorporated by bacterial cells, and identified and visualized by coupling with nanoscale secondary ion mass spectrometry (nanoSIMS) [131]. In mature biofilms up to 80 μm thick, this approach concluded that the metabolic activity of bacterial cells follows a gradient, with the most active cells being found on the surface of the anode, and this activity progressively decreases layer by layer with the distance from the surface of the graphite anode.

All these works performed with *Geobacter sulfurreducens* biofilms finally challenge certain theories concerning electronic conductivity in electroactive biofilms, the syntrophy existing between electroactive and non-electroactive populations (direct interspecies electron transfer), and, more generally, the homogeneity of the production of electron flow within the three-dimensional structure of biofilms.

3.4. Contributions Examining the Impact of Electrolyte Conditions

The physics and chemistry present inside the electrolyte(s) are key factors conditioning the establishment, performance, and durability of the various pathways of EET performed by the bacteria inside the BES. Oxygen concentration, the nature and concentrations of substrates and nutrients, pH, temperature, buffer strength and electrolyte flow rate (see full details in Figure 2) are crucial factors to be taken into account to achieve an effective BES. Through the advantages it offers for the design of particular BES microreactors or microchannels and for adapting the flow rate, creating gradient concentrations and easily substituting or changing soluble chemical compounds in the extracellular electrolytic medium, microfluidics helps to explore and increase the spectrum of molecules and conditions favorable to electroactive biofilm development and activity.

Using a microfluidics approach, the impact of oxygen on the electrochemical activity of *S. oneidensis* was observed, providing evidence of a change in metabolism in the presence of oxygen, and a preference to use oxygen rather than an anode as a terminal electron acceptor [61]. On the other hand, the culture of *S. oneidensis* in a microfluidic BES under aerobic conditions revealed a more diversified use of the number of substrates that the bacterial strain was able to oxidize to transfer electrons to the anode. In the microfluidic MFC they designed, Biffinger et al. demonstrated that glucose and fructose were serious candidates for use by *S. oneidensis* in aerobic conditions [130]. In this case, microfluidics significantly improved the precision of the results thanks to the scaling down of the system, and the fluidic approach enabled accurate control of the flow in the experiment. These advantages are especially handy as the efficiency of EET depends on the substrates and the condition of the electrolyte.

The effect of pH upon the EET has also been well studied, especially for *Geobacter* species [44,51,122]. Franks et al., by associating real-time imaging and microfluidic management, monitored the effect of the accumulation of protons upon a biofilm formed by *G. sulfurreducens* [122]. The accumulation of protons led to EET inhibition and therefore decreased anodic current generation. This inhibition was reversible, since further pH management to maintain a neutral pH brought the anode current density back to its maximum level. In a recent work, Zarabadi et al. attempted to solve this pH inhibition problem by increasing the flow rate in their microfluidic BES with the aim of promoting the release of protons out of the biofilm and consequently limiting the acidification [51]. Unfortunately, the strategy was only effective with a flow rate that simultaneously led to a starvation mode for the bacteria inside the biofilm.

The importance of flow dynamics and its consequences on the formation of biofilms on solid surfaces in microfluidic systems has been really well studied with non-electroactive bacteria [102,132,133], whereas the same type of studies on biofilms of electroactive bacterial species are limited [51,103,134]. In particular, microfluidic work with non-electroactive bacteria has shown that the shear force applied by the circulating fluid has many effects on a bacterial biofilm, from the early stages of biofilm formation, where it traps planktonic cells on a solid support, to its inhibition by high shear forces causing erosion of the biofilm

[102,133]. Microflow dynamics can also affect the mass transport of soluble molecules, particularly nutrients, molecules of quorum sensing and protons, thus playing a major role in maintaining the condition of the extracellular medium, i.e., the electrolyte for the microfluidic BES. The flow rate is then crucial as, if it is too low or too high, it can negatively influence the growth of a sturdy and efficient biofilm. In the intention of estimating the best flow rate for electroactive species, Vigolo et al. defined an optimal flow condition of 20 μL. min^{-1} with *S. oneidensis* [101]. However, it is important to understand that this optimal flow rate could be dependent on the anode chamber volume, the bacterial species constituting the biofilm, and the EET pathway expected in the system, i.e., whether it is essentially based on direct or mediated EET. In another work, Ren et al. also underlined the importance, for the bacteria attached to electrodes [132], of mass transfer through hydrodynamic management, since it would be important to recharge the cytochromes c excreted on the biofilm matrix, as was predicted by an enzymatic model with cytochromes c alone [135].

A microfluidic set-up also informs on the importance of the electrode chamber configuration. Luo et al. showed that better formation of biofilm and higher current generation were obtained when the hydraulic retention time (HRT) of the electrode chamber was increased [45]. However, a balance between this parameter and the internal resistance of the microfluidic BES is needed as the rise of HRT values is strongly correlated with an increase in the internal resistance. On this topic, Choi and Chae demonstrated that a minimum height of 20 μm was absolutely necessary in the electrode chamber to allow the formation of a multilayer biofilm in a microfluidic BES [136].

4. Outlook

Over the last decade, microfluidic tools have significantly helped to clarify the fundamental domain of bacterial EET, as well as proposing new optimization strategies to improve and design new BES systems, and microfluidics will no doubt continue to contribute to several exciting strategic areas of research. When thinking about what microfluidics can do to help the study and progress of the BES field, it is important to focus on the strengths that microfluidics systems possess. Microfluidic BES systems are characterized by their ability to precisely control the flow, to manipulate (sort, fuse, aggregate) bacteria, cells, droplets and solid particles, and the possibilities they offer for building particular architectures of experimental systems that are transparent and thus compatible with many real-time macroscopic and microscopic in situ observation techniques, and other non-destructive analytical strategies by spectroscopy. There are many transparent electrode materials commercially available as they were originally developed for solar cell technologies. Some of them, such as indium tin oxide (ITO), modified ITO with transparent deposits of graphene, graphene oxides or PEDOT, or fluorine-doped ITO (FTO), have already been used as a support for electroactive biofilms. ITO has been the subject of several studies with the electroactive bacterial strain *Geobacter sulfurreducens* [127]. FTO, which has a higher electrical conductivity, close to that of carbon, has recently made it possible to visualize the macroscopic development of an electroactive biofilm formed from wastewater in real time and thus acquire kinetic data on biofilm formation [137].

The very attractive feature of microfluidics is the possibility it provides to precisely and almost instantaneously control the flow inside a process and thus, in the specific case of BES, at the interface between the electroactive biofilm and the electrolyte. This property, specific to microfluidics, makes it possible to work in greater depth on many important factors interacting with the EET performed by the bacteria with the electrode, such as the nutrient concentration, the pH, the concentration of oxygen or any molecule, enabling us to create gradients or to quickly switch the flow rate of the circulating electrolyte [138]. Then, microfluidics also allows the importance of shear force for the electroactive biofilm and its electroactivity [103,134] to be characterized. In addition, it offers a microfluidic BES a quick response to any modification of its electrolyte properties [63,139,140]. All these attributes are already well exploited in microfluidic BESs. However, much more promising research is waiting to be done, as most fundamental results have so far been obtained with monoculture biofilms, i.e., biofilms formed from model single electroactive bacterial strains. The diversity of the bacterial community present in biofilms established from complex natural or industrial media, such as wastewater sludge or digester sludge or marine soils, presents a future field of investigation that will also be interesting for microfluidic BESs. The simplification and precise control inherent in microfluidic approaches could help unravel the participants and mechanisms involved, the

mechanistic and partnership interactions within bacterial communities, and the pattern of biochemical reactions and electronic exchanges that occur at the scale of an electroactive biofilm.

This ability to precisely control the flow at the precise level of the interfaces of interest, added to the high adaptability of the experimental systems in terms of materials and architecture, sets microfluidics apart as a platform available in all contexts and limited only by the usage the experimenter requires. The possibility of manufacturing simple, microscope-adaptable microfluidic devices for real-time observation [141], where operational parameters can be easily modulated [142], opens the door for in situ investigation of the early stages of bacterial adhesion [143] and the formation of electroactive biofilms directly at the microscale [144]. The compatibility of most microfluidics materials with observational methods allows for easy monitoring and probing of the electroactive biofilm in real time—a real asset when the transient nature of biofilm is considered. A wide range of microscopic techniques, from confocal microscopy [145] and scanning electrochemical microscopy [146] to spectroscopic techniques [139,147,148], have been successfully coupled into microfluidic platforms for live observation of biofilm. Other techniques can also be integrated, such as the widely studied optical density for quorum sensing analysis [149,150] or the innovative use of electrochemical imaging, where specific positions of a voltammogram are converted into pixels, enabling identification of redox currents and peak positions of an electroactive biofilm [151]. The combination of microbial engineering approaches, including matter balance transformation, target microbe selection, mutant characterization, and microbial function analysis, with microfluidic BESs will provide really new information as is already a trend in other domains exploring the activity and behavior of microorganisms in microfluidic study systems [140]. Considering the strengths of microfluidic BESs in screening electroactive bacterial strains [55], the association of the two strategies would lead us to discover and investigate new EET pathways, as in extremophile species, for example, which are difficult to study in macro systems even though they give fairly convincing electrochemical results [141]. The large amenability and compatibility of microfluidic set-ups also encourages great hopes that this technology will form part of an all-inclusive micro research platform for electroactive biofilm characterization.

5. Conclusions

Work on microfluidic BESs has grown and flourished in their short ten-year life span and is having a significant impact on fundamental scientific advances in the field of microbial bioelectrochemistry. The progress made on the integration of polyphasic electrode–electrolyte systems at the micrometer scale associated with the availability of a wide variety of materials means that, today, the architecture, composition and arrangement of electrodes in microfluidic BESs seem to be limited only by the objectives of the scientists and the means available to them. Microfluidic BESs can be succinctly divided into two categories: microfluidic BESs with two electrodes, which include microfluidic membrane MFCs and co-laminar MFCs, or microfluidic membraneless MFCs; and BESs with three-electrode systems, including the addition of a reference electrode. Over the years, microfluidic BESs have contributed to the fundamental field of EET by disentangling some fundamental mechanisms, such as the importance of mediated EET for *S. oneidensis*, or by confirming hypotheses and models about EET predicted from macro systems. Thanks to their advantages, microfluidic approaches have also made it possible to propose multiple hypotheses on how the EET properties of electroactive bacteria could interfere with or participate in the formation of electroactive biofilms on electrodes and modulate the performance of their electroactivity. Finally, microfluidic BESs have proved to be interesting for their huge potential to advance the understanding of EET mechanisms and electroactive bacteria behavior and interaction to a new level, as they are compatible with numerous analysis strategies, such as real-time monitoring or microbial engineering.

Author Contributions: Conceptualization, S.P. and L.M.O.; methodology, S.P.; validation, B.E.; writing—original draft preparation, S.P. and L.M.O.; writing—review and editing, B.E. and S.T.; supervision, B.E. and S.T.; funding acquisition, B.E. All authors have read and agreed to the published version of the manuscript.

Funding: This work of literature review and analysis was funded by the French "Agence Nationale de le Recherche", grant number ANR-18-CE05-0024.

Conflicts of Interest: The authors declare no conflict of interest.

References

1. Kato, S. Microbial extracellular electron transfer and its relevance to iron corrosion. *Microb. Biotechnol.* **2016**, *9*, 141–148, doi:10.1111/1751-7915.12340.

1. Fredrickson, J.K.; Zachara, J.M. Electron transfer at the microbe–mineral interface: A grand challenge in biogeochemistry. *Geobiology* **2008**, *6*, 245–253, doi:10.1111/j.1472-4669.2008.00146.x.
2. Wang, H.; Park, J.-D.; Ren, Z.J. Practical Energy Harvesting for Microbial Fuel Cells: A Review. *Environ. Sci. Technol.* **2015**, *49*, 3267–3277, doi:10.1021/es5047765.
3. Logan, B.E.; Rabaey, K. Conversion of Wastes into Bioelectricity and Chemicals by Using Microbial Electrochemical Technologies. *Science* **2012**, *337*, 686–690, doi:10.1126/science.1217412.
4. Lovley, D.R.; Nevin, K.P. Electrobiocommodities: Powering microbial production of fuels and commodity chemicals from carbon dioxide with electricity. *Curr. Opin. Biotechnol.* **2013**, *24*, 385–390, doi:10.1016/j.copbio.2013.02.012.
5. Abrevaya, X.C.; Sacco, N.J.; Bonetto, M.C.; Hilding-Ohlsson, A.; Cortón, E. Analytical applications of microbial fuel cells. Part II: Toxicity, microbial activity and quantification, single analyte detection and other uses. *Biosens. Bioelectron.* **2015**, *63*, 591–601, doi:10.1016/j.bios.2014.04.053.
6. Pinck, S.; Jorand, F.; Etienne, M. *Electrochemistry of Biofilms*; Elsevier: Amsterdam, The Netherlands, 2018.
7. Aghababaie, M.; Farhadian, M.; Jeihanipour, A.; Biria, D. Effective factors on the performance of microbial fuel cells in wastewater treatment—A review. *Environ. Technol. Rev.* **2015**, *4*, 71–89, doi:10.1080/09593330.2015.1077896.
8. Santoro, C.; Arbizzani, C.; Erable, B.; Ieropoulos, I. Microbial fuel cells: From fundamentals to applications. A review. *J. Power Sources* **2017**, *356*, 225–244, doi:10.1016/j.jpowsour.2017.03.109.
9. Blasco-Gómez, R.; Batlle-Vilanova, P.; Villano, M.; Balaguer, M.D.; Colprim, J.; Puig, S. On the Edge of Research and Technological Application: A Critical Review of Electromethanogenesis. *Int. J. Mol. Sci.* **2017**, *18*, 874, doi:10.3390/ijms18040874.
10. Lies, D.P.; Hernandez, M.E.; Kappler, A.; Mielke, R.E.; Gralnick, J.A.; Newman, D.K. Shewanella oneidensis

MR-1 Uses Overlapping Pathways for Iron Reduction at a Distance and by Direct Contact under Conditions Relevant for Biofilms. *Appl. Environ. Microbiol.* **2005**, *71*, 4414–4426, doi:10.1128/aem.71.8.4414-4426.2005.

11. Basséguy, R.; Délia, M.-L.; Erable, B.; Bergel, A. Electroactive biofilms. *Underst. Biocorrosion* **2014**, *2014*, 107– 143, doi:10.1533/9781782421252.1.107.
12. Barchinger, S.E.; Pirbadian, S.; Sambles, C.M.; Baker, C.S.; Leung, K.M.; Burroughs, N.J.; El-Naggar, M.Y.; Golbeck, J.H. Regulation of Gene Expression in Shewanella oneidensis MR-1 during Electron Acceptor Limitation and Bacterial Nanowire Formation. *Appl. Environ. Microbiol.* **2016**, *82*, 5428–5443, doi:10.1128/aem.01615-16.
13. Steidl, R.J.; Lampa-Pastirk, S.; Reguera, G. Mechanistic stratification in electroactive biofilms of Geobacter sulfurreducens mediated by pilus nanowires. *Nat. Commun.* **2016**, *7*, 12217, doi:10.1038/ncomms12217.
14. Kotloski, N.J.; Gralnick, J.A. Flavin Electron Shuttles Dominate Extracellular Electron Transfer by Shewanella oneidensis. *mBio* **2013**, *4*, 10–13, doi:10.1128/mbio.00553-12.
15. Okamoto, A.; Nakamura, R.; Nealson, K.H.; Hashimoto, K. Bound Flavin Model Suggests Similar ElectronTransfer Mechanisms inShewanellaandGeobacter. *ChemElectroChem* **2014**, *1*, 1808–1812, doi:10.1002/celc.201402151.
16. Yang, G.; Huang, L.; You, L.; Zhuang, L.; Zhou, S. Electrochemical and spectroscopic insights into the mechanisms of bidirectional microbe-electrode electron transfer in Geobacter soli biofilms. *Electrochem. Commun.* **2017**, *77*, 93–97, doi:10.1016/j.elecom.2017.03.004.
17. Shi, L.; Rosso, K.M.; Clarke, T.A.; Richardson, D.J.; Zachara, J.M.; Fredrickson, J.K. Molecular Underpinnings of Fe(III) Oxide Reduction by Shewanella Oneidensis MR-1. *Front. Microbiol.* **2012**, *3*, 50, doi:10.3389/fmicb.2012.00050.
18. Richter, H.; Nevin, K.P.; Jia, H.; Lowy, D.A.; Lovley, D.R.; Tender, L.M. Cyclic voltammetry of biofilms of wild type and mutant Geobacter sulfurreducens on fuel cell anodes indicates possible roles of OmcB, OmcZ, type IV pili, and protons in extracellular electron transfer. *Energy Environ. Sci.* **2009**, *2*, 506–516, doi:10.1039/b816647a.
19. Rimboud, M.; Pocaznoi, D.; Erable, B.; Bergel, A. Electroanalysis of microbial anodes for bioelectrochemical systems: Basics, progress and perspectives. *Phys. Chem. Chem. Phys.* **2014**, *16*, 16349–16366, doi:10.1039/c4cp01698j.
20. Erable, B.; Féron, D.; Bergel, A. Microbial Catalysis of the Oxygen Reduction Reaction for Microbial Fuel Cells: A Review. *ChemSusChem* **2012**, *5*, 975–987, doi:10.1002/cssc.201100836.
21. Debuy, S.; Pécastaings, S.; Bergel, A.; Erable, B. Oxygen-reducing biocathodes designed with pure cultures of microbial strains isolated from seawater biofilms. *Int. Biodeterior. Biodegrad.* **2015**, *103*, 16–22, doi:10.1016/j.ibiod.2015.03.028.

22. Steinbusch, K.J.J.; Hamelers, H.V.M.; Schaap, J.D.; Kampman, C.; Buisman, C.J.N. Bioelectrochemical Ethanol Production through Mediated Acetate Reduction by Mixed Cultures. *Environ. Sci. Technol.* **2010**, *44*, 513–517, doi:10.1021/es902371e.
23. Rozendal, R.A.; Jeremiasse, A.W.; Hamelers, H.V.M.; Buisman, C.J.N. Hydrogen Production with a Microbial Biocathode. *Environ. Sci. Technol.* **2008**, *42*, 629–634, doi:10.1021/es071720+.
24. Soussan, L.; Riess, J.; Erable, B.; Delia, M.-L.; Bergel, A. Electrochemical reduction of CO2 catalysed by Geobacter sulfurreducens grown on polarized stainless steel cathodes. *Electrochem. Commun.* **2013**, *28*, 27– 30, doi:10.1016/j.elecom.2012.11.033.
25. Rabaey, K.; Rozendal, R.A. Microbial electrosynthesis—Revisiting the electrical route for microbial production. *Nat. Rev. Genet.* **2010**, *8*, 706–716, doi:10.1038/nrmicro2422.
26. Jeremiasse, A.W.; Hamelers, H.V.M.; Buisman, C.J.N. Microbial electrolysis cell with a microbial biocathode. *Bioelectrochemistry* **2010**, *78*, 39–43, doi:10.1016/j.bioelechem.2009.05.005.
27. Luo, H.; Teng, W.; Liu, G.; Zhang, R.; Lu, Y. Sulfate reduction and microbial community of autotrophic biocathode in response to acidity. *Process. Biochem.* **2017**, *54*, 120–127, doi:10.1016/j.procbio.2016.12.025.
28. Al-Mamun, A.; Baawain, M.S.; Egger, F.; Al-Muhtaseb, A.H.; Ng, H.Y. Optimization of a baffled-reactor microbial fuel cell using autotrophic denitrifying bio-cathode for removing nitrogen and recovering electrical energy. *Biochem. Eng. J.* **2017**, *120*, 93–102, doi:10.1016/j.bej.2016.12.015.
29. Pocaznoi, D.; Erable, B.; Delia, M.-L.; Bergel, A. Ultra microelectrodes increase the current density provided by electroactive biofilms by improving their electron transport ability. *Energy Environ. Sci.* **2012**, *5*, 5287– 5296, doi:10.1039/c1ee01469b.
30. Champigneux, P.; Renault-Sentenac, C.; Bourrier, D.; Rossi, C.; Delia, M.-L.; Bergel, A. Effect of surface roughness, porosity and roughened micro-pillar structures on the early formation of microbial anodes. *Bioelectrochemistry* **2019**, *128*, 17–29, doi:10.1016/j.bioelechem.2019.03.002.
31. Li, Z.J.; Venkataraman, A.; Rosenbaum, M.A.; Angenent, L.T. A Laminar-Flow Microfluidic Device for Quantitative Analysis of Microbial Electrochemical Activity. *ChemSusChem* **2012**, *5*, 1119–1123, doi:10.1002/cssc.201100736.
32. Yang, Y.; Ye, D.; Liao, Q.; Zhang, P.; Zhu, X.; Li, J.; Fu, Q. Enhanced biofilm distribution and cell performance of microfluidic microbial fuel cells with multiple anolyte inlets. *Biosens. Bioelectron.* **2016**, *79*, 406–410, doi:10.1016/j.bios.2015.12.067.
33. Pousti, M.; Zarabadi, M.P.; Amirdehi, M.A.; Paquet-Mercier, F.; Greener, J. Microfluidic bioanalytical flow cells for biofilm studies: A review. *Analyst* **2019**, *144*, 68–86, doi:10.1039/c8an01526k.
34. Rochex, A.; Godon, J.-J.; Bernet, N.; Escudié, R. Role of shear stress on composition, diversity and dynamics of biofilm bacterial communities. *Water Res.* **2008**, *42*, 4915–4922, doi:10.1016/j.watres.2008.09.015.
35. Sawyer, L.K.; Hermanowicz, S.W. Detachment of biofilm bacteria due to variations in nutrient supply. *Water Sci. Technol.* **1998**, *37*, 211–214, doi:10.1016/s0273-1223(98)00108-5.
36. Dickschat, J.S. Quorum sensing and bacterial biofilms. *Nat. Prod. Rep.* **2010**, *27*, 343–369, doi:10.1039/b804469b.
37. Richter, H.; McCarthy, K.; Nevin, K.P.; Johnson, J.P.; Rotello, V.M.; Lovley, D.R. Electricity Generation byGeobacter sulfurreducensAttached to Gold Electrodes. *Langmuir* **2008**, *24*, 4376–4379, doi:10.1021/la703469y.
38. Ringeisen, B.R.; Henderson, E.; Wu, P.K.; Pietron, J.; Ray, R.; Little, B.; Biffinger, J.C.; Jones-Meehan, J.M. Erratum: High power density from a miniature microbial fuel cell using Shewanella oneidensis DSP10. *Environ. Sci. Technol.* **2006**, *40*, 2629–2634, doi:10.1021/es052254w.
39. Biffinger, J.C.; Pietron, J.; Ray, R.; Little, B.; Ringeisen, B.R. A biofilm enhanced miniature microbial fuel cell using Shewanella oneidensis DSP10 and oxygen reduction cathodes. *Biosens. Bioelectron.* **2007**, *22*, 1672– 1679, doi:10.1016/j.bios.2006.07.027.
40. Qian, F.; Baum, M.; Gu, Q.; Morse, D.E. A 1.5 μL microbial fuel cell for on-chip bioelectricity generation. *Lab Chip* **2009**, *9*, 3076–3081, doi:10.1039/b910586g.
41. Chen, Y.-P.; Zhao, Y.; Qiu, K.-Q.; Chu, J.; Lu, R.; Sun, M.; Liu, X.-W.; Sheng, G.-P.; Yu, H.-Q.; Chen, J.; et al. An innovative miniature microbial fuel cell fabricated using photolithography. *Biosens. Bioelectron.* **2011**, *26*, 2841–2846, doi:10.1016/j.bios.2010.11.016.
42. Mateo, S.; Mascia, M.; Fernandez-Morales, F.J.; Rodrigo, M.A.; Di Lorenzo, M. Assessing the impact of design factors on the performance of two miniature microbial fuel cells. *Electrochim. Acta* **2019**, *297*, 297– 306, doi:10.1016/j.electacta.2018.11.193.
43. Chouler, J.; Di Lorenzo, M. Pesticide detection by a miniature microbial fuel cell under controlled operational disturbances. *Water Sci. Technol.* **2019**, *79*, 2231–2241, doi:10.2166/wst.2019.207.
44. Luo, X.; Xie, W.; Wang, R.; Wu, X.; Yu, L.; Qiao, Y. Fast Start-Up Microfluidic Microbial Fuel Cells with Serpentine Microchannel. *Front. Microbiol.* **2018**, *9*, 2816, doi:10.3389/fmicb.2018.02816.

45. Nath, D.; Kiran, P.S.; Rewatkar, P.; Krishnamurthy, B.; Ganesh, P.S.; Goel, S. Escherichia Coli Fed PaperBased Microfluidic Microbial Fuel Cell With MWCNT Composed Bucky Paper Bioelectrodes. *IEEE Trans. NanoBiosci.* **2019**, *18*, 510–515, doi:10.1109/TNB.2019.2919930.
46. Mardanpour, M.M.; Yaghmaei, S. Characterization of a microfluidic microbial fuel cell as a power generator based on a nickel electrode. *Biosens. Bioelectron.* **2016**, *79*, 327–333, doi:10.1016/j.bios.2015.12.022.
47. Ye, D.; Zhang, P.; Zhu, X.; Yang, Y.; Li, J.; Fu, Q.; Chen, R.; Liao, Q.; Zhang, B. Electricity generation of a laminar-flow microbial fuel cell without any additional power supply. *RSC Adv.* **2018**, *8*, 33637–33641, doi:10.1039/c8ra07340f.
48. Li, Z.; Zhang, Y.; LeDuc, P.R.; Gregory, K.B. Microbial electricity generation via microfluidic flow control. *Biotechnol. Bioeng.* **2011**, *108*, 2061–2069, doi:10.1002/bit.23156.
49. Li, F.; Zheng, Z.; Yang, B.; Zhang, X.; Li, Z.; Lei, L. A laminar-flow based microfluidic microbial threeelectrode cell for biosensing. *Electrochim. Acta* **2016**, *199*, 45–50, doi:10.1016/j.electacta.2016.03.138.
50. Zarabadi, M.P.; Charette, S.J.; Greener, J. Flow-Based Deacidification of Geobacter sulfurreducens Biofilms Depends on Nutrient Conditions: A Microfluidic Bioelectrochemical Study. *ChemElectroChem* **2018**, *5*, 3645– 3653, doi:10.1002/celc.201800968.
51. Bruchmann, J.; Sachsenheimer, K.; Rapp, B.E.; Schwartz, T. Multi-Channel Microfluidic Biosensor Platform Applied for Online Monitoring and Screening of Biofilm Formation and Activity. *PLoS ONE* **2015**, *10*, e0117300, doi:10.1371/journal.pone.0117300.
52. Zarabadi, M.P.; Paquet-Mercier, F.; Charette, S.J.; Greener, J. Hydrodynamic Effects on Biofilms at the Biointerface Using a Microfluidic Electrochemical Cell: Case Study of *Pseudomonas* sp. *Langmuir* **2017**, *33*, 2041–2049, doi:10.1021/acs.langmuir.6b03889.
53. Chen, Y.Y.; Su, J.Y.; Huang, C.Y.; Wang, H.Y. Microfluidic microbial fuel cells for rapid screening of electroactive microorganisms. In Proceedings of the 16th International Conference on Miniaturized Systems for Chemistry and Life Sciences, MicroTAS 2012, Okinawa, Japan, 28 October–1 November 2012; pp. 1435–1437.
54. Dang, T.C.; Yin, Y.; Yu, Y.; Phan, D.-T.; Yang, C.; Cao, B.; Song, H.; Kang, Y. A membrane-free micro-fluidic microbial fuel cell for rapid characterization of exoelectrogenic bacteria. *Microfluid. Nanofluidics* **2016**, *20*, 144, doi:10.1007/s10404-016-1811-5.
55. Hou, H.; Li, L.; Cho, Y.; De Figueiredo, P.; Han, A. Microfabricated Microbial Fuel Cell Arrays Reveal Electrochemically Active Microbes. *PLoS ONE* **2009**, *4*, e6570, doi:10.1371/journal.pone.0006570.
56. Dávila, D.; Esquivel, J.P.; Sabaté, N.; Mas, J. Silicon-based microfabricated microbial fuel cell toxicity sensor. *Biosens. Bioelectron.* **2011**, *26*, 2426–2430, doi:10.1016/j.bios.2010.10.025.
57. Di Lorenzo, M.; Thomson, A.R.; Schneider, K.; Cameron, P.J.; Ieropoulosc, I. A small-scale air-cathode microbial fuel cell for on-line monitoring of water quality. *Biosens. Bioelectron.* **2014**, *62*, 182–188, doi:10.1016/j.bios.2014.06.050.
58. Yang, W.; Wei, X.; Fraiwan, A.; Coogan, C.G.; Lee, H.; Choi, S. Fast and sensitive water quality assessment: A μL-scale microbial fuel cell-based biosensor integrated with an air-bubble trap and electrochemical sensing functionality. *Sens. Actuators B Chem.* **2016**, *226*, 191–195, doi:10.1016/j.snb.2015.12.002.
59. Michelson, K.; Sanford, R.A.; Valocchi, A.J.; Werth, C.J. Nanowires ofGeobacter sulfurreducensRequire Redox Cofactors to Reduce Metals in Pore Spaces Too Small for Cell Passage. *Environ. Sci. Technol.* **2017**, *51*, 11660–11668, doi:10.1021/acs.est.7b02531.
60. Kim, B.J.; Chu, I.; Jusuf, S.; Kuo, T.; TerAvest, M.A.; Angenent, L.T.; Wu, M. Oxygen Tension and Riboflavin Gradients Cooperatively Regulate the Migration of Shewanella oneidensis MR-1 Revealed by a HydrogelBased Microfluidic Device. *Front. Microbiol.* **2016**, *7*, 1438, doi:10.3389/fmicb.2016.01438.
61. He, L.; Du, P.; Chen, Y.; Lu, H.W.; Cheng, X.; Chang, B.; Wang, Z. Advances in microbial fuel cells for wastewater treatment. *Renew. Sustain. Energy Rev.* **2017**, *71*, 388–403, doi:10.1016/j.rser.2016.12.069.
62. Wang, H.-Y.; Bernarda, A.; Huang, C.-Y.; Lee, D.-J.; Chang, J.-S. Micro-sized microbial fuel cell: A minireview. *Bioresour. Technol.* **2011**, *102*, 235–243, doi:10.1016/j.biortech.2010.07.007.
63. Yang, Y.; Ye, D.; Li, J.; Zhu, X.-M.; Liao, Q.; Zhang, B. Microfluidic microbial fuel cells: From membrane to membrane free. *J. Power Sources* **2016**, *324*, 113–125, doi:10.1016/j.jpowsour.2016.05.078.
64. Elmekawy, A.; Hegab, H.M.; Dominguez-Benetton, X.; Pant, D. Internal resistance of microfluidic microbial fuel cell: Challenges and potential opportunities. *Bioresour. Technol.* **2013**, *142*, 672–682, doi:10.1016/j.biortech.2013.05.061.
65. Slate, A.J.; Whitehead, K.A.; Brownson, D.A.; Banks, C.E. Microbial fuel cells: An overview of current technology. *Renew. Sustain. Energy Rev.* **2019**, *101*, 60–81, doi:10.1016/j.rser.2018.09.044.
66. Hindatu, Y.; Annuar, M.; Gumel, A.M. Mini-review: Anode modification for improved performance of microbial fuel cell. *Renew. Sustain. Energy Rev.* **2017**, *73*, 236–248, doi:10.1016/j.rser.2017.01.138.
67. Du, Z.; Li, H.; Gu, T. A state of the art review on microbial fuel cells: A promising technology for wastewater treatment and bioenergy. *Biotechnol. Adv.* **2007**, *25*, 464–482, doi:10.1016/j.biotechadv.2007.05.004.

68. Choudhury, P.; Uday, U.S.P.; Bandyopadhyay, T.K.; Ray, R.N.; Bhunia, B. Performance improvement of microbial fuel cell (MFC) using suitable electrode and Bioengineered organisms: A review. *Bioengineered* **2017**, *8*, 471–487, doi:10.1080/21655979.2016.1267883.
69. Rusli, S.F.N.; Abu Bakar, M.H.; Loh, K.S.; Masdar, M.S. Review of high-performance biocathode using stainless steel and carbon-based materials in Microbial Fuel Cell for electricity and water treatment. *Int. J. Hydrogen Energy* **2019**, *44*, 30772–30787, doi:10.1016/j.ijhydene.2018.11.145.
70. Ahmed, I.; Iqbal, H.M.N.; Akram, Z. Microfluidics Engineering: Recent Trends, Valorization, and Applications. *Arab. J. Sci. Eng.* **2018**, *43*, 23–32, doi:10.1007/s13369-017-2662-4.
71. Qian, F.; He, Z.; Thelen, M.P.; Li, Y. A microfluidic microbial fuel cell fabricated by soft lithography. *Bioresour. Technol.* **2011**, *102*, 5836–5840, doi:10.1016/j.biortech.2011.02.095.
72. Yoon, J.Y.; Ahn, Y.; Schröder, U. Parylene C-coated PDMS-based microfluidic microbial fuel cells with low oxygen permeability. *J. Power Sources* **2018**, *398*, 209–214, doi:10.1016/j.jpowsour.2018.07.064.
73. Mousavi, M.R.; Ghasemi, S.; Sanaee, Z.; Nejad, Z.G.; Mardanpour, M.M.; Yaghmaei, S.; Ghorbanzadeh, M. Improvement of the microfluidic microbial fuel cell using a nickel nanostructured electrode and microchannel modifications. *J. Power Sources* **2019**, *437*, doi:10.1016/j.jpowsour.2019.226891.
74. Ye, D.; Yang, Y.; Li, J.; Zhu, X.; Liao, Q.; Deng, B.; Chen, R. Performance of a microfluidic microbial fuel cell based on graphite electrodes. *Int. J. Hydrogen Energy* **2013**, *38*, 15710–15715, doi:10.1016/j.ijhydene.2013.05.034.
75. Yang, Y.; Ye, D.; Li, J.; Zhu, X.; Liao, Q.; Zhang, B. Biofilm distribution and performance of microfluidic microbial fuel cells with different microchannel geometries. *Int. J. Hydrogen Energy* **2015**, *40*, 11983–11988, doi:10.1016/j.ijhydene.2015.04.144.
76. Abgrall, P.; Conedera, V.; Camon, H.; Gue, A.-M.; Nguyen, N.-T. SU-8 as a structural material for labs-onchips and microelectromechanical systems. *Electrophoresis* **2007**, *28*, 4539–4551, doi:10.1002/elps.200700333. 77. Rodriguez-Ruiz, I.; Llobera, A.; Vila-Planas, J.; Johnson, D.W.; Gómez-Morales, J.; Garcia-Ruiz, J.M. Analysis of the Structural Integrity of SU-8-Based Optofluidic Systems for Small-Molecule Crystallization Studies. *Anal. Chem.* **2013**, *85*, 9678–9685, doi:10.1021/ac402019x.
78. Rodriguez-Ruiz, I.; Teychené, S.; Van Pham, N.; Radajewski, D.; Lamadie, F.; Llobera, A.; Charton, S. Broadcasting photonic lab on a chip concept through a low cost manufacturing approach. *Talanta* **2017**, *170*, 180–184, doi:10.1016/j.talanta.2017.04.010.
79. Mcdonald, J.C.; Duffy, D.C.; Anderson, J.R.; Chiu, D.T. Review General Fabrication of microfluidic systems in poly (dimethylsiloxane). *Electrophoresis* **2000**, *21*, 27–40.
80. Carlborg, C.F.; Moraga, F.; Saharil, F.; Van Der Wijngaart, W.; Haraldsson, T. Rapid permanent hydrophilic and hydrophobic patterning of polymer surfaces via off-stoichiometry thiol-ene (OSTE) photografting. In Proceedings of the 16th International Conference on Miniaturized Systems for Chemistry and Life Sciences, MicroTAS 2012, Okinawa, Japan, 28 October–1 November 2012; pp. 677–679.
81. Ogończyk, D.; Węgrzyn, J.; Jankowski, P.; Dąbrowski, B.; Garstecki, P. Bonding of microfluidic devices fabricated in polycarbonate. *Lab Chip* **2010**, *10*, 1324–1327, doi:10.1039/b924439e.
82. Becker, H.; Gärtner, C. Polymer microfabrication technologies for microfluidic systems. *Anal. Bioanal. Chem.* **2008**, *390*, 89–111, doi:10.1007/s00216-007-1692-2.
83. Guckenberger, D.J.; De Groot, T.E.; Wan, A.M.D.; Beebe, D.J.; Young, E.W.K. Micromilling: A method for ultra-rapid prototyping of plastic microfluidic devices. *Lab Chip* **2015**, *15*, 2364–2378, doi:10.1039/c5lc00234f.
84. Au, A.K.; Huynh, W.; Horowitz, L.F.; Folch, A. 3D-Printed Microfluidics. *Angew. Chem. Int. Ed.* **2016**, *55*, 3862–3881, doi:10.1002/anie.201504382.
85. Bressan, L.P.; Adamo, C.B.; Quero, R.F.; de Jesus, D.P.; da Silva, J.A. A simple procedure to produce FDMbased 3D-printed microfluidic devices with an integrated PMMA optical window. *Anal. Methods* **2019**, *11*, 1014–1020, doi:10.1039/c8ay02092b.
86. Fraiwan, A.; Choi, S. A stackable, two-chambered, paper-based microbial fuel cell. *Biosens. Bioelectron.* **2016**, *83*, 27–32, doi:10.1016/j.bios.2016.04.025.
87. Veerubhotla, R.; Bandopadhyay, A.; Das, D.; Chakraborty, S. Instant power generation from an airbreathing paper and pencil based bacterial bio-fuel cell. *Lab Chip* **2015**, *15*, 2580–2583, doi:10.1039/c5lc00211g.
88. Fraiwan, A.; Mukherjee, S.; Sundermier, S.; Lee, H.-S.; Choi, S. A paper-based microbial fuel cell: Instant battery for disposable diagnostic devices. *Biosens. Bioelectron.* **2013**, *49*, 410–414, doi:10.1016/j.bios.2013.06.001.
89. Lee, H.; Choi, S. An origami paper-based bacteria-powered battery. *Nano Energy* **2015**, *15*, 549–557, doi:10.1016/j.nanoen.2015.05.019.
90. Jeuken, L.J.C. Structure and Modification of Electrode Materials for Protein Electrochemistry. In *Biophotoelectrochemistry: From Bioelectrochemistry to Biophotovoltaics*; Springer: Cham, Switzerland, 2016.

91. Ren, H.; Pyo, S.; Lee, J.-I.; Park, T.-J.; Gittleson, F.S.; Leung, F.C.C.; Kim, J.; Taylor, A.D.; Lee, H.-S.; Chae, J. A high power density miniaturized microbial fuel cell having carbon nanotube anodes. *J. Power Sources* **2015**, *273*, 823–830, doi:10.1016/j.jpowsour.2014.09.165.
92. Wang, H.; Wang, G.; Ling, Y.; Qian, F.; Song, Y.; Lu, X.; Chen, S.; Tong, Y.; Li, Y. High power density microbial fuel cell with flexible 3D graphene–nickel foam as anode. *Nanoscale* **2013**, *5*, 10283–10290, doi:10.1039/c3nr03487a.
93. Dominguez-Benetton, X.; Sevda, S.; Vanbroekhoven, K.; Pant, D. The accurate use of impedance analysis for the study of microbial electrochemical systems. *Chem. Soc. Rev.* **2012**, *41*, 7228–7246, doi:10.1039/c2cs35026b.
94. Yang, Y.; Liu, T.; Tao, K.; Chang, H. Generating Electricity on Chips: Microfluidic Biofuel Cells in Perspective. *Ind. Eng. Chem. Res.* **2018**, *57*, 2746–2758, doi:10.1021/acs.iecr.8b00037.
95. Choi, S.; Lee, H.-S.; Yang, Y.; Parameswaran, P.; Torres, C.I.; Rittmann, B.E.; Chae, J. A μL-scale micromachined microbial fuel cell having high power density. *Lab Chip* **2011**, *11*, 1110–1117, doi:10.1039/c0lc00494d.
96. Ismagilov, R.F.; Stroock, A.D.; Kenis, P.J.A.; Whitesides, G.M.; Stone, H.A. Experimental and theoretical scaling laws for transverse diffusive broadening in two-phase laminar flows in microchannels. *Appl. Phys. Lett.* **2000**, *76*, 2376–2378, doi:10.1063/1.126351.
97. Tian, W.C.; Finehout, E. *Microfluidics for Biological Applications*; Springer Science & Business Media: Berlin/Heidelberg, Germany, 2009, doi:10.1007/978-0-387-09480-9.
98. Jayashree, R.S.; Gancs, L.; Choban, E.R.; Primak, A.; Natarajan, D.; Markoski, L.J.; Kenis, P.J.A. AirBreathing Laminar Flow-Based Microfluidic Fuel Cell. *J. Am. Chem. Soc.* **2005**, *127*, 16758–16759, doi:10.1021/ja054599k.
99. Son, K.; Brumley, D.R.; Stocker, R. Live from under the lens: Exploring microbial motility with dynamic imaging and microfluidics. *Nat. Rev. Microbiol.* **2015**, *13*, 761–775, doi:10.1038/nrmicro3567.
100. Vigolo, D.; Al-Housseiny, T.T.; Shen, Y.; Akinlawon, F.O.; Al-Housseiny, S.T.; Hobson, R.K.; Sahu, A.; Bedkowski, K.I.; DiChristina, T.J.; Stone, H.A. Flow dependent performance of microfluidic microbial fuel cells. *Phys. Chem. Chem. Phys.* **2014**, *16*, 12535–12543, doi:10.1039/c4cp01086h.
101. Södergren, S. Electrochemical Microsensor with In-Situ Fabricated Ag/AgCl Reference Electrode for HighPressure Microfluidics. Ph.D. Thesis, Uppsala University, Uppsala, Sweden, September 2017.
102. Kim, J.; Elsnab, J.R.; Gehrke, C.; Li, J.; Gale, B.K. Microfluidic integrated multi-walled carbon nanotube (MWCNT) sensor for electrochemical nucleic acid concentration measurement. *Sens. Actuators B Chem.* **2013**, *185*, 370–376, doi:10.1016/j.snb.2013.05.018.
103. Dungchai, W.; Chailapakul, O.; Henry, C.S. Electrochemical Detection for Paper-Based Microfluidics. *Anal. Chem.* **2009**, *81*, 5821–5826, doi:10.1021/ac9007573.
104. Shi, L.; Dong, H.; Reguera, G.; Beyenal, H.; Haluk, B.; Liu, J.; Yu, H.-Q.; Fredrickson, J.K. Extracellular electron transfer mechanisms between microorganisms and minerals. *Nat. Rev. Microbiol.* **2016**, *14*, 651–662, doi:10.1038/nrmicro.2016.93.
105. Jiang, X.; Hu, J.-S.; Fitzgerald, L.A.; Biffinger, J.C.; Xie, P.; Ringeisen, B.R.; Lieber, C.M. Probing electron transfer mechanisms in Shewanella oneidensis MR-1 using a nanoelectrode platform and single-cell imaging. *Proc. Natl. Acad. Sci. USA* **2010**, *107*, 16806–16810.
106. Humphries, J.; Xiong, L.; Liu, J.; Prindle, A.; Yuan, F.; Arjes, H.A.; Tsimring, L.; Süel, G.M. SpeciesIndependent Attraction to Biofilms through Electrical Signaling. *Cell* **2017**, *168*, 200–209.e12, doi:10.1016/j.cell.2016.12.014.
107. Huang, K.C. Staying in Touch while on the Go. *Cell* **2017**, *168*, 15–17, doi:10.1016/j.cell.2016.12.024.
108. Wang, Q.; Iii, A.-A.D.J.; Gralnick, J.A.; Lin, L.; Buie, C.R. Microfluidic dielectrophoresis illuminates the relationship between microbial cell envelope polarizability and electrochemical activity. *Sci. Adv.* **2019**, *5*, eaat5664, doi:10.1126/sciadv.aat5664.
109. Du, Q.; Mu, Q.; Cheng, T.; Li, N.; Wang, X. Real-Time Imaging Revealed That Exoelectrogens from Wastewater Are Selected at the Center of a Gradient Electric Field. *Environ. Sci. Technol.* **2018**, *52*, 8939– 8946, doi:10.1021/acs.est.8b01468.
110. Zhang, X.; Prévoteau, A.; Louro, R.O.; Paquete, C.M.; Rabaey, K. Periodic polarization of electroactive biofilms increases current density and charge carriers concentration while modifying biofilm structure. *Biosens. Bioelectron.* **2018**, *121*, 183–191, doi:10.1016/j.bios.2018.08.045.
111. Ter Heijne, A.; Pereira, M.A.; Pereira, J.; Sleutels, T. Electron Storage in Electroactive Biofilms. *Trends Biotechnol.* **2020**, doi:10.1016/j.tibtech.2020.06.006.
112. Erable, B.; Bergel, A. First air-tolerant effective stainless steel microbial anode obtained from a natural marine biofilm. *Bioresour. Technol.* **2009**, *100*, 3302–3307, doi:10.1016/j.biortech.2009.02.025.
113. Erable, B.; Vandecandelaere, I.; Faimali, M.; Delia, M.-L.; Etcheverry, L.; Vandamme, P.; Bergel, A. Marine aerobic biofilm as biocathode catalyst. *Bioelectrochemistry* **2010**, *78*, 51–56, doi:10.1016/j.bioelechem.2009.06.006.

114. Virdis, B.; Millo, D.; Donose, B.C.; Batstone, D.J. Real-Time Measurements of the Redox States of c-Type Cytochromes in Electroactive Biofilms: A Confocal Resonance Raman Microscopy Study. *PLoS ONE* **2014**, *9*, e89918, doi:10.1371/journal.pone.0089918.
115. Commault, A.S.; Lear, G.; Packer, M.; Weld, R.J. Influence of anode potentials on selection of Geobacter strains in microbial electrolysis cells. *Bioresour. Technol.* **2013**, *139*, 226–234, doi:10.1016/j.biortech.2013.04.047.
116. Zhu, X.; Yates, M.D.; Hatzell, M.C.; Rao, H.A.; Saikaly, P.E.; Logan, B.E. Microbial Community Composition Is Unaffected by Anode Potential. *Environ. Sci. Technol.* **2014**, *48*, 1352–1358, doi:10.1021/es404690q.
117. Blanchet, E.; Desmond, E.; Erable, B.; Bridier, A.; Bouchez, T.; Bergel, A. Comparison of synthetic medium and wastewater used as dilution medium to design scalable microbial anodes: Application to food waste treatment. *Bioresour. Technol.* **2015**, *185*, 106–115, doi:10.1016/j.biortech.2015.02.097.
118. Franks, A.E.; Glaven, S.M.; Lovley, D.R. Real-Time Spatial Gene Expression Analysis within CurrentProducing Biofilms. *ChemSusChem* **2012**, *5*, 1092–1098, doi:10.1002/cssc.201100714.
119. Bonanni, P.S.; Bradley, D.F.; Schrott, G.D.; Busalmen, J.P. Limitations for Current Production in Geobacter sulfurreducens Biofilms. *ChemSusChem* **2013**, *6*, 711–720, doi:10.1002/cssc.201200671.
120. Sun, D.; Chen, J.; Huang, H.; Liu, W.; Ye, Y.; Cheng, S. The effect of biofilm thickness on electrochemical activity of Geobacter sulfurreducens. *Int. J. Hydrogen Energy* **2016**, *41*, 16523–16528, doi:10.1016/j.ijhydene.2016.04.163.
121. Franks, A.E.; Nevin, K.P.; Jia, H.; Izallalen, M.; Woodard, T.L.; Lovley, D.R. Novel strategy for threedimensional real-time imaging of microbial fuel cell communities: Monitoring the inhibitory effects of proton accumulation within the anode biofilm. *Energy Environ. Sci.* **2009**, *2*, 113–119, doi:10.1039/b816445b.
122. Torres, C.I.; Marcus, A.K.; Rittmann, B.E. Proton transport inside the biofilm limits electrical current generation by anode-respiring bacteria. *Biotechnol. Bioeng.* **2008**, *100*, 872–881, doi:10.1002/bit.21821.
123. Renslow, R.S.; Babauta, J.T.; Dohnalkova, A.C.; Boyanov, M.I.; Kemner, K.M.; Majors, P.D.; Fredrickson, J.K.; Beyenal, H. Metabolic spatial variability in electrode-respiring Geobacter sulfurreducens biofilms. *Energy Environ. Sci.* **2013**, *6*, 1827–1836, doi:10.1039/c3ee40203g.
124. Jain, A.; Gazzola, G.; Panzera, A.; Zanoni, M.; Marsili, E. Visible spectroelectrochemical characterization of Geobacter sulfurreducens biofilms on optically transparent indium tin oxide electrode. *Electrochimica Acta* **2011**, *56*, 10776–10785, doi:10.1016/j.electacta.2011.02.073.
125. Robuschi, L.; Tomba, J.P.; Schrott, G.D.; Bonanni, P.S.; DeSimone, P.M.; Busalmen, J.P. Spectroscopic Slicing to Reveal Internal Redox Gradients in Electricity-Producing Biofilms. *Angew. Chem. Int. Ed.* **2013**, *52*, 925– 928, doi:10.1002/anie.201205440.
126. Robuschi, L.; Tomba, J.P.; Busalmen, J.P. Proving Geobacter biofilm connectivity with confocal Raman microscopy. *J. Electroanal. Chem.* **2017**, *793*, 99–103, doi:10.1016/j.jelechem.2016.11.005.
127. Babauta, J.T.; Nguyen, H.D.; Harrington, T.D.; Renslow, R.; Beyenal, H. pH, redox potential and local biofilm potential microenvironments within Geobacter sulfurreducens biofilms and their roles in electron transfer. *Biotechnol. Bioeng.* **2012**, *109*, 2651–2662, doi:10.1002/bit.24538.
128. Chadwick, G.L.; Otero, F.J.; Gralnick, J.A.; Bond, D.R.; Orphan, V.J. NanoSIMS imaging reveals metabolic stratification within current-producing biofilms. *Proc. Natl. Acad. Sci. USA* **2019**, *116*, 20716–20724, doi:10.1073/pnas.1912498116.
129. Biffinger, J.C.; Byrd, J.N.; Dudley, B.L.; Ringeisen, B.R. Oxygen exposure promotes fuel diversity for Shewanella oneidensis microbial fuel cells. *Biosens. Bioelectron.* **2008**, *23*, 820–826, doi:10.1016/j.bios.2007.08.021.
130. Rusconi, R.; Guasto, J.S.; Stocker, R. Bacterial transport suppressed by fluid shear. *Nat. Phys.* **2014**, *10*, 212– 217, doi:10.1038/nphys2883.
131. Ren, H.; Torres, C.I.; Parameswaran, P.; Rittmann, B.E.; Chae, J. Improved current and power density with a micro-scale microbial fuel cell due to a small characteristic length. *Biosens. Bioelectron.* **2014**, *61*, 587–592, doi:10.1016/j.bios.2014.05.037.
132. Mikkonen, S.; Rokhas, M.K.; Jacksén, J.; Emmer, Åsa Sample preconcentration in open microchannels combined with MALDI-MS. *Electrophoresis* **2012**, *33*, 3343–3350, doi:10.1002/elps.201200129.
133. Choi, S.; Chae, J. Optimal biofilm formation and power generation in a micro-sized microbial fuel cell (MFC). *Sens. Actuators A Phys.* **2013**, *195*, 206–212, doi:10.1016/j.sna.2012.07.015.
134. Molenaar, S.D.; Sleutels, T.; Pereira, J.; Iorio, M.; Borsje, C.; Zamudio, J.A.; Fabregat-Santiago, F.; Buisman, C.J.; Ter Heijne, A. In situ Biofilm Quantification in Bioelectrochemical Systems by using Optical Coherence Tomography. *ChemSusChem* **2018**, *11*, 2171–2178, doi:10.1002/cssc.201800589.
135. Diao, J.; Young, L.; Kim, S.; Fogarty, E.A.; Heilman, S.M.; Zhou, P.; Shuler, M.L.; Wu, M.; Delisa, M.P. A three-channel microfluidic device for generating static linear gradients and its application to the quantitative analysis of bacterial chemotaxis. *Lab Chip* **2006**, *6*, 381–388, doi:10.1039/b511958h.

136. Kim, J.; Park, H.-D.; Chung, S. Microfluidic Approaches to Bacterial Biofilm Formation. *Molecules* **2012**, *17*, 9818–9834, doi:10.3390/molecules17089818.
137. Ahmed, I.; Akram, Z.; Bule, M.H.; Iqbal, H.M.N. Advancements and Potential Applications of Microfluidic Approaches—A Review. *Chemosensors* **2018**, *6*, 46, doi:10.3390/chemosensors6040046.
138. Feng, J.; De La Fuente-Núñez, C.; Trimble, M.J.; Xu, J.; Hancock, R.E.W.; Lu, X. An in situ Raman spectroscopy-based microfluidic "lab-on-a-chip" platform for non-destructive and continuous characterization of Pseudomonas aeruginosa biofilms. *Chem. Commun.* **2015**, *51*, 8966–8969, doi:10.1039/c5cc02744f.
139. Kou, S.; Cheng, D.; Sun, F.; Hsing, I.-M. Microfluidics and microbial engineering. *Lab Chip* **2016**, *16*, 432– 446, doi:10.1039/c5lc01039j.
140. Shrestha, N.; Chilkoor, G.; Vemuri, B.; Rathinam, N.; Sani, R.K.; Gadhamshetty, V. Extremophiles for microbial-electrochemistry applications: A critical review. *Bioresour. Technol.* **2018**, *255*, 318–330, doi:10.1016/j.biortech.2018.01.151.
141. Chen, T.; Gomez-Escoda, B.; Munoz-Garcia, J.; Babic, J.; Griscom, L.; Wu, P.-Y.J.; Coudreuse, D. A drugcompatible and temperature-controlled microfluidic device for live-cell imaging. *Open Biol.* **2016**, *6*, 160156, doi:10.1098/rsob.160156
142. Straub, H.; Eberl, L.; Zinn, M.; Rossi, R.M.; Maniura-Weber, K.; Ren, Q. A Microfuidic Platform for in Situ Investigation of Bio lm Formation and Its Treatment under Controlled Conditions. *J. Nanobiotechnology* **2020**, *18*, 166, doi:10.1186/s12951-020-00724-0.
143. Ye, D.; Zhang, P.; Li, J., Zhu, X.; Chen, R.; Liao, Q. In situ visualization of biofilm formation in a microchannel for a microfluidic microbial fuel cell anode. **2020**, *Int. J. Hydrog. Energy,* in press, doi:10.1016/j.ijhydene.2020.08.170.
144. Yawata, Y.; Toda, K.; Setoyama, E.; Fukuda, J.; Suzuki, H.; Uchiyama, H.; Nomura, N. Bacterial growth monitoring in a microfluidic device by confocal reflection microscopy. *J. Biosci. Bioeng.* **2010**, *110*, 130–133, doi:10.1016/j.jbiosc.2010.01.009.
145. Connell, J.L.; Kim, J.; Shear, J.B.; Bard, A.J.; Whiteley, M. Real-time monitoring of quorum sensing in 3Dprinted bacterial aggregates using scanning electrochemical microscopy. *Proc Natl Acad Sci USA* **2014**, *111*, 18255–18260, doi:10.1073/pnas.1421211111.
146. Holman, H.-Y.N.; Miles, R.; Hao, Z.; Wozei, E.; Anderson, L.M.; Yang, H. Real-time chemical imaging of bacterial activity in biofilms using open-channel microfluidics and synchrotron FTIR spectromicroscopy *Anal. Chem*., **2009**, *81*, 8564–8570, doi:10.1021/ac9015424.
147. Renslow, R.S.; Marshall, M.J.; Tucker, A.E.; Chrisler, W.B.; Yu, X.Y. In situ nuclear magnetic resonance microimaging of live biofilms in a microchannel *Analyst.* **2017**, *142*, 2363–2371, doi:10.1039/c7an00078b.
148. Meyer, M.T.; Roy, V.; Bentley, W.E.; Ghodssi, R. Development and validation of a microfluidic reactor for biofilm monitoring via optical methods. *J. Micromech. Microeng.* **2011**, *21*, 054023, doi:10.1088/0960-1317/21/5/054023.
149. Kim, Y.W.; Mosteller, M.P.; Subramanian, S.; Meyer, M.T.; Bentley, W.E.; Ghodssi, R. An optical microfluidic platform for spatiotemporal biofilm treatment monitoring. *J. Micromech. Microeng*. **2015**, *26*, doi:10.1088/0960-1317/26/1/015013.
150. Kara, A.; Reitz, A.; Mathault, J.; Mehou-Loko, S.; Abbaszadeh Amirdehi, M.; Miled, A.; Greener, J. Electrochemical imaging for microfluidics: A full-system approach. *Lab Chip*, **2016**, *16*, 1081–1087, doi:10.1039/c6lc00077k.

I.4. Bacterial taxis at the microscale

Bacterial taxis refers as the directed bacterial displacement towards or away from an external stimulus or gradient. If the displacement is induced by changes in the chemical composition of the bacterial environment, the phenomenon is classified as chemotaxis. Moreover, if internal energetic conditions are not optimal, motile bacteria is able to swim to areas that provide higher levels of energy, by an energy-taxis mechanism (Schweinitzer and Josenhans, 2010). For *S. Oneidensis MR-1*, it was demonstrated that in the presence of electrons acceptors such as MnO_2 and $Fe(OH)_3$ particles, the speed of displacement of bacteria towards the metallic particles was proportional with its concentration. Furthermore, by reproducing the same experiences but by adding riboflavin to the medium that contained the metallic particles, the speed of displacement was considerably increased. This proved that *S.Oneidensis* was capable of chemotaxis and energy taxis, since the flavins, which are normally secreted by the bacterial strain, enhanced the motility towards the solid electron acceptor (Li et al., 2012).

An additional type of taxis can occur when bacteria move under the effect of current or an electric field, defining this process as electrotaxis or galvanotaxis. Adler and Shi (1988) were pioneers in detecting electrotaxis in bacterial cells, reporting that motile *E. coli* and *S. Typhimurium* swam in random directions in the absence of an electric field. However, when applying an electric field of 4 V/cm, *E.coli* aligned to the anode and *S. Typhimurium* to the cathode. When polarity was reversed, the cells made a U-turn to migrate in the opposite direction. To study this, they used a computerized motion analysis platform, where cell behavior was observed through a microscope recorded on a videotape. Bacteria and a mix of phosphate buffer with EDTA were contained in a transparent glass compartment with platinum electrodes connected to power supply. Years later, Shi et al (1996) from the same research group determined that the reason why *E.coli* swam to the anode and *S. Typhimurium* to the cathode was linked to differences in the nature of bacterial surface. Apparently, depending on whether the bacteria contained a type of polysaccharide that provided them with a more or less negative charged structure, they would travel to the anode or cathode in the presence of an electric field.

The study of bacterial taxis can help to understand how electroactive bacteria in BES are able to swim towards the electrode and colonize its surface. Recently, Chong et al. (2021) developed a three-electrode electrochemical set-up that could discriminate the response of bacterial cells from a mixed-inoculum to an electric field or to electrode surface polarization. They evidenced that when applying an electric field for 3 hours followed by electrode polarization of 7 days, an EAB was formed. Opposite case, no EAB was formed if the electric field was not applied before the 7 days of polarization. They stated that bacteria could detect the ion concentration gradient of Na^+ and K^+ generated by the electric field, which is also typically formed when the an electrode is polarized, therefore providing more evidence of how bacteria reaches and colonizes the anode.

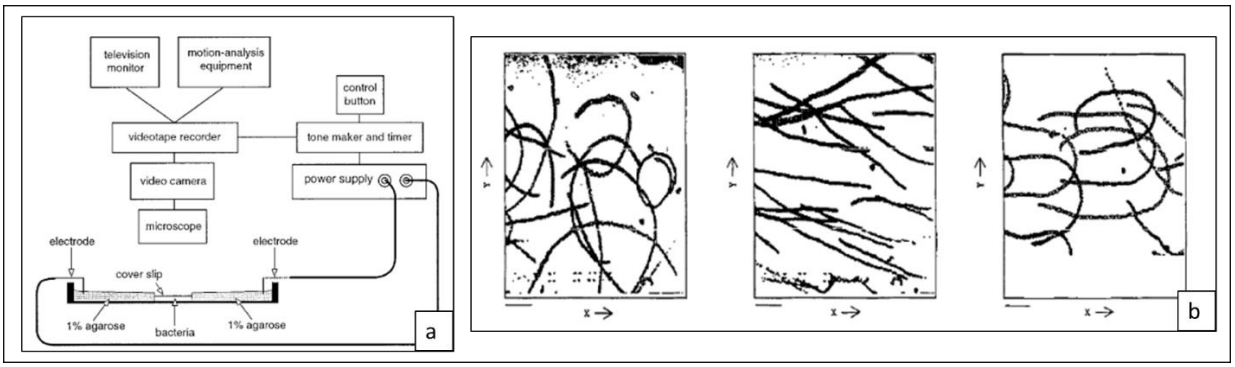

Figure I-5 : a) Device for observing bacterial galvanotaxis. Extracted from Shi et al. (1996), b) Behavior of E.coli in the absence (left image), under the effect (center image) and after the inversion (right image) of an electric field of 4 V/cm. Extracted from Adler and Shi, 1988.

The device used by Adler and Shi in 1988 to study galvanotaxis and to illustrate bacterial displacement lines (Figure I-5) might have served as an early step to a further microfluidic device integrated to a microscope, a power source and real-time acquisition instrument. J. Li and Lin (2011) described the advantages of using microfluidic devices for investigating microbial taxis since they contemplate the precise configuration and flexible manipulation of chemical concentration gradients and electric fields. Microdevices can be useful to study the complex guiding mechanisms for cell locomotion allowing real-time quantification and visualization of displacements at the single-cell level. A more recent review Pérez-Rodríguez et al. (2022) summarized a wide variety of microfluidic cell designs to study external stimulus, concluding that bacterial taxis can be studied with simple channel geometries.

The study of taxis mechanisms in EABs using microBES has been only limited to single species, more precisely to *S.Oneidensis MR-1*, since it is known that it is capable of several types of taxis. A very interesting study is the one of Harris et al. (2010). Firstly, they observed cell displacement towards MnO_2 and $Fe(OH)_3$ as solid electron acceptors in a 24-hour period. Subsequently, they repeated the experiment by observing the movements of cells towards a graphite electrode polarized at different potentials. As a result, a dramatic increase in cell swimming speed towards the solid electron acceptor was observed in the presence of MnO_2 and the solid electrode polarized at high potentials. The successful quantification of these phenomena was due to the coupling of microBES with real-time optical microscopy and post-processing of microscope images with MATLAB algorithms for cell displacement. Years later, Kim et al. (2016) also observed the displacement of *S.Oneidensis MR-1* cells in a microfluidic device under a riboflavin gradient, where the speed of displacement was increased in anaerobic conditions. The absence of oxygen as an electron acceptor enhanced the chemotaxis of *S.Oneidensis* towards riboflavin gradients (Figure I-6 (a)). For the quantification of these displacements, they imaged the individual cells in the microfluidic channel with an epifluorescence microscope capturing a stack of 500 images at 30 frames per second after 10 minutes after the *S.Oneidensis* cells were introduced. Post-processing with MATLAB software allowed characterize bacteria motility in aerobic and anaerobic conditions.

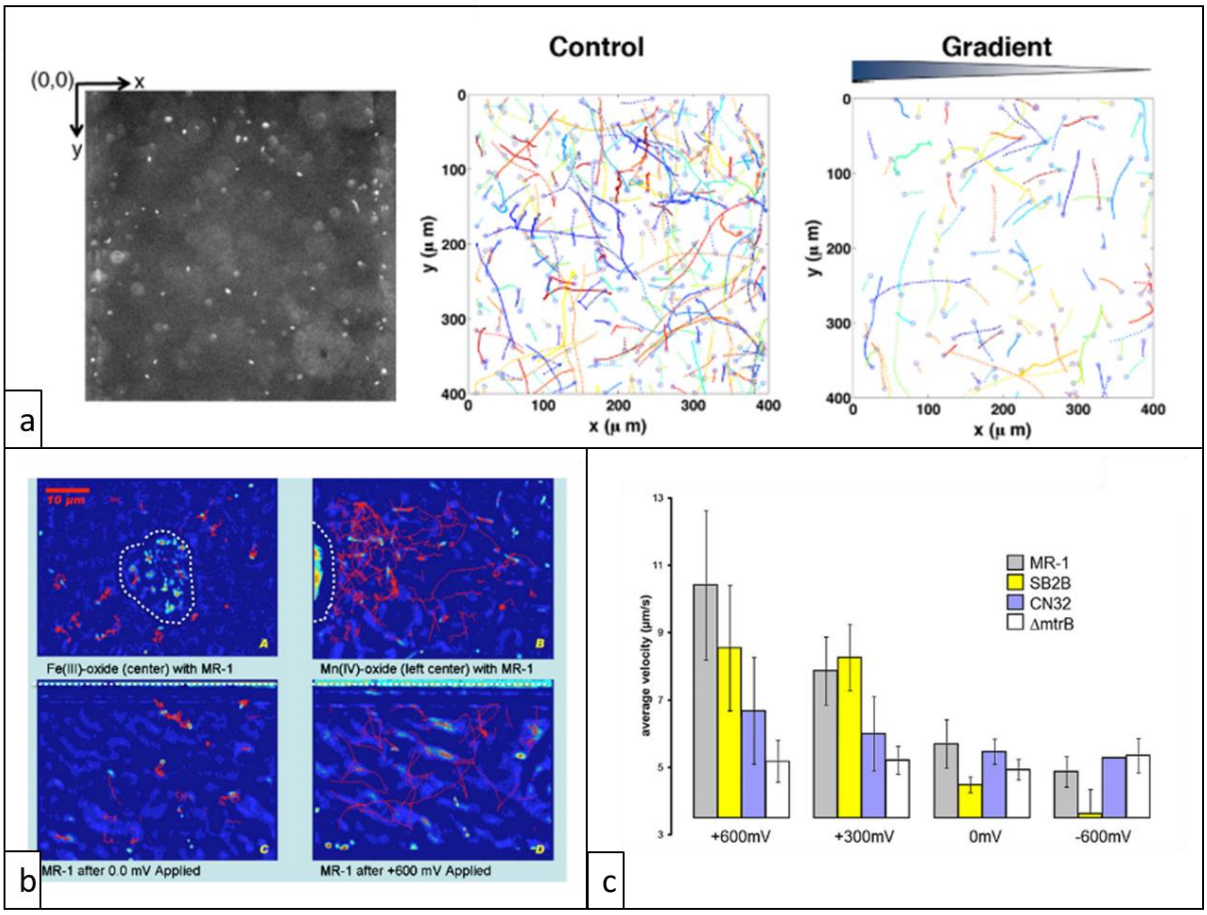

Figure I-6 : a) Left: Microscopic image of S.Oneidensis in the microfluidic channel. Center: Cell tracking in the microfluidic channel in anaerobic conditions. Right: Motility patterns when an oxygen gradient is applied. Extracted from Kim et al., 2016. b) Bacterial trajectories (red lines) of S.Oneidensis under different stimulus, c) calculation of average velocity for four different S.Oneidensis MR-1 mutants at different applied potentials. Extracted from Harris et al., 2010.

It is clear that taxis mechanisms play an important role in the early stages of biofilm formation since they are involved on how electroactive bacteria are selected from a mixed inoculum and how they displace themselves towards the anode surface. As described above, until the present day, the investigation of taxis mechanisms in electroactive bacteria was mainly done using single bacterial species in macro and microBES. For multi-species biofilms, the research was only carried in macroBES. The combination of microfluidics with microscopy techniques and post-processing of microscope images with cell displacement algorithms could be advantageous to study bacterial taxis in multi-species biofilms, where deeper insights on the early processes of biofilm formation could be gained as to lead to more sustainable and robust bioanodes.

Chapter II : Materials and Methods

II.1. Culture medium, microbial inoculum and substrates

In this work, the term anolyte makes reference to the liquid solution including the culture medium, inoculum and substrate.

II.1.1. Culture medium

Four different media were tested during the course of this thesis work. These included three synthetic culture media and one real environmental medium.

- Synthetic media

The choice to work with a synthetic medium can be resumed into two reasons: the first, in order to have a better control of the anolyte composition and to avoid reproducibility issues that could be generated by the variation in its composition. Secondly, when working with small volumes in microfluidic reactors, a synthetic medium could be more suitable; for example, one that does not contain suspended particles that could clog channels in the microreactors. Table II-1 shows each synthetic medium composition used in the experiments.

- Residual wastewater

In the cases where it was decided to work with a real environmental medium, domestic residual wastewater was collected from a local wastewater treatment plant (WWTP) *(Castanet-Tolosan, France)* and stored in a cold room at 4°C until use and for a maximum of one month.

Table II-1 : Composition of different synthetic media. For Synthetic wastewater I, the vitamin and mineral trace solution were commercially available (ATCC). Micronutrients solution for Synthetic wastewater II and Starkey medium were prepared in the laboratory.

Synthetic wastewater I	
Compound	**Concentration**
Buffer phosphate	100 mM
KCl	0.1 g/L
NH4Cl	0.2 g/L
Vitamin solution	1% V/V
Mineral trace solution	1% V/V

Vitamin solution (commercial)	
Compound	**Concentration**
Folic acid	2 mg/L
Pyridoxine hydrochloride	10 mg/L
Riboflavin	5 mg/L
Biotin	2 mg/L
Thiamine	5 mg/L
Nicotinic acid	5 mg/L
Calcium Pantothenate	5 mg/L
Vitamin B12	0.1 mg/L
p-Aminobenzoic acid	5 mg/L
Thiotic acid	5 mg/L
Monopotassium phosphate	900 mg/L

Mineral trace solution (commercial)	
Compound	**Concentration**
EDTA	0.5 g/L
Mg_2SO_4 $7H_2O$	3 g/L
$MnCl_2$ $4H_2O$	0.5 g/L
NaCl	1 g/L
$Fe(SO_4)$ $7H_2O$	0.1 g/L
$Co(NO_3)_2$ $6H_2O$	0.1 g/L
$CaCl_2$	0.1 g/L
$ZnSO_4$ $7H_2O$	0.1 g/L
$CuSO_4$ $5H_2O$	0.01 g/L
$AlK(SO_4)_2$	0.01 g/L
H_3BO_3	0.01 g/L
Na_2MoO_4 $2H_2O$	0.01 g/L
Na_2SeO_3	0.001 g/L
Na_2WO_4 $2H_2O$	0.01 g/L

Synthetic wastewater II	
Compound	**Concentration**
Urea	30 mg/L
KH_2PO_4	25 mg/L
NH_4Cl	20 mg/L
$NaHCO_3$	20 mg/L
KCl	20 mg/L
Mg_2SO_4 $7H_2O$	5 mg/L
$CaCl_2$	5 mg/L
$MnSO_4$	3 mg/L
Micronutrients solution	0.1% V/V

Micronutrients solution	
Compound	**Concentration**
$FeCl_2$	1.28 g/L
Na_2MoO_4 $2H_2O$	0.212 g/L
$CuCl_2$ $2H_2O$	3.4 g/L
$CuSO_4$	0.8 g/L
$ZnSO_4$	0.96 g/L
$ZnCl_2$	1.7 g/L
$CoCl_2$ $6H_2O$	1 g/L
H_3BO_3	0.1 g/L
$NiCl_2$ $6H_2O$	0.131 g/L
Na_2WO_4 $2H_2O$	0.22 g/L

Starkey medium	
Compound	**Concentration**
NaCl	45 g/L
NH_4Cl	2 g/L
K_2HPO_4	0.5 g/L
Micronutrients solution	0.1% V/V

Micronutrients solution	
Compound	**Concentration**
HCl 37%	46 mL/L
$MgCl_2$ $6H_2O$	55 g/L
$Fe(SO_4)$ $7H_2O$	7 g/L
$ZnCl_2$ $2H_2O$	1 g/L
$MnCl_2$ $4H_2O$	1.2 g/L
$CuSO_4$ $5H_2O$	0.4 g/L
$CoSO_4$ $7H_2O$	1.3 g/L
BO_3H_3	0.1 g/L
Na_2MoO_4 $2H_2O$	1 g/L
$NiCl_2$ $6H_2O$	0.05 g/L
Na_2SeO_3 $5H_2O$	0.01 g/L
$CaCl_2$ $2H_2O$	60 g/L

For experiments requiring quorum-sensing (QS) molecules, three commercial types were tested and added to the anolyte: N-(3-Oxododecanoyl)-L-homoserine lactone *(Sigma Aldrich)*, N-Hexanoyl-L-homoserine lactone *(Sigma Aldrich)* and N-Butyryl-DL-homoserine lactone *(Sigma Aldrich).* The

molecules were directly solubilized with the anolyte in order to attain the appropriate concentration and were only used in Starkey medium.

II.1.2. Different types of microbial inoculum

- Activated sludge (AS):

For experiments carried out with "synthetic wastewater I" and residual wastewater, the medium was inoculated with AS collected from the aeration tank of the WWTP plant (*Castanet-Tolosan, France*) and stored in a cold room at 4°C until use. Approximately once a month, new batches of AS were recollected.

- Garden compost:

The garden compost used in the PhD works of Morgane Hoareau (Hoareau,2021) was composed of a mix of one volume of vermicompost *(OR brun)* and 15 volumes of garden potting soil *(OR brun)*.

- Salt marsh sediments (SMS):

SMS were collected from the Mediterranean coast of France (*Salines de Saint Martin, Gruissan*) in an area as observed in Figure II-1 (A). The collection of these SMS was repeated in multiples occasions throughout the three years of the PhD. After the sampling, sediments were stored in a closed tank at room temperature for periods of several months. In a previous PhD work at LGC, the stability of the microbial population of the inoculum at long periods was demonstrated (Rousseau, 2013). SMS are composed of a supernatant liquid part that remains on the surface of the tank, and a solid part, which deposits at the bottom of the tank. In general, reactors were inoculated with the liquid part of the sediments, unless otherwise indicated.

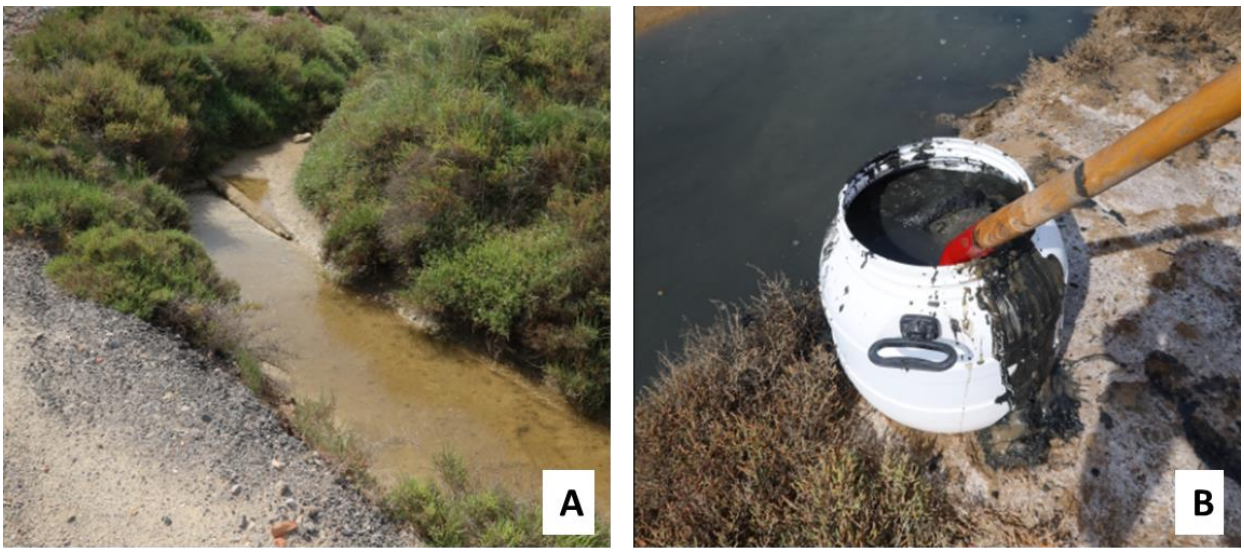

Figure II-1 : Salt marsh sediments collection. (A) SMS collection site. (B) SMS transfer into the storage tank.

II.1.3. Substrates

Acetate (*Sigma Aldrich*) was mainly used as a model substrate in this thesis work. The acetate concentration was determined in the anolyte by measuring the chemical oxygen demand (COD). COD represents the amount of oxygen needed to oxidize carbon compounds into CO_2 and H_2O. COD is classified in soluble COD (COD_s) which are simple organic molecules easy to biodegrade, and particulate COD (COD_p), corresponding to large and complex molecules which are more difficult to biodegrade. By measuring the soluble COD in mg/L of O_2, substrate concentration can be correlated to COD value. For example, in the case of acetate as substrate:

Acetate oxidation $CH_3COO^- + 4H_2O \rightarrow HCO_3^- + 9H^+ + 8e^-$ Eq. II-1

Oxygen reduction: $O_2 + 4H^+ + 4e^- \rightarrow 2H_2O$ Eq. II-2

Balanced equation: $CH_3COO^- + 2O_2 \rightarrow 2HCO_3^- + H^+$ Eq. II-3

The balanced equation Eq. II-3 indicates that 2 mM of O_2 (64 mg) are needed to oxidize 1 mM of CH_3COO^-, which translates that 1mM of acetate corresponds to a COD value of 64 mg/L. For other substrates that were also used in this PhD work, such as glucose (*Sigma Aldrich*), formate (S*igma Aldrich*) or butyrate (*Sigma Aldrich*), the corresponding oxidation reaction was balanced with the oxygen reduction in order to obtain the correlation between substrate and COD concentration values.

For COD measurement, 4 mL of the supernatant anolyte contained in the reactors were sampled. In order to obtain the soluble COD, each sample was filtered with a 0.22 µm acetate filter. If the culture medium was Starkey medium, as high chloride concentration avoided the direct measurement of COD, samples were diluted with distilled water and filtered for chloride elimination *(LCW 925, Hach Lange)*. Subsequently, COD measurements were performed according to the concentration ranges: from 15 to 150 mg O_2/L *(LCK 314, Hach Lange)* or from 100 to 2000 mg O_2/L *(LCK 514, Hach Lange)*. The HT15' heating cycle, comprising 15 minutes at 170°C, was performed in a HT200S oven *(Hach Lange)* and the COD value reading was performed with the DR 3900 spectrophotometer *(Hach Lange)*. This method was used for all media (real and synthetic).

II.2. Experimental devices

The experimental devices or systems used for experiments carried out in this work are divided into two types of electrochemical reactors, which are classified as macroBES and microBES, referring to their size. In the case of macroBES, a simple experimental scheme was used. The most complex development was only the construction of a microelectrode. For the micro BES, the development and protocols used for their construction are part of Chapter VI and the Annexes of this manuscript. Here only the materials and equipments required for their development are presented.

II.2.1. Macro BES

II.2.1.1. Electrodes

- Microelectrodes

The first microelectrode prototype was inspired from the PhD work of Diana Pocaznoi (Pocaznoi, 2012). 15 cm of metallic wire was threaded into a 5 mL plastic microtip (*Thermofischer*), leaving approximately, 3 cm of wire free at the top and bottom ends. The metallic wire was sealed into the microtip with an inert resin (*Epofix*) and was left to dry for 24 hours. Once ready, the upper end of the metallic wire was directly connected with a crocodile clamp to the potentiostat, while the lower end served as the microelectrode. In this first prototype, platinum (Pt) microwires (Ø=50µm, *Goodfellow*) were used to build working and counter electrodes and silver (Ag) microwires (Ø=50µm, *Goodfellow*) to make pseudo-reference electrodes. The main problem with this first design of microelectrode was that the connection between the crocodile clamp and the microwire was not strong. The wire was very fragile and prone to break. In addition, the resistance of the microelectrode could be improved by decreasing the length of the metal microwire in the whole electrode structure.

For these reasons, two improvements have been made to develop a second microelectrode prototype. To ameliorate the conductivity, 15 cm of copper wire (Ø=1.4mm) were welded to a 2 cm metallic microwire (Ø=50µm, *Goodfellow*). As with the first prototype, the welded copper wire-microwire system was threaded into a microtip and sealed with resin. In this case, the copper wire upper end was welded to a connector that served as the electrical connection to the potentiostat, while the bottom end served as the working electrode, obtaining the microelectrode assembly as seen in Figure II-2(A). Once finished, electrical conductivity was checked with a multimeter to ensure the correct functioning of the microelectrode assembly.

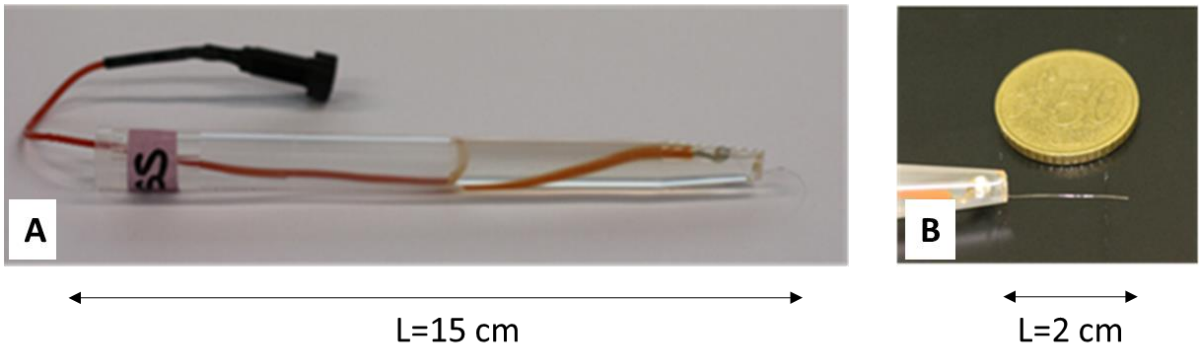

Figure II-2: Second prototype of lab-made microelectrodes. (A) Microelectrode full assembly. (B) Zoomed on the microelectrode end.

Microelectrodes of Pt, Ag and SS were rebuilt as indicated for the second prototype. For carbon cloth (CC) (Ø=250µm), the lower end could not be welded into the copper wire, therefore it was glued with a conductive carbon glue *(SPI Supplies).*

Before usage, Pt microelectrodes were cleaned under the flame with a Bunsen burner. For SS and Ag microelectrodes, no pretreatment was done In the case of CC, the electrodes were cleaned by immersion in successive baths: Distilled water: 20 min, NaOH 1M: 30 min, distilled water: 20 min, HCl 1M: 30 min, Distilled water: 20 min.

For calculations in which the area of the microelectrode was needed, the projection of the cylinder area was used.

- Reference and counter electrodes

Saturated calomel electrodes (*SCE, Radiometer Analytical*) were used as reference electrodes. For information, the standard SCE, available in the laboratory, had a diameter of 8 to 12 mm. These electrodes present a fixed potential of +0.248 V vs. SHE due to the Hg/Hg_2Cl_2 redox pair, which is in contact with a saturated solution of KCl. Before and after each experience, the potential of the SCE was measured against a high precision reference electrode (*SI Analytical*). Electrodes saturation with KCl solution was checked every two days in the course of the experiences and replenished if needed.

Counter electrodes were assembled by connecting Pt grids to Pt wires. Before usage, platinum grids were cleaned under the flame with a Bunser burner. In some cases, ITO electrodes were used as counter electrodes. For constructing them, a platinum wire was glued with a carbon conductive glue *(SPI Supplies)* to a conductive ITO transparent glass sheet *(Indium Tin Oxide coated glass, 8-12 Ω, Sigma Aldrich)*. Carbon conductive tape was added in the point of contact to ensure the connection. A layer of conformal coating *(High performance acrylic coating, Electrolube)* was sprayed on top of the conductive tape to protect the connection from the anolyte when submerged in the reactor. Once finished, proper electrical connections were checked with a multimeter.

II.2.1.2. Reactors

For macroBES, 550 mL Duran Schott-type glass transparent reactors (Figure II-3) were implemented. A twist off lid with four circular openings was set at the top of the reactors allowing the insertion into the anolyte of three electrodes. The reference was placed between the working and the counter electrode. For electrical connection, each electrode was connected to one of the three wires that form a potentiostat channel.

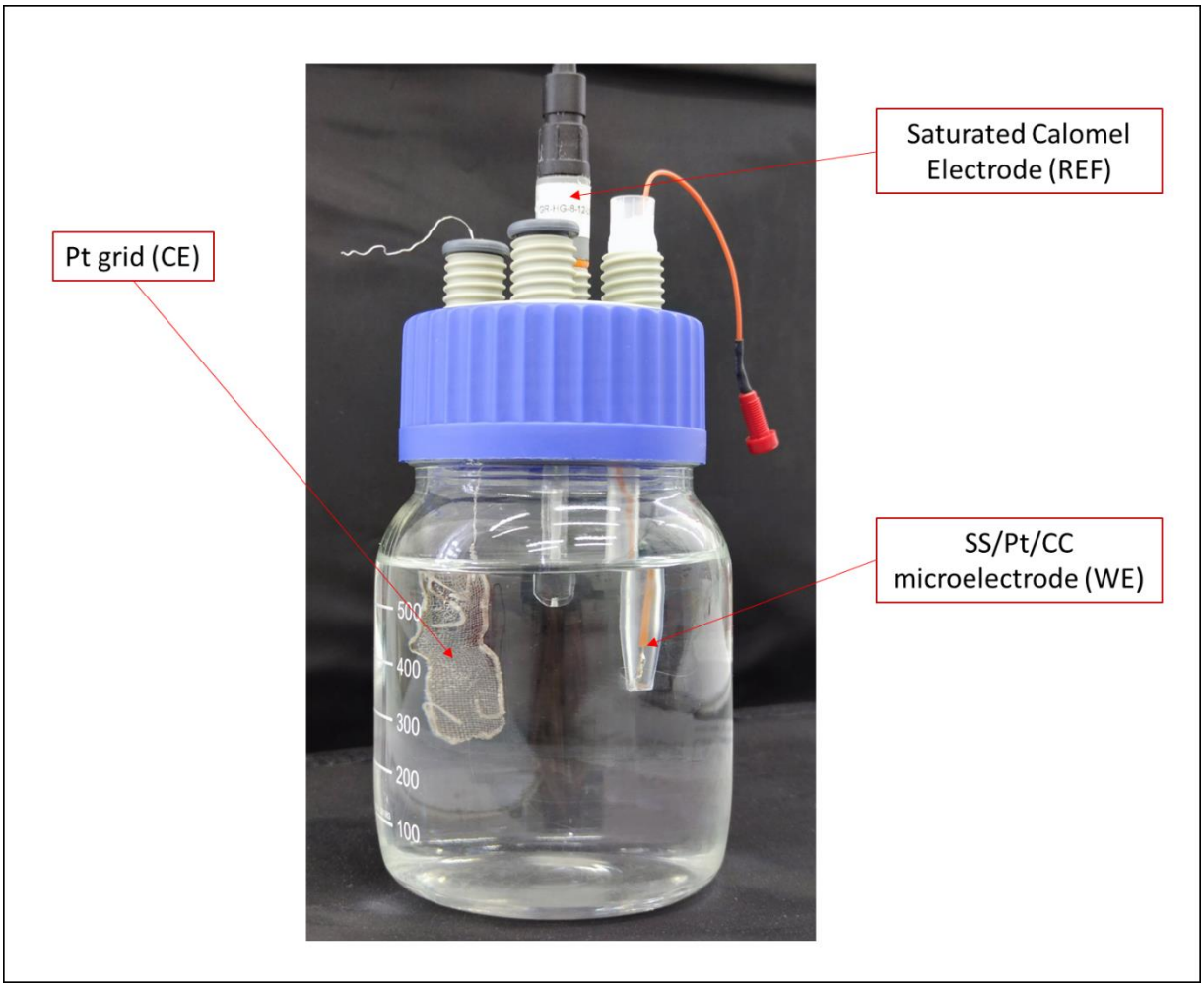

Figure II-3 : Image of a three-electrode system referred as MacroBES. The REF is placed between the CE and the WE.

Some slight differences exist between the macro BES used throughout the experiments, as described in Figure II-4:

- Standard configuration: In this set-up, the fourth opening in the lid was left closed most of the time. It can be used to measure substrate evolution in the anolyte and/or to purge the reactors with nitrogen when necessary. Regarding the electrodes, only the working electrode was a microelectrode. SCE were used as references and either a platinum grid or an ITO electrode were implemented as counter electrodes.
- Set-up (a): Similar to the standard configuration, only counter electrodes were Pt microelectrodes instead of Pt grids.
- Set-up (b): Here, the four openings of the coverlid were occupied. Two Pt microelectrodes were used as WE and CE, one Ag microelectrode was used as pseudo-reference, and a SCE was added as a REF in the fourth opening. The glass reactor had a side outlet through which it was possible to measure substrate concentration and/or purge the reactor with nitrogen.

The electrical connections for this set-up involved the use of two potentiostat channels. In the first, the three microelectrodes (Pt WE, Pt CE and Ag pseudo-ref) were connected. Later, an auxiliary channel was linked the Ag pseudo-ref (connected as a WE) and the SCE (connected as the CE + REF).

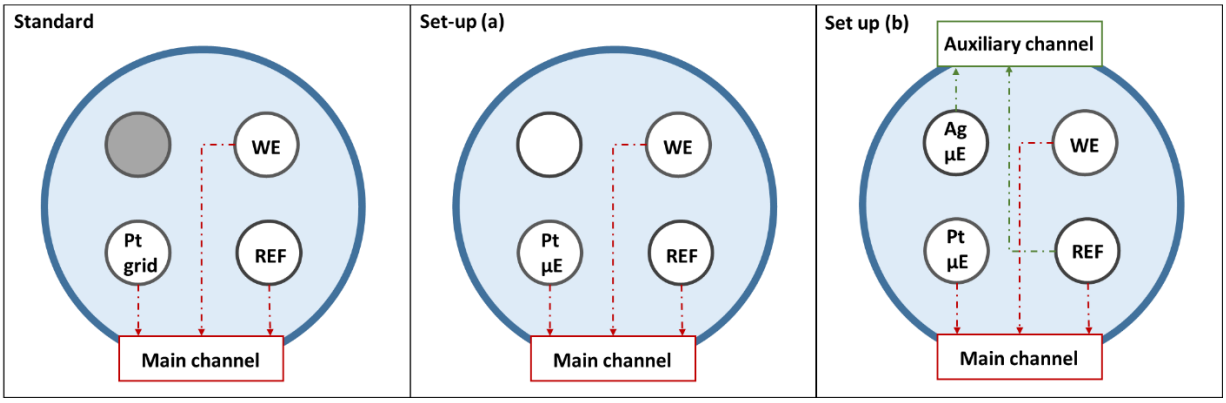

Figure II-4 : Top view of the lid scheme for macroBES showing the electrical connections between the electrodes and the potentiostat channel(s). µE refers to microelectrode.

II.2.1.3. Setting up macro BES experiences

When launching experiments, reactors were filled with the culture medium and inoculated. Then substrate was added and the reactor was placed on a magnetic plate at room temperature. With the help of a magnetic diver, the liquid mix was integrated within 5 minutes (with the exception of garden compost inoculum, as already indicated in section II.1.2. The lids were then placed to close the reactors and the electrodes were inserted into the corresponding openings.

Reactors were introduced into a water bath set at a constant temperature of 30°C during the course of the experiment and oxygen was purged for 20 minutes with nitrogen gas. Later, reactors were connected to the potentiostat and electrochemical techniques were launched. Every two to three days, a sample was taken from the inside of the reactors for COD analysis, and substrate was replenished according to requirements.

In the case of fed-batch operation, the reactors were disconnected from the potentiostat for a change in the anolyte. By opening the free opening in the reactor lid, a plastic tube was placed and the medium was pumped out. A new fresh batch of anolyte was consequently added through the same opening, allowing the reactor to be minimally disassembled. Oxygen was purged with nitrogen again and then, the connections to the potentiostat were reestablished.

II.2.2. Micro BES

The development of the microBES was carried out in a UV-protected room, as the materials used for their construction are sensitive to UV radiation. The materials and the equipment used are listed below:

- Materials

Table II-2 : List of materials that are needed for fabrication whether is a PDMS or OSTEMER microBES.

PDMS microBES	OSTEMER microBES
DF-3000 series dry film	WBR 2000 series dry film
Cyclohexane	Potassium Carbonate
PDMS	PDMS
	OSTEMER
	NOVEC

Table II-2 resumes the materials for the fabrication of the microBES. In the case of PDMS microBES, DF-3000 series dry film photoresist (*Nagase*) were used. Cyclohexane (*Sigma Aldrich*) was the developer solution. For OSTEMER microBES, WBR 2000 series dry film photoresists (*DuPont*) were implemented. Potassium carbonate at a ratio of 1:100 (*Carlo Erba*) was the developer solution.

Polydimethilsiloxane or PDMS (*SYLGARD™ 184 Silicone Elastomer Kit, Dow*) was prepared by mixing the pre-polymer and curing agent with a ratio of 10:1. PDMS was also necessary in a step of the OSTEMER chip preparation protocol. OSTEMER 322 Crystal Clear kit (*Mercene Labs*) was stored in a cold and dark environment until use. For OSTEMER preparation, a volume of bottle of hardener A was mixed with the base B in a ratio of 1.09:1.

NOVEC 1720 (*3M*) was implemented to modify the sticking properties of the molds for OSTEMER microBES.

Pt, Ag, SS microwires (Ø=50µm, *Goodfellow*) and ITO transparent glass sheet *(Indium Tin Oxide coated glass, 8-12 Ω, Sigma Aldrich)* were used as electrodes.

- Equipment

The main devices used for the construction of the microBES were:

- Hot roll laminator (*Mega Electronics*)
- Hot plate (*ATP GmbH*)
- Stove (*Jouan*)
- UV Led exposure masking system UV-KUB 2 (*Kloe*)
- Vacuum pump (*Edwards*)

II.2.2.1. Setting up micro BES experiences

- Batch or fed-batch experiments placed directly under a microscope objective

Teflon tubes (*VICI*) were inserted to the inlet and outlet of the microBES. In the inlet, a bubble trap (*Elveflow*) was connected to the feeding syringe containing the anolyte. Consequently, the microBES was placed and fixed under the microscope objective and the electrodes were connected to the potentiostat. The microchannel was filled with the anolyte by pressing the syringe manually. Electrochemical techniques were launched simultaneously with the use of the optical microscope as depicted in Figure II-5.

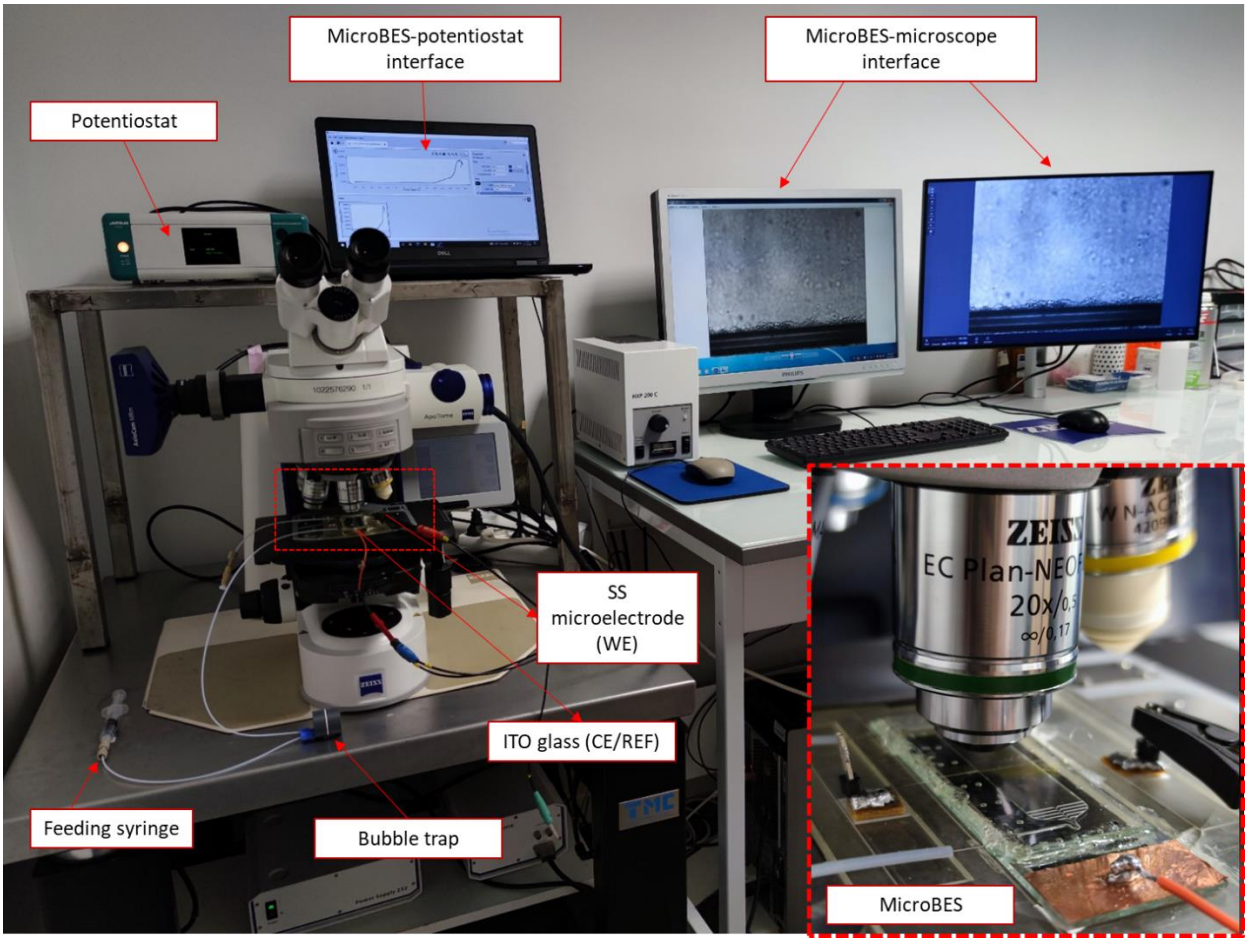

Figure II-5: Experimental platform, where the simultaneous application of electrochemical and microscopic techniques is depicted. The microBES is fed in batch mode with a syringe connected to a bubble trap.

- Continuous flow experiments

A micro-syringe pump system was used to work with microBES in continuous mode. The Nemesys module (*CETONI*) was equipped with 10 mL glass syringes (*Hamilton*) which vacuumed up the anolyte from a reservoir and then injected it into the microchannel. The QMixElements software (*CETONI*) controlled this process, where the aspiration and pumping rate were customized. The electrodes were connected to the potentiostat. The whole system was placed inside a stove in order to regulate the temperature, if needed as seen in Figure II-6.

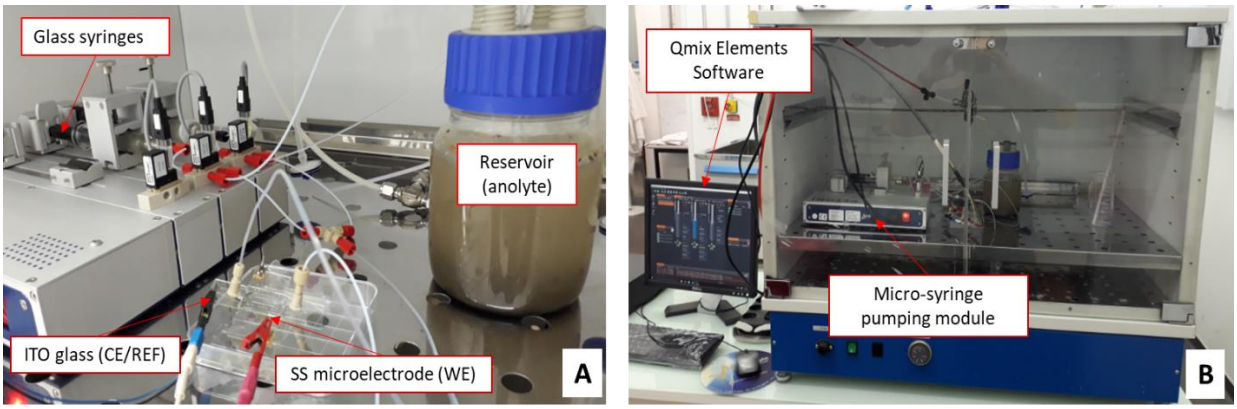

Figure II-6 : Experimental set-up for working in continuous feeding mode. (A) Inside the stove. A T-joint connects the two syringes that alternate to fill the cell. (B) Entire set-up. The potentiostat is behind the stove (not seen). A small hole was made in the stove door to insert the potentiostat channels for electrical connection.

II.3. Analytical techniques

II.3.1. Electrochemical techniques

For the application of electrochemical techniques, a 16-channel potentiostat (*BioLogic*) controlled by the EcLab software (10.37 version) was used in the macroBES. In the case of microBES, for some experiments, the EcLab software (11.26 version) controlled a 5-channel potentiostat (*BioLogic*). In other experiments, the NOVA 2.1 software commanded the one single channel µAutolab potentiostat (*Metrohm*).

II.3.1.1. Open circuit potential

No current nor potential is applied with this electrochemical technique. Only the open circuit potential (OCP) of the working electrode is be registered in time. This phase was commonly used as a preconditioning time for the electrodes to be at the electrochemical potential of the anolyte and it was generally applied at the beginning of the experiences for about 10 minutes before launching a chronoamperometry or a cyclic voltammetry.

II.3.1.2. Cyclic voltammetry

Cyclic voltammetry (CV) consists on recording the current produced at the working electrode while linearly varying its potential between two potential limits. Potential is scanned cyclically between the two limits. For each CV, three cycles were executed, where usually the first cycle was slightly different from the following two. For this reason, it was only the second cycle that was represented in the chapters presenting the experimental results.

Regarding parameters to be taken into consideration when launching a CV, the first correspond to the potential limits, which range between -0.6 V/SCE to 0.4 V/SCE. The second one is the scan rate that was typically fixed at 1 mV/s.

II.3.1.3. Chronoamperometry

This electrochemical technique was mainly used to form an EAB over the microelectrodes. This technique involves imposing a fix potential to the working electrode, which is applied against the reference electrode. As a response, the current produced at the working electrode is recorded as a function of time. The current is then normalized by dividing it by the projected surface of the working electrode, obtaining current density values in A/m^2. It is also possible when running this technique in the Ec-Lab software, to follow the evolution of the potential of the counter electrode in time, simultaneously with the polarization of the working electrode.

- Calculation of Coulombic efficiency

The ratio between the amounts of charge (Coulombs) produced at the anode (C_{anode}) and the amount of charge theoretically contained in the substrate (C_T) is known as Coulombic efficiency (CE). This CE indicates the part of the substrate involved to produce current in relation to the total substrate in the reactors.

$$CE = \frac{C_{anode}}{C_T} \quad \text{Eq. II-4}$$

C_{anode} is calculated by integrating current produced in the anode in time, which is given by the CA:

$$C_{anode} = \int_{t0}^{tf} I.dt \quad \text{Eq. II-5}$$

C_T represents the quantity of electricity theoretically provided by the substrate:

$$C_T = \frac{F.n.C.V}{M} \quad \text{Eq. II-6}$$

Where F is the Faraday constant (96.485 C/mol e^-), n is the amount of electrons produced by the oxidation of the substrate, C is substrate concentration in the anolyte (g/L), V is the liquid volume of the anolyte (L) and M is the molar mass of the substrate (g/mol).

II.3.1.4. Chronopotentiometry

This electrochemical technique of chronopotentiometry (CP) consists of imposing a constant current on the working electrode and measuring the potential in time as a response. This technique was used as an alternative method to form EABs and for electrodeposition processes.

- Formation of Ag/AgCl microelectrodes by electrodeposition

A protocol for forming Ag/AgCl references electrodes developed at LGC in the works of Rosas et al. was adapted here to Ag microelectrodes. First, a cleaning of the Ag microelectrodes was done in successive steps (Table II-3).

Table II-3 : Step-by-step of the Ag microelectrodes cleaning protocol.

Cleaning of Ag microelectrodes	Action	Time
Step 1	Distilled water	Just for rinsing
Step 2	NaOH 1M	5 hours
Step 3	Distilled water	Just for rinsing
Step 4	HNO_3 1M	1 minute
Step 5	Distilled water	Just for rinsing

Clean Ag microelectrodes were innmersed in a 0.1 M HCl solution saturated with KCl with a platinum grid as a counter electrode. Both electrodes were connected to the potentiostat; the silver electrode as the working electrode, and the platinum grid both as the reference and counter electrode, as seen in Figure II-7. In this case, a 150 mL reactor was used for containing both electrodes where two circular openings were drilled in the lid for electrode insertion. The electrodeposition was conducted at room temperature.

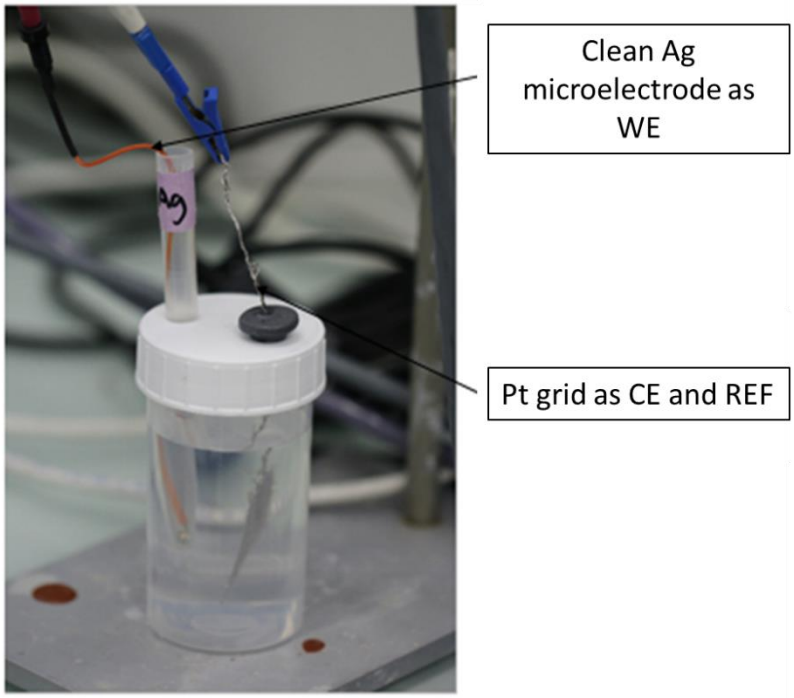

Figure II-7 : Experimental set-up to deposit AgCl over Ag microelectrodes.

A CP technique was executed for 10 minutes by applying a current of 0.188 mA to the Ag microelectrode. This value was extracted from the LGC protocol, where the current density applied was 6 mA/cm^2, therefore recalculated for a 2 cm microelectrode of a 50 µm of diameter. During the anodic deposition, the following reaction took place:

$$Ag_{(s)} + Cl^-_{(aq)} \leftrightarrow AgCl_{(s)} + e^- \quad \text{Eq. II-7}$$

To confirm the homogeneous formation of the AgCl layer over the Ag microelectrode and its thickness, the wires were observed under the microscope and later stored in KCl 1M until usage.

II.3.2. Microscopic techniques

II.3.2.1. Epifluorescence microscopy

Biofilms were first stained with acridine orange. This fluorescent stain is able to penetratre the membrane of cells while bounding to its DNA or RNA. Acridine orange stains both intracellular and extracellular nucleic acids, therefore giving a fair representation of the global biofilm structure.

First, electrodes were set in contact with an acridine orange solution at 0.01% (A6014 *Sigma*) for approximately 20 minutes and then carefully rinsed with distilled water. In theory, distilled water is only recommended in low volumes when the biofilm contains a minimum of salts or ions, because it may cause cell break-up by osmosis. For biofilms grown in media with high salt content, physiological water (NaCl 0.9 g/L) was used instead of distilled water. Once rinsed, the electrodes were left out in the open air and protected from light to dry for at least 24 hours before observation.

Biofilms were then imaged with a Carl Zeiss Axio Imager-M2 microscope (*Carl Zeiss*) equipped for epifluoresence with an HXP 200C light source and the Zeiss 09 filter (excitor HP450r HP450200 C light source). The objective used was the EC Plan-Neofluar 10x/0.30. Images were acquired with a digital camera (Zeiss AxioCam MRm) along the Z-axis and the set of images was processed with the Zen (*Carl Zeiss*) ® software (Blanchet, 2016; Oliot et al., 2017a). For each sample, two observations were made. The Zen software optimized the z-step of the stack. Biofilm thickness was measured with the toolbox of the Zen software, taking nine points per image. Biofilm growth rate was calculated as the increase of thickness divided by the time interval.

II.3.2.2. Confocal laser scanning microscopy (CLSM)

This type of microscopy was used for the observation and later quantification of the EPS of the EABs. A staining protocol was developed prior to the imaging of the biofilm EPS, described in the annexes (see Annex Table 1, Annex Figure 3, Annex Figure 4)

Therefore, EABs were stained using a mix of the four selected stains: Concavalin A tetramethylrhodamine conjugate (ConA-TMR, *Thermofischer Scientific*) for α-polysaccharides, Fluorescein isothiocyanate isomer I (FITC, *Merck*) for proteins, 1,1′-Dioctadecyl-3,3,3′,3′-tetramethylindocarbocyanine perchlorate (DiD oil, *Merck*) for lipids and 4′,6-Diamidino-2-phenylindole dihydrochloride (DAPI, *Merck*) for total cells. 25 mL of working solution was prepared in physiological water solution with the following concentrations: FITC at 0.05 g/L, DAPI at $1.05.10^{-4}$ g/L, Con-A TMR at 0.1 g/L and DiD'oil at 0.08 g/L. Microelectrodes were set in contact with the working solution for 30

minutes then carefully rinsed with physiological water solution. Once rinsed, the electrodes were left out in the open air and protected from the light to dry for at least 24 hours before observation.

- Image acquisition:

Each biofilm was observed under the confocal microscope Leica SP8-2017 (*Leica Microsystems*) with a HC PC FLUOTAR 10x/30 objective in dry immersion and a zoom value of 2.98. The gain of the photomultiplier tubes (PMT) of each channel was adjusted on the maximum possible value before the image pixels become saturated. The biofilm was scanned by obtaining images/slices of 1024x1024 pixels (390.24 µm x 390.24 µm) with the Leica Application Suite X: LAS X software (*Leica Microsystems*). For each sample, two stacks of horizontal plane images were taken from two randomly chosen areas. The LAS-X software optimized the z-step of the stack depending on the sample. Once the acquisition was completed, four different stack of images, one for each stain used were saved in a TIFF format.

II.3.2.3. Scanning electron microscopy (SEM)

EABs formed on microelectrodes and clean microelectrodes were observed at the SAP of the LGC under the guidance of Marie-Line de Solan, using a scanning electron microscope Leo 435 VP-Carl Zeiss SMT. Prior to observation, samples colonized by biofilms were treated following three successive steps: fixation, dehydration and metallization.

In detail, samples were firstly fixed in phosphate buffer solution (0.4 M, pH 7.4) containing 4% of glutaraldehyde. Later, samples were later dehydrated by immersion in increasing concentrations of acetone (50%, 70%, 100%), then in a 1/1 mixture of acetone and hexamethyldisilazane (HDMS), and finally in 100% of HDMS. The last batch of HDMS was dried until complete evaporation. Finally, a metallization step was necessary to avoid the accumulation of electrons on the surface of the biofilm, as this phenomenon is detrimental to the quality of the final image. The samples were then covered with a gold nanolayer (10/20 nm) by cold cathodic sputtering (Chong, 2018).

II.3.2.4. Differential interference contrast microscopy (DIC)

The microbial cells and biofilm in the microBES was imaged with the Carl Zeiss Axio Imager-M2 microscope (*Carl Zeiss*). In this case, the bright-field filter was used where illumination light was transmitted through the sample and contrast was generated by absorbing the light in the denser areas.

The Time Series module (*Carl Zeiss*) was implemented in the Zen software in order to execute the acquisition of stacks of images. This module contains the Experiment Designer functionality where the time between two stacks of images, the duration of the acquisition and the interval between images of one stack can be customized and programmed. It must be clarified that stacks here refers to a series of images obtained in the course of time and not a z-stack as obtained for epifluorescence and CLSM.

Once the acquisition was finished, the software presented the option of exporting the recorded images as stack of individual images or as a time-lapse in the form of a video.

For the biofilm average thickness measurement, nine thickness values of the biofilm along with the microelectrodes were taken from the DIC microscope images with the toolbox of the Zen software.

II.3.3. Microbial population analyses

The following analyses were done in collaboration with Dr. Wafa Achouak from the LEMIRE Laboratory (CEA Cadarache, France).

- Characterization of the microbial communities colonizing the microelectrodes:

Microelectrodes containing the EABs were stored in 2 ml Eppendorf tubes. 150µL of PCR grade water and a spatula tip of 425-600 µm glass beads (G8772, *Sigma*) were added to the tubes. A negative control was made with only water and beads. Two one-minute mechanical grindings with a robot (Fast-prep 24 MP Biomedicals, *Thermofischer Scientific*) at a maximum speed of 6.5 m/s were performed to loosen the biofilms formed on the surface of the microelectrode. The clean microelectrode was retrieved from the tube and the remaining suspension was subjected to two thermal shocks by alternating ice and water bath at 95°C for 1 min each time, in order to lyse the cells and release the DNA.
The 16S amplification was then performed on 1µL of the suspension with the GoTaq Flexi G2 enzyme (*Promega*) with the primers:
Genewiz515Fmod:5'-
ACACTCTTTCCCTACGACGCTCTTCCGATCTGTGYCAGCMGCCGCGGTAA-3'
Genewiz806Rmod:5'-
GACTGGAGTTCAGACGTGTGCTCTTCCGATCTGGACTACNVGGGTWTCTAAT-3'
35 cycles of PCR were carried at a temperature of 55°C. The primers were designed to contain overhang compatible sequences with Nextera XT index (*Illumina*). The purified amplicons were sequenced using the MiSeq platform (*Illumina*).

- Post data treatment

Microbiome bioinformatics were performed by the open-source software QIIME2, version 2021.11 (https://qiime2.org) (Bolyen et al., 2019). Raw reads were demultiplexed, quality-filtered, denoised and chimera-checked using DADA2 (Callahan et al., 2016). DADA2 uses a parametric model to infer true biological sequences from reads. The model relies on input read abundances (true reads are likely to be more abundant) and the pairwise similarity between sequences. Sequences were aligned using MAFFT (Katoh and Standley, 2013), and were used to construct a phylogeny using FastTree (Price et al., 2009). The taxonomic annotation of the resulting amplicon sequence variants (ASVs) was assigned using the feature-classifier command with default parameters in QIIME2 and sequences were matched against the

Greengenes 13_8 database (McDonald et al., 2012). Finally, scaling with ranked subsampling (SRS) curves (Beule and Karlovsky, 2020) were drawn to determine whether the sequencing depth was sufficient to represent the true diversity of the samples.

II.4. Computational techniques

II.4.1. Post-processing of CLSM images

The post-treatment of the CLSM images for the quantification of the EPS components was executed on the basis of two protocols. In the first, ImageJ quantified pixel images with a manual thresholding. In the second one, the protocol was considerably automatized to allow a larger amount of images to be treated by using MATLAB algorithms.

II.4.1.1. Pixel quantification of CLSM images in image J

Once the confocal microscope acquired the images, each stack of images (four stacks for one sample) was converted after into a 3D structure by the LAS-X software (*Leica Microsystems*). Subsequently, the 3D structure was transformed into a 2D image projection. 2D images were treated with the ImageJ software.

First, the color image was transformed into an 8 bit-image to convert it to greyscale. Then, with the threshold tool, a threshold value was manually selected. This allowed labeling each pixel as marked or empty (biofilm or not biofilm). After, the software showed the amount of empty pixels by image, and the calculation of marked pixels per image was calculated as the difference between total pixels and empty pixels.

The percentage of each EPS component was determined. An example is given for proteins based EPS:

$$Proteins\ (\%) = \left(\frac{FITC\ labeled\ pixels}{FITC\ labeled\ pixels + DAPI\ labeled\ pixels + DID'oil\ labeled\ pixels + Con{-}A\ labeled\ pixels}\right) * 100\% \quad \text{Eq. II-8}$$

II.4.1.2. Pixel quantification of CLSM images in MATLAB

This method for image treatment and EPS quantification was developed during the internship of Juan Diego Carvajalino Olave in 2022. Images were processed with MATLAB (*MathWorks*) and then a statistical analysis was performed. The complete MATLAB algorithm is found in the Annexes as "PixelQuantification".

The TIFF images obtained in section II.3.2.2. were treated with MATLAB. For clarification, a single image of 1024x1024 pixels was loaded as a single matrix of 1024x1024 containing pixel information where each value (from 0 to 1) represented the emission light intensity detected by the confocal microscope.

After importing the stack of images into MATLAB, three steps were followed:

i) Removal of the images corresponding to the beginning and end of the stack, since they correspond to the images close to the glass slides that contain the biofilm.

ii) Noise removal for each image, if needed

iii) Automatic thresholding and pixel quantification

First, a differentiation between the biofilm and the background was performed because the biofilm was placed between two glass slides at the time of the observation under the microscope (step i). To remove the images corresponding to glass slides, two options were available: manually, specifying the images corresponding to the glass support, or automatically, removing them by an intensity analysis as shown in Figure II-8 (A). Each image/slice was obtained at a different depth, where a typical slice of a glass and a biofilm is shown in Figure II-8 (B, C).

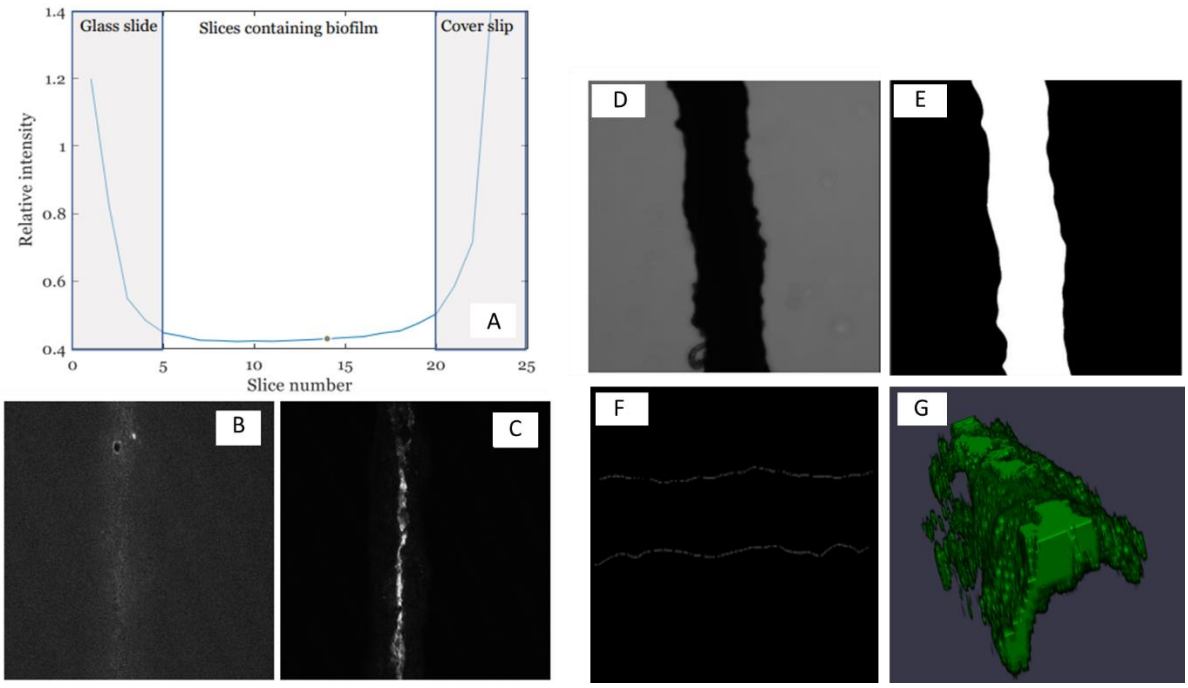

Figure II-8 : (A) Glass slide identification in a CLSM stack of images. Relative intensity of the background portion of each slice of a biofilm stack. (B) Original image/slice at a depth located in the top glass slide. (C) Original image/slice at a depth located in the biofilm. (D) Original slice obtained from the transmission (bright light) channel. (E) Binarization of the slice shown in D. (F) Biofilm rotation for thickness measurement. (G) 3D MATLAB structure for extracellular proteins of the biofilm.

Secondly, the biofilm was rotated to its horizontal position and afterwards its thickness was quantified by measuring the distance between the upper and lower biofilm edges (see Figure II-8 (F)) where all its length was considered for the calculation of the average thickness, and then the theoretical microelectrode diameter (50 µm) was subtracted. The background pixels were used to quantify and remove noise (step ii) from the whole slice using the gamma correction function:

$$Pv = (Pv_0)^{\gamma} \quad \text{Eq. II-9}$$

Where Pv and Pv_0 refers to the corrected and not corrected pixel value, and γ is the gamma correction factor. Gamma values from 1 to 5 (0.1 step) were tested for each slice until more than 99.5% of the pixels have a value lower than (8/255). This combination of values, the percentage of pixels and the gamma limit value, was set by the user after testing with several images. The idea was that the background of the image did not have any noise, meaning pixels values close to zero in the background (no biofilm). A gamma value lower than one, reduced the intensity of low intensity pixels in higher proportion as shown in Figure II-9, as it accounted for most of noisy values without affecting high intensity values from the biofilm fluorescence.

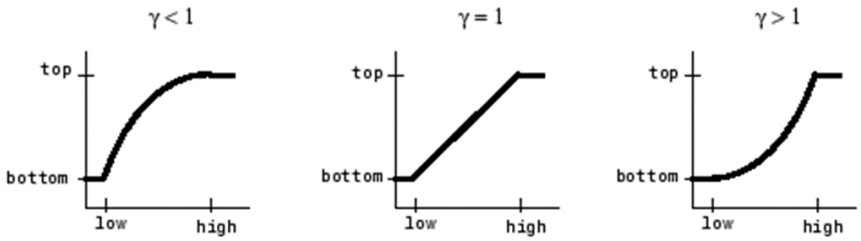

Figure II-9 : Gamma correction. The x-axis represents the original intensity values, while the y-axis shows the corrected intensity values. Extracted from: https://www.mathworks.com/help/images/gamma-correction.html

For step ii), once the noise was removed from the images, it was needed to decide which threshold value determined what was biofilm and what was not in the images. Each image was represented by matrices where pixel values ranged between 0 and 1. As an example, a threshold value of 0.3 would have replaced all values greater than 0.3 by 1 (classifying them as biofilm) and the rest of them by 0 (classifying them as background, not biofilms). The thresholding algorithm, known as the iterative selection method (Lewandowski and Beyenal, 2013) was used here. This histogram-based algorithm assumes that the best threshold value corresponds to the mean value of all the intensity values found in the image. The before and after binarization can be observed in Figure II-8 (D) and (E) respectively.

After selecting this threshold value and binarizing the whole stack, the last step was counting the number of 1 (biofilm) on each binarized image. The only parameters used in the whole quantification algorithm (steps i, ii, iii) were the ones mentioned for the noise reduction step. The noise reduction algorithm was skipped for channels with low noise according to the criteria specified in step ii.

- Statistical analysis:

The correlation of each EPS component with the current density were analyzed using an analysis of variance (ANOVA) (Guo et al., 2021). Its significance is expressed in p-values, where most significant factors have low p-values. A value of p = 0.05 is often used as a threshold value to categorize between significant and non-significant effects. For example, in a series of experiments, the protein EPS content can be correlated with current density produced by the EAB. If p-value from the ANOVA analysis is

lower than 0.05, this means that the protein EPS content has a significant effect (whether positive or negative) on current density. If it is higher than 0.05, it does not have a significant effect.

II.4.2. Post-processing of optical microscopy image stacks

Stacks of images obtained in time from DIC microscopy in the microBES, as explained in section II.3.2.4. , were post-treated with MATLAB algorithms to determine quantitatively the displacement of bacterial cells (see Annexes routines: CalculMeanImage, ImageSubstraction, OpticalFlow). For this purpose, the optical flow technique was selected, as it is suitable for describing the motion patterns of a group of objects. In order to apply it, two conditions must be met: (i) the series of images have to be acquired with a small interval of time between them, in order to ensure that the pixel intensities of the object are constant between consecutive images. (ii) The displacement of the object between one image and the next one must be also short as to avoid losing information about their position (Shah and Xuezhi, 2021).

If the two conditions are met, optical flow can be expressed by the following equation:

$$I(x, y, t) = I(x + \delta x, y + \delta y, t + \delta t) \quad \text{Eq. II-10}$$

Where I is the same pixel intensity in the first image and in the consecutive one; t, x, y are the time and spatial coordinates of the object in the first image; δt is the time interval between two images; δx is the displacement of the object in the x-axis and δy the displacement in the y-axis.

If Taylor series approximation is applied to solve equation $I(x, y, t) = I(x + \delta x, y + \delta y, t + \delta t)$ Eq. II-10, the following is obtained

$$\frac{\partial I}{\partial x}\delta x + \frac{\partial I}{\partial y}\delta y + \frac{\partial I}{\partial t}\delta t = 0 \quad \text{Eq. II-11}$$

And Eq. II-11 is divided by delta t,

$$\frac{\partial I}{\partial x}u + \frac{\partial I}{\partial y}v + \frac{\partial I}{\partial t} = 0 \quad \text{Eq. II-12}$$

Therefore,

$$u = \frac{\delta x}{\delta t};\ v = \frac{\delta x}{\delta t} \quad \text{Eq. II-13}$$

Where $\frac{\partial I}{\partial x}, \frac{\partial I}{\partial y}, \frac{\partial I}{\partial t}$ represent the intensity gradients along x,y axis and time respectively.

Optical flow is resumed in solving equation Eq. II-13, which determines movement over time. As to solve the equation, the MATLAB optical flow algorithm developed Sun et al. (2010) was implemented

for particle velocity calculation, together with the PIVMAT toolbox created for particle image velocimetry as to obtain the graphic bacterial displacement velocity fields.

Chapter III : Electroactivity of multi-species EABs on microelectrodes formed from different types of inocula in macroBES

III.1. Introduction

The electrochemical performance of bioanodes is widely described in literature, where in general, current density of multi-species EABs on anodes typically reaches a maximum value that drops beyond 50% of the maximum after a tenth days of operation. It is thought that the loss in the electroactivity on EABs is the main bottleneck to overcome in order to improve the performances of BES. Most experiments carried out in bioanodes do not investigate in depth the reasons why they lose their electroactivity over time, and this is mainly due to a methodologic approach. In general, bioanodes are studied on electrodes and reactors that are thousands of times larger than the size of bacteria, in which the object of study is clearly lost. In addition, in these types of experimental setup it is implied that in order to study the multi-species EAB, the latter is exposed to destructive techniques, where much information is also lost with respect to its active and living state.

This is the reason for the interest in developing a transparent microBES for the study of multi-species EABs. These kind of devices facilitate the approach to the electrode-EAB interface, allowing the access to local phenomena such as cell-to-cell and cell-to-electrode interactions, which would not be possible in a macroBES. In addition, transparency enhances the combination of microBES with real-time microscopic techniques, to live monitoring the processes taking place at all the stages of EAB formation.

At the time of starting the thesis, a Post-Doc participating in the MICROBE project was developing the first prototype of a microBES in the laboratory by microfluidic techniques. This transparent microfluidic cell was composed of a three-electrode system, consisting of two platinum (Pt) microelectrodes (50-µm diameter) as working and counter electrode, and a silver (Ag) microelectrode as the reference electrode. Pt microelectrodes (50-µm diameter) had already been used to successfully form EABs from garden compost in the thesis of D.Pocaznoi in macroreactors (Pocaznoi, 2012). As the microBES was designed for the study of EABs, the first objective was to form an EAB on the working electrode of this reactor.

The formation of an EAB on a microelectrode involves that the microelectrode must fit into a microfluidic reactor (or microBES), where its volume is in the microliter scale and that the biofilm formed on the microelectrode should express a similar electroactivity to that classically observed when multi-species EABs are formed on macroelectrodes. The aim is to reproduce this behavior described in section I.2.4.

As the microBES was not completely operational, and the control of certain parameters such as temperature, substrate concentration and proper functioning of the Ag reference electrode could have been challenging at that point for the formation of an EAB, it was decided to take the work of Pocaznoi as reference and to start working in a classical three-electrode system in a 550 mL reactor. In this reactor, the working electrode (macroelectrode) was replaced for a Pt microelectrode. The objectives were to:

- Form an EAB in the microelectrode that showed a comparable electroactivity to that reported in macroelectrodes.
- To standardize the protocol of EAB formation as to obtain the expected electroactivity in a reproducible way. To this end, a series of experiments were carried out successively, being the source of electroactive microorganisms (inoculum) the main parameter.

Table III-1 resumes the experimental conditions of each test. All experiments were conducted at a controlled temperature of 30 °C and sodium acetate was selected as the electron donor. The main division was made according to the source of electroactive microorganisms used (inoculum). For activated sludge (AS), four tests were carried. In Test 3.1, 3.2 and 3.3, the potential of the working electrode (E_{WE}), the inoculum size and the effect of working on a fed-batch system were tested. In those three tests, "synthetic wastewater I" was used. The composition of the synthetic wastewater can be found in section II.1.1. In Test 3.4, "synthetic wastewater I" was replaced by residual wastewater, whereas stainless steel (SS) and carbon cloth (CC) were tested as other working electrode materials. In Test 3.5, garden compost was implemented as inoculum in another synthetic medium ("Synthetic wastewater II"). In this case, the anode potential value was taken from bibliography data. For SMS, "Synthetic wastewater II", a low conductivity medium, and Starkey medium with 45 g/L of NaCl were tested as culture medium. The working electrode potential was also determined from bibliography.

Table III-1: Summary of experimental conditions.

Inoculum	AS				Garden compost	SMS
Temperature	30°C					
Substrate	Sodium acetate					
Culture medium	Synthetic wastewater I			Residual wastewater	Synthetic wastewater II	Starkey medium/Synthetic wastewater II
N° of Test	Test 3.1	Test 3.2	Test 3.3	Test 3.4	Test 3.5	Test 3.6
Time (d)	10 to 12	8	10	24 to 30	29	22 to 55
N° of reactors	8	8	8	9	4	8
E_{we} vs. SCE	-0.25,-0.1, 0.05, 0.2	-0.1	-0.1	-0.1	-0.2	0.1
Inoculum size % V/V	0.5	0.5, 2.5, 5, 10	0.5	0.5	5	5
Operation mode	Batch	Batch	Batch/Fed-batch	Fed-batch	Batch	Batch
WE material	Pt	Pt	Pt	Pt, SS, CC	Pt, SS	Pt, SS
Reactor type	Set up (a)/Set up (b)	Standard	Standard	Standard	Standard	Standard
Tracking of E_{CE}	No	No	No	No	Yes	Yes
Test of Ag microelectrodes	Yes	No	No	No	No	No

Meanwhile, referring to the microBES prototype already developed, the stability of Ag microelectrodes was highlighted in this chapter. As fundamental requirements, a reference electrode in a microBES must comply with the following: first, it must fit within the volume of the order of microliters; second, it must be able to measure the potential of the working microelectrode; and third, its potential must be stable (at least during two weeks) over time when in contact with the anolytes under study. In Test 3.1., the evolution of the Ag microelectrodes potential in 550 mL reactors was tested. In addition, the further idea of moving from a three-electrode system to a two-electrode system in the microBES began to be considered, as developed in section III.2.4. of this chapter. With that motivation, the potential of the counter electrode (E_{CE}) was tracked in Tests 3.5 and 3.6.

III.2. Results

III.2.1. Experiments with activated sludge (AS) as inoculum

III.2.1.1. Test 3.1: Effect of the polarization potential on Pt microelectrodes/Evaluation of Ag microelectrodes as pseudo references

The purpose of this first test had two objectives. Firstly, to assess the effect of the potential of the working electrode on the formation of an EAB over Pt wire microelectrodes, in order to define an optimal anode potential. Secondly, to determine the stability of Ag microelectrodes as pseudo references

for applications in microBES. For this end, the experimental set-ups (a) and (b) described in section II.2.1.2. were implemented.

In the reactors with the set-up (a), the working electrode was polarized at the four selected potentials (-0.25, -0.1, 0.05, 0.2) versus a saturated calomel electrode (SCE). The reactors with the set-up (b) had initially the working electrode polarized at the four polarization potentials (-0.25, -0.1, 0.05, 0.2), yet in this case versus the Ag microelectrode. To measure the evolution of the Ag microelectrode potential in time, a SCE was added into the reactors as a fourth electrode. As in a period of two days the deviations of the potential of the Ag microelectrode against the SCE were considerable, it was decided to abandon this strategy and to polarize the working electrodes versus the SCE, as done in set-up (a). The evolution of the potential of the Ag microelectrode in the liquid environment was followed by an open circuit potential (OCP) technique.

- Effect of the polarization potential

Figure III-1 shows the current density curves for duplicates at each applied potential. Experiments launched in set-up (a) and in set-up (b) operated respectively to 12 and 10 days. Acetate in a concentration of 20 mM was added daily to the reactors, with an increase to 40 mM to avoid possible substrate depletion before weekends (~3 days period).

Results from Figure III-1 showed that no significant current density was produced whatever the applied potential. Current density values were extremely low compared to the expected ones. Pt microelectrodes with a similar design (Ø=50 µm) polarized at -0.2 V/SCE used as anodes in garden compost leachate fed with acetate giving a maximum current density of 19 A/m^2 (Pocaznoi et al., 2012b). However, for this set of experiments, the maximum value of current density was only of 0.0044 A/m^2. As the most similar current production curves were for the applied potential of -0.1 V/SCE (Figure III-1 (B)), this potential value was the one applied in the following two tests (3.2 and 3.3).

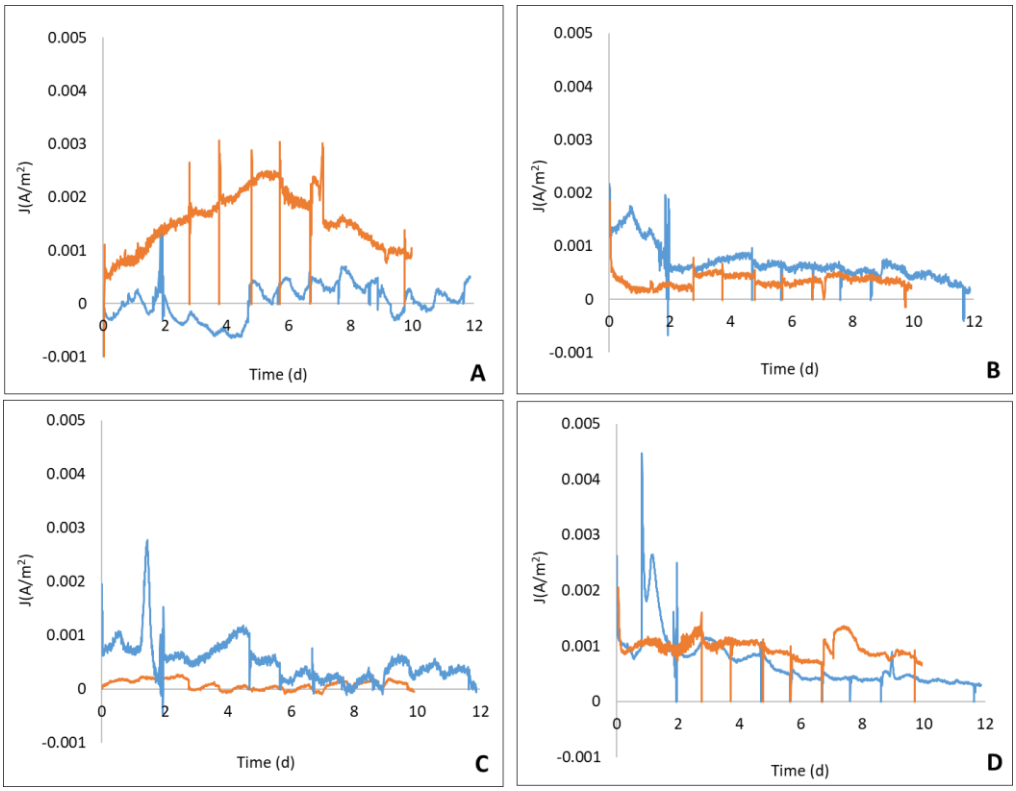

Figure III-1: Evolution of current density in time for duplicates for Pt microelectrodes different polarization potentials: (A) -0.25 V/SCE, (B) -0.1 V/SCE, (C) 0.05 V/SCE, (D) 0.2 V/SCE.

Certain decisions at the time of conducting the experiments may have contributed to the very low current values obtained. Soluble oxygen was not purged from the anolyte at the start of the experiments, probably competing with the polarized electrode, therefore acting as the final soluble electron acceptor. Another cause could be the use of a microelectrode as the counter electrode (Beyenal and Babauta, 2015). In the three-electrode system, electrons flow from the Pt microelectrode working electrode to the Pt microelectrode counter electrode. It is possible that the small size of the microelectrode limited the current passage in the circuit, affecting the electrochemical reactions occurring in the working electrode.

Furthermore, acetate concentration was not adjusted, as at that time the validation of a measuring method for acetate concentration (i.e. enzymatic measurement, chemical oxygen demand) in the reactor was still in development. Therefore, it was not possible to know whether the bacteria in a planktonic state inside the reactors minimally consumed the substrate. As a first hypothesis, the impossibility to form EABs over the Pt microelectrodes did not seem to be linked to the polarization potential value since EABs were proved to be formed under a wide range of applied potentials (Rimboud et al., 2014).

- Ag microelectrodes as pseudo-references for preparing microBES

Due to the impossibility of using commercial SCE references in microBES because of their 12 mm diameter, Ag microelectrodes were firstly evaluated as possible pseudo-references. A pseudo-reference refers to a metal wire submerged in the same solution of the working electrode, which is not in

equilibrium with their redox couple. In the case of Ag, the potential obtained is due to the presence of compounds formed on the metal surface, such as Ag oxides (Torriero, 2019).

When Ag microelectrodes were used as pseudo-references in the first two days of experiment, their potential values were not stable at all (Figure III-2). Indeed, in most cases, the polarization of the working electrode versus the Ag microelectrode had to be shortly stopped as a rapid draft towards more negative potentials was observed. A longer monitoring of the evolution for the Ag microelectrode potential as a pseudo-reference (Figure III-2(A)) confirms the wide range of potential the electrode, from 0.5 V/SCE to -2 V/SCE. One of the reasons why the potential may have been affected is the presence of soluble oxygen in the medium, which can modify the equilibrium between Ag oxides present on the surface of the metal. In any case, after two days, it was decided to stop using the Ag microelectrode as a pseudo-reference and just follow the evolution of electrode potential in time versus the SCE.

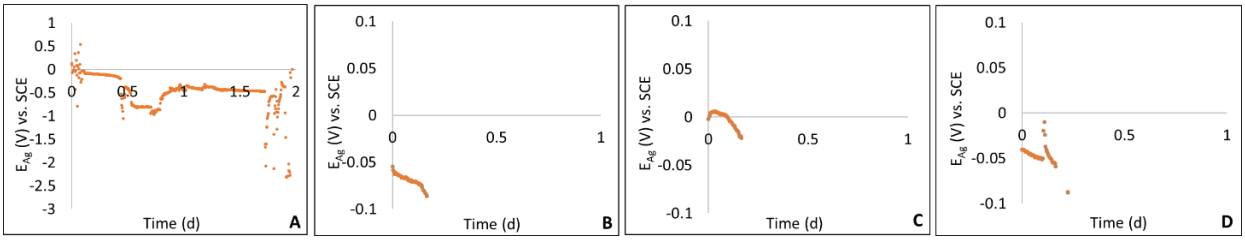

Figure III-2: Evolution of the Ag microelectrode potential against a commercial SCE. Letters correspond to polarization potentials of the Pt working electrode: (A) -0.25 V/SCE, (B) -0.1 V/SCE, (C) 0.05 V/SCE, (D) 0.2 V/SCE.

Figure III-3 shows the variation of the potential for the Ag microelectrodes after day 2. The delta of potential for the Ag microelectrodes was the following: 56 mV (A), 167 mV (B), 31 mV (C) and 84 mV (D). The delta of potential was calculated as the difference between the initial and final potential value in the 10-day period, discarding the fast initial drop for (B) and the fast initial increase in (D). Consequently, the potential closely depended on each microelectrode and on the anolyte, which was identical at the beginning and might have evolved depending on the metabolic activity and the microbial species that predominately developed. In conclusion, it was not possible to apply this type of pseudo-reference for a use in synthetic wastewater inoculated with AS. Thus, alternatives that are more suitable are presented in Chapter VI.

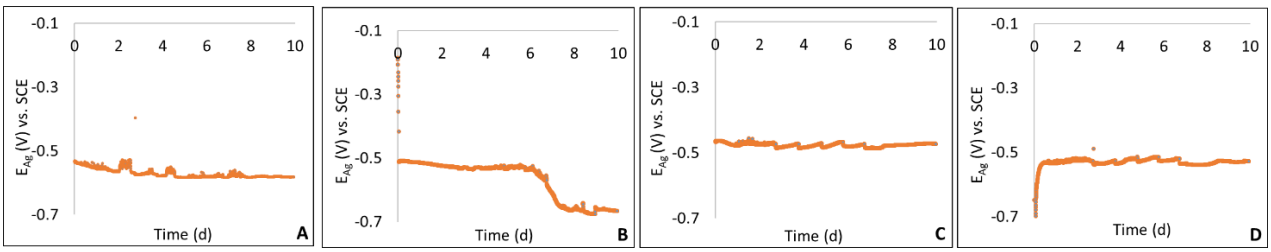

Figure III-3: Evolution of the Ag microelectrodes potential against a commercial SCE. Letters correspond to polarization potentials of the Pt working electrode: (A) -0.25 V/SCE, (B) -0.1 V/SCE, (C) 0.05 V/SCE, (D) 0.2 V/SCE.

III.2.1.2. Test 3.2: Effect of the inoculum size for initiating biofilm formation on Pt microelectrodes

The question that arose after the first experiment was whether the inoculum size was probably not large enough for electroactive bacteria to initiate biofilm formation on the microelectrode. The inoculum size refers to the quantity of inoculum added into the reactors and is expressed as the volume-volume ratio between the inoculum added to the reactor and the volume of the synthetic medium. As the inoculum was not composed of a single specie or a controlled cocktail of bacteria, it was not exactly known whether the amount of electroactive bacteria was proportional to its size. The idea of this experiment was to work with larger inoculum sizes as to generate more chances for the microelectrode to be colonized by electroactive bacteria

The selected values for inoculation ranged from 0.5% to 10.0% V/V ratio for synthetic wastewater. Therefore, the choice of this range was intended for maintaining an applicable low concentration in future microfluidic systems, while at the same time avoiding large deviations in the inoculum microbial population. Regarding the experimental set-up, a platinum grid replaced the counter electrode in order to avoid any possible current limitation. In this experiment, the polarization potential was -0.1 V/SCE. Oxygen was not purged in the anolyte before starting the polarization.

Eight reactors were launched in duplicates during eight days where the inoculation size was of 0.5%, 2.0%, 5.0% and 10.0% V/V for the synthetic medium (Figure III-4). Nevertheless, there was no evidence that the inoculum size had an influence on current production. Inoculating at 0.5% with AS would seem an adequate ratio to set in future experiments, opening up the possibility of applying diluted sludge in microfluidic systems.

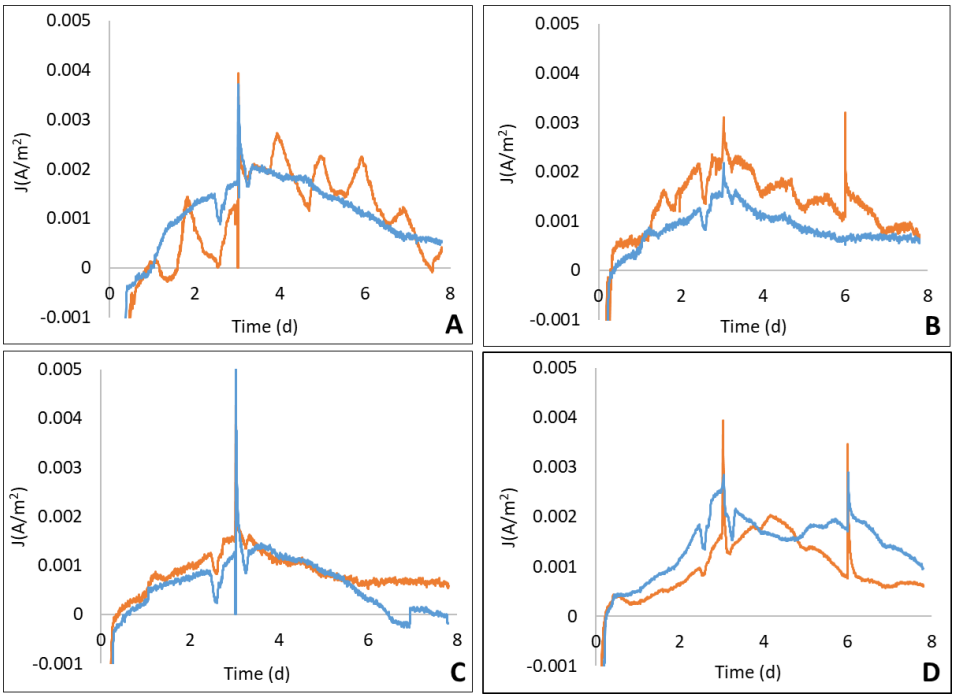

Figure III-4: Evolution of current density in time for duplicates conducted at -0.1 V/SCE on Pt microelectrodes. Letters correspond to inoculum size (% V/V) for synthetic wastewater: (A) 0.5, (B): 2.0, (C) 5.0, (D) 10.0.

In this experiment, substrate concentration was measured and adjusted daily to 20 mM of acetate, except for weekends where no measurement and adjustment was done. Figure III-5 shows the evolution of acetate concentration for every duplicate. At day 3, before a weekend, concentration was taken to 40 mM in all reactors, except for one duplicate in Figure III-5 (A) where acetate concentration was 60 mM. Between day 3 and day 6, no measurements or adjustments were done; therefore, there was no quantification of the kinetics of acetate consumption in those days. Starting from day 6, acetate concentration remained quite stable when the inoculation size was 0.5%, whether for the rest of the series consumption increased, but at a lower rate than at the initial days.

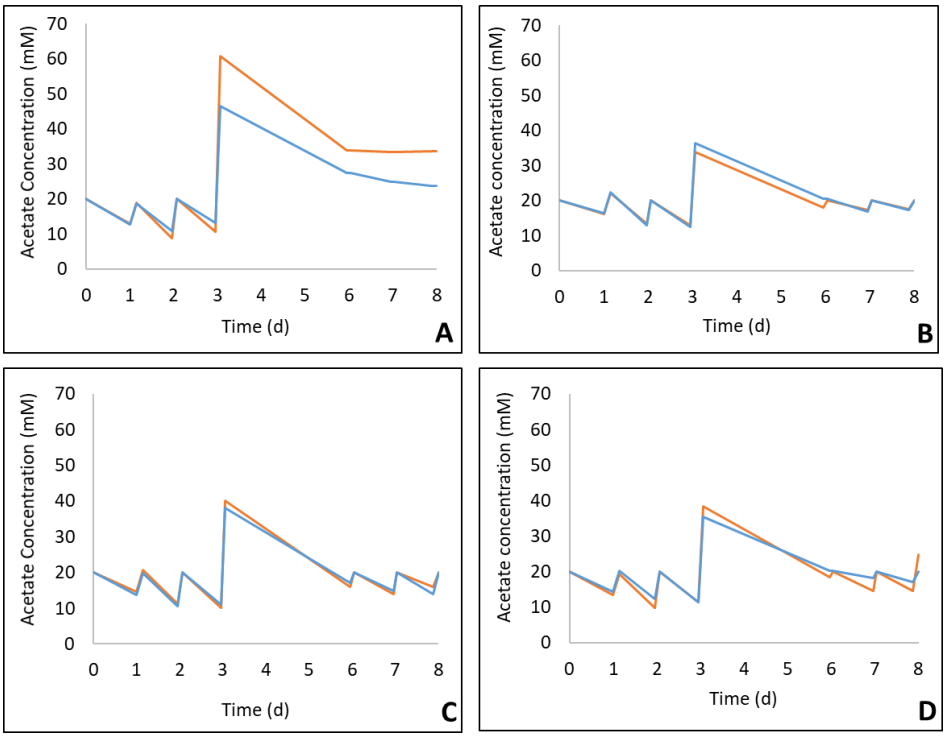

Figure III-5: Acetate concentration in the anolyte. Acetate was replenished on a daily basis to 20 mM (except for day 3). Letters correspond to inoculum size (% V/V) for synthetic wastewater: (A) 0.5, (B): 2.0, (C) 5.0, (D) 10.0.

The calculation of coulombic efficiency can be useful to represent the ratio between the acetate actually consumed by electroactive bacteria (measured via the amount of electrons passing through the electrode) and the overall acetate consumed by all the microorganisms present in the anolyte (electroactive + non electroactive aerobic and anaerobic bacteria). However, the large size of the volume of the reactor (550 cm^3) in contrast to the very small surface area of the Pt microelectrode wire (0.031 cm^2) led to very low coulombic efficiency values. Therefore, it was very likely that a very small fraction of acetate was used as electron source by electroactive bacteria that could attach themselves to the Pt microelectrode surface. On the other hand, planktonic bacteria present in the anolyte probably consumed a higher amount of substrate as a carbon source for other functionalities. By observing the acetate concentration trend after day 6, acetate consumption was more marked for inoculum sizes of 5.0% and 10.0%, meaning that probably the acetate planktonic consumption was higher at a larger inoculation size.

After eight days, the microelectrodes were retrieved from the reactors for epifluorescence microscopy imaging. Figure III-6 shows that some bacteria deposited on the surface of the microelectrode, however in any case, a biofilm was formed.

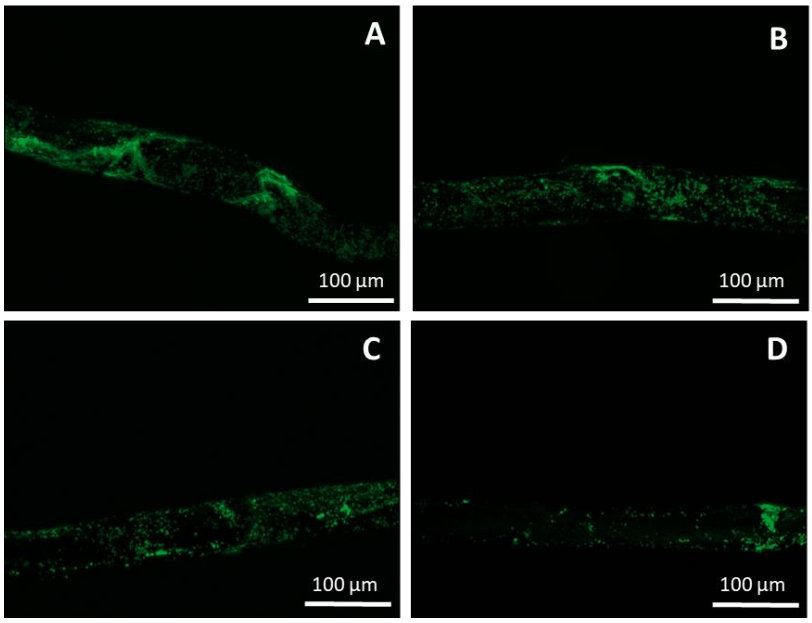

Figure III-6: Pt microelectrodes imaging by epifluorescence microscopy. Letters correspond to inoculum size (% V/V) ratio for synthetic wastewater: (A) 0.5, (B): 2, (C) 5, (D) 10. One duplicate for each case was presented.

As no EAB was able to develop over the Pt microelectrodes regardless of the inoculum size, the inoculation ratio of 0.5% V/V was decided to be maintained as an operational parameter as well as the polarization potential of -0.1 V/SCE. Nevertheless, the impossibility of forming an EAB at different inoculation percentages did not provide any clues as how this variable might influence the electroactivity. The new hypothesis that arose was whether batch operation of the reactors could have inhibited biofilm formation. Therefore, a fed-batch system was proposed. Starting from this point, the absence of oxygen in the reactors was ensured by means of nitrogen gas bubbling for 20 minutes before the start of the polarization. The design of the Pt working microelectrodes was also revisited in order to improve their electric performance, as described in section II.2.1.1.

III.2.1.3. Test 3.3: Evaluation of a fed batch system

In the last experiment of this section, it was decided to investigate the effect of a fed-batch system, meaning that synthetic wastewater was refreshed at periodic time intervals. The aim of testing this relies on whether a nutrient depletion and/or the generation of side products could inhibit bacterial cell growth. In addition, anolyte replacement by a fed-batch operation can be helpful to highlight if the biofilm exploits on soluble molecules present in the medium for EET. Once the anolyte was replaced, the reactors were re-purged with bubbling nitrogen gas to eliminate soluble oxygen. In addition, Pt microelectrodes were re-designed in order to improve their electrical conductivity. Pt microelectrodes were constantly polarized during 10 days and later retrieved for microscopic observation. Acetate concentration was daily measured and adjusted to a concentration of 20 mM.

Six reactors were launched (Figure III-7). In the first two, the anolyte was not replaced. In the other two 50% of the volume was replaced and two more where 90% was replaced. Current density values for

reactors where no anolyte was replaced were of the same order to what was observed in Tests 3.1 and 3.2. When volume was replaced to a 50% of its totality, current did not increase, and current re-started from the same value it had reached before the anolyte change. For volume replacement up to 90%, current dropped and later restarted or restarted directly from zero.

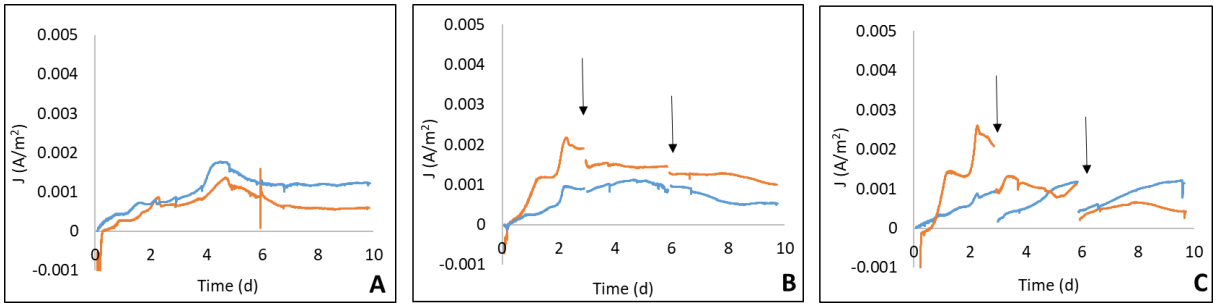

Figure III-7: Evolution of current density in time for duplicates conducted at -0.1 V/SCE on Pt wire microelectrodes. Arrows represent the changement of medium. (A) No volume change, (B) 50% volume change, (C) 90% volume change.

When polarization was stopped at day 10, Pt microelectrodes were imaged by epifluorescence microscopy as seen in Figure III-8. Samples were not homogeneous in terms of bacterial coverage, showing regions of higher and lower colonization.

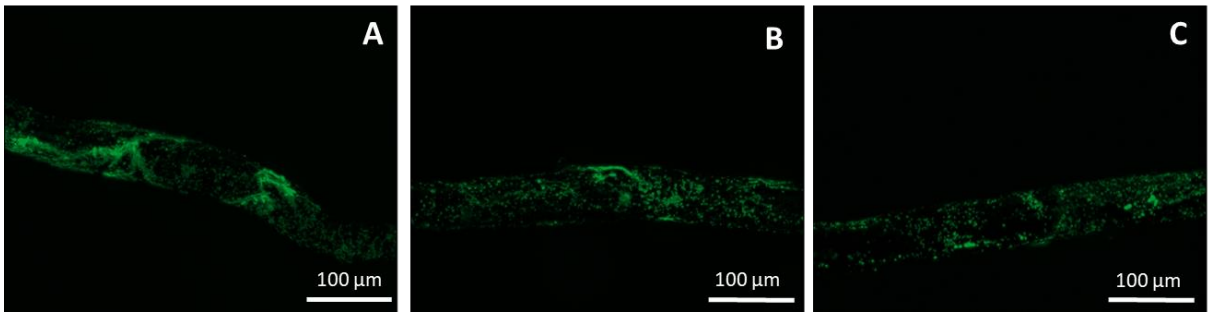

Figure III-8: Pt microelectrodes imaging by epifluorescence microscopy. Letters correspond to the operation mode: (A) No volume change, (B) 50% volume change, (C) 90% volume change. One duplicate for each case was presented.

At this point, the formation of an EAB on Pt microelectrodes remained as the main bottleneck, since attained current density values were considerably low when comparing to bibliography data and former works performed in our research group. In addition, epifluorescence images showed the colonization of the microelectrode by bacteria but not the formation of a proper biofilm structure. The following parameters were studied, with no successful outcomes:

- Optimal polarization potential of the Pt microelectrode
- Optimal inoculum size
- Essay in fed-batch vs. batch mode
- Improved Pt microelectrode electrical conductivity
- Strict anaerobic conditions

The most probable hypothesis was linked to the fact that the actual synthetic wastewater composition was not suitable for the experimental conditions: consequently, no biofilm was able to develop over the microelectrode. The second one, less likely, since Pt microelectrodes were already tested before, was that the microelectrode surface was not biocompatible (at least for this reference of product) and prevented bacterial deposition and attachment. In order to validate this, the next set of experiments was carried out using real residual wastewater and other electrode materials (stainless steel and carbon cloth) were tested for the microelectrodes as working electrodes.

III.2.1.4. Test 3.4: Effect of residual wastewater as the electrolyte/Test of stainless steel (SS) and carbon cloth (CC) as alternative microelectrode materials.

As previous experiments were unsuccessful, the main goal of this test was to evaluate:

- The effect of residual wastewater instead of synthetic wastewater in EAB formation over Pt microelectrodes,
- The feasibility of other microelectrode materials instead of Pt. The implementation of residual wastewater collected from the wastewater treatment plant (WWTP) of Castanet-Tolosan, France has already successfully led to EAB formation in BES in the framework of the thesis of E. Roubaud (2019) and M. Hoareau (2021).

SS and CC were alternative tested as microelectrode materials. The description of their design and is depicted in section II.2.1.1. The CC diameter was around 250 µm, which is slightly far from the microelectrode theory (around 50 µm), but there was not a commercial alternative for that diameter limit.

Reactors containing Pt, SS or CC as a working microelectrode were carried out in triplicates. All working electrodes were polarized at -0.1 V/SCE and inoculated at 0.5 % V/V for the residual wastewater, meaning that the anolyte inside the reactor was 99.5% residual wastewater and 0.5% AS. Before polarization, nitrogen was bubbled into the liquid medium to ensure anaerobic conditions. Acetate concentration was fixed on a daily basis at 20 mM. When indicated, a new batch of residual wastewater was reflushed in the reactors.

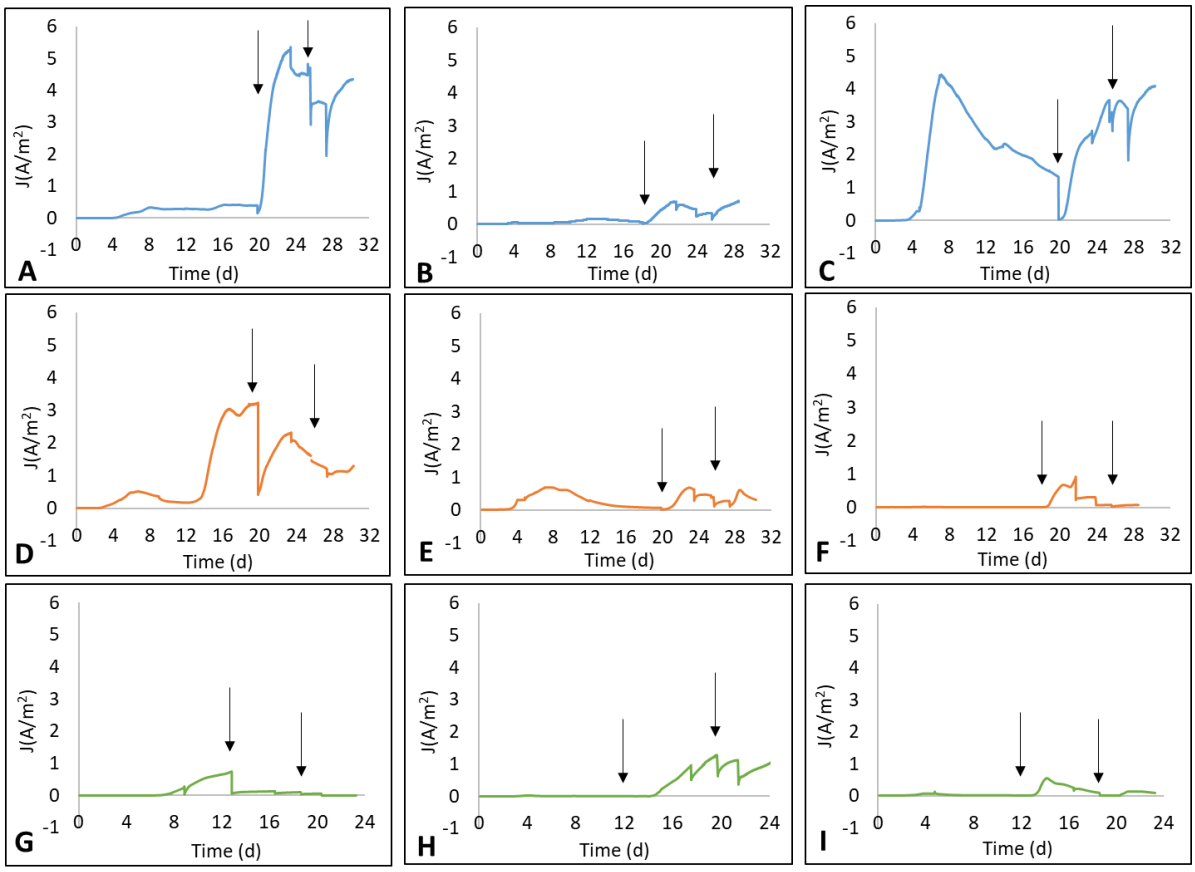

Figure III-9: Evolution of current density versus time for AS EABs triplicates with each microelectrode material conducted at -0.1 V/SCE. (A, B, C) SS microelectrode, (D, E, F) Pt microelectrode, (G, H, I) CC microelectrode. Arrows represent a new batch of fresh residual wastewater.

- First batch of residual wastewater:

In a first step, while working in batch mode, the microelectrodes were polarized over a period of 20 days for Pt and SS microelectrodes, and for a period of 12 days for CC microelectrodes. This mismatch between start-up times was due to some technical obstacles to develop viable CC microelectrodes in the laboratory, as they design process is different from the one for Pt and SS. Current density curves, as seen in Figure III-9, showed a remarkable improvement in the values of current density yielded by the EABs in relation to the ones achieved when working with the synthetic wastewater in the previous experiments. With Pt microelectrodes, with the exception of one triplicate, current reached a peak between 0.5 and 0.7 A/m^2 in the first 10 days of polarization. Later, current density for one of the triplicates increased up to 3.2 A/m^2, which was almost 700 times higher in relation to maximum current density obtained using synthetic wastewater in Test 3.1. This can be observed with more detail in Figure III-10. The hypothesis that platinum was not a suitable material for biofilm development was discarded, since the latter was improved when working with residual wastewater.

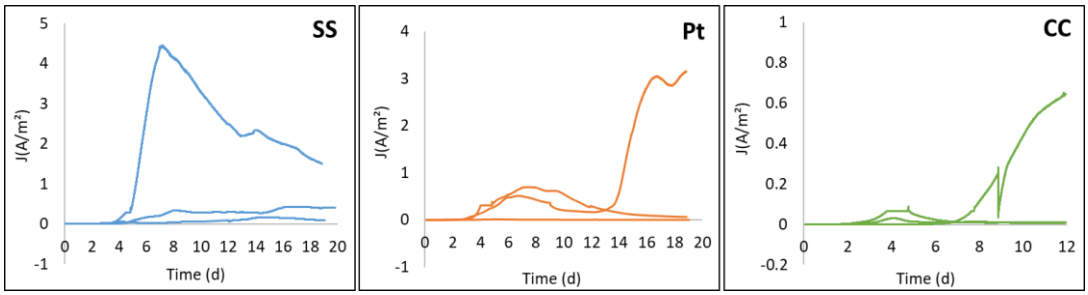

Figure III-10: Evolution of current density versus time for AS EABs for each electrode material conducted at -0.1 V/SCE in the first batch of residual wastewater. The scales are not the same for each material to enable a better visualization of the results.

A boost in current production compared to the previous experiments was clearly seen in all reactors, regardless of the electrode material. This would validate the hypothesis that the composition of synthetic wastewater in the previous experiments was not adequate for bacterial growth and biofilm development in the proposed experimental design. This composition of the synthetic wastewater was tested in the work of Liu et al. (2008) and Blanchet et al. (2015) where bioanodes from wastewater inoculum and AS respectively were successfully formed. Two possible explanations are: (i) Synthetic wastewater might have missed a key component; (ii) our specific conditions (acetate concentration, reactor and electrode size, temperature, inoculation conditions, among others), could have contributed to the adverse results. However, the use of a suitable and improved composition of synthetic wastewater was not discarded for future experiments since synthetic artificial liquid media are advantageous to control their composition and their effect on biofilm formation, and in general, as no solids are suspended, they are preferable for the work in microfluidic systems, avoiding possible clogging in the microchannel.

The microbial community present in the residual wastewater may have also contributed to bring electroactive microbial populations to the anode. Because the microbial concentration is higher in AS than in residual wastewater (Foladori et al., 2010), the co-addition of sludge to wastewater usually gives higher electrochemical performances and accelerates biofilm formation on the anode (Min et al., 2013). This possibility could have been investigated from experiments without AS as inoculum. The wastewater (residual or synthetic) used in the reactors can led to a bacterial enrichment that is different in the EABs (Yu et al., 2012, Blanchet et al., 2015).

As observed in Figure III-10, chronoamperometries (CAs) showed a very different evolution of current production profiles, even between triplicates. Reproducibility in the electroactivity at this point was still low. It was observed that in general, current was not maintained. It was initially zero and later increased. Current later dropped, with the exception in some cases where it then recovered (as in one triplicate for Pt and for CC). It was therefore decided to add a new batch of fresh residual wastewater in order to try to restore current production.

- Second and third batch of residual wastewater:

As observed in Figure III-9, after the second batch of residual wastewater (see arrows), current started growing from zero or from values close to zero. Probably the microelectrode manipulation when opening the reactor, while changing the medium and quickly exposing them to ambient oxygen was the cause. If anaerobic bacteria mainly composed the EABs, and in addition if these EABs were not thick, direct exposition to oxygen might have negatively affected them. A way of testing if oxygen exposure was the cause of current starting from zero would be to perform wastewater replacement with a hydraulic pumping system, under anaerobic atmosphere (constant flow of nitrogen gas or in an anaerobic box). Another explanation may refer to the presence of soluble electron acceptors in the new batch of residual wastewater, such as sulfate and nitrate, which could have diverted electron flow after the addition of a new batch.

However, the same trend on current production was observed as for the first batch: the electroactivity increased again to reach a second maximum and later dropped. Another drawback corresponded to the non-reproducibility in CA curves replicates, even for the same anode material. The differences in performances may be due to the non-uniformity in the wastewater and AS bacterial and chemical composition. A third batch of fresh residual domestic wastewater was therefore added. Nevertheless, the experiment had to be stopped four days after the third batch due to the lockdown in 2020. Polarization was stopped and no final cyclicvoltammetries (CVs) were recorded.

Figure III-11 shows CVs that were conducted at initial conditions (before launching the CA), and before each change of medium, corresponding to the black arrows on the Figure III-9. For the initial CV, the scanning range was of -0.35V/SCE to 0.35 V/SCE. Pt and CC showed unusual positive oxidation current values. In general, initial CVs are flat, but for Pt and CC, probably some anolyte components started to oxidize from 0 V/SCE. As the polarization potential was -0.1 V/SCE, this shouldn't have influenced the results. For the CVs before the second and third batch, it was decided to maintain the positive limit of 0.35 V/SCE. However, as for some cases the system was still in oxidation beyond the -0.35 V/SCE lower limit, it was decided to extend it up to -0.6 V/SCE. The scale of the current density axis was not kept constant in order to better appreciate the results for each material. Before the third batch, it seemed that two SS microelectrodes, one Pt and one CC, gave the higher current density values in the scanned potentials. From a material point of view, no capacitive effect was observed in the case of Pt due to its low double layer capacitance (Pocaznoi et al., 2012).

In terms of electroactivity, EABs formed on SS microelectrodes showed the highest performances, given that two of three triplicates reached maximum current densities between 4.3 A/m^2 and 5.2 A/m^2. EABs formed on CC electrodes presented the lowest values in terms of current production. EABs on Pt yielded current values between SS and CC; however, a single triplicate reached a maximum current value of 3.2 A/m^2. It is noteworthy to clarify that no reproducibility was reached in terms of electroactivity, being

this obstacle more important to overcome in experimental terms, compared to obtaining high current values.

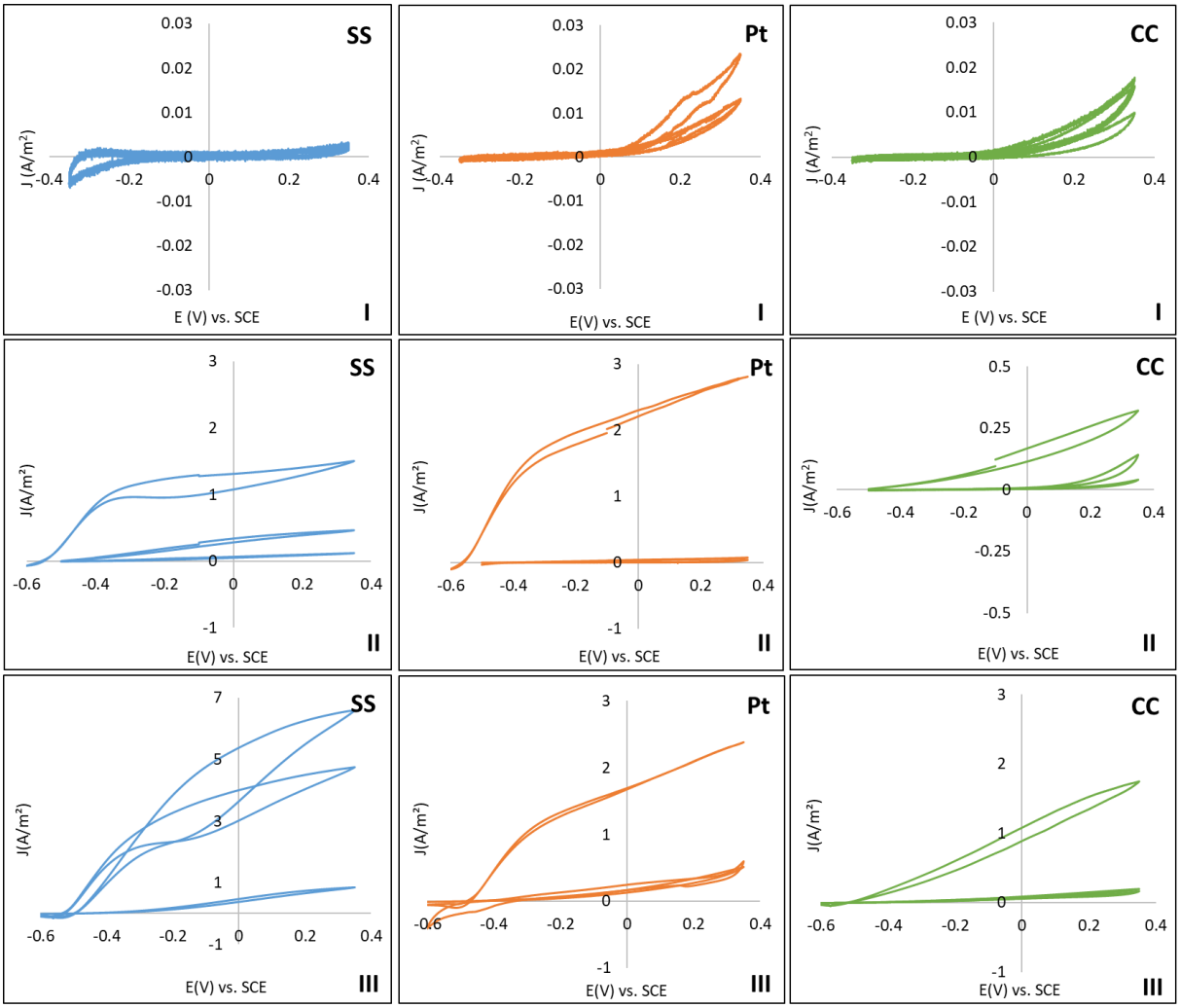

Figure III-11: CVs performed at a scanning rate of 1 mV/s for each material and at three different times of the experiment. (I) initial CV (before polarization), (II) before second batch of residual wastewater, (III) before third batch of residual wastewater.

In this experience, the formation of a biofilm was observed for the first time. By comparing Figure III-6 and Figure III-8 with Figure III-12, in the latter a biofilm structure can be observed, in contrast with single bacteria deposited on the microelectrode surface. For CC, as one triplicate was detached from the electrode structure, it was not imaged. In the case of SS, it can be clearly seen the difference between triplicates, where some biofilms were thicker than others. This can be related to the improved electrochemical performance in those cases.

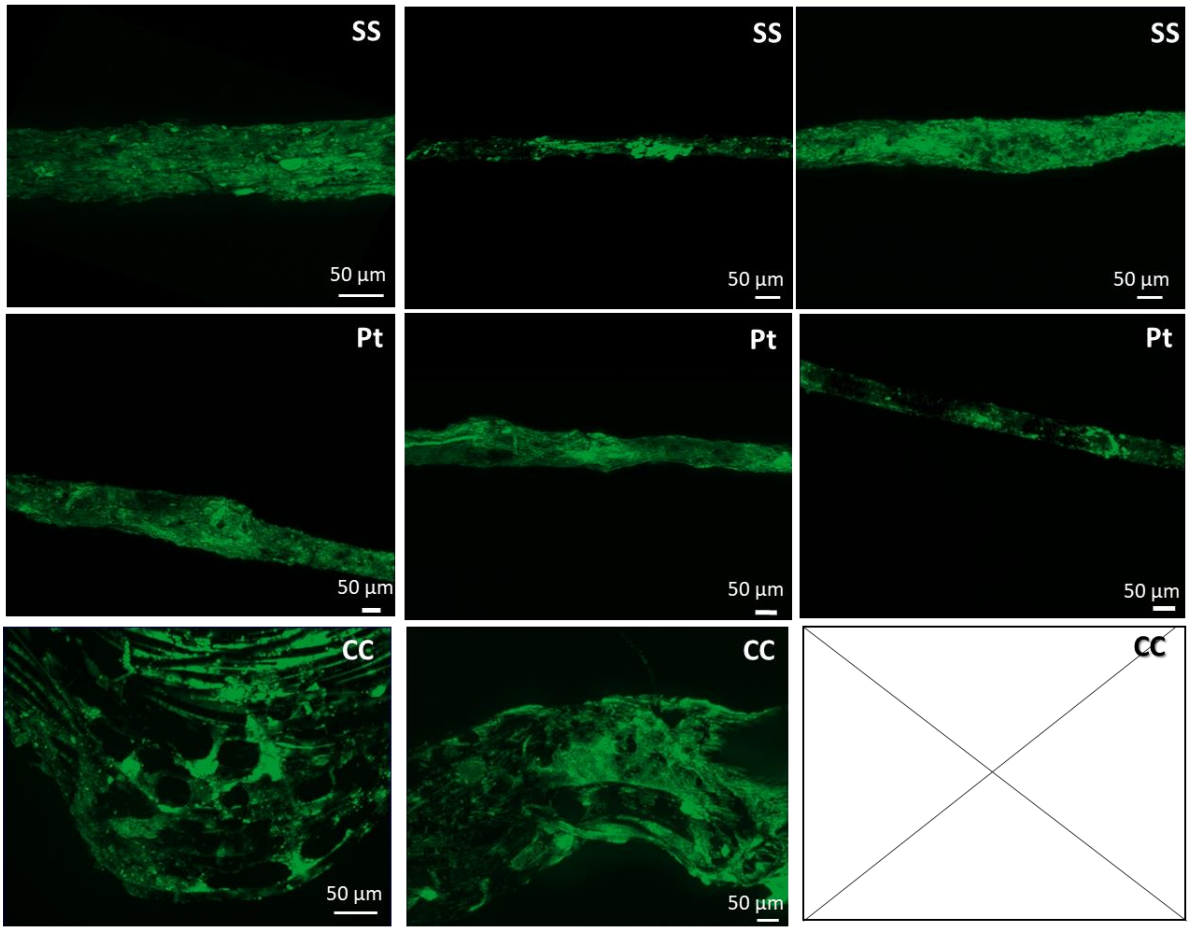

Figure III-12: Biofilm imaging by epifluorescence microscopy. Triplicates were represented for SS and Pt, whether only duplicates for CC.

The very positive aspect of this test was that the bottleneck of forming an EAB over microelectrodes was overcome. However, results in terms of current evolution and maximal current production were still no reproducible. It would have been ideal to continue this line of research, by using a synthetic medium that allowed obtaining reproducible results.

In terms of electrode material, CC was discarded for the upcoming work since its size did not compile with the microelectrode definition and the electroactivity of the biofilms formed on CC was the lowest for the three tested materials. For this reason, SS and Pt microelectrodes will be further studied as anode materials in the following sections.

Since it was no longer possible because of the sanitary conditions, to work in the laboratory with AS and residual wastewater, a change on the experimental conditions had to be revisited. New sources of inoculum had to be considered in order to form EABs on Pt and SS microelectrodes.

III.2.2. Test 3.5: Experiments with garden compost as inoculum

After the impossibility of continuing with the previous line of research, it was decided to work with garden compost as microbial inoculum and with an improved synthetic wastewater composition

("Synthetic wastewater II"). Garden compost was used several times in previous works in the laboratory as a source of electroactive microorganisms in the thesis of Pocaznoi (2012), Oliot (2017) and Chong (2018). As previously reported, Pocaznoi et al., (2012) successfully formed EABs with garden compost as inoculum over Pt microelectrodes (diameter 50 µm) obtaining current density values of 19 A/m^2. In their work, microelectrodes were polarized under a constant potential of -0.2 V/SCE.

A series of four reactors containing Pt and SS microelectrodes as working electrodes were launched in duplicates. All reactors were polarized at -0.2 V/SCE and inoculated at 5% V/V for synthetic wastewater. Before polarization, nitrogen gas was bubbled into the liquid medium to ensure anaerobic conditions. Microelectrodes were polarized for 29 days, and only polarization was interrupted on day 11 to record a CV close to the maximum current values. Acetate concentration was measured and adjusted every two days to a value of 20 mM, unless another concentration was indicated.

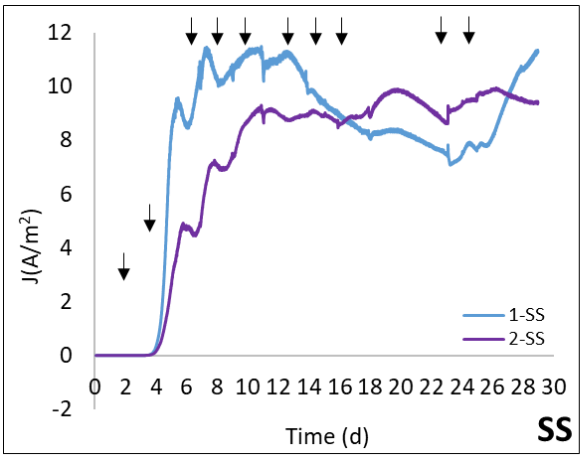

[Ac] (mM)	Δt(d)	$[Ac]_{c1}$ (mM)	$[Ac]_{c2}$ (mM)	CE1(%)	CE2(%)
20	0 – 2	7.55	6.91	0.00	0.00
20	2 – 4	8.69	6.92	0.02	0.01
20	4 – 7	10.27	10.34	5.56	2.50
20	7 – 9	7.97	8.73	7.02	4.18
20	9 – 11	8.34	6.55	6.83	6.75
20	11 – 14	9.83	9.88	8.49	6.91
20	14 – 16	7.45	6.84	6.63	6.86
20	16 – 18	6.45	6.12	6.98	7.55
30	18 – 23	15.19	14.8	7.04	8.43
-	23 – 25	3.16	3.58	11.89	13.99
20	25 – 27	7.95	7.13	5.57	7.41

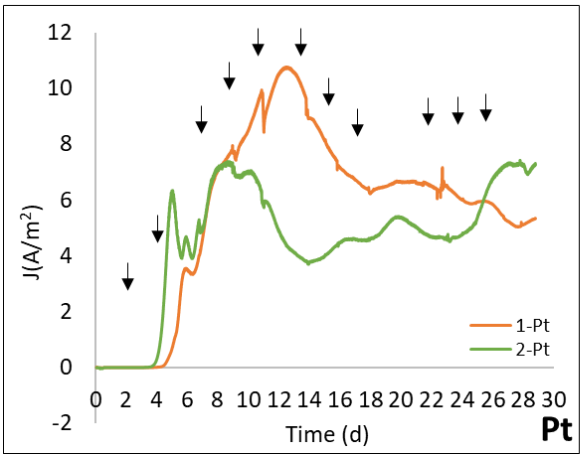

[Ac] (mM)	Δt(d)	$[Ac]_{c1}$ (mM)	$[Ac]_{c2}$ (mM)	CE1%)	CE2(%)
20	0 – 2	6.55	6.55	0.00	0.00
20	2 – 4	7.48	8.19	0.00	0.02
20	4 – 7	7.77	7.89	2.04	4.06
20	7 – 9	6.44	6.73	5.48	5.24
20	9 – 11	6.16	7.38	7.14	4.77
20	11 – 14	8.66	9.00	8.93	3.94
20	14 – 16	7.19	7.92	5.98	2.70
20	16 – 18	6.19	6.19	5.72	3.91
30	18 – 23	8.11	18.3	10.42	3.58
20	23 – 25	2.35	6.99	13.96	3.64
20	25 – 27	3.86	6.58	7.86	5.29

Figure III-13: Evolution of current density versus time for garden compost EABs formed on SS and Pt microelectrodes polarized at -0.2 V/SCE. Triangle tips arrows show acetate additions. The tables shows the set acetate concentration [Ac], its consumption $[Ac]_c$ along with the CE (x1000).

Figure III-13 shows current production for EABs formed over SS and Pt microelectrodes. Current production started approximately at day 4 for all samples. However, after start-up, trends in the evolution of current density were not reproducible. In the case of SS, for one duplicate, current increased and remained constant (2-SS); and in the other, it declined after the maximum and later recovered (1-SS).

For Pt, both duplicates followed the same trend up to day 8, but later in one (1-Pt) current kept on increasing and later abruptly decreased. The other duplicate reached a maximum value (2-Pt), decreased and recovered the maximum current value by the end of the polarization.

In order to have a deeper understanding of the differences in the CAs, acetate consumption was analyzed along with the coulombic efficiency (CE) of the SS or Pt working electrode. It has already been mentioned that CE values are very low due to the great difference between the area of the microelectrode and the anolyte volume; however, in this case, values were used only for comparison between duplicates. The analysis is divided between SS and Pt samples for an easier description.

- SS as a working microelectrode:

Days 0 to 4: In this stage, CE was zero given the fact that no current was produced. Non-electroactive populations only consumed acetate.
Days 4 to 9: The most remarkable difference in current production was observed in this period. The difference between acetate consumption in 1-SS and 2-SS was of 0.7% from days 4 to 7 and 9.5% from days 7 to 9. However, the difference in CE in the respective periods was of 122.4% and 67.9%.
Some hypothesis could be drawn here. It was possible that the biofilm microbial population was greater in electroactive bacteria in the case of 1-SS, which was translated into a higher rate of acetate bacterial oxidation and consequently of current production. As another explanation, acetate could have diffused better in the biofilm from reactor 1-SS, thus increasing its electroactivity as a result.
Days 9 to 18: In this period current seemed to stabilize, however in reactor 1-SS, there was a decrease in the electroactivity. The values obtained for acetate consumption and CE did not show considerable deviations.
Days 18 to 27: At day 18, acetate was adjusted to 30 mM. Current improved for 2-SS, but it still decreased for 1-SS.

- Pt as a working microelectrode:

Days 0 to 4: Like for the use of SS as a microelectrode, the CE was zero since no current was produced in a four days period.
Days 4 to 9: In this period, current production followed the same trend in both reactors. The most remarkable difference was seen from days 4 to 7, when the difference in acetate consumption was only 1.5% different, but for CE there was a difference of 101.0%. This was due to the peak of current observed for reactor 2-Pt at day 5. From days 7 to 9, CE was similar between the reactors such as the CA curves.
Days 9 to 18: This was the period when both curves showed the most dissimilarity. CE was 49.7% higher for 1-Pt from day 9 to 11, 126.7% from day 11 to 14. This was translated to the increase of current in 1-Pt in comparison to 2-Pt. In the upcoming days, the CE was still superior for reactor 1-Pt.

Days 18 to 27: Here, acetate consumption in 2-Pt surpassed the values for 1-Pt, but the trend on the CE was the inverse. This means that in reactor 2-Pt, acetate was consumed more importantly by non-electroactive populations.

At some key points of the experiment (days 11 and 29) a CV was performed. The results are presented for each individual reactor, superposing the curves at the two days. The scanning limits where set from -0.6 V/SCE to 0.35 V/SCE. It is relevant to see that oxidation started around a potential value between -0.56 V/SCE to -0.46 V/SCE, thus confirming that at -0.2 V/SCE acetate was indeed being oxidized. It is also interesting to note that the CV shapes were similar despite of the anode material and no capacitive effects were observed.

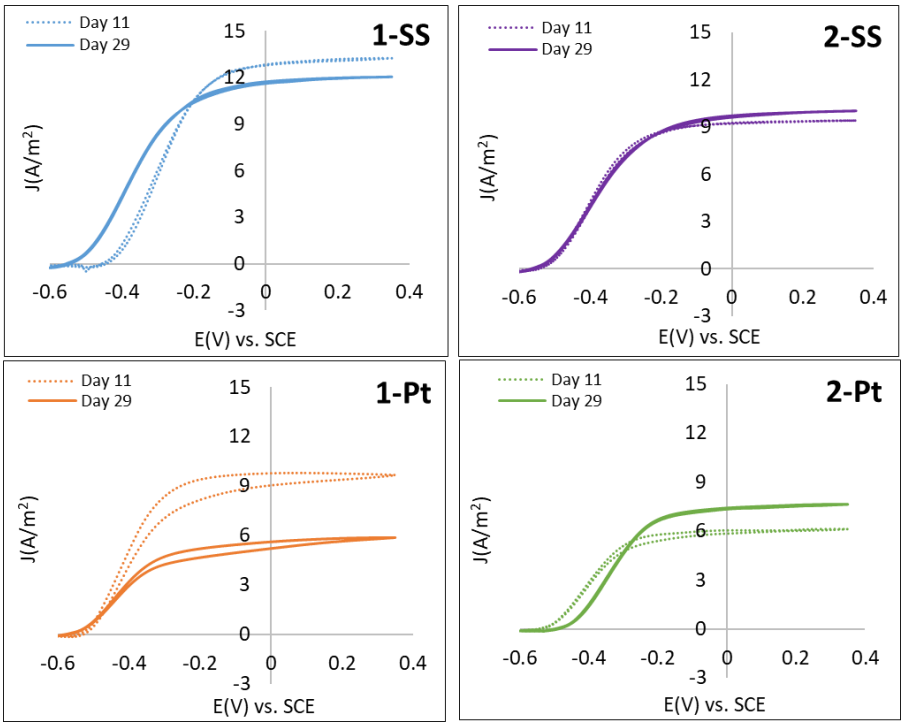

Figure III-14: CVs performed at a scanning rate of 1 mV/s of garden compost EABs formed over SS and Pt microelectrodes at two different days of the experiment.

After the final CV, bioanodes were retrieved from the reactors and stained with acridine orange for epifluorescence microscopy observation. In addition, the average thickness of the EAB was measured, by taking nine thickness values of the biofilm along with the microelectrodes with the help of image analysis.

Table III-2: Average thickness of garden compost EABs and their standard deviation in µm.

Reactor	1-SS	2-SS	1-Pt	2-Pt
Biofilm average thickness (µm)	75.6±16.8	110.0±16.8	48.9±5.2	45.6±10.8

Thicker biofilms were formed on SS, although more heterogeneous than in the case of Pt. By looking at the standard deviation values, the EABs formed on Pt were more homogeneous than the ones formed

on SS, since there was more variation. From CAs, SS donated more reproducible curves than for Pt, and higher maximal current densities. It would be therefore interesting to future correlate the biofilm growth with the electroactivity, since in this experiment, thickest biofilms showed an improved electrochemical performance.

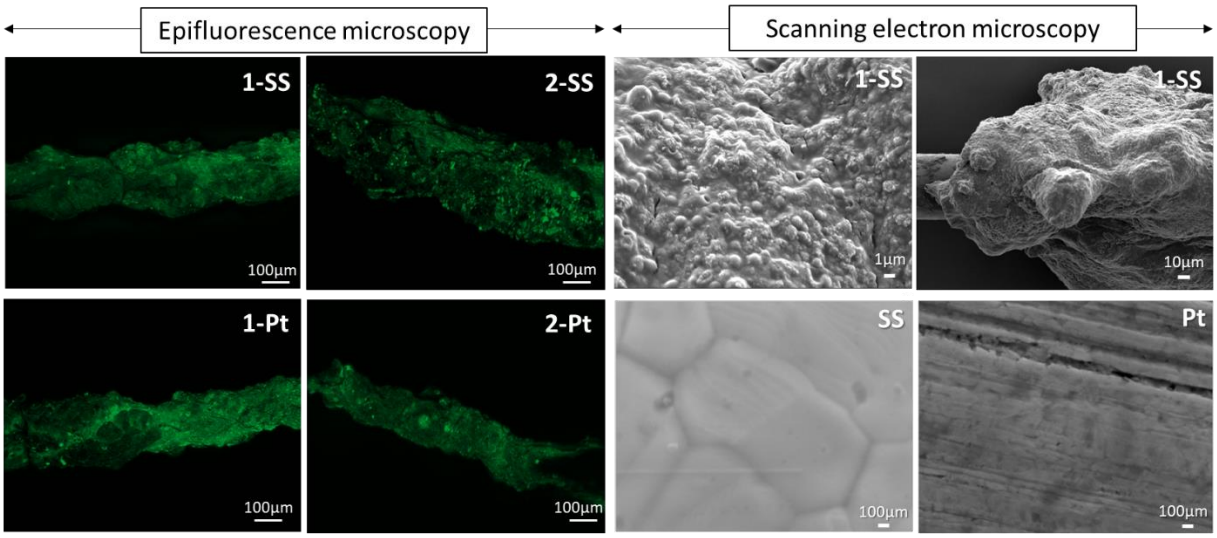

Figure III-15: Microscopy images for garden compost biofilms formed over Pt and SS microelectrodes. Epifluorescence microscopy images for each sample. SEM images of the biofilm surface for sample 1-SS and for the bare microelectrode surface of SS and Pt.

EABs were also observed by scanning electron microscopy (SEM). The coverage by the biofilm seemed full over the microelectrodes, but not homogeneous, which could explain the biofilm thickness deviations as seen in Table III-2. Garden compost biofilms appeared to have formed from initial clusters or colonies (as a sort of nucleation), with a lumpy, non-smooth surface. SEM images of Pt and SS clean microelectrodes seemed not to show any roughness that could have favored biofilm formation. Champigneux et al., (2018) remarked the importance of the roughness of electrode materials at the microscale for bacterial cell adhesion when compared to flat surfaces. It is still unclear why SS performed better than Pt, and why thicker biofilms were formed on this material.

Garden compost proved to be a suitable inoculum to form EABs over Pt and SS microelectrodes in a low conductive anolyte; however, reproducibility between samples was still difficult to obtain. Comparing acetate kinetics by itself is not an adequate indicator of the electrochemical performance. Acetate concentration in the anolyte was similar between duplicates at the point of maximum current density; however, J_{max} was different between duplicates. The difference between CE indicated that acetate oxidation follows different metabolic routes depending on the composition of the inoculum bacterial community, specific enrichment in electroactive bacteria (competition with methanogens) and chemical composition of the anolyte, especially soluble oxygen or other soluble electron acceptors. The discrepancies in the CAs could be due to many different phenomena. Starting with the fact that the chemical and microbial composition of the inoculum may have not been the same in each reactor, as the

biofilm grows and evolves the latter is exposed to several changes in its viability, morphology and chemical composition that might have finally affected its electroactivity.

III.2.3. Test 3.6: Experiments with salt marsh sediments (SMS) as inoculum

As the MICROBE ANR project proposed to work with anolytes of two very different salinity, in this last experiment, a new kind of inoculum adapted for a saline anolyte was tested. In several previous projects at the LGC, SMS from the marine environment of Gruissan (France) were successfully used as a source of electroactive microorganisms for developing EABs oxidizing acetate on carbon felt and graphite felt electrodes. In those works, the formation of bioanodes from SMS was verified in a Starkey medium with yeast extract replaced by acetate only at different salinity concentrations ranging from 30 g/L of NaCl to 60 g/L of NaCl. The bioanodes that generated the highest current density was for a NaCl content of 45 g/L, that corresponds to a electrolyte conductivity 1.5 higher than seawater (Rousseau et al., 2013).

Therefore, in this experiment it was decided to implement SMS in the same Starkey medium composition (see section II.1.1.) with 45 g/L of NaCl, to form EABs over Pt and SS microelectrodes. As the halotolerant microbial community of SMS was demonstrated to grow successfully in a medium with high amount of salt, we also tested the feasibility of EAB formation in a liquid medium without NaCl. For this purpose, the "Synthetic wastewater II' was used. As to simplify the denomination, the Starkey medium is replaced by HS (high salinity) and the synthetic wastewater II for LS (low salinity) for the rest of this section.

A series of eight reactors were launched. Four reactors with HS medium and four with LS medium, with duplicates containing Pt and SS microelectrodes. Before polarization, nitrogen gas was bubbled into the reactors to ensure anaerobic conditions. Microelectrodes were polarized between 22 to 55 days at a potential of 0.1 V/SCE, according to a previous work that determined the optimal potential for SMS inoculum (Rousseau, 2013). Polarization was only interrupted at day 13 to record a CV. Reactors were initially inoculated at 0.5% V/V for the medium; however the inoculation size seemed very low. Therefore, after 24 hours of running the experiment, the inoculation size was increased to 5% V/V. Acetate concentration was measured and adjusted every two days to a value of 40 mM.

Figure III-16 shows the electroactivity for the EABs formed from SMS. The first observation may relate to the medium. The performances reached in the HS medium were expected, since halophilic bacteria thrives in high saline concentrations. Halotolerant bacteria can use two strategies for adapting themselves to a high salinity environment. Either they can accumulate ions, to increase the intracellular ion concentration and balance the osmotic pressure or they can adapt to the increased osmotic stress by accumulating solutes, i.e. aminoacids. (Grattieri and Minteer, 2020).

The behavior of halophilic bacteria in low salinity media can be a little more complex to explain. As the mechanism for halophilic bacteria to accumulate ions at high salt concentrations require that the proteins maintain their conformation and activity, most proteins denature when they are suspended in low salty environments. Therefore, such microorganisms generally do not survive in low salt medium. However, the second strategy of halophilic bacteria is based on the biosynthesis and/or accumulation of organic osmotic solutes, where cells that use this strategy exclude salt from their cytoplasm as much as possible, and where the concentration of solutes does not interfere with the enzymatic activity (Oren, 2008).

For the LS medium, the CAs showed that for each duplicate, one sample seemed to work while the other did not, ruling out that the difference in the microelectrode material may have affected the results. The difference in the strategies explained above may serve as a potential hypothesis as to why in some cases there was the formation of an EAB and in others there was not. It is possible that from the original microbial consortium present in the inoculum, under low salinity conditions, certain electroactive species could adapt themselves to the environmental conditions and colonize the electrode, whether in other cases they did not. It can also be seen that the adaptation time was slower, since the lag-phase for 1-SS-LS and 1-Pt-LS was longer than for the HS medium. As for reactors 2-SS-LS and 2-Pt-SS no current production was detected after 22 days of polarization, those experiments were stopped.

To continue with the analysis, the electrochemical performances of SS duplicates performed in HS medium were more reproducible than in the case of Pt in the same medium. The formation of EABs from salt marsh inoculum in the HS anolyte did not only show reproducible electroactivity, yet the behavior of the CAs at the microscale was similar to the ones obtained for classical macroelectrodes. The electrochemical performance in bioanodes is typically marked by a lag-phase where no current is produced, followed by a sharp increase until a maximum value of 8 A/m^2, a gradual decrease in the range of 50% of the maximum and a final stabilization in this latest value (Chong et al., 2018). This led to two very important results: firstly, that it was possible to obtain reproducible results, and secondly, that microelectrodes were a very convinient tool to study the mechanisms of biofilm formation since they were able to succesfully reproduce the same behaviour in terms of the bioanode electroactivity and its evolution as for macroelectrodes. The CA curves are not explained with detail in this section, since they are a part of the published Research Article 2.

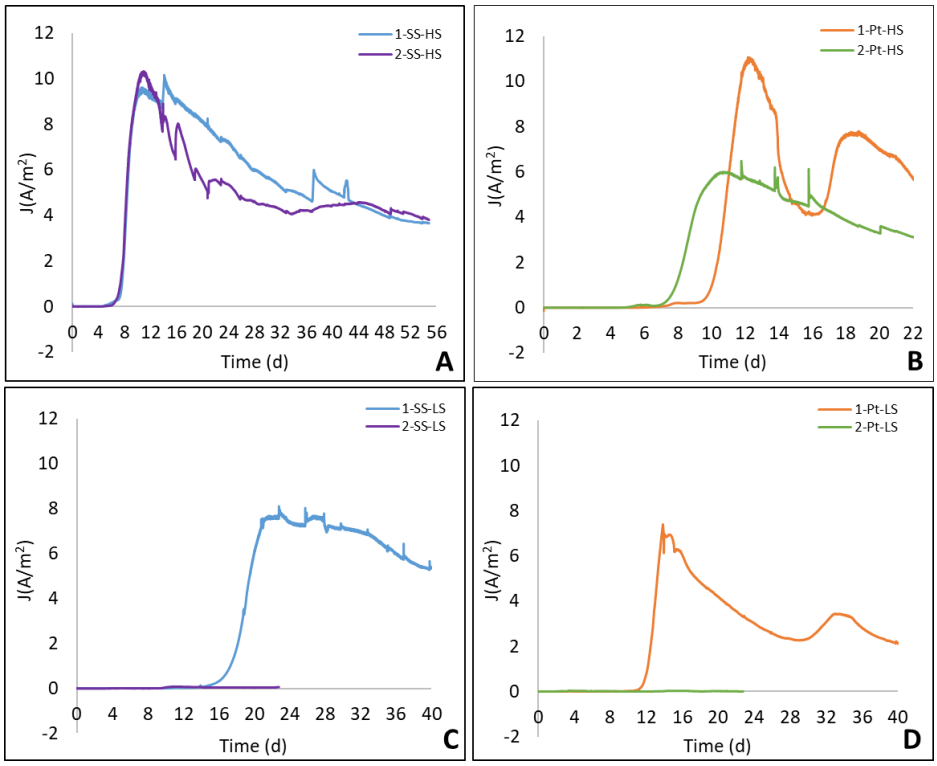

Figure III-16: Evolution of current density versus time for salt marsh EABs formed on Pt and SS polarized at 0.1 V/SCE. HS corresponds to the Starkey medium with a NaCl concentration of 45 g/L, whether LS corresponds to the synthetic wastewater with no NaCl content.

At day 13 and by the end of the experiments, constant polarization was stopped in order to perform a CV technique. The results are presented for each individual reactor, superposing the curves at the two different days. Scanning limits in all cases were -0.6 V/SCE to 0.35 V/SCE. The scale of the current density axis was not kept constant in order to better appreciate the results for each case.

It is clear that the shapes of the curves differed greatly from those obtained for the previous test using garden compost as inoculum (Figure III-14). In the previous experiment, the shape of the CV was maintained independently of the time the CV was executed. Here, the shapes of the CV were not the same at day 13 and at the end of the experiment, and in most cases, a large hysteresis effect was observed between the starting and final potential scanning. This was also reported by Rousseau et al. (2014) for the same type of bioanodes formed on graphite felt electrodes. In his work, authors reported that the non-symmetry of the forward and backward curves indicated that the hysteresis phenomena could not be due to a capacitive effect only (since capacitive currents are similar in both scanning directions), attributing this effect to a modification of the biofilm redox state while recording the CV at low-scanning rates.

For reactors containing LS medium, electroactivity was only highlighted in reactor 1-SS-LS at day 13. Therefore, for the rest of the reactors using LS medium at day 13, current was always close to zero at the time of launching the CV. For biofilms grown in HS medium, with the exception of 1-Pt-HS, it seemed that the hysteresis effect decreased at the final CV.

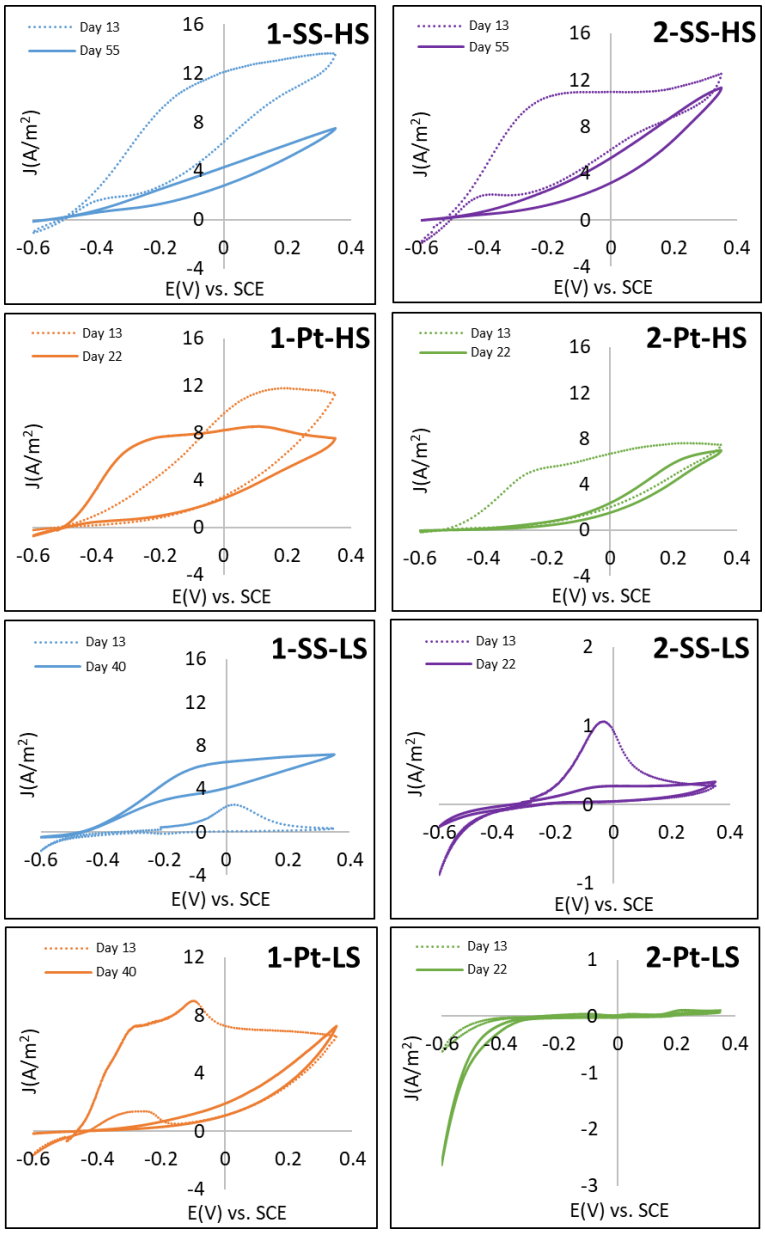

Figure III-17: CVs performed at a scanning rate of 1 mV/s for salt marsh EABs formed over SS and Pt microelectrodes at two different days of the experiment at their corresponding medium.

Salt marsh biofilms were imaged by epifluorescence microscopy and SEM, as seen in Figure III-18. For reactors 2-SS-LS and 2-Pt-LS, biofilms were not imaged since they did not express any electroactivity. From the images from epifluorescence microscopy, a difference in biofilm thickness can be easily observed. Therefore, as equally done for garden compost biofilms, the average thickness of the biofilm was calculated by taking nine measurements for each sample and calculating the standard deviation. Values are presented in Table III-3.

In addition, SEM images showed a significant contrast between the morphology of the biofilms formed in the HS and the LS medium. Biofilms formed in LS medium were not able to produce extracellular exopolymeric substances, since the morphology showed a very porous and opened structure of the

biofilm. On the other hand, biofilms formed in the HS medium showed a more compact and closed structure. It has been described, for electroactive and non-electroactive bacteria, that salinity promotes biofilm formation by the production of exopolymeric substances, enhancing bacterial cell irreversible adhesion to the electrode surface (Xu et al., 2010, Rousseau et al., 2014).

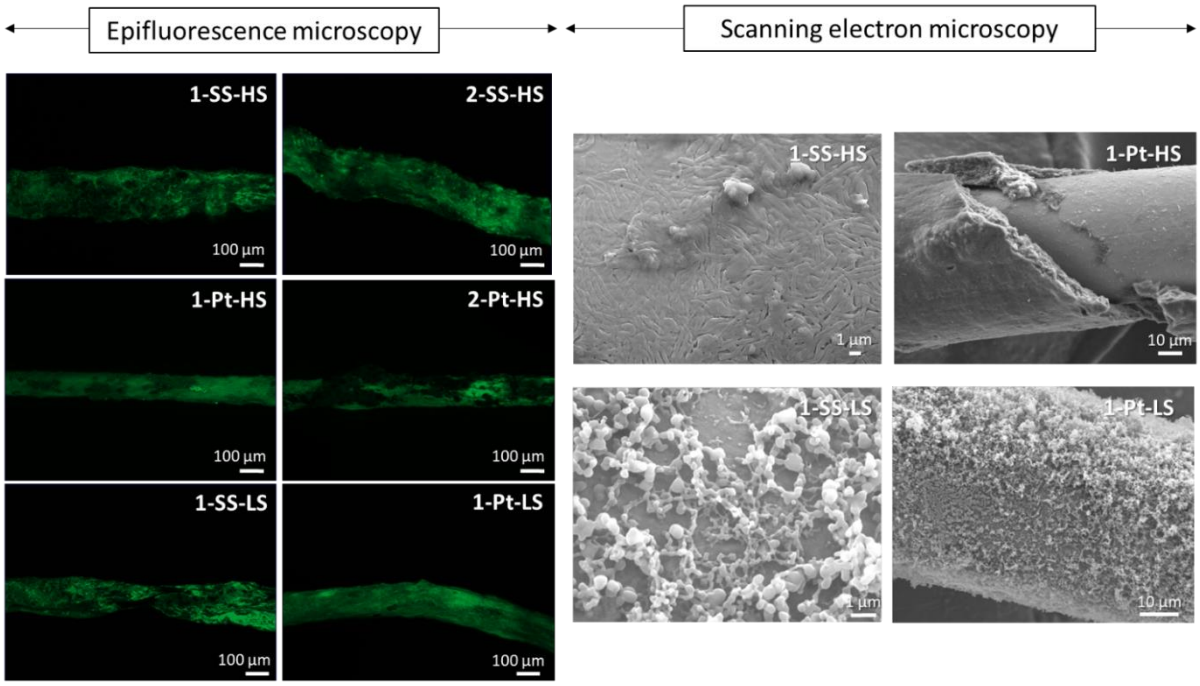

Figure III-18: Microscopy images for salt marsh biofilms formed over Pt and SS microelectrodes. Only one duplicate was imaged by SEM.

From the previous experiment, it was observed that for biofilms that were grown for the same period, thicker biofilms were formed over SS microelectrodes. In this experiment, even if polarization times were not similar, it can be seen in Table III-3 that there was an evolution of the biofilm thickness in time. This was mainly observable for the HS medium. The link between polarization time, biofilm thickness and biofilm electroactivity is more deeply developed in Chapter IV.

Table III-3: Average thickness of salt marsh EABs and their standard deviation in µm.

Reactor	**1-SS-HS**	**2-SS-HS**	**1-Pt-HS**	**2-Pt-HS**	**1-SS-LS**	**1-Pt-LS**
Biofilm average thickness (µm)	63.6±5.1	55.4±5.2	22.9±2.3	28.4±7.1	25.6±5.1	38.9±4.2
Polarization time (d)	55	55	22	22	40	40

SMS proved to be another suitable source of microorganisms to form EABs over Pt or SS microelectrodes. Even if higher electroactivity was observed for a high salinity medium, it was also possible to form a bioanode in low salt conditions. In addition, maximum current density values were again obtained using SS microelectrodes and more reproducible current curves.

This experiment marks the lines of work to be followed in the next chapters. The reproducibility in results obtained using SS microelectrodes to form EABs with SMS inoculum in a high salinity medium and their ability to replicate the behavior in macroelectrodes, positioned these conditions as optimal for further work. Therefore, in the next chapters the following experimental conditions will be fixed:

- SS microelectrode as the working electrode
- Polarization potential of the working electrode at 0.1 V/SCE
- SMS with an inoculation size of 5% V/V
- Starkey medium at a NaCl concentration of 45 g/L as the culture medium
- 40 mM of acetate as substrate

III.2.4. Evolution of the potential of the counter electrode

In the series of experiments described in between Test 3.2 and Test 3.6, a three-electrode system always composed the reactor set-up. First, the working electrode (or the anode), where oxidation occurs and biofilm develops; then a counter electrode (or the cathode), to where electrons travel and reduction reactions take place; and a reference electrode (mainly commercial SCE), to ensure a constant potential on the anode throughout the experiment. When a constant potential is applied to the working electrode, in fact it is a difference of potential applied by the potentiostat between the working electrode and the reference electrode. In a macroreactor, a three-electrode system is simple to implement; however, for a microfluidic cell, a commercial reference electrode is quite impossible to incorporate.

In Test 3.1, the use of Ag microelectrodes as pseudo-reference in a three-electrode system was discarded. Therefore, the idea of working in a two-electrode system in the microscale was raised with the condition that the potential of the counter electrode remains constant. In a typical three-electrode system, electrons flow from the anode to the cathode. If the potential of the anode is fixed versus a reference electrode, current can increase or decrease but the potential of the anode will be constant. For the cathode, in order to flow the same amount of current produced in the anode, the potential of the cathode shifts. In a two-electrode system, current also flows from the anode to the cathode. The difference is that here, the cathode has the function of closing the circuit and maintaining a constant potential regardless of the current that flows. This last task is very difficult under most experimental conditions. One possible exception is if the cathodic surface area is much larger than the anodic one. In this case, the current produced at the anode will be small for the large cathode, which will probably not affect its potential.

In the experimental set up for the standard reactors, the area for the Pt grids as counter electrodes, variated between 6 to 12 cm^2, whether the area for the microelectrode of 2 cm of length and 50 μm of diameter was of 0.031 cm^2. This means that the cathodic surface area was between 200 to 400 times larger than the anodic one. In theory, the Pt grid potential should be stable; otherwise, the ratio between 200 to 400 was not large enough. To test this hypothesis, in Test 3.5 and Test 3.6, the potential of the Pt

grid counter electrode was tracked in some reactors all along the experiment while the anode was polarized by an open circuit potential technique. Results are shown in Figure III-19.

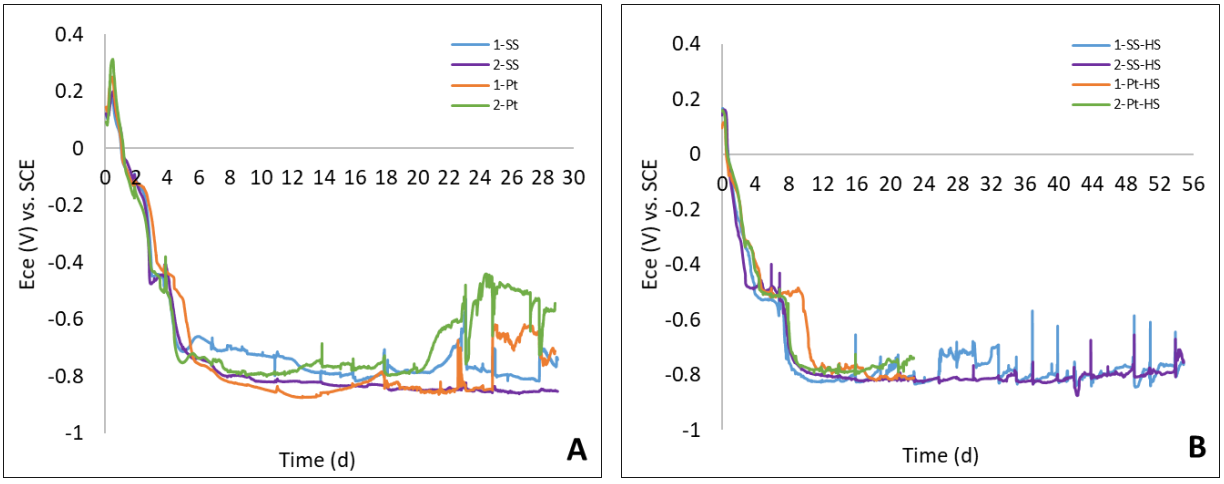

Figure III-19 : Evolution of the Pt grids potential as counter electrode by OCP techniques vs SCE. (A) Corresponds to the experiments in Test 3.5 (B) for the experiments in Test 3.6.

Trends were similar for both tests. At the beginning, where no current was produced in the anode and soluble oxygen was still present in traces in the anolyte, the potential of the counter electrode was positive around 0.2 V/SCE. Later, when acetate started to be oxidized by the biofilm and current went up in the anode, water was reduced into hydrogen in the cathode producing the shift to negative potentials. The potential of the counter electrode stabilized at 8 days at an approximate value of -0.8 V/SCE. In the cases where the potential increased or varied, such as in Figure III-19 (A) for 2-Pt, it was possible that the production of HCO_3^- as a product of acetate oxidation could have catalyzed the water reduction reaction (Roubaud et al., 2018). The addition of a higher concentration of acetate at day 18 for reactor 2-Pt could have been the cause of this effect.

These results suggest that it would be possible to work in a two-electrode system in the microBES if the area of the counter electrode is at least 200 times larger (larger would be even better) than that of the microelectrode. Further tests are clearly required and they are be presented in Chapter VI.

III.3. Conclusions of chapter III

The experimental steps described in this chapter served to find the optimal conditions to form multi-species EABs by using a microelectrode as the anode in a three-electrode system, as to reproduce the electroactivity reported in macroelectrodes. Despite the fact that the first series of experiments with AS as inoculum were unsuccessful, they allowed to ameliorate certain aspects of the experimental system along the way, such as the importance of anaerobic conditions, the improvement of the microelectrode design for better electrical conductivity and manipulation in the experiments, and the choice of a suitable culture medium. In this chapter, it was shown that SS microelectrodes donated better electrochemical

performances and more reproducible results. This electrode material and design has been selected as the working electrode in the following chapters.

For salt marsh and garden compost EABs, maximum current density values were in the order of 10 to 12 A/m^2. Comparing with the 19 A/m^2 obtained by Pocaznoi et al. (2012) the differences can be due to the acetate addition in pulses and the experiment temperature of 40°C. In our case, attaining high current density values was not the main goal; the two combined objectives to achieve were to obtain reproducible results and to mimic the electrochemical behavior of the bioanodes in macroelectrodes over a long period. This is why the best operational conditions were selected for salt marsh biofilms formed over SS microelectrodes in a high salinity medium.

From this point forward, the manuscript bifurcates into two main sections. On one hand, in the course of this chapter, questions arose regarding the performance of the multi-species EABs. It would appear that there is a link between the electroactivity, the biofilm thickness and the polarization time. Certain hypothesis, such as the effect of the extracellular exopolymeric substances in biofilm formation and the evolution of the microbial population were also briefly questioned. In Chapter IV and Chapter V, the standard experimental set-up is be maintained and the spatio-temporal evolution of the biofilms together with their electrochemical performance is investigated. On the other hand, in this chapter the implementation of Ag microelectrodes as pseudo-references was tested and discarded for their use in microBES. The idea of working on a two-electrode system at the microscale arose by the end of this chapter, which is further developed in Chapter VI.

Chapter IV : Correlation of the spatio-temporal evolution of salt marsh EABs on microelectrodes with their electroactivity in macroBES

IV.1. Introduction

In the previous chapter, experimental conditions for the formation of EABs on microelectrodes in 550 mL reactors were determined as to reproduce the typical current gradual decrease on bioanodes. The choice of SMS as the source of electroactive microorganisms to form EABs over SS microelectrodes polarized at 0.1 V/SCE, cultured in a synthetic saline medium with 40 mM of acetate added on a daily basis, played a role in the reproducibility of the temporal evolution of EABs electroactivity. The evolution of EABs electroactivity was in accordance with similarities between the SS microelectrodes and carbon macroelectrodes, both in terms of current density ranges generated and in terms of its evolution over time.

The aim of this chapter is to obtain further information on the spatio-temporal evolution of salt marsh EABs regarding biocolonization, cell viability, microbial and chemical composition in order to correlate them with the progression of the EABs electroactivity. The main results are summarized in the Research Article 2, which follows this introduction and represents the core of this chapter. Overall, salt marsh EABs were analyzed at four key stages of current production defined on the EABs electroactivity level. Biofilm growth, biofilm total cells and cell viability, EPS distribution and composition, and microbial relative abundance were studied at each stage. This systemic work involved a combination of state-of-the-art electroanalytical, confocal microscopy and genomic techniques. The development of protocols for identifying and observing the composition of EPS, as well as the successful recovery of small amounts of biofilm to study the microbial diversity, were key to reach a complete analysis at each stage, thus allowing a direct link to the salt marsh EABs electroactivity.

Following the article, a section is devoted to complementary experiments, which discuss the reliability of SMS as the source of electroactive microorganisms. Firstly, EABs were formed using the same batch of sediments than in Research Article 2 (Sampling date: March 2021) with the aim to confirm the evolution of the biofilm microbial population described in the article and the reproducibility of the EABs electroactivity. Then, as sediments were sampled every two to three months, EABs were also formed using two additional sediment batches (Sampling dates: October 2020 and January 2021) and using salt marsh in different sediment phases. The objective was to confirm if the electrochemical performance of the EABs was still reproducible and if the microbial diversity was maintained when the source of electroactive bacteria was sampled at different periods.

IV.2. Research Article 2

Systemic Analysis of the Spatiotemporal Changes in Multi-species Electroactive Biofilms to Clarify the Gradual Decline of Current Generation in Microbial Anodes

Lucila Martinez Ostormujof [a], Sébastien Teychené [a], Wafa Achouak[b], Sylvain Fochesato[b], Mohamed Bakarat[b], Issac Rodriguez Ruiz [a], Alain Bergel [a], Benjamin Erable* [a]

[a] L. Martinez Ostormujof, Dr. S. Teychené, Dr. I. Rodriguez Ruiz, Dr. A. Bergel, Dr. B. Erable.
Laboratoire de Génie Chimique
Université de Toulouse, CNRS, INPT, UPS.
4 allée Emile Monso, BP 94234
31432 Toulouse (France)
E-mail: benjamin.erable@toulouse-inp.fr

[b] Dr. W. Achouak, Sylvain Fochesato, Mohamed Bakarat
Lab of Microbial Ecology of the Rhizosphere (LEMiRE)
BIAM, UMR 7265 CNRS-CEA-Aix Marseille University
CEA Cadarache
13115 Saint Paul lez Durance (France)

Supporting information for this article is given via a link at the end of the document.

Abstract: The decrease in the electrochemical activity of multi-species microbial anodes in bioelectrochemical systems is the main bottleneck to overcome for bringing these technologies one-step closer to the industrialization stage. In this study, microsized stainless steel electrodes were implemented to investigate the distinctive electrochemical behaviour of salt marsh electroactive biofilms (EABs). Four main temporal stages of biocolonization and electrochemical activity were thoroughly described. Maximum biofilm growth rate, high viability and high extracellular protein matrix content favoured the increasing electrochemical activity of the EAB up to its maximum current peak. Then, when gradual fall in current became irreversible, biofilm growth rate decreased together with dead cells accumulation and an increase for extracellular polysaccharides. In addition, analyses of microbial populations showed a shift from *Marinobacterium* spp. to *Desulfuromonas* spp. These findings suggest a chemical and microbial temporal evolution of the EAB, which can be directly correlated to the electrochemical performance of the bioanode.

1. Introduction

Bioelectrochemical systems (BES) are unique environmental technologies with a wide range of applications today: energy conversion, wastewater treatment, soil remediation, electrofermentation, bioelectrosynthesis of energy carriers and chemical building blocks, and biosensors [1-3]. Their ability to transform organic waste streams into energy positions BES as a promising technology for a circular bioeconomy [4], a reduction of the environmental footprint of processes and an environmental biorefinery strategy. The operating principle of BES is based on the central operation of EAB which catalyses bioelectrochemical reactions of mass and energy transformation. In the specific case of the bioanode, the electroactive microbial biofilm catalyses the oxidation of various organic substances to produce an electric current that is captured by the anode. Microbial bioanodes thus represent the functional core of BES [5].

However, despite all the strategic, economic and ecological advantages and opportunities offered by BES, their implementation is still at the laboratory scale, even though these technologies were first demonstrated more than 20 years ago [6-7]. The issue of scaling-up of BES or the low current densities supported are widely recognized obstacles to the industrial democratization of these technologies [8-9]. Also, the loss of electrochemical activity on microbial bioanodes seems to be the main barrier to overcome in order to improve the long-term sustainability of BES. A large number of studies (Table 1) have indeed documented anode current densities with mixed electroactive biofilms that severely drop after a few days or tens of days of operation, sometimes even losing more than 50% of their maximum performance. Among the possible causes reported to explain the loss of electrochemical activity of microbial bioanodes, it is acknowledged:

(i) a restrictive active biofilm thickness: this means that the biofilm is electrochemically active at low thicknesses and then its activity gradually decreases as the biofilm grows [10]. This phenomenon can be explained by a change in the predominant electron transfer mechanism when the biofilm reaches a threshold thickness [11] or limitations in the respiration rates of the biofilm when it is distant from the electrode [12-13].This has been mainly studied using pure strain bacteria of *Geobacter Sulfurreducens*.

(ii) nutrient and/or substrate depletion in the anolyte, and/or generation of metabolic by-products over time, and/or the presence of oxidized chemical compounds that may inhibit microbial growth or compete with the electrode as an electron acceptor [14]. Working in fed-batch mode when current generation in the bioanode decreases showed improvements in the electroactivity of the EAB. In addition, the use of artificial wastewater allows the composition of the anolyte to be controlled, thus avoiding deficiencies and the contribution of possible soluble electron acceptors in the liquid medium [15](Blanchet et al., 2015).

(iii) Increasing spatial, microbial and chemical heterogeneity within the biofilm, creating inactive regions that do not contribute

to electrochemical activity. This is mainly caused by nutrient and substrate gradients between the liquid bulk and the internal body of the biofilm [16], variation in redox potential in the biofilm matrix as the distance between the bacterial cells and the electrode increases [17-18], as well as a local acidification due to proton production from substrate oxidation [19-20].

(iv) Excessive accumulation of extracellular polysaccharides in the exopolymeric biofilm matrix. Studies with pure *Geobacter Soli* strains [21] and mixed population inoculums enriched with *Geobacter* [22-23] showed a negative correlation between increased polysaccharide and current production, due to their insulating nature.

Table 1. Overview of diverse BES that reported a decline in the anodic electrochemical activity when working with mixed-culture EABs.

Ref.	Year	Electrode	Size of the electrode (cm^2)	Inoculum	Substrate	Medium	Polarization time (days)	Polarization potential	T (°C)	System	Decline in electrochemical activity (%)
This work [1]	2022	Stainless steel microwire/ Platinum microwire	0.031	Salt marsh sediments	Acetate	Synthetic medium	56	0.1 V/SCE	56	Three-electrode system	60
[24]	2019	Graphite plates	4	Activated sludge	-	Domestic wastewater	25	-0.1 V/SCE	Not controlled	MEC	50
[25]	2019	Carbon granules	137	Second generation of inoculum[2]	Acetate	Synthetic medium	73	Variable	28	Three-electrode system	80
[26]	2019	Carbon felt	6	Hypersaline sediments	Acetate	Synthetic medium	10	-0.1 V/SCE	45	MEC	85
[27]	2019	Carbon felt	2	Activated sludge	Acetate	Tannery wastewater	40	-0.2 V/SCE	30	Three-electrode system	90
[28]	2018	Fluorine-doped tin oxide (FTO) plates	22.3	Second generation of inoculum[3]	Acetate	Synthetic medium	24	-0.35 V/AgAgCl	not controlled	Three-electrode system	40
[29]	2018	Carbon cloth	4	Garden compost	Acetate	Synthetic medium	31	-0.2 V/SCE	40	Three-electrode system	50
[30]	2018	Carbon felt	7	Hypersaline sediments	Acetate	Synthetic medium	21	0.34 V/SHE	not controlled	Three - electrode system	20 to 40
[31]	2018	Carbon glass plates	4	Second generation of inoculum[4]	Acetate	Synthetic medium	10	-0.1 V/AgAgCl	28	Three-electrode system[7]	20 to 40
[32]	2011	Graphite felt	4	Compost lechate	-	Dairy waste	20	0.1 V/SCE	not controlled	Three-electrode system	85
[33]	2009	Stainless steel plates/Plain graphite plates	25	Marine biofilm	Acetate	Seawater	10	-0.1 V/SCE	not controlled	three-electrode system	35 for plain graphite, 85 for stainless steel grid
[34]	2009	Graphite felt	250	Second generation of inoculum[5]	Acetate	Synthetic medium	67	-	30	MEC	50
[35]	2008	Roughened graphite plates/ Pt-coated titanium plates/ Flat graphite plates	22	Second generation of inoculum[6]	Acetate	Synthetic medium	30	Variable	30	MFC	90 in all cases

[1] See section 2.1. [2] Mixed community from a MEC running on acetate. [3] Biomass from active acetate oxidizing bioanodes. [4] Effluent from an acetate-fed BES. [5] Effluent from a MEC running on acetate. [6] Effluent from a MFC running on acetate. [7] Eight working electrodes in the anodic chamber.

All of these fundamental achievements are of major interest, even if most of them are limited to research on pure model strains such as *Geobacter Sulfurreducens*. However, the use of a bacterial consortium implies that the mechanisms of biofilm formation are different from one species to another, that electroactive bacteria coexist with non-electroactive bacteria, and that the mechanisms of electron transfer and extracellular polymeric substances (EPS) synthesis can be significantly diversified within the biofilm. This makes multi-species electroactive biofilms a very complex topic of investigation, especially if we are interested in its dynamics over long time scales. Therefore, the usual methodological approaches to investigate anodic biofilms of microbial bioanodes are classically conducted at the global scale of the biofilm, by implementing macroelectrodes in BES of several milliliters to several liters. With these configurations, the control of constant physico-chemical conditions at the anode - liquid bulk interface is difficult to guarantee. Also, the use of non-planar electrodes such as felts, cloths, brushes or any other geometry with minimal porosity or roughness results in potential gradients that are not ideal for conducting fundamental studies [36] .(Pinck et al., 2020)Structural analyses of biofilms are mostly performed after sampling the bioanodes in BES and after post-treatments (collecting, cleaning, fixing, specific labelling, dehydration...) that heavily affect the native configurations and properties of the biofilms. These analyses, whether chemical, microscopic, genetic or functional, are generally carried out at a single time point in the experiment, usually at the end of the run. This non-consideration of the dynamics of the biofilm as an evolutive living system, where its properties evolve temporally and spatially, contributes to a great loss of valuable information in relation to its electroactivity.
The integration of wire-based microelectrodes in BES allows, on the contrary, to work with physicochemical conditions and theoretically homogeneous potentials at the microelectrode - bulk liquid interface. Also the mass transfer is considerably less limited in the periphery of the wire microelectrodes [37](Salvatore and Bragato, 2014). This property is valid both for promoting the formation of homogeneous anodic electroactive biofilms [38], as well as for post-treating the biofilms homogeneously and rapidly with aqueous marking solutions (dye, DNA probes, fluorescent substances) or cleaning solutions.
In the present study, we investigated the correlation between the electrochemical activity of multi-species microbial bioanodes and the spatio-temporal dynamics of biofilm formation. For this purpose, stainless steel microelectrodes were implemented as anode materials in BES. Electroactive salt marsh biofilms were formed under constant polarization on these stainless steel microelectrodes. Biofilm growth, microbial viability, EPS composition, and bacterial species abundance were determined on the biofilm volume at four key stages of microelectrode biocolonisation. The use of a fed-batch feeding system was also applied in stages where electrochemical activity falls with the objective to recover the loss of electroactivity observed over the long term. We aim to elucidate the process change that contributes to the loss of performance of the microbial anodes for the future definition of strategies that could improve their long-term durability.

2. Results and Discussion

2.1. Microelectrodes are a suitable tool to study the mechanisms of biofilm formation

Salt marsh electroactive biofilms from hypersalty sediments were formed in duplicate under constant polarization of 0.1 V/SCE for a total time of 55 days. This potential value was applied according to similar experiments performed in the last 10 years with salt marsh inoculum and a concentration of 45 g/L of NaCl [39]. After the polarization, the biocolonization and physical structure of biofilms was observed under epifluorescence microscopy and scanning electron microscopy.

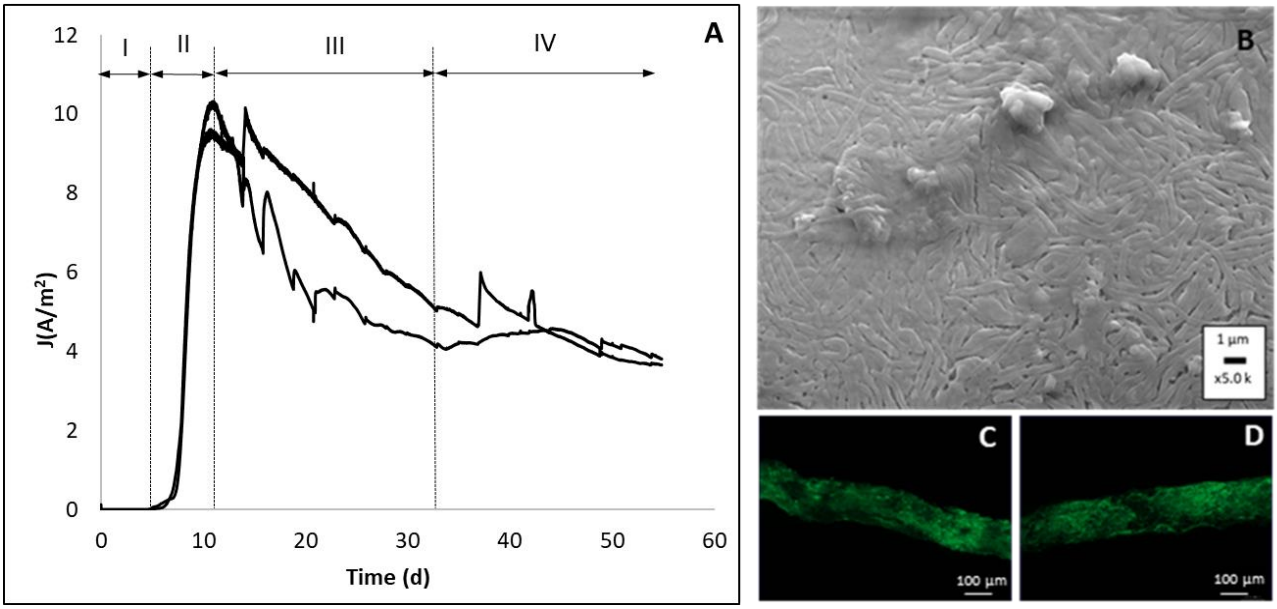

Figure 1. (A) Current production versus time for duplicate experiments obtained with stainless steel microelectrodes colonized by salt marsh EABs under constant potential of 0.1 V/SCE. (B) Scanning electron microscopy imaging of the biofilm surface over the stainless steel microelectrode. (C, D) Biofilm imaging by epifluorescence microscopy after staining the electrode with acridine orange.

The four stages shown in Figure 1 (A) can be described as it follows:

Stage I: Initial lag phase: After inoculation, electroactive bacteria present in the microbial salt marsh consortium needs to adapt to the anoxic and highly saline environment, and to the 40 mM of acetate in the synthetic medium. In this period, current is not produced in the anode. Stage I was described for the time when current reaches 0.1 A/m^2 as adapted from a previous study [29]. In our case, duplicates reached that value at a time of 5.9±0.5 days.

Stage II: Maximum current production phase: Later, current increased sharply, reaching a maximum current density value. This peak is known as J_{max} and for the two duplicates it corresponded to J_{max}=10.0±0.5 A/m^2.

Stage III: Current decrease phase: Even if the concentration of electron donor was regularly monitored and kept at a constant value of 40 mM all along the experiment, the maximum current value was not mantained. Current decreased progressively in both reactors in a period of 20 days, reaching a final value at day 31 of 4.9±0.8 A/m^2.

Stage IV: Stabilization – long term current phase: Starting from day 31 of the experiment, the decrease in the electrocatalytic activity of the biofilm changed its slope, to a less drastic one, reaching an average current density value of 3.7±0.1 A/m^2 at day 55. The loss of current density in comparison to J_{max} reached at stage II was of 62.5±0.8%. This not only corroborated the same behaviour between duplicates, but also a loss of the electrochemical activity of the bioanodes of more than 60% of their maximum capacities.

Epifluorescence microscopy images performed at day 55 showed a complete coverage of the SS microelectrode by the salt marsh EAB. The scanning electron microscopy (SEM) image confirmed this since the biofilm exhibited a dense and compact rearrangement of cells, tightly spaced within each other.

As the results presented were reproducible in terms of current production curves, the experimental conditions were repeated in the sections below. Figure S2 shows the totality of the normalized current density curves obtained for this work with the removal of the lag phase. Despite the duration of the lag-phase (stage I), the kinetic behaviour was reproducible for stage II. This trend was followed by a decrease in current in all cases (stage III and IV). Thus, the first conclusion indicates that microelectrodes are a very convinient tool to study the mechanisms of biofilm formation since they are able to succesfully reproduce the same behaviour in terms of catalytic activity of the bioanode as for large-scaled electrodes.

2.2. Spatiotemporal investigation of biofilm thickness and cell viability

The experiment described in section 2.1 was repeated. However, in this case, the experience was stopped at four strategic points, corresponding to the end of the four stages previously described. The experiments were one more time conducted in duplicates, as seen in Figure 2. A cyclic voltammetry (CV) was also performed. At each stage, biofilm thickness, biofilm growth rate and cell viability were primarily quantified using numerical methods associated with image analysis. Results are summarized in Figure 3, and more detailed information can be found in Table S1.

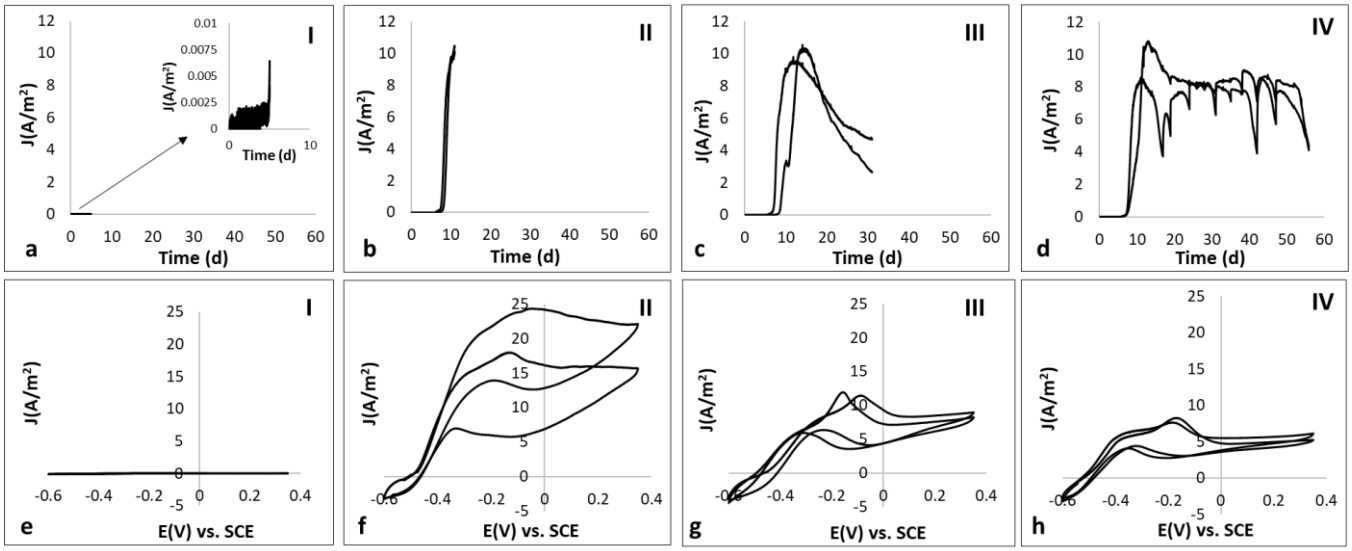

Figure 2. Evolution of current density versus time for duplicate experiments (a-d) at different stages of the experiment and their corresponding final cyclic voltammetry at a scan rate of 1 mV/s (e-h). (I) at t=5 days, (II) at t=11 days, (III) at t=31 days and (IV) at t=55 days of experiment.

At stage I, the average thickness of biofilms was of 6.2±1.1 µm and the colonization of the biofilm over the microelectrode was heterogeneous, where different cell clusters were observed in the electrode surface. Average current measured in this point was of 0.005±0.001 A/m^2. The counting of dead cells was the minimum for this stage, where confocal laser scanning microscopy (CLSM) viability images showed the microelectrode surrounded mostly by living cells.

At stage II, six days later, the biofilm reached a thickness of 32.1±5.7 µm, with a maximum biofilm growth rate of 4.3 µm per day. At this point, current density was at its maximum of 10.2±0.4 A/m^2. The SS microelectrode appeared now to be completely colonized by the biofilm. The average percentage of dead cells increased to 65.2±6.3% in the outer layer of the biofilm. The rapid growth of the biofilm, while reaching the limit of its electrochemical

activity, may have also contributed to the accumulation of inactive cells.

At stage III, current dropped to an average value of 3.7±1.4 A/m^2. The thickness of the biofilm kept on increasing but with a lower rate of 0.8 µm per day. The structure of the biofilm was less rough and appeared to be more compact, as seen in scanning electron microscopy images in Figure 4.

Finally, for the reactors stopped at stage IV, average registered current density was of 4.2±0.1 A/m^2. At this stage, current density values should have been lower than in stage III; however, salt marsh EABs still performed better in the reactors intended for stage IV. Biofilm growth rate was only 0.4 µm per day, with no significant changes in the structure of the biofilm comparing with stage III. The percentage of dead cells reached the maximum value of 77.3±9.3%.

In addition, cyclic voltammograms from different stages showed a progressive evolution on the anodic catalytic properties of the biofilm (Figure S3 for more detail). At stage I, the electrode was barely colonized; therefore, the anodic current was low independently of the potential. At stage II, when the maximum current production was measured, the largest hysteresis was observed between the forward and backward scan of the voltammetry. At higher accumulation of charges, more marked was the capacitive effect. Since the curves in this stage were not equal in both scanning directions, the hysteresis phenomenon was not only attributed to a simple capacitive effect. It is possible that the scanning of the potential induced reactions in the biofilm, which are not reversible. Starting from stage II, the effect of the capacitive current seemed to diminish. At stages III and IV, when current was lower, the shapes of the CVs were similar. An oxidation peak could be seen at -0.2 V/SCE.

The changes on biofilm viability showed an external layer evolving from active cells at the start of the experiment towards a dead cell outer-layer by the end. Despite precautions, the possibility that the exposure to oxygen may have inactivated certain external cells when removing the bioanode from the reactors for dye labeling did not seem to be an influencing factor since the biofilm with the smallest biovolume had the higher amount of viable cells. Although it was not possible to quantify the ratio of live/dead cells in the inner layers of the biofilm (probably only for stage I where the biofilm was still very thin) since the cylindrical geometry of the bioanode only allowed the quantification in the outer layer, the trend seemed to match previous observations for EABs applying the same dead/live staining protocol. In these cases, an inner active core is surrounded by inactive cells, where it would appear that current production was achieved by the cells near the electrode surface. However, when the biofilm reaches a specific thickness threshold, the cells farther away from the electrode become limited in terms of respiration rates. The distant solid electron acceptor makes these cells unable to contribute to biofilm growth and sustained current production [13,40,41](Chadwick et al., 2019; Nevin et al., 2008; Schrott et al., 2014). The opposite case, an inner dead core and an external viable layer was also reported. In these cases, biofilm internal acidification due to acetate oxidation and diffusional gradients inside the biofilm, as well as the fraction of reduced and oxidized extracellular components involved in the electric conductivity such as c-type cytochromes, could lead to an internal layer of dead cells [10,19]. In this case, it was proved that the outer layer was responsible for current production whether the inner dead-layer served as a conductive matrix [16-42].

Our results affirm that the biofilm must be growing and their cells must be active to express electroactivity. Therefore, although thick biofilms up to 57.7±8.5 µm can be formed, the maximum electrochemical activity was found at a much thinner thickness of 32.1±5.7 µm. SEM images showed that the major growth in biovolume occurred between stage I and II, matching with the increasing current density slope in the chronoamperometry. From the end of stage II, electroactivity dropped and the viability of the anode kept on decreasing together with the biofilm growth rate. Starting from stage III onwards, it would appear that the biofilm underwent very slight changes. In terms of morphology, SEM images showed very similar structures between stage III and IV. Current reached a steady state and the amount of dead cells in the external surface augmented. Biovolume increased but at the lowest pace. At these final stages, the thickening of the biofilm was possibly related to higher exopolymeric substances secretion rather than cell multiplication.

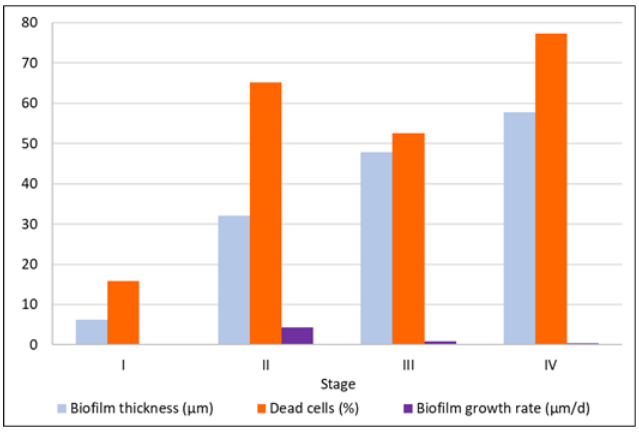

Figure 3: Evolution of the biofilm thickness, the biofilm growth rate and the percentage of dead cells in each of the four stages as defined in section 2.2.

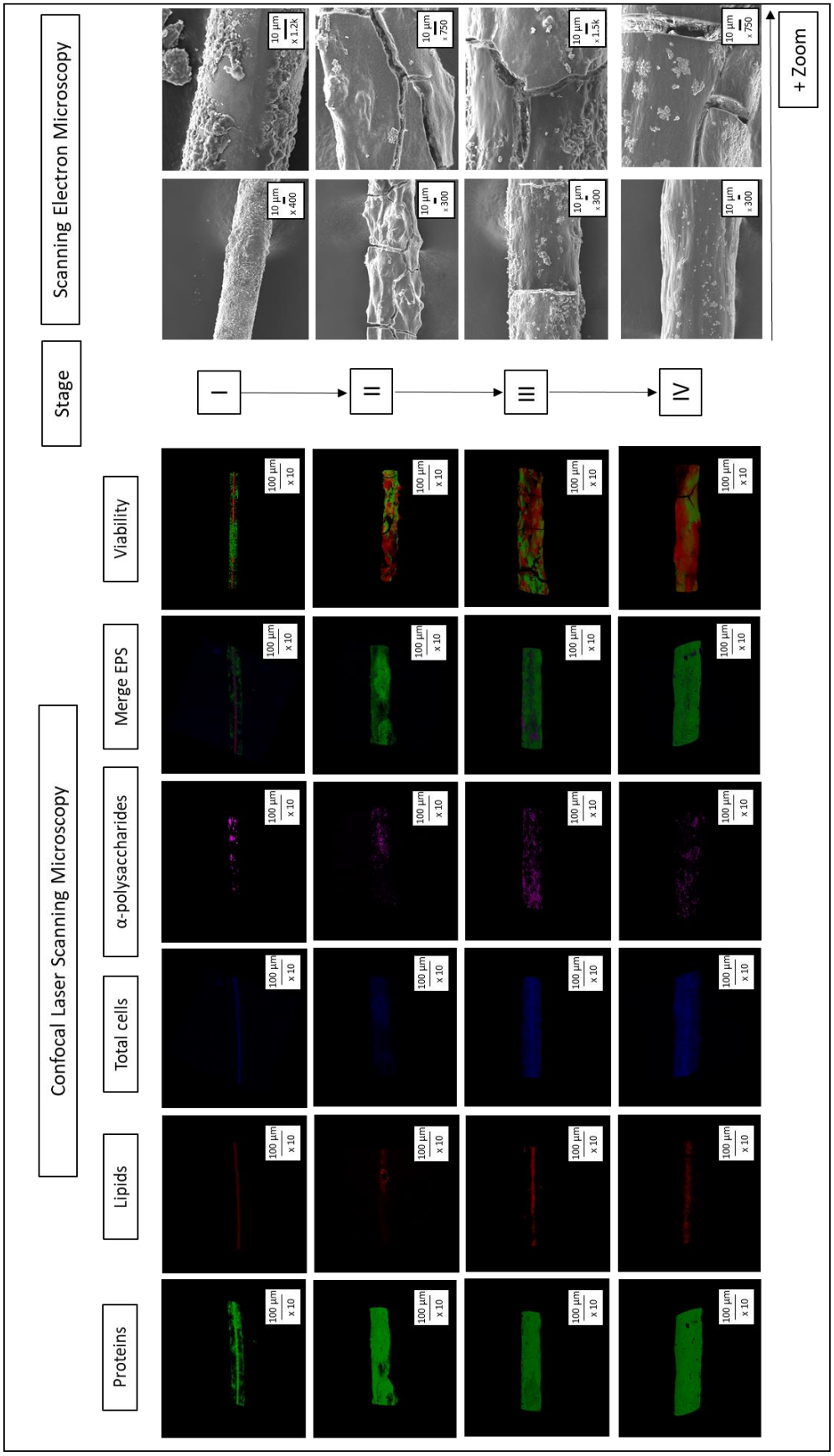

Figure 4: CLSM 3D-images and SEM images of salt marsh biofilms formed on stainless steel microelectrodes at each of the four stages defined in section 2.2 and section 2.3

2.3. Spatiotemporal investigation of exopolymeric substances, microbial populations and soluble electron acceptors

A new series of experiments was launched with the objective of continuing the study at the four stages, focusing in the evolution EPS composition and the dynamics of microbial population. The 3D representations of the biovolumes from different EPS (proteins, lipids, α-polysaccharides and total cells) obtained from the CLSM analysis are presented in Figure 4. Following the post-processing of CLSM images, the quantification of the EPS percentages at each stage are graphically represented in Figure 6 and centralized in Table S1.

The results of the relative abundances of the different bacterial orders and genera present in the biofilms at the four stages of bioanode formation are summarized in Figure 7 and Table 2. The analysis goes until the genera level in all cases with the exception of *Desulfuromondales* and *Bacteroidales*, which correspond to the order level. It is worth clarifying that *Marinilabilia* classifies into the *Bacteroidales* order and *Desulfuromonas* to *Desulfuromondales*. In addition, Table S2 shows the results for inductively coupled plasma (ICP) analysis of the evolution in the concentration of sulfur, iron and manganese contained in the synthetic medium.

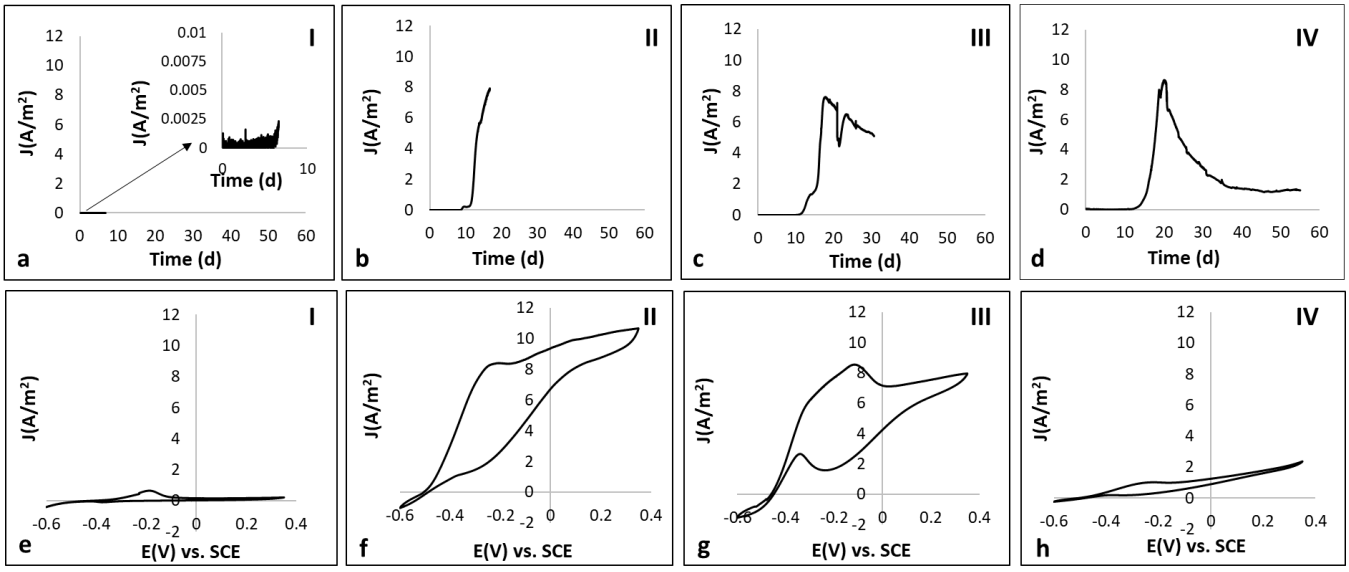

Figure 5. Evolution of current density versus time for duplicate experiments (a-d) at different stages of the experiment and their corresponding final cyclic voltammetry at a scan rate of 1mV/s (e-h). (I) at t=7 days, (II) at t=11 days, (III) at t=31 days and (IV) at t=55 days of experiment.

At stage I, current density did not exceed a value of 0.002 A/m^2. For the determination of the components of the polymeric matrix at this stage, the biofilm was mainly composed by proteins at a percentage of 60.2±1.6%. In terms of bacterial diversity, there was an important dominance of *Marinobacterium* with 87.0% of abundance. This was followed by *Arcobacter* with 9.3%.

At stage II, when current density production reached a value of 7.9 A/m^2, the amount of total cells increased as well as the amount of proteins. At this stage, the occurrence of proteins reached a maximum of 71.1±8.6%. The abundance of *Marinobacterium* decreased to 72.9% and *Arcobacter* was only scarcely present. The biofilm community became more diverse, with the appearance of other bacterial genera such as *Halanerobium* and *Thermotalea* present at 4.0% and 3.5% respectively.

At day 31, current reached a final value of 5.1 A/m^2. At stage III, the biovolume of total cells over the total biovolume was the highest of the stages, reaching a value of 38.5±3.7%. Concerning EPS, the production in protein based polymers decreased in comparison to stage II to 45.7±1.2%, whereas the amount of polysaccharides almost doubled its value (from 5.0±1.5% to 9.1±0.3%). The presence of *Marinobacterium* remained almost stable in comparison to stage II. There was an emergence of *Desulfuromondales* order and *Marinilabilia* genera. In addition, the concentration of sulfur in the synthetic medium decreased abruptly, from 17.8 mg L^{-1} in stage II to 1.1 mg L^{-1} in stage III.

At stage IV, final current density was of 1.3 A/m^2. The biovolume of total cells decreased with respect to stage III, whether the production of protein polymers increased and the value for polysaccharides-protein ratio was the lowest of the series. An important shift on the genera present in the biofilm community was observed, since *Desulfuromonas* became dominant with 68.5% of abundance and the presence of *Marinobacterium* was hardly detectable.

The cyclic voltammograms showed the same trend that in section 2.2. There was likewise an evolution on the biofilm, with more marked hysteresis at higher current (Figure S4 for more detail). Yet, an oxidation peak was found around -0.2 V/SCE.

The temporal evolution of the exopolymeric substances showed an increase throughout the four stages, as highlighted in the CLSM images of Figure 4, where a widening of the EPS was observed from stage I to IV. To support results from section 2.2, as the biovolume of total cells diminished from stage III to stage IV, the increase of thickness between these two stages was probably due to an enlargement of the matrix rather than cell multiplication. It can be hypothesized that the presence of a thick layer of EPS could play a role as a diffusive barrier, thus preventing the substrate and/or nutrient diffusion needed for cell growth [43].

The EPS of electroactive biofilms work as a tridimensional conductive matrix when electrons are transferred from the bulk to

the anode within the biofilm. Extracellular proteins store redox compounds, such as cytochrome-c, involved in electron transfer [44,45]. Polysaccharides, on the other hand, are known to be in the conductive range between semiconductors and insulators, probably decreasing the electrical conductivity of the matrix [46]. However, their presence in the matrix is essential for cell anchoring and protection mechanisms, in addition to many other structural, ion exchange and nutrient source (e.g. carbon source) functions [47]. The highest percentage of extracellular proteins was found in stage II, in coincidence with the peak of electrochemical activity of the biofilm. Significant positive correlation has already been found between steady-state current in mixed-culture bioanodes and protein content in EPS [22]. For α-polysaccharides, the highest content was in stage I. Nevertheless, it is relevant not to lose sight of the fact that the temporal analysis of the matrix implies that the volume of the exopolymeric substances also evolves in time. Probably, the elevated percentage values of stage I in comparison to the rest of the series, was due to the low colonization of the electrode, which exacerbated the results. This was also confirmed with the results of CLSM images, which showed the highest polysaccharides content at stage III.

The ratio of α-polysaccharides to proteins can be seen as a useful parameter to normalize the results when analyzing the EPS evolution of EABs. The highest value was obtained at stage I, probably due to the adhesive function of polysaccharides to the anode at the early stages of biofilm formation [48]. Later, in stage II, the ratio decreased to a third of its value and later re-increased 2.5 times at stage III. Extracellular polysaccharides production after the current peak might have decreased the conductivity of the biofilm matrix. This was already reported for Geobacter biofilms, where the secretion of extracellular polysaccharides was more elevated in the bioanodes with the weakest electrochemical performance [21]. The ratio decreased for a second time at stage IV. As the percentage of total cells was lower in stage IV than in stage III, proteins content raised in the total biovolume regarding stage III, therefore decreasing the ratio of α-polysaccharides to proteins.

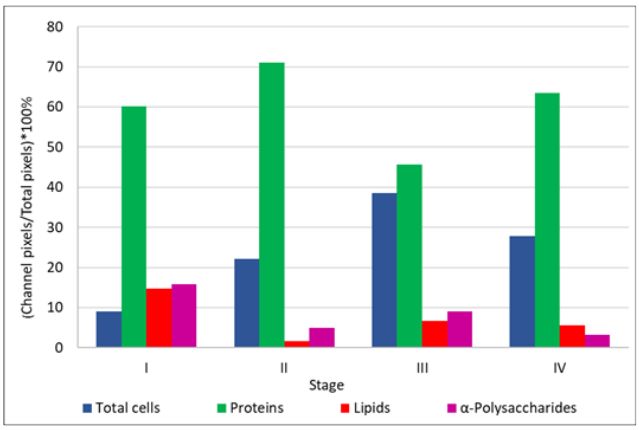

Figure 6. Bar chart illustrating the evolution of EPS composition at each of the four stages.

The dynamics of microbial community showed a sparse colonized bioanode at the end of stage I highly dominated by *Gammaproteobacteria*, mainly enriched with *Marinobacterium*. Species present in this genus were typically found in electroactive biofilms formed from natural marine environments [49], salt marsh sediments [50] and hypersaline coastal lagoons [51. *Marinobacterium* strains are gram-negative, facultative anaerobic and they require NaCl for growth in a concentration range of 1.0–7.5% NaCl [52]. *Arcobacter* species were also present in the biofilm community of the bioanode. Their abundance in coastal environments and their electroactivity were also reported [53-55]. Their incidence at the early stages could be related to their ability of enhancing the secretion of flagellin proteins at anaerobic conditions [56].

At stage II, the relative abundance of the community shifted and the amount of *Marinobacterium* decreased from 87.0% to 72.9%. In addition, *Arcobacter* was merely present in the biofilm. At this step, the bacterial diversity included species from Clostridia, such as *Thermotalea* (3.5%) and *Halanaerobium* (4.0%), and from *Deltaproteobacteria* with the presence of *Desulfuromondales* (2.2%) order and *Desulfuromonas* (2.0%). The appearance of strictly anaerobic microorganisms in the biofilm was not surprising. *Halanaerobium* is known as a halophilic electroactive bacteria [26], which probably grew in the highly saline environment of the synthetic medium at the early stages and then was able to colonize the electrode. At day 31, the dominance of *Marinobacterium* (74.1%) remained constant with respect to the previous stage. *Halanaerobium* abundance decreased to 2.4% and *Thermotalea* was not detectable. *Desulfuromonas* increased to 2.6% and *Desulfuromondales* order to 5.7%. In this stage, there was the appearance of *Marinilabilia* (3.7%), a facultative anaerobic bacteria usually found in mud marine sediments.

The most relevant observation from the microbial analysis occurred at stage IV. At day 55 there was a dominance of *Desulfuromonas* (68.5%) with the quasi undetectable amount of *Marinobacterium* (0.6%). *Desulfuromonas* species were already identified in EABs from the same inoculum source [57]. The interest in analyzing the temporal evolution in the amount of sulfur, iron and manganese in the culture medium containing the inoculum was based in the properties of certain bacteria to use these compounds as terminal electron acceptors [6,58]. In the case of *Desulfuromonas*, species from the genera can reduce elemental sulfur to sulfide and also grow by transferring electrons to insoluble iron oxides [59,60](Pfennig and Biebl, 1976; Pierra et al., 2015). The evolution of the microbial population over time is hypothetically based on the initial planktonic growth of *Desulfuromonas* in the liquid phase through acetate oxidation and elemental sulfur reduction to sulfide. The incidence of *Desulfuromonas* in the biofilm was visible from stage II and later slightly increased in stage III, where sulfur concentration in the liquid phase decreased abruptly. As in stage III the sulfur content was scarce, probably the amount of *Desulfuromonas* present in the liquid environment had to shift their respiring mechanism from sulfur to the electrode, which could explain the prevalence of *Desulfuromonas* in the biofilm at stage IV.

It can be supposed that at the early stages *Marinobacterium* was the most efficient anode respiring bacteria, taking advantage of a fresh synthetic medium with NaCl and acetate, and prevailing in a non-strictly anaerobic environment. The temporal medium evolution along with the growth of other planktonic electroactive bacterial species that later colonized the anode led to a sharp increase in the electroactivity. Given the fact that the almost complete shift from *Marinobacterium* to *Desulfuromonas* between stage III and IV did not generate drastic changes in the catalytic activity of the bioanode and that *Marinobacterium* was present since stage I, it could be thought that it is the contribution of the

minority bacteria that played the most important role in the production of current.

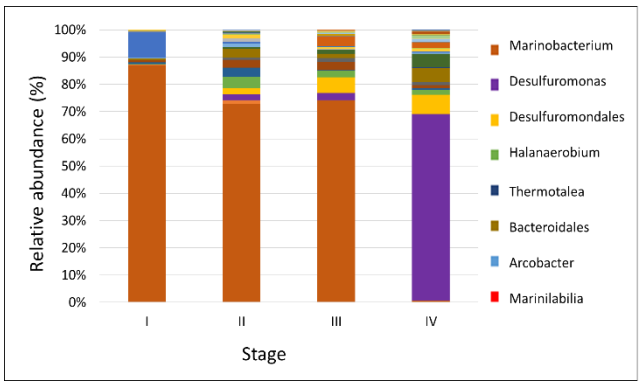

Figure 7. Relative abundance of different order or genera at the four stages of biofilm formation. Main abundances are resumed in the list on the right.

Table 2. Detailed relative abundance at different order or genera in the biofilm at the end of each stage. The three more relevant microbial abundances for each stage are in bold.

	Stage			
Order/Genera	I	II	III	IV
Marinobacterium	**87.0**	**72.9**	**74.1**	0.6
Desulfuromondales	-	2.2	**5.7**	**6.9**
Desulfuromonas	-	2.0	2.6	**68.5**
Arcobacter	**9.3**	0.5	-	0.5
Halanaerobium	-	**4.0**	2.4	1.1
Marinilabilia	-	-	**3.7**	2.1
Bacteroidales	0.5	3.1	1.6	**5.2**
Thermotalea	0.7	**3.5**	0.2	0.5

2.4. Late stages of biofilm formation: Reversibility or irreversibility of the electrochemical activity?

A series of two duplicates were again carried out under constant polarization of 0.1 V/SCE in order to test whether at the end of stage III, the anodic current density could be reestablished to its maximum value. For this reason, at day 27, corresponding in practice here at the end of stage III, the polarization was stopped and a fresh batch of medium with 40 mM of acetate was added to the reactors. As no considerable change in current production was observed, the reactors were re-inoculated with salt marsh sediments on day 29. At day 55, the polarization was stopped and microelectrodes were retrieved for future microbial population analysis.

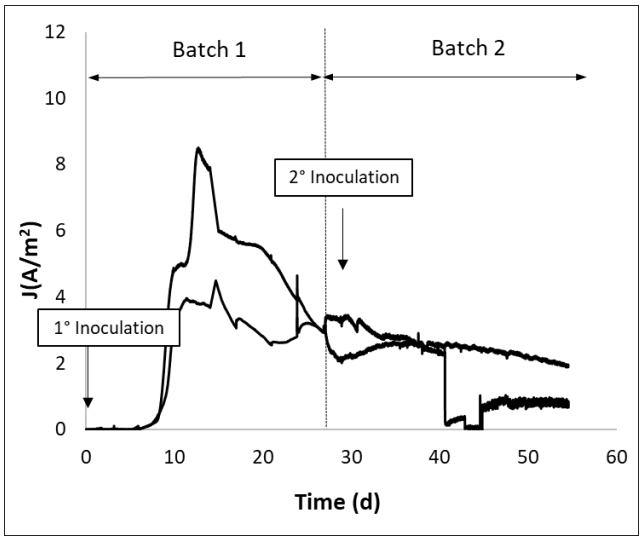

Figure 8. Evolution of current density versus time for duplicate experiments. The reactors were inoculated with salt marsh at t=0 days (1st Inoculation). At t=27 days, the medium was replaced with a fresh batch of Starkey medium (Batch 2). At t=29 days, 30 mL of salt marsh were added to the reactors (2nd inoculation).

The average current registered before the addition was of 2.8 ± 0.9 A/m^2 and of 2.7 ± 0.8 A/m^2 after the inoculation. The dramatic drop of current for one duplicate at day 40 was probably due to a connection issue, since current slightly increased when the connections and the reference electrode were changed. Acetate concentration was also checked to ensure that the drop was not due to a depletion in the quantity of the electron donor. Therefore, the replacement of a new batch of medium, and consequently of inoculum, did not improve significantly the catalytic activity of the biofilm. The shape of current production profiles showed the same trend that in the sections above.

The results discard the hypothesis that working in batch mode can lead to the depletion of certain bacterial nutriments or components in the medium, which could work as electron shuttles. Strategies linked to medium replacement were already described for *S.Oneidensis* biofilms to probe mediated electron transfer [61] and also for *G.Sulfurreducens* to demonstrate that the cells attached to the anode surface were responsible for current production [62]. In the case that bacteria could use soluble compounds for electron transfer, current would have increased considerably when replacing the medium. Examples of in current production were already observed when switching from real medium BES operation to synthetic medium. This was due to the resupply in vitamins or minerals present in the synthetic medium and/or the absence of dissolved electron acceptors, such as nitrates and sulfates, that could compete with the electrode to accept electrons [14]. Working with a synthetic medium from the start of the experiment avoids the presence of electron sinks, which proved to be the case as the electrochemical activity of the biofilm was not improved. This is also consistent with what was observed for the cyclic voltammetries in Figure S5. The difference between Batch 1 and Batch 2 could be due to the biofilm short exposure to air when replacing the medium. In addition, before and after inoculation, curves were also similar.

Relative abundance of microbial population at day 55 showed two biofilms with the same dominance but in different proportions. *Marinobacterium* accounted to 38.3% and *Desulfuromonas* to

44.3% in the sample with the highest current peak. In the other replicate, *Marinobacterium* only represented 9.8%, while *Desulfuromonas* constituted 14.1% and *Desulfuromondales* 33.0 %. Therefore, the total presence of sulfur reducing bacteria was similar in both cases, yet minor than in the bioanode at stage IV in section 2.3 (68.5%). This means that what the change of medium might have affected is the amount of sulfur-reducing bacteria already grown in the liquid electrolyte at day 27. In section 2.3 it was described that the period between stage II and III corresponded to the depletion of sulfur in the liquid environment. Re-inoculation on day 29 probably restored sulfur concentration, giving the possibility to sulfur-reducing bacteria to proliferate, grow and later colonize the electrode.

2.5. General discussion

Microbial bioanodes formed on stainless steel microelectrodes with salt marsh inoculum at an applied potential of 0.1 V/SCE accurately reproduced the classical time evolution of the electrochemical activity of biofilms already reported with macro-scale bioelectrodes. The long-term (>50 days) loss of J performance was also consistent with that described in the literature, ranging from 30 to 50% of J_{max}. This systemic study on mixed population electroactive biofilms, including microscopic, electrochemical, biochemical and microbiological characterisations, allowed significant progress to be made on the correlation between anode current production and the spatio-temporal evolution of mixed population microbial biofilms on metallic anodes.

In terms of biocolonisation on the surface of the stainless steel microelectrode, the bacterial cells initially developed as isolated clusters until they gradually formed a thick homogeneous layer on the surface of the microelectrode. This rough-edged structure then became much smoother at the end of stage III, mainly due to the production of EPS. Regarding the kinetics of biofilm growth and thickening, the biofilm reached maximum electrochemical activity at a thickness of ~ 32 µm while growing at a rapid rate (4.3 µm/d). However, the electrochemical activity then decreased, accompanied by a lower growth rate (0.4 µm/d) which led to an increasing thickness to ~ 57 µm. The cell viability rate also changed significantly as the biofilm thickened for 17 days. The high viability in the early stages of biocolonisation suggested that current generation was more related to viability rate than to biofilm thickness.

The role of the biofilm EPS matrix and its evolution over time in relation to the electrochemical activity of the biofilm is not yet so simple to explain. On the one hand, when the microbial biofilm reaches a threshold thickness, electron transfer can be quite limited depending on the mechanisms used by the exo-electrogenic microorganisms. Mixed population bioanodes add further complexity because several types of electron transfer mechanisms coexist and because insulating, non-active EPS, hindering the chemical diffusion of species, can be synthesised by non-electroactive microbial populations. On the other hand, the progressive production of EPS, and the change over time of the chemical composition of the EPS matrix also has an impact on the overall electrical conductivity of the biofilm. In the early stages of biocolonisation, as soon as the biofilm adhered to the anode, the ratio of polysaccharides to proteins was balanced in favour of the protein content, meaning that the electrical conductivity of the matrix was increased. In addition, the coupled effect of a thin and more viable biofilm probably annihilated all kinds of gradients as well as promoting metabolic and electrochemical processes accordingly. After the current reached its peak J_{max}, the widening of the EPS matrix and the specific accumulation of polysaccharides, at the detriment of proteins, inhibited the possibility of maintaining a stable and high current approaching the maximum value.

The temporal distribution of microbial populations showed that the time of biocolonisation associated with the continuous production of anodic current progressively affected the bacterial community of biofilms established on the surface of stainless steel microelectrodes. The radical shift from a strong predominance of *Marinobacterium* during stages I and II to *Desulfuromonas* especially during stage IV was explained by the depletion of sulphur in the liquid medium and the growth of sulphate-reducing bacteria that subsequently colonized the electrode.

Since *Desulfuromonas* is known to be electroactive, this respiring-anode bacterial rearrangement alone could not explain the sharp loss in the electrochemical activity that is observed. Apart from the fact that electrochemical activity based on much slower electron transfer mechanisms than those engaged by *Marinobacterium* would be a plausible explanation. However, it is still open for discussion whether subtle changes in microbial abundance from one stage to the next play an important role in the performance of the bioanode or not.

The regeneration of the synthetic liquid medium when the biofilm has reached stage III of development did not seem to have any impact on the electrochemical activity of the biofilm. It would therefore indicate that after the current peak and its consequent drop, the loss of electrochemical activity is irreversible. Re-inoculation with fresh salt marsh sediment also confirmed the evolution of the microbial population in the bioanode by obtaining a dominant relative abundance of sulphur-reducing bacteria in the last stage of biofilm formation.

Finally, the use of microelectrodes for the study of electroactive biofilms opens up attractive research prospects since it offers more homogeneous and less limited study conditions in terms of electrode potential distribution, mass transfer and biocolonisation [38]. Their small size allows for freedom from risky post-experimental slicing and other manipulations that could affect the integrity of the biofilms prior to their microscopic analysis. Also analytical post-processing such as fixation, dehydration or staining and labelling are more homogeneous as the chemical diffusion fronts progress without major limitations. Microelectrodes also offer the possibility of integration into transparent microdevices. By downscaling the liquid bulk-biofilm-anode interface, in-situ and real-time non-invasive investigation of local phenomena could give more hints of the spatiotemporal evolution of microbial anodes and its link to the loss of electroactivity. These technologies can contribute to a deeper understanding of gradients inside the biofilm, bacterial adhesion and biofilm formation, the effects of hydrodynamics and of the liquid electrolyte, among others. In addition, efforts should also be made to implement a more accurate viability detection method than the one routinely used nowadays. To gain more knowledge about how proteins and polysaccharides are formed in the matrix, and how to optimize their production could be an interesting scope of study in terms of bioanode conductivity.

Conclusion

The distinctive electrochemical behaviour of multi-species bioanodes was succesfully reproduced in microsized electrodes, where four distinct temporal stages of biocolonisation and electrochemical activity were extensively described. To the best of our knowledge, this is the first time investigation of biofilm electrochemical activity, spatial bacterial cells viability, EPS production and composition, and relative abundance of microbial biofilm population has been performed simultaneously with a spatiotemporal approach. From the early stages of biocolonisation of the stainless steel microelectrode to the peak of current production J_{max}, the maximum growth rate of the biofilm, the high viability and the high content of extracellular proteins in the matrix, favored the auspicious electrochemical activity. After the maximum J_{max} peak was reached, the loss of electrochemical performance turned irreversible. This was coupled with a decrease in biofilm growth rate, an accumulation of dead cells and an increase in the proportion of polysaccharides in the EPS matrix. In addition to a chemical evolution of the biofilm, the shift of the microbial community from *Marinobacterium* to *Desulfuromonas* also reflects a microbial evolution of the biofilm. Focusing on the early stages of biofilm development and understanding how to control the phenomena that promote current production until it reaches its maximum, and how to avoid the processes that subsequently adversely affect electrochemical activity, should be a research priority to improve the long-term functioning of multi-species microbial bioanodes.

Experimental section

Inoculum origin and synthetic medium

Sediments collected from a salt marsh (Mediterranean Sea coast, Gruissan, France) were used as microbial inoculum. The sediments were stored in a sealed recipient at room temperature until use. A volume of 30 mL of sediments was mixed with 600 mL of synthetic medium based on the Starkey medium (NH4Cl 2.0 g L^{-1}, K2HPO4 0.5 g L^{-1}, NaCH3COO 40 mM, HCl 37% 46 mL, MgCl2·6H2O 55.0 mg L^{-1}, FeSO4(NH4)2SO4·6H2O 7.0 mg L^{-1}, ZnCl2·2H2O 1.0 mg L^{-1}, MnCl2·4H2O 1.2 mg L^{-1}, CuSO4·5H2O 0.4 mg L^{-1}, CoSO4·7H2O 1.3 mg L^{-1}, BO3H3 0.1 mg L^{-1}, Mo7O2(NH4)6·4H2O 1.0 mg L^{-1}, NiCl2·6H2O 0.05 mg L^{-1}, Na2SeO3·5H2O 0.01 mg L^{-1}, CaCl2·2H2O 60.0 mg L^{-1}) with the addition of 45g L^{-1} of NaCl.

Reactor design, microelectrode fabrication and electrochemical techniques

Each reactor (Duran Schott type glass 550 mL) was equipped with a three-electrode system (Figure S1). A twist-off lid with four circular openings was set at the top of the reactor allowing the insertion into the medium of the three electrodes. Stainless steel microelectrodes were implemented as working electrodes. For its design, 15 cm of copper wire was welded into a 2 cm wire of stainless steel (Ø=50µm, Goodfellow). The system was threaded into a plastic tip and sealed with an inert resin (Epofix). The upper end was welded to a connector that served as electrical connection, while the bottom end served as the working electrode. Platinum grids previously cleaned under the flame were used as counter electrodes. A saturated calomel electrode with a fixed potential of +0.248 V/SHE (SCE, Radiometer Analytical) was set between the counter and working electrodes. A fourth remaining opening was used for sampling addition. The medium was purged with nitrogen for 20 minutes to eliminate oxygen before launching the electrochemical techniques. The working electrode potential was controlled under the operation of a multichannel potentiostat (Biologic SA) operated by a data acquisition software that permits the control of the potentiostat (Ec-Lab). Stainless steel microelectrodes were constantly polarized at 0.1 V/SCE. 40 mM of sodium acetate was used as a substrate. COD levels were regularly monitored and kept at a value of 2560 mgO_2 L^{-1} to correspond to the equivalent of 40 mM of sodium acetate. LCK 514 COD kits (Hach Lange, range of measurement 100-2000 mgO2L-1) were used for COD measurements. Samples for the COD measurement were previously filtered with a chloride filter kit Hach LCW925 (Hach Lange). When the polarization was stopped, cyclic voltammetry at 1 mV/s was performed in the range of potential from -0.6 V/SCE to 0.35 V/SCE. Three successive cycles were performed, the second scan was only presented.

Microscopy

Staining of EABs

For the imaging of total cells, samples were labeled with a solution of acridine orange at 0.01 % (A6014, Sigma) for approximately 20 minutes and then carefully rinsed with physiological solution (NaCl 0.9 g L^{-1}).

The exopolymeric matrix of the biofilm was marked by using a mix of four fluorescent dyes: Concavalin A tetramethylrhodamine conjugate (ConA-TMR, Thermofischer Scientific) for α-polysaccharides, Fluorescein isothiocyanate isomer I (FITC, Merck) for proteins, 1,1′ -Dioctadecyl-3,3,3′ ,3′ -tetramethylindocarbocyanine perchlorate (DiD oil, Merck) for lipids and 4′ ,6-Diamidino-2-phenylindole dihydrochloride (DAPI, Merck) for total cells. 25 mL of working solution was prepared in physiological solution with the following concentrations: FITC at 0.05 g L^{-1}, DAPI at $1.05.10^{-4}$ g L^{-1}, Con-A TMR at 0.1 g L^{-1} and DiD'oil at 0.08 g L-1. Microelectrodes were set in contact with the working solution for 30 minutes then carefully rinsed with physiological solution.

Dead/Live assessment was carried by treating the samples as soon as they were retrieved from the reactor with a mix of SYTO 9 (7.5 µM in final solution) and Propidium Iodide (0.015 g L^{-1} in final solution) diluted in physiological solution (Live/Dead Baclight Bacterial Viability Kits L7012, Thermofischer Scientific).

In all cases once rinsed once rinsed, the electrodes were left out in the open air and protected from the light to dry for at least 24 hours before observation.

Table 3. Stains used for the study of the cellular and extracellular structure of salt marsh biofilms and their corresponding microscopic parameters.

Dye	Acridine Orange	Syto 9	PI	DAPI	DiD' Oil	FITC	Con-A
Target	Total cells	Live cells	Dead cells	Total cells	Lipids	Proteins	α-Polysaccharides
Maximum excitation wavelength (nm)	502	482	305	358	648	497	552
Maximum emission wavelength (nm)	525	499	620	461	670	517	576
Imaging device	Carl Zeiss Axio Imager-M2	Leica SP8-2017	Leica SP8-2017	Leica SP8-2017	Leica SP8-2017	Leica SP8-2017	Leica SP8-2017

Epifluorescence microscopy

Biofilms stained with acridine orange were imaged with a Carl Zeiss Axio Imager-M2 microscope (Carl Zeiss) equipped for epifluorescence with an HXP 200C light source and the Zeiss 09 filter (excitor HP450r HP450200 C light source). Biofilms were observed with the objective EC Plan-Neofluar 10x/0.30. Images were acquired with a digital camera (Zeiss AxioCam MRm) along the Z-axis and the set of images was processed with the Zen (Carl Zeiss) ® software. For each sample, two observations were made. The Zen (Carl Zeiss) ® software optimized the z-step of the stack. Thickness was measured with the toolbox of the Zen (Carl Zeiss) ® software, taking nine points per image. Biofilm growth rate was calculated as the increase of thickness divided by the time interval.

Confocal laser scanning microscopy (CLSM) and image analysis

The exopolymeric matrix of the biofilm and biofilm viability was imaged with a Leica SP8-2017 microscope (Leica Microsystems) with the Leica Application Suite X: LAS-X software (Leica Microsystems). The image acquisition was made by using the HC PC FLUOTAR 10x/0.30 objective in dry immersion. For each sample, two stacks of horizontal plane images (1024x1024 pixels) were taken from two randomly chosen areas. The LAS-X software optimized the z-step of the stack depending on the sample. Once the acquisition was completed, the LAS-X software represented the projection of the stack in a 3D view.

For image analysis, 3D images were treated with the Image J software. In the case of viability analysis, since a two-color image was obtained, the color threshold tool was used. For the analysis of the exopolymeric substances, as the sample was treated with four different stains, the 3D images were treated individually channel by channel, corresponding to each component in the exopolymeric matrix of the biofilm. First, the color image was transformed into an 8-bit image and later a threshold value was set. The threshold value allows the labeling of each pixel as empty or marked.

After, the software showed the amount of empty pixels by image, and the calculation of marked pixels per image was calculated as the difference between total pixels and empty pixels.

For the viability analysis, eight images were treated. The amount of dead cells (cells labeled with PI) is the ratio of PI labeled pixels over the total pixels, as calculated in [Eq. (1)]:

$$Dead\ cells\ (\%) = \left(\frac{PI\ \ pixels}{PI\ \ pixels + SYTO\ 9\ \ pixels}\right).100\% \qquad (1)$$

For the EPS analysis, four biofilms were observed in two random sections for the four different stains, resulting in a total of thirty-two images processed. The amount of each component was calculated as the ratio of the channel pixels over the total pixels. For the case of proteins, it is described in [Eq. (2)] as it follows:

$$Proteins\ (\%) = \left(\frac{FITC\ pixels}{FITC\ \ pixels + DAPI\ pixels + DID\ oil\ pixels + ConA\ \ pixels}\right).100\% \qquad (2)$$

This was likewise calculated for total cells, lipids and α-polysaccharides.

Scanning electron microscopy (SEM)

The samples were metallized with gold (Au) prior to observation in order to reduce charging effects. Samples were observed under the scanning electron microscope Leo 435 VP-Carl Zeiss SMT.

Microbial population analysis

Microelectrodes containing the EABs were stored in 2 ml Eppendorf tubes. 150µL of PCR grade water and a spatula tip of 425-600 µm glass beads (G8772, Sigma) were added to the tubes. A negative control was made with only water and beads. Two one-minute mechanical grindings with a robot (Fast-prep 24 MP Biomedicals, Thermofischer Scientific) at a maximum speed of 6.5 m s^{-1} were performed to loosen the biofilms formed on the surface of the microelectrode. The clean microelectrode was retrieved from the tube and the remaining suspension was subjected to two thermal shocks by alternating ice and water bath at 95°C for 1 min each time, in order to lyse the cells and release the DNA.

The 16S amplification was then performed on 1µL of the suspension with the GoTaq Flexi G2 enzyme (Promega) with the primers:

Genewiz515Fmod:5'-
ACACTCTTTCCCTACGACGCTCTTCCGATCTGTGYCAGCMG
CCGCGGTAA-3'

Genewiz806Rmod:5'-
GACTGGAGTTCAGACGTGTGCTCTTCCGATCTGGACTACNV
GGGTWTCTAAT-3'

35 cycles of PCR were carried at a temperature of 55°C. The primers were designed to contain overhang compatible sequences with Nextera XT index (Illumina). The purified amplicons were sequenced using the MiSeq platform (Illumina).

Microbiome bioinformatics were performed by the open-source software QIIME2, version 2021.11 (https://qiime2.org) [63]. Raw reads were demultiplexed, quality-filtered, denoised and chimera-checked using DADA2 [64]. DADA2 uses a parametric model to infer true biological sequences from reads. The model relies on input read abundances (true reads are likely to be more abundant) and the pairwise similarity between sequences. Sequences were aligned using MAFFT [65], and were used to construct a phylogeny using FastTree [66]. The taxonomic annotation of the resulting amplicon sequence variants (ASVs) was assigned using the feature-classifier command with default parameters in QIIME2 and sequences were matched against the Greengenes 13_8 database [67] . Finally, scaling with ranked subsampling (SRS) curves [68] were drawn to determine whether the sequencing depth was sufficient to represent the true diversity of the samples.

Inductively coupled plasma (ICP) analysis

Sulphur, iron and manganese concentration was determined from the reactors. 5 mL of the anolyte were taken at the time of 7, 11, 31 and 55 days. The samples were diluted with distilled water to a volume of 20 mL and then filtered to remove chloride ions. Chloride filter kit Hach LCW925 (Hach Lange) was used for filtration. Every sample was treated with 3 mL of HNO3 65% for analysis. Calibration solutions for sulfur, iron and manganese were prepared by diluting a certified solution of the elements of 1000 µg/ml in the synthetic medium. It was diluted in a 1:4 ratio and treated with 3 mL of HNO3 65% for analysis. The solutions were analyzed using an ICP-OES Ultima 2 (Horiba). Sulfur quantification was measured at a wavelength of 180.676 nm, iron at 259.940 nm and manganese at 257.610 nm.

Acknowledgements

This work was part of the “MICROBE” project funded by the French “Agence Nationale de le Recherche” grant number ANR-18-CE05-0024.

Keywords: Electrochemistry • Extracellular polymeric substances • Oxidation • Salt marsh bioanodes • Stainless steel microelectrodes

References

[1] B. Erable, N. M. Duţeanua, M. M. Ghangrekar, C. Dumas, K. Scott, Biofouling 2010, 26, 57–71.

[2] F. Harnisch, U. Schröder, Chem. Soc. Rev. 2010, 39, 4433–4448.

[3] A. A. Mier, H. Olvera-Vargas, M. Mejía-López, A. Longoria, L. Verea, P. J. Sebastian, D. M. Arias, Chemosphere 2021, 283, DOI 10.1016/j.chemosphere.2021.131138.

[4] S. Jung, J. Lee, Y. Park, E. E. Kwon, Bioresour. Technol. 2020, 300, 122748.

[5] M. Rimboud, D. Pocaznoi, B. Erable, A. Bergel, Phys. Chem. Chem. Phys. 2014, 16, 16349–16366.

[6] D. R. Bond, D. E. Holmes, L. M. Tender, D. R. Lovley, Science (80-.). 2002, 295, 483–485.

[7] C. E. Reimers, L. M. Tender, S. Fertig, W. Wang, Environ. Sci. Technol. 2001, 35, 192–195.

[8] T. H. Pham, P. Aelterman, W. Verstraete, Trends Biotechnol. 2009, 27, 168–178.

[9] W. H. Tan, S. Chong, H. W. Fang, K. L. Pan, M. Mohamad, J. W. Lim, T. J. Tiong, Y. J. Chan, C. M. Huang, T. C. K. Yang, Processes 2021, 9, 1–13.

[10] D. Sun, J. Chen, H. Huang, W. Liu, Y. Ye, Int. J. Hydrogen Energy 2016, 41, 16523–16528.

[11] R. J. Steidl, S. Lampa-Pastirk, G. Reguera, Nat. Commun. 2016, 7, DOI 10.1038/ncomms12217.

[12] P. S. Bonanni, D. F. Bradley, G. D. Schrott, J. Pablo, 2013, 711–720.

[13] G. L. Chadwick, F. J. Otero, J. A. Gralnick, D. R. Bond, V. J. Orphan, Proc. Natl. Acad. Sci. U. S. A. 2019, 116, 20716–20724.

[14] M. Oliot, P. Chong, B. Erable, A. Bergel, Chem. Eng. J. 2017, 327, 218–227.

[15] E. Blanchet, E. Desmond, B. Erable, A. Bridier, T. Bouchez, A. Bergel, Bioresour. Technol. 2015, 185, 106–115.

[16] R. Renslow, J. T. Babauta, A. C. Dohnalkova, M. I. Boyanov, K. M. Kemmer, P. D. Majors, J. K. Fredrickson, H. Beyenal, Bone 2013, 23, 1–7.

[17] J. T. Babauta, H. D. Nguyen, T. D. Harrington, R. Renslow, H. Beyenal, 2013, 109, 2651–2662.

[18] D. Sun, S. Cheng, F. Zhang, B. E. Logan, J. Power Sources 2017, 356, 566–571.

[19] B. Ranjan, J. Sim, H. Ryu, H. Ren, J. W. Santo, J. Chae, H. Lee, Water Res. 2017, 127, 230–238.

[20] G. Yang, Q. Mai, Z. Zhuang, L. Zhuang, Environ. Res. 2021, 201, 111572.

[21] G. Yang, L. Huang, Z. Yu, X. Liu, S. Chen, Water Res. 2019, 159, 294–301.

[22] J. Guo, G. Yang, Z. Zhuang, Q. Mai, L. Zhuang, Sci. Total Environ. 2021, 797, 149207.

[23] T. Li, Q. Zhou, L. Zhou, Y. Yan, C. Liao, L. Wan, J. An, N. Li, X. Wang, Water Res. 2020, 177, 115776.

[24] E. Roubaud, R. Lacroix, S. Da Silva, L. Etcheverry, A. Bergel, R. Basséguy, B. Erable, Front. Energy Res. 2019, 7, DOI 10.3389/fenrg.2019.00106.

[25] C. Borsje, T. Sleutels, M. Saakes, C. J. N. Buisman, A. ter Heijne, J. Chem. Technol. Biotechnol. 2019, 94, 2738–2748.

[26] R. Askri, B. Erable, M. Neifar, L. Etcheverry, A. S. Masmoudi, A. Cherif, H. Chouchane, Bioelectrochemistry 2019, 129, 179–188.

[27] A. Elabed, R. El Khalfaouy, S. Ibnsouda, R. Basseguy, S. Elabed, B. Erable, Appl. Sci. 2019, 9, DOI 10.3390/app9112259.

[28] S. D. Molenaar, T. Sleutels, J. Pereira, M. Iorio, C. Borsje, J. A. Zamudio, F. Fabregat-Santiago, C. J. N. Buisman, A. Ter Heijne, ChemSusChem 2018, 11, 2171-2178.

[29] Poehere Chong, B. Erable, A. Bergel, 2018, 24–26.

[30] M. González-Muñoz, X. Dominguez-Benetton, J. Domínguez-Maldonado, D. Valdés-Lozano, D. Pacheco-Catalán, O. Ortega-Morales, L. Alzate-Gaviria, Energies 2018, 11, 1–13.

[31] X. Zhang, A. Prévoteau, R. O. Louro, C. M. Paquete, K. Rabaey, Biosens. Bioelectron. 2018, 121, 183–191.

[32] B. Cercado-Quezada, M. L. Delia, A. Bergel, Electrochem. commun. 2011, 13, 440–443.

[33] B. Erable, A. Bergel, Bioresour. Technol. 2009, 100, 3302–3307.

[34] A. W. Jeremiasse, H. V. M. Hamelers, C. J. N. Buisman, Bioelectrochemistry 2009, 78, 39–43.

[35] A. ter Heijne, H. V. M. Hamelers, M. Saakes, C. J. N. Buisman, Electrochim. Acta 2008, 53, 5697–5703.

[36] S. Pinck, L. M. Ostormujof, S. Teychené, B. Erable, 2020, 1–23.

[37] D. Salvatore, C. Bragato, 2014.

[38] D. Pocaznoi, B. Erable, M. L. Delia, A. Bergel, Energy Environ. Sci. 2012, 5, 5287–5296.

[39] R. Rousseau, X. Dominguez-Benetton, M. L. Délia, A. Bergel, Electrochem. commun. 2013, 33, 1–4.

[40] K. P. Nevin, H. Richter, S. F. Covalla, J. P. Johnson, T. L. Woodard, A. L. Orloff, H. Jia, M. Zhang, D. R. Lovley, Environ. Microbiol. 2008, 10, 2505–2514.

[41] G. D. Schrott, M. V. Ordoñez, L. Robuschi, J. P. Busalmen, ChemSusChem 2014, 7, 598–603.

[42] D. Sun, S. Cheng, A. Wang, F. Li, B. E. Logan, K. Cen, Environ. Sci. Technol. 2015, 49, 5227–5235.

[43] L. Karygianni, Z. Ren, H. Koo, T. Thurnheer, Trends Microbiol. 2020, 28, 668–681.

[44] B. Cao, L. Shi, R. N. Brown, Y. Xiong, J. K. Fredrickson, M. F. Romine, M. J. Marshall, M. S. Lipton, H. Beyenal, 2011, 13, 1018–1031.

[45] S. W. Li, G. P. Sheng, Y. Y. Cheng, H. Q. Yu, Sci. Rep. 2016, 6, 1–7.

[46] A. P. Borole, G. Reguera, B. Ringeisen, Z. W. Wang, Y. Feng, B. H. Kim, Energy Environ. Sci. 2011, 4, 4813–4834.

[47] J. B. Rollefson, C. S. Stephen, M. Tien, D. R. Bond, J. Bacteriol. 2011, 193, 1023–1033.

[48] J. Wang, G. Li, H. Yin, T. An, Environ. Res. 2020, 185, 109451.

[49] B. Erable, M.-A. Roncato, W. Achouak, A. Bergel, 2009, 43, 3194–3199.

[50] M. Rimboud, L. Etcheverry, M. Barakat, W. Achouak, A. Bergel, 2021, 337, DOI 10.1016/j.biortech.2021.125448.

[51] R. Tapia-Tussell, R. E. Valle-Gough, I. Peraza-Baeza, J. Domínguez-Maldonado, M. Gonzalez-Muñoz, A. Cortes-Velazquez, R. M. Leal-Baustista, L. Alzate-Gaviria, Sci. Total Environ. 2019, 681, 258–266.

[52] H. Kim, Y. J. Choo, J. Song, J. S. Lee, K. C. Lee, J. C. Cho, Int. J. Syst. Evol. Microbiol. 2007, 57, 1659–1662.

[53] V. Fedorovich, M. C. Knighton, E. Pagaling, F. B. Ward, A. Free, I. Goryanin, 2009, 75, 7326–7334.

[54] M. T. Fera, T. L. Maugeri, C. Gugliandolo, C. Beninati, M. Giannone, E. La Camera, M. Carbone, E. Marina, 2004, 70, 1271–1276.

[55] S. Li, K. H. Nealson, 2015, DOI 10.3389/fmicb.2015.00111.

[56] A. G. Pereira-medrano, M. Knighton, G. J. S. Fowler, Z. Yen, T. Khoa, S. Yen, A. Free, B. Ward, P. C. Wright, J. Proteomics 2012, 78, 197–210.

[57] R. Rousseau, C. Santaella, W. Achouak, J. J. Godon, A. Bonnafous, A. Bergel, M. L. Délia, ChemElectroChem 2014, 1, 1966–1975.

[58] B. Thamdrup, R. Rosselló-Mora, R. Amann, Appl. Environ. Microbiol. 2000, 66, 2888–2897.

[59] N. Pfennig, H. Biebl, Arch. Microbiol. 1976, 110, 3–12.

[60] M. Pierra, A. A. Carmona-martínez, E. Trably, J. Godon, N. Bernet, 2015, 106, 221–225.

[61] E. Marsili, D. B. Baron, I. D. Shikhare, D. Coursolle, J. A. Gralnick, D. R. Bond, Proc. Natl. Acad. Sci. U. S. A. 2008, 105, 3968–3973.

[62] D. R. Bond, D. R. Lovley, Appl. Environ. Microbiol. 2003, 69, 1548–1555.

[63] E. Bolyen, J. R. Rideout, M. R. Dillon, N. A. Bokulich, C. C. Abnet, G. A. Al-Ghalith, H. Alexander, E. J. Alm, M. Arumugam, F. Asnicar, Y. Bai, J. E. Bisanz, K. Bittinger, A. Brejnrod, C. J. Brislawn, C. T. Brown, B. J. Callahan, A. M. Caraballo-Rodríguez, J. Chase, E. K. Cope, R. Da Silva, C. Diener, P. C. Dorrestein, G. M. Douglas, D. M. Durall, C. Duvallet, C. F. Edwardson, M. Ernst, M. Estaki, J. Fouquier, J. M. Gauglitz, S. M. Gibbons, D. L. Gibson, A. Gonzalez, K. Gorlick, J. Guo, B. Hillmann, S. Holmes, H. Holste, C. Huttenhower, G. A. Huttley, S. Janssen, A. K. Jarmusch, L. Jiang, B. D. Kaehler, K. Bin Kang, C. R. Keefe, P. Keim, S. T. Kelley, D. Knights, I. Koester, T. Kosciolek, J. Kreps, M. G. I. Langille, J. Lee, R. Ley, Y. X. Liu, E. Loftfield, C. Lozupone, M. Maher, C. Marotz, B. D. Martin, D. McDonald, L. J. McIver, A. V. Melnik, J. L. Metcalf, S. C. Morgan, J. T. Morton, A. T. Naimey, J. A. Navas-Molina, L. F. Nothias, S. B. Orchanian, T. Pearson, S. L. Peoples, D. Petras, M. L. Preuss, E. Pruesse, L. B. Rasmussen, A. Rivers, M. S. Robeson, P. Rosenthal, N. Segata, M. Shaffer, A. Shiffer, R. Sinha, S. J. Song, J. R. Spear, A. D. Swafford, L. R. Thompson, P. J. Torres, P. Trinh, A. Tripathi, P. J. Turnbaugh, S. Ul-Hasan, J. J. J. van der Hooft, F. Vargas, Y. Vázquez-Baeza, E. Vogtmann, M. von Hippel, W. Walters, Y. Wan, M. Wang, J. Warren, K. C. Weber, C. H. D. Williamson, A. D. Willis, Z. Z. Xu, J. R. Zaneveld, Y. Zhang, Q. Zhu, R. Knight, J. G. Caporaso, Nat. Biotechnol. 2019, 37, 852–857.

[64] B. J. Callahan, P. J. McMurdie, M. J. Rosen, A. W. Han, A. J. A. Johnson, S. P. Holmes, Nat. Methods 2016, 13, 581–583.

[65] K. Katoh, D. M. Standley, Mol. Biol. Evol. 2013, 30, 772–780.

[66] M. N. Price, P. S. Dehal, A. P. Arkin, Mol. Biol. Evol. 2009, 26, 1641–1650.

[67] D. McDonald, M. N. Price, J. Goodrich, E. P. Nawrocki, T. Z. Desantis, A. Probst, G. L. Andersen, R. Knight, P. Hugenholtz, ISME J. 2012, 6, 610–618.

[68] L. Beule, P. Karlovsky, PeerJ 2020, 8, DOI 10.7717/peerj.9593.

Supporting Information

1. Experimental set-up

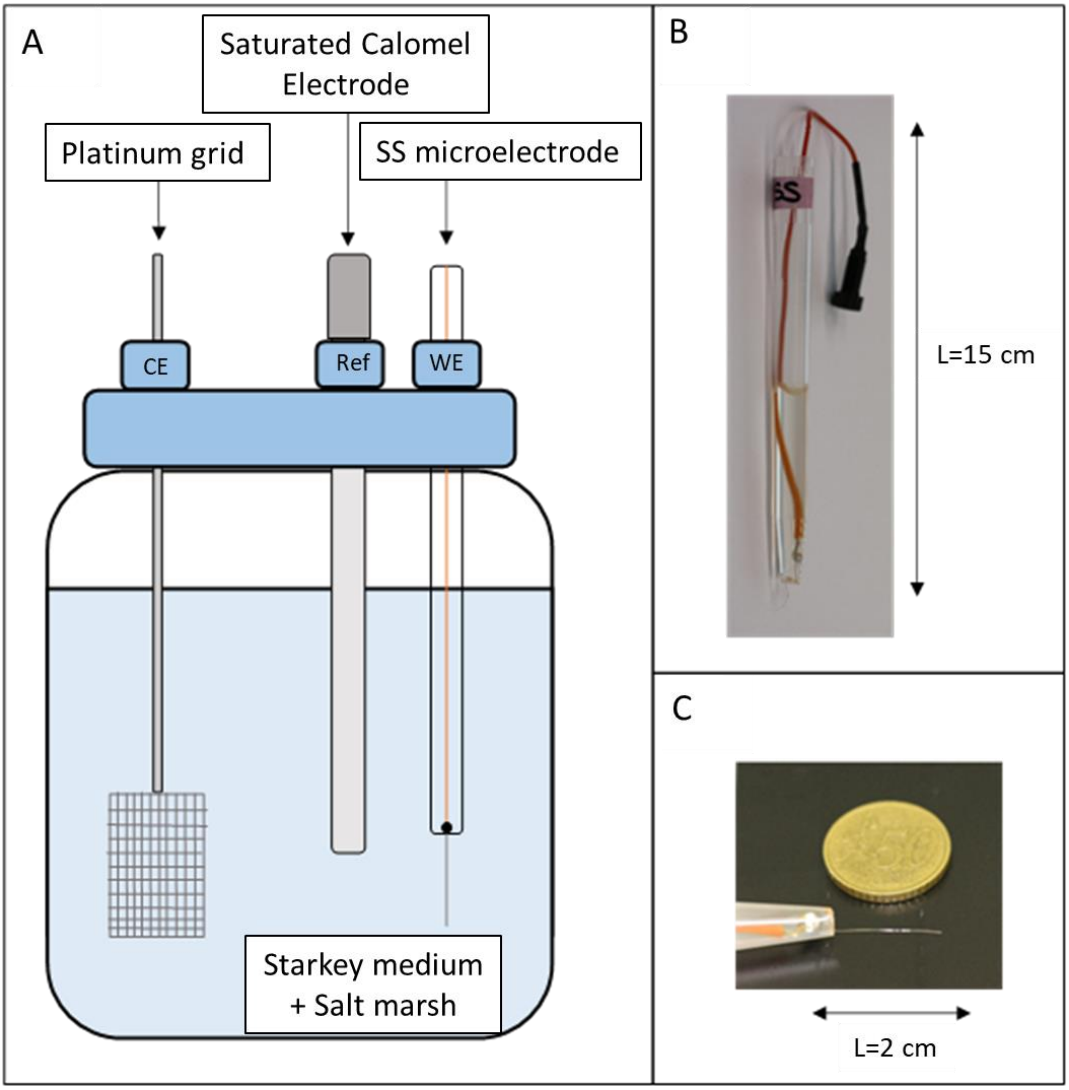

***Figure S1**. Experimental set-up. (A) Schematic representation of a three-electrode system: A stainless steel microelectrode is introduced in the reactor as the working electrode (WE), while a platinum grid is used as a counter electrode (CE) and a saturated calomel electrode as the reference electrode (Ref). (B, C) Stainless steel microelectrode (d=50 µm).*

2. Normalization of current density curves

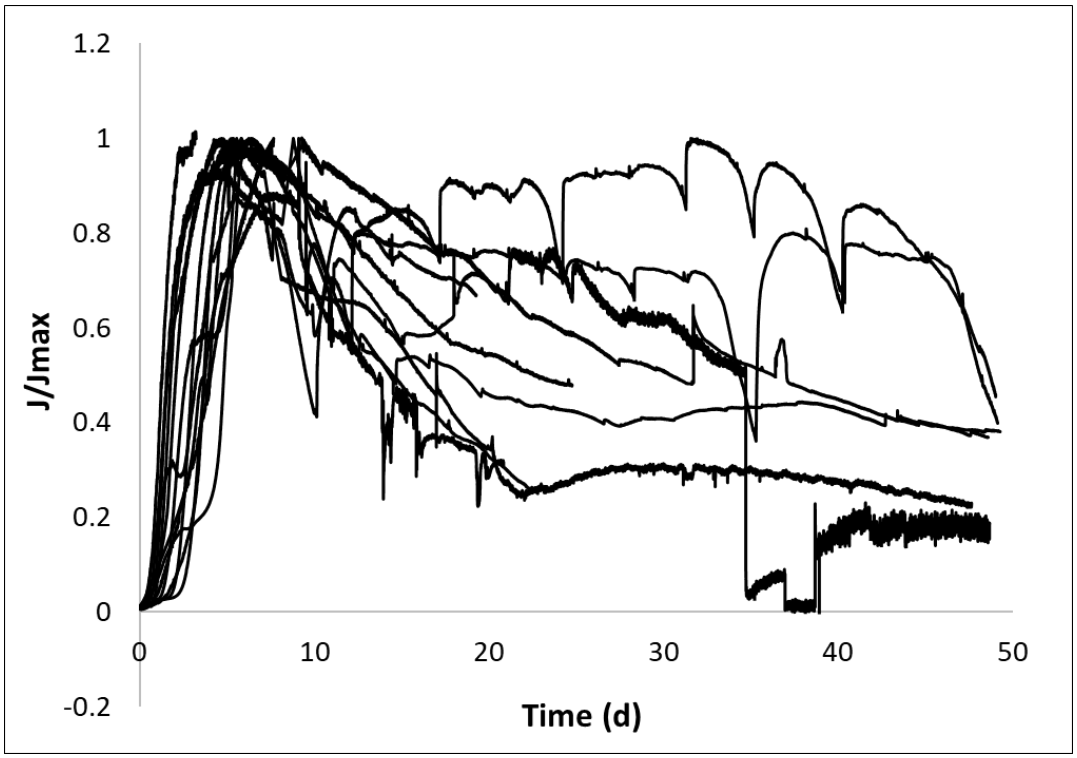

***Figure S2**. Normalization of the total of the curves of current density versus time presented in this work. The initial phase was removed. All stainless steel microelectrodes were colonized by salt marsh bacteria under a constant potential of 0.1 V/SCE.*

3. Cyclic voltammetries (section 2.2)

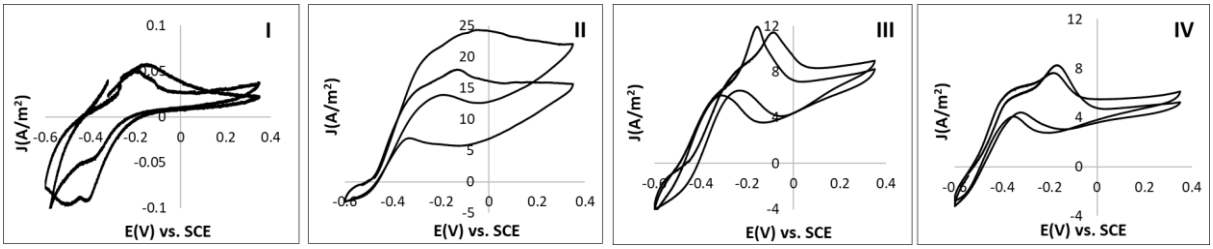

***Figure S3**. Cyclic voltammetries for duplicate experiments performed at 1 mV/s at the end of each stage without adjusting the y-axis scale.*

4. Cyclic voltammetries (section 2.3)

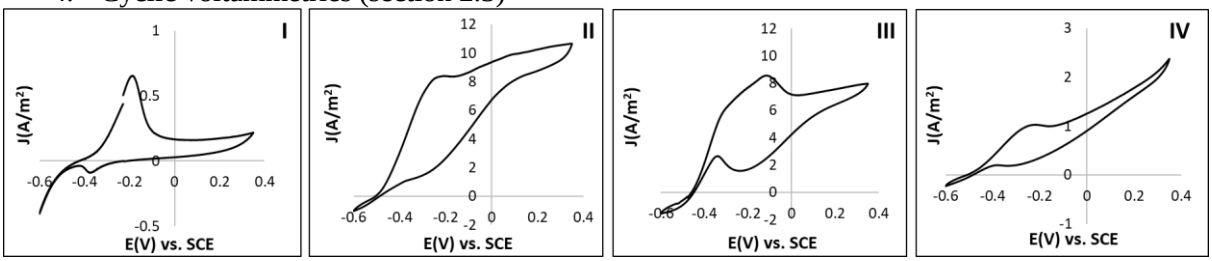

***Figure S4**. Cyclic voltammetries for duplicate experiments performed at a scan rate of 1 mV/s at the end of each stage without adjusting the scale the y-axis scale.*

5. Cyclic voltammetries (section 2.4)

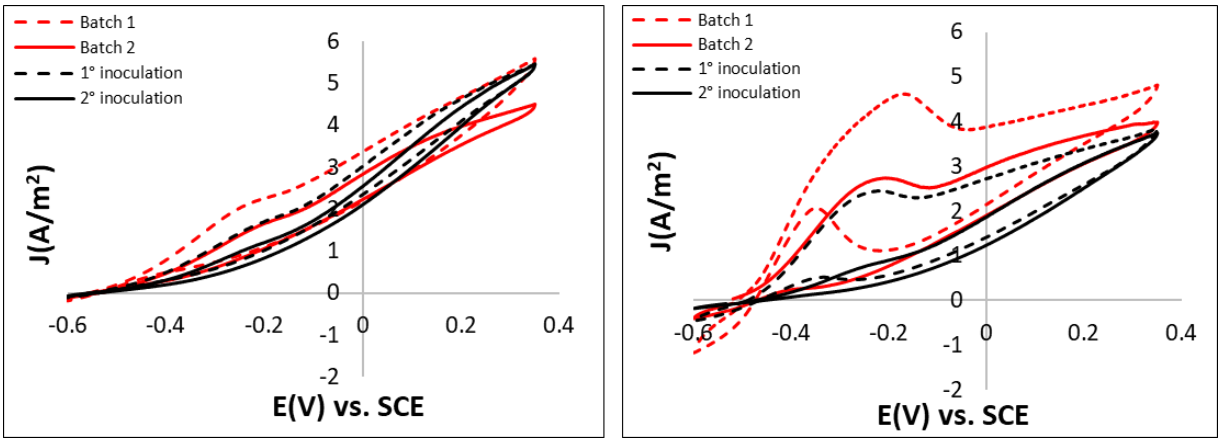

***Figure S5**. Cyclic voltammetries for duplicate experiments performed at a scan rate of 1 mV/s. The red curves show the cyclic voltammetry at t=27 days, before and after the medium change. The black curves show the cyclic voltammetries at t=29 days, before and after the second inoculation.*

6. Biofilm thickness, viability and EPS composition

***Table S1**. Salt marsh biofilms spatial, viability and EPS chemical composition parameters at the four different stages.*

Stage	Time interval (d)	Biofilm average thickness (µm)	Biofilm growth rate (µm D^{-1})	Dead cells (%)	Total cells (%)	Proteins (%)	Lipids (%)	α-Polysaccharides (%)	Ratio α-Polysaccharides / Proteins
I	5	6.2±1.1	-	15.8±10.8	9.1±3.6	60.2±1.6	14.8±0.9	15.8±6.1	0.208
II	6	32.1±5.7	4.3	65.2±6.3	22.1±9.7	71.1±8.6	1.7±0.3	5.0±1.5	0.066
III	20	47.9±7.3	0.8	52.6±9.3	38.5±3.7	45.7±1.2	6.7±2.1	9.1±0.3	0.165
IV	24	57.7±8.5	0.4	77.3±9.3	27.8±7.8	63.4±8.4	5.6±0.9	3.3±1.5	0.049

7. ICP analysis

***Table S2**. Concentration of Sulphur, iron and manganese in the synthetic medium at the four different stages.*

	Stage			
Concentration (mg L^{-1})	I	II	III	IV
Sulphur	19.6	17.8	1.1	0.5
Iron	< 0.1	< 0.1	< 0.1	< 0.1
Manganese	< 0.1	< 0.1	< 0.1	< 0.1

IV.3. Effect of the seasonal sampling of salt marsh sediments (SMS) on microbial population and electrochemical performance of the bioanode

The results published in the Research Article 2 showed a temporal evolution of the microbial population in EABs formed over the microelectrodes. It would appear that as the biofilm develops while working in batch mode, the amount of sulfate-reducing bacteria accumulates in the EAB at the end of stage IV. This is mainly due to a significant drop in the anolyte sulfur concentration between stages II and III, thus favoring the growth of planktonic-state *Desulfuromonas* that later colonizes the anode at stage IV. However, it is very complex to determine the role that each bacterial specie plays in the biofilm electroactivity, which is beyond the scope of this thesis.

Therefore, the aim of this section is:

- To corroborate the temporal evolution of the microbial population described in the article.
- To determine if the electroactivity of the anode and the biofilm microbial diversity is maintained when inoculating the reactors using samples of sediments collected at different seasons of the year.

It is worth noting that for the microbial population of EABs, the DNA analysis can go up to different phylogenetic levels. However, there is no overlap between their quantification. Results of relative abundances of EABs microbial population are presented in tables in this section. A histogram merging all the results is presented in the **Erreur ! Source du renvoi introuvable.**.

IV.3.1. Additional results from research Article 2

In the article section *"2.3: Spatiotemporal investigation of exopolymeric substances, microbial populations and soluble electron acceptors",* four additional EABs were formed as to obtain duplicates for each stage of biofilm electroactivity. In this case, the batch of SMS dated from March 2021. These results were not included in the article; therefore, they are exclusively presented in this section. For stage I, no duplicate was obtained since it was decided to keep the rest of the reactors running for a longer time. For stage II, two reactors were stopped at day 17, yet any current was produced. A value of around 8 A/m^2 would have been expected at this stage. For stage III and IV, two replicates were indeed obtained with current production patterns that are in accordance with those identified in Research Article 2. The experiments were stopped at day 31 and 55 for stage III and IV respectively.

Figure IV-1 shows the CA curves both for the salt marsh EABs presented in the article (black curves) and the extra experiments (blue curves). After the polarization experiments were stopped and the EABs were detached and collected from the surface of the microelectrodes, the relative abundances at the order, family or genus level of the bacteria present in the biofilms were analyzed.

In terms of the EABs electroactivity, for stage II, the duplicates reached a current density average value of 0.11±0.10 A/m^2 at day 17. The fact that the error is almost the same than the average value shows that EABs from the duplicates did not show a reproducible electroactivity. Furthermore, the current value at day 17 reached by the EAB presented in the article was of 7.93 A/m^2, being from one to two orders of magnitude larger. At stage III, the average of J_{max} between the article bioanode and the duplicate was of 7.64±0.03 A/m^2 at day 17. However, at day 31 final current density was 5.09 A/m^2 for the article bioanode and 2.71 A/m^2 for the duplicate. Finally, at stage IV, J_{max} was of 8.64 A/m^2 for the article bioanode and 5.90 A/m^2 for the duplicate. Current density values were more similar by the end of the experience, at day 55, reaching an average current value of 1.57±0.31 A/m^2. The temporal evolution of the salt marsh biofilms electroactivity when using the same batch of SMS was more reproducible at stages III and IV than at stage II.

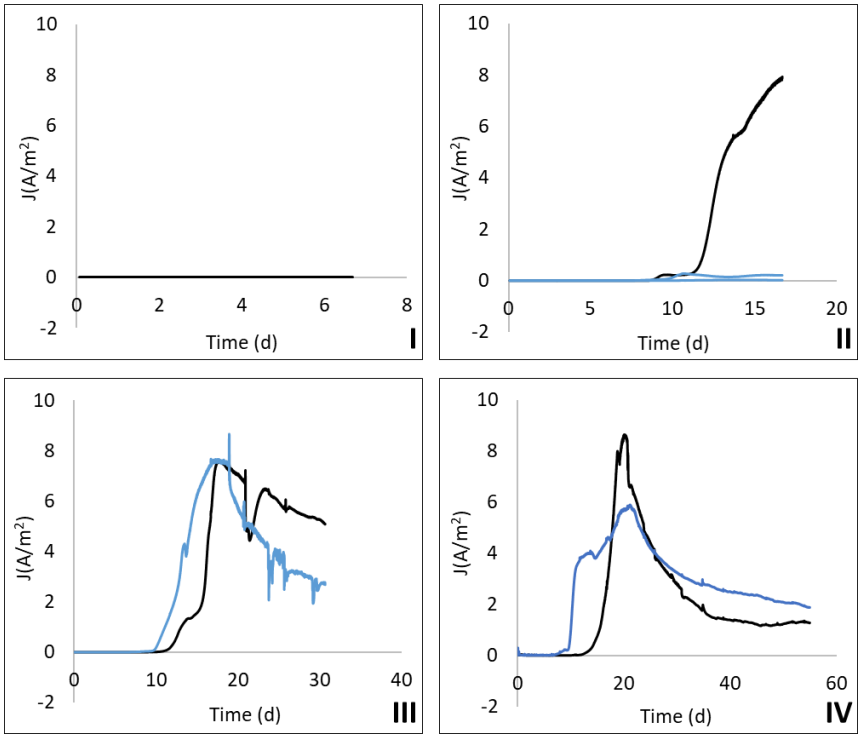

Figure IV-1: Evolution of current density versus time for duplicate experiments at the four different stages: (I) at t=7 days, (II) at t=17 days, (III) at t=31 days and (IV) at t=55 days.

Bioinformatics analysis of the OTUs (Operational Taxonomic Units) from the sequencing identified a majority of taxa down to the genus level in all cases with the exception of *Desulfuromondales* and *Bacteroidales* orders and *Acidaminobacteraceae* family. Comparing with the bacterial communities already described in Research Article 2, the dominant bacterial species that were enriched in the EABs remained broadly the same, with the exception of *Arcobacter* and *Marinilabilia*, which were no longer present in this set of duplicate experiments. Instead, species from *Acidaminobacteraceae* and *Desulfovibrio* were detected. This is summarized in Table IV-1.

.

Table IV-1 : Detailed relative abundances (%) of microbial population in salt marsh EABs for additional results of Research Article 2. (g) indicates that the DNA analysis classification went until the genus level, while (f) to the family level and (o) to the order level. The most relevant values for each stage are in bold. Relative abundances from article 2 were also added for comparison.

	Stages additional results				**Stages Article 2**			
Order/Family/Genus	I	II	III	IV	I	II	III	IV
Marinobacterium (g)	**80.8**	**80.9**	**38.3**	**11.1**	**87.0**	**72.9**	**74.1**	0.6
Desulfuromondales (o)	0.0	0.0	0.9	5.3	0.0	2.2	5.7	6.9
Desulfuromonas (g)	1.3	0.0	**40.8**	**59.7**	0.0	2.0	2.6	**68.5**
Halanaerobium (g)	1.8	1.8	1.2	0.9	0.0	4.0	2.4	1.1
Bacteroidales (o)	4.0	2.8	4.4	**10.1**	0.5	3.1	1.6	5.2
Thermotalea (g)	3.0	0.4	0.2	0.3	0.7	3.5	0.2	0.5
Acidaminobacteraceae (f)	1.0	3.1	3.5	0.3	0.0	0.0	0.0	0.0
Desulfovibrio (g)	2.9	2.3	1.8	1.1	0.0	0.0	0.0	0.0

Comparison of the biofilm microbial population was made between the sample presented in the article and its duplicate(s) presented in this section. Thus, the major differences by stage were found as:

- For stage I, there was no duplicate.
- For stage II, the amount of *Marinobacterium* increased from 72.9% in the sample of the article to 80.8% and 80.9% in the duplicates.
- For stage III, *Marinobacterium* decreased from 74.1% of abundance in the sample from the article to 38.3% in the duplicate, whether *Desulfuromonas* increased also from 2.6% to 40.8% respectively.
- For stage IV, *Marinobacterium* increased from 0.6 % in the sample from the article to 11.1% of abundance in the duplicate. *Desulfuromonas* and *Desulfuromondale*s abundances remained similar, whether *Bacteroidales* increased from 5.2% to 10.1%.

When comparing at stage II, it is complex to determine whether the slight difference in *Marinobacterium*, variations in the low percentages of other bacterial species present, or other non-microbial factors are responsible for the near-zero electroactivity of the two duplicates at this stage. Another hypothesis for the low electroactivity could have been a longer initial lag-phase for current production in these bioanodes. At the end of stage III, the difference in the final current values at day 31 could be explained by the increase in *Desulfuromonas* presence, which seems to dominate the EAB when the current is at its lowest values. At the end of stage IV, the already described shift of the predominant *Marinobacterium* population towards *Desulfuromonas* was again observed.

Bacteria of the *Bacteroidales* order are present in a minority of 2 to 4% during stages I to III. In stage IV, their enrichment is noticeable since their presence has increased to 10%. This was also the case in Research Article 2, where their proportion more than doubled in Stage IV. Species originating from *Bacteroidales* order are basically present in marine sediments and follow fermentation pathways as they are known for fermenting complex organics (Mann et al., 2013; Ki et al., 2017). In addition, they are known for not being important drivers of extracellular electron transfer and can remove dead cells from the anode (Yuan et al., 2017). This may explain the increase of species from this order in biofilm at the latest stages together with its decreased electroactivity. Probably bacteria grew in the anolyte in a planktonic form at the early stages and later adhered to the biofilm to serve other functions rather than to contribute with its electroactivity.

The results obtained in this section confirm the temporal shift in the microbial population of the salt marsh EABs from *Marinobacterium* to *Desulfuromonas*, as observed in the article. It would seem that if the shift occurs before in time, as seen in the duplicate from stage III, the electroactivity of the biofilm reaches lower values.

IV.3.2. Salt marsh EABs with reduced electroactivity

The experiments presented in the Research Article 2 were carried with salt marsh sediment batches sampled at different seasonal periods as shown in

Table IV-2. Experiments belonging to the section *2.1: Microelectrodes are a suitable tool to study the mechanisms of biofilm formation* used as inoculum the first batch of sediments collected in October 2019. The following sampling expedition took place in June 2020, and these sediments were used to inoculate reactors described in section *2.2: Spatiotemporal investigation of biofilm thickness and cell viability*. It is important to note that microbial diversity in salt marsh EABs was not analyzed for these two batches.

Later, two new samplings of SMS were performed in October 2020 and January 2021. Since the bioanodes cultured with these two batches did not perform as expected, the experiments presented in section *"2.3: Spatiotemporal investigation of exopolymeric substances, microbial populations and soluble electron acceptors"* were conducted with a posterior salt marsh inoculum, dating from March 2021. However, for the less performing bioanodes, CAs were registered and biofilms formed over microelectrodes were retrieved for further microbial population analysis.

Table IV-2 : Summary of salt marsh sediment batches used in each section of the Research Article 2.

Article 2 Section	Sediment batch	Biofilm microbial population analysis?
2.1 Microelectrodes are a suitable tool to study the mechanisms of biofilm formation	October 2019	No
2.2.Spatiotemporal investigation of biofilm thickness and cell viability	June 2020	No
2.3: Spatiotemporal investigation of exopolymeric substances, microbial populations and soluble electron acceptors	March 2021	Yes
2.4. Late stages of biofilm formation: Reversibility or irreversibility of the electrochemical activity?	March 2021	Yes

Experiments involving SMS collected from October 2020 and January 2021 are classified as Test 10-2020 and Test 01-2021, respectively. For both tests, temperature was maintained at 30°C and sodium acetate 40 mM was added as the substrate on a daily basis. Before polarization, a nitrogen gas stream was injected into the liquid medium to establish anoxic conditions. Stainless steel microelectrodes were constantly polarized at 0.1 V/SCE. In test 01-2021, SMS were used in three different physical aspects as inoculum: solid, a liquid+solid mixture and liquid. This will be explained in more detail in section IV.3.2.2. The main experimental conditions are summed up in Table IV-3.

Table IV-3: Summary of experimental conditions.

Inoculum	SMS	
Temperature	30°C	
Substrate	Sodium acetate 40 mM	
Culture medium	Starkey medium (45 g/L of NaCl)	
E_{we} vs. SCE	0.1	
Inoculation size % V/V	5	
Operation mode	Batch	
WE material and design	SS microelectrode	
Reactor type	Standard (600 mL)	
Test	10-2020	01-2021
Date of inoculum sampling	October 2020	January 2021
No. of reactor units	4	6
Physical aspect of the inoculum	Liquid	Solid, Liquid+Solid, Liquid
Time (d)	17	13 to 35

IV.3.2.1. Test SMS 10-2020

Figure IV-2 (A) shows current production for salt marsh EABs formed under constant polarization for a period of 17 days. This was the first time where reproducibility was difficult to obtain regarding the results presented in the article, with the exception of the duplicates of stage II presented in the previous

section of additional results. Typically, J_{max} was in the order of 8 to 10 A/m^2, while here J_{max} only reached 6 A/m^2 for one of the bioanodes and for the rest it was below that value. In addition, the gradual decrease on the electroactivity to more than 50%, which usually takes about one month to reach the end of stage III, occurred faster, at day 17.

Nevertheless, normalized curves, Figure IV-2 (B), for this experiment showed that curves of current density had a similar behavior between them, mostly starting from day 10. For reactor 1 and 2, the drop in current production was of 80% of J_{max}, whether for reactor 3 the drop was 60% of J_{max} and for reactor 4 it was of 70%.

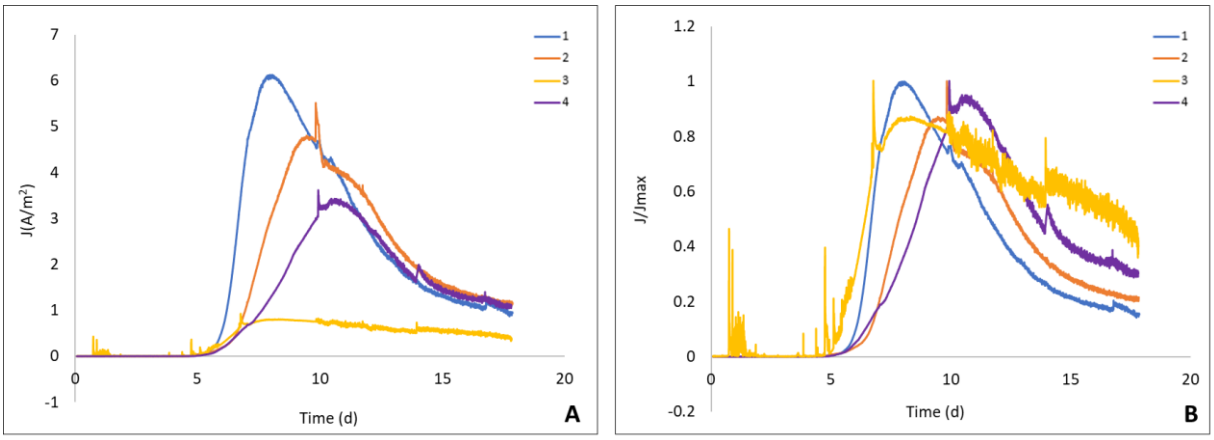

Figure IV-2 : Evolution of current density versus time for salt marsh EABs. The batch of sediments dates from October 2020. (A) Raw current density curves. (B) Normalized current density curves.

In both test 10-2020 and test 01-2021, the presence of two genera such as *Desulfovibrio* and *Halomonas*, in addition of species from *Acidaminobacteraceae* family, were detected with an increased relative abundance compared to biofilms cultured with the batch from March 2021. The main characteristics of these genera and family already described in the literature on EABs or BES bioanodes are given below:

- *Desulfovibrio* species are electroactive bacteria able to form biofilms on the anode of a MFC, where they produce nano-pili filaments to attach themselves to the electrode surface and transfer electrons from the biofilm to the anode (Eaktasang et al., 2013). Their respiration mechanism involves the reduction of sulfate or sulfur, but they can also use other oxidized compounds, such as nitrate, as final electron acceptors (Cordas et al., 2008). It is possible for this species to take electrons from iron-containing metals such as steel. Metallic iron oxidation can be coupled with proton reduction to hydrogen, and subsequently, hydrogen can work as an electron donor for sulfate reduction (Ueki and Lovley, 2022).
- Species from *Acidaminobacteraceae* family, included in the *Clostridiales* order, are anaerobic bactreia. They can be found in marine environments and are assumed relevant for organic matter degradation in aquatic systems (Ape et al., 2019). However, there is no consistent information regarding the expression of electroactivity in these species, yet members of *Clostridiales* order were found to be present in bioanodes. Their role seems to be related to scavenging inhibitory

metabolites, proteins, dead cells and bicarbonate produced by acetate oxidation, rather than to extracellular electron transfer (Yuan et al., 2017).

- *Halomonas* genus includes halotolerant bacteria, capable of growing in 20% of salinity (Askri et al., 2019) and transferring electrons to the electrode of a BES (Liu and Wu, 2021). Bacterial species of this genus have been already found in EABs formed from marine sediments and hypersaline environments (Erable et al., 2010; Tapia-Tussell et al., 2019). As far as their electroactivity is concerned, they can certainly form EABs but their performance is rather poor, since the maximum current production reached only a few mA/m^2 (Saidi et al., 2022).

Table IV-4 resumes the main relative abundances for the microbial population of salt marsh biofilms after 17 days of polarization. Samples 1 and 2 did not show a marked predominance of certain species, as samples 3 and 4 did for *Marinobacterium* at 64.7% and 66.6% of abundance respectively. The main abundance for samples 1 and 2 was *Desulfuromonas* with 37.5% and 26.8%. An explanation for the low electroactive performance may be given by the determination of non-electroactive bacteria in the biofilms, such as those belonging to *Acidaminobacteraceae* and *Bacteroidales.* Bacterial species included in that family and order might play other role in the bioanode. In addition, it seems complex to explain why in the four replicates where the biofilm was formed with the same SMS, there were discrepancies between the electrochemical performance and the microbial population diversity. A simple explanation can be given because of the chemical and microbial inhomogeneity of the inoculum (i.e. SMS). The 5% of inoculum added to the reactors could in this case be different and led to a differing selection and final population in the biofilm.

Table IV-4: Detailed relative abundances (%) of microbial population in salt marsh EABs in the four replicas. (g) indicates that the DNA analysis classification went until the genus level, while (f) to the family level and (o) to the order level. The most relevant values for each stage are in bold.

	Sample			
Order/Family/Genus	**1**	**2**	**3**	**4**
Marinobacterium (g)	7.3	17.0	**64.7**	**66.6**
Desulfuromondales (o)	1.8	0.0	0.0	0.3
Desulfuromonas (g)	**37.5**	**26.8**	0.1	6.4
Halanaerobium (g)	3.6	4.9	10.4	3.8
Bacteroidales (o)	9.2	11.9	4.9	5.6
Thermotalea (g)	0.5	0.7	0.8	0.5
Halomonas (g)	4.0	6.4	2.2	1.0
Acidaminobacteraceae (f)	6.0	8.4	4.8	2.7
Desulfovibrio (g)	4.8	2.6	1.6	0.5

IV.3.2.2. Test SMS 01-2021

SMS collected in January 2021 were used as inoculum source in this test. It should be noted that the method of sediment collection does not avoid collecting both the sediment in solid form accompanied by an aqueous phase, which represents hydration seawater saturated in salts. The inoculum is therefore made up of two phases, one in a liquid state, and the other in a solid state. The sediment and hydration water are stored in a single container, where the solid part is at the bottom and the liquid part is the supernatant. Usually, only the liquid part of the sediment has been used to inoculate the reactors. Here, now, we performed the inoculation in three different ways to test the influence of the sediment state (or rather phase) on the anode performance and on the microbial population of the anode. For this purpose, six reactors were started: the first two were inoculated with solid sediment, the next two with an equal mixture of liquid and solid, and the last two with the liquid part of the sediment, as is usually done.

Figure IV-3 presents the CA curves for the three-inoculum sources: solid sediments, solid/liquid sediments and liquid sediments. In no case tested, EABs electroactivity reached the maximum current density values of 8 to 10 A/m^2 typically expected. When working with solid sediments, reactor 1-solid showed an increase in current after day 5, but current later dropped abruptly. In addition, the shape after the absence of current with a vertical increase at day 10 rather suggests a connection issue. For reactor 2-solid there was no detectable electroactivity. For the reactors inoculated with the mix of liquid and solid sediments, the electroactivity was similarly low yet. Only a sudden increase and decrease in current production at day 10 was detected. EABs electroactivity inoculated with liquid fraction of the SMS was improved, but the maximum current was still 5 times lower than expected.

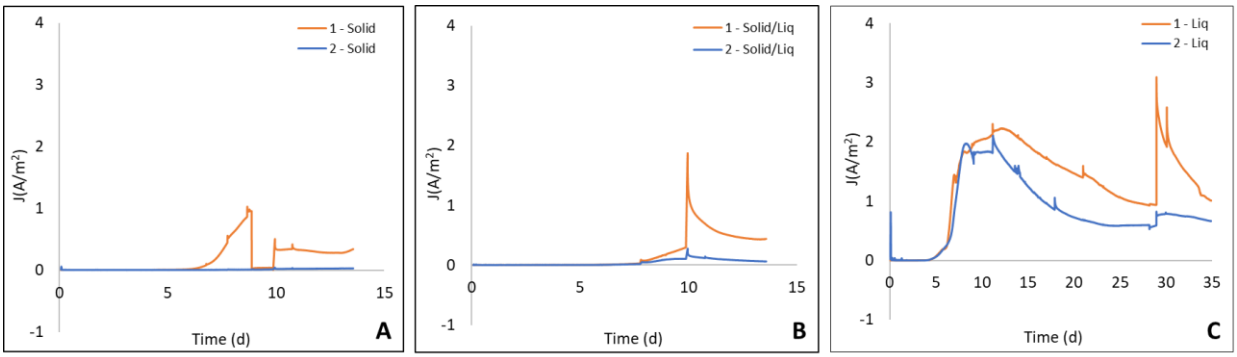

Figure IV-3 : Evolution of current density versus time for salt marsh EABs with a batch of sediments from January 2021. (A) Corresponds to inoculation with solid sediments, (B) to a mix of solid and liquid sediments and (C) to liquid sediments.

Relative abundances analysis of salt marsh EABs microbial populations showed different predominance according to the physical state of the inoculum:

- For solid sediments, *Halomonas* species were dominant in 26.6% and 25.5% for both duplicates, respectively. *Marinobacterium* species were also present, together with *Acidaminobacteraceae*, *Bacteroidales* and *Halanaerobium*, as described in Table IV-5.
- For the mix of solid and liquid sediments, *Marinobacterium* was mainly found in salt marsh EABs in 56.9% and 41.9% of abundance. *Acidaminobacteraceae* and *Bacteroidales* were both in second and third place of high proportion.
- For liquid sediments, *Desulfovibrio* was principally present in biofilms with 25.3% and 15.9%. In addition, the order *Desulfovibrionales*, where the genus *Desulfovibrio* is included, was also determined. *Marinobacterium* and *Bacteroidales* were also present.

It is not relevant to compare the microbial population of the EABs formed from liquid sediments since the polarization time was 35 days vs 13 days for solid and mix of sediments, and it has been previously shown that the polarization time influences the composition of the salt marsh EABs microbial population. However, this experiment helped to confirm that the use of liquid sediments was the proper choice, even if the batch of sediments did not represent the most efficient one. It would seem that the majority of electroactive bacteria was found in SMS. Another hypothesis might be that electroactive bacteria in the liquid state were more motile than those embedded in the solid sediments might. In the solid state, bacteria should be first in suspension before reaching the electrode; therefore, it should have been extracted first from the solid sediments in order to suspend it before inoculation.

With regard to the differences found in the microbial population in the bioanodes formed from solid sediments and the mix of sediments, the analysis of a vertical profile of SMS could help to elucidate this issue. Solid sediments are found in the bottom of the marshes, probably in an oxygen-depleted environment. Liquid supernatant sediments on the top are able to receive more light and surely develop mostly aerobic or aero-anaerobic microorganisms. Variation in the chemical composition of the sediments can also lead to variations in the microbial diversity. Wilms et al., (2006) studied the vertical

chemical profile of SMS, determining especially the concentrations of sulfate and organic matter in 400 cm deep sediments. They found that the higher sulfate content was in the first 100 cm of sediments and a higher ratio of organic matter was found in the deepest sediments.

Table IV-5 : Detailed relative abundances (%) of microbial population in salt marsh EABs inoculated in three different ways. (g) indicates that the DNA classification went until the genus level, while (f) for the family level and (o) to the order level. The most relevant values for each stage are in bold.

	Sample					
Order/Family/Genus	**1-Solid**	**2-Solid**	**1-Solid/Liq**	**2-Solid/Liq**	**1-Liq**	**2-Liq**
Marinobacterium (g)	13.5	20.6	**56.9**	**41.9**	12.2	13.3
Desulfuromondales (o)	1.1	0.7	0.0	0.0	3.8	1.2
Desulfuromonas (g)	0.7	0.0	1.1	5.5	8.2	4.0
Halanaerobium (g)	6.4	6.9	3.5	4.3	1.6	0.8
Bacteroidales (o)	12.9	5.1	7.6	7.2	10.5	11.5
Thermotalea (g)	2.7	7.0	1.4	1.0	0.8	0.5
Halomonas (g)	**26.6**	**25.5**	1.6	5.5	0.5	1.7
Acidaminobacteraceae (f)	10.1	12.5	12.2	10.6	1.0	0.6
Desulfovibrionales (o)	0.2	0.0	0.1	0.1	7.2	6.2
Desulfovibrio (g)	3.2	4.9	2.1	4.2	**25.3**	**15.9**

Taking into account the variability within a set of tests performed on the same sediment, results from test 10-2020 and test 01-2021 first demonstrated that replicates of experiments involving the same source of electroactive microorganisms for forming bioanodes do not always lead to reproducible results of current production. This was observed for domestic wastewater sampled from different geographic locations to inoculate the anaerobic anodic chamber of MFCs. More electric current was produced in the anode when wastewater from a location containing anaerobic bacteria was used (Santoro et al., 2021). In another study, (Velasquez-Orta et al., 2011) formed bioanodes with different types of industrial wastewater. MFCs fed with paper wastewater produced the highest current densities in comparison to dairy, brewery and bakery wastewater. The difference was mainly in the microbial population of the EABs formed from paper wastewater, which were electroactive and able to produce electrons mediators for electron transfer.

Now taking into account the variability associated with sediment sampling at different times of the year, it is quite likely that SMS were exposed to environmental conditions in which the bacterial consortium was affected. It was proved that external factors, such as rainfall, tidal changes, presence of pollutants and heavy metals can affect the microbial population of SMS (Córdova-Kreylos et al., 2006). In addition, temperature-related seasonal changes can affect the ratio of bacterial sulfate reduction in the sediments: in summer, rates are higher than in winter. This was shown to result in a cycle of increasing and decreasing amount of sulfate-reducing bacteria in the sediments, such as *Desulfovibrio* and *Desulfobacter* (Koretsky et al., 2002).

It is unknown if storage time and conditions could also alter the microbial community of the sediments that are collected. It would be ideal to be able to analyze and follow in time the chemical composition of the inoculum, for example by EDX analysis in the case of solid inoculum, with the microbial population of the batch before usage. This would help to achieve reproducible results and determine the composition of the microbial consortium that could provide the best performant bioanodes.

IV.4. Conclusions of Chapter IV

The experiments described in this chapter showed the importance of studying bioanodes with a temporal approach, thus demonstrating that the viability, EPS composition, microbial population and morphology of the salt marsh EABs change over time and are intrinsically related to its electroactivity. Although the analyses carried out were of a destructive nature (microscopy, cell staining, molecular biology), it was possible to identify that the stages of most interest are those occurring between the early stages of EAB formation (start of stage I) and to where the current density curve reaches the maximum value (end of stage II).

Although SMS proved to be a source of electroactive microorganisms, leading to the formation of robust and performant bioanodes, it is necessary to take into account the variability that different batches of sediments could introduce to the electroactivity and microbial population of EABs. This applies for the date of sampling in the marshes and for the sampling at the time of inoculation in the laboratory. It was demonstrated that liquid sediments are more suitable to form more efficient bioanodes when comparing to solid or a mix of solid and liquid SMS. However, it would be interesting to know which parameters impact on the inoculum microbial population the most, e.g. date of sampling of the inoculum, physical state, storage time, in order to obtain the expected electroactivity in the bioanodes. This would require a training on data science and programming skills in order to apply, for example, a PCA (principal component analysis) that could help to elucidate which is the most influential parameter.

Nevertheless, a field of research that is still largely unexplored is the role of the EPS in the electroactivity of multi-species EABs. It is well known that EPS are particularly indispensable for the electron transfer mechanisms within the biofilm, but most studies have been carried out in single-species biofilms or have focused on studying EPS production under stress conditions. As the method for identifying the EPS

composition using CLSM proved to be successful, the following chapter will attempt to study in depth the relationship between EPS and the electroactivity of salt marsh EABs. This will be investigated by modifying certain operational BES parameters, such as anode potential, acetate addition and concentration, nature of the substrate, age of the anolyte and quorum sensing mechanisms.

Chapter V : Study of the role of EPS in the electroactivity of salt marsh EABs in MacroBES

V.1. Introduction

The findings of the previous chapter showed that the relationship between protein EPS and polysaccharides EPS was closely linked to the electroactivity of EABs. When bioanodes yielded the maximum current value, the amount of extracellular proteins in the EABs was the highest. Otherwise, after the current drop of more than 50% of the peak, the quantity of extracellular polysaccharides raised. This analysis was made possible due to the development of a staining protocol to specifically target the different EPS components, followed by microscopic observations and subsequent image processing to quantify the presence of each component in the biofilm.

As already described in Chapter I, EPS proteins and EPS polysaccharides in the biofilm perform physical, structural and metabolic functions. Polysaccharides serve as a scaffold for structuring the matrix while proteins catalyze metabolic reactions. However, the role of proteins in a semiconductive matrix has begun to take more relevance in the recent years since it was demonstrated that EABs with higher fraction of extracellular proteins and lower fractions of extracellular polysaccharides showed a higher electroactivity. This was based on discoveries where proteins have been shown to contain the redox machinery for electron transfer, such as c-cytochromes, and conversely polysaccharides were proven to be of an insulative nature, interfering with electron transfer between the anode and the biofilm. Although it would appear that EPS are indispensable for the biofilm electroactivity, their fundamental role in multispecies EABs has been barely studied to date. For this reason, it was decided to continue with the investigation on the production and evolution of EPS composition in salt marsh EABs and their impact on the biofilm electroactivity.

The aim of this chapter is to verify if the described relationship between EPS proteins and EPS polysaccharides with the salt marsh EAB electroactivity is still true when operational parameters such as anode potential, acetate addition mode and concentration, substrate nature, age of the anolyte and quorum sensing (QS) mechanisms are modified.

Results were subdivided into two sections according to the protocol used for the post-processing of EPS CLSM images. Section V.2.1. contains experiments that were carried out in continuation of those presented in Research Article 2. Two tests studying the effect of the anode potential and the acetate addition mode attempted to correlate the electroactivity of the bioanode with the amount of polysaccharides and proteins. For determining the EPS composition, post treatment of CLSM images was performed with the ImageJ software.

Subsequently, as there was an interest in further investigating the influence on the EAB electroactivity and EPS production of other operational parameters, section V.2.2. of this chapter presents the results obtained during the Master 2 internship of Juan Diego Carvajalino Olave, which I supervised. This section includes experiments where the addition of acetate at different concentrations, the test of different substrates, the effect of the anolyte age and the addition of QS molecules were investigated. As a part of the internship, another method for quantifying EPS from CLSM images was developed in MATLAB allowing the automatic treatment of a larger amount of images and the performance of statistical analysis.

V.2. Results

V.2.1. Study of the role of EPS in the electroactivity of the EAB by pixel quantification of CLSM images in ImageJ

As presented in Research Article 2 section 2.3, where EPS composition was determined after treating the EABs images obtained from the CLSM by pixel quantification in image J, this procedure will be reutilized in this section to study the role of the EPS components in the performance of salt marsh EABs. The protocol is explained in more detail in section II.4.1.1.

In this section, two ways of adding acetate were tested: regularly and in pulses. In the first, as usually done in the experiments already presented in the manuscript, acetate was measured on a daily basis and adjusted to 40 mM. This means that there was a regular addition of acetate in order to maintain a constant acetate concentration in the reactors. In the second, a pulse of 40 mM of acetate was added into the reactors only when the electroactivity of the bioanode dropped to zero.

Table V-1: Summary of experimental conditions for section V.2.1.

Shared parameters		
Inoculum	SMS	
Temperature	30°C	
Substrate	Sodium acetate 40 mM	
Culture medium	Starkey medium (45 g/L of NaCl)	
Inoculation size % V/V	5	
Operation mode	Batch	
WE material	Stainless steel (SS)	
Reactor type	Standard	
Individual parameters		
Test	Test 5.1	Test 5.2
Date of inoculum sampling	March 2021	March 2021
Acetate addition	Regularly	In pulses
N° of reactors	5	8
E_{we} (V) vs. SCE	-0.4, -0.2, 0, 0.2, 0.4	-0.2, 0, 0.1, 0.4
Polarization time (d)	18 to 21	32

Table V-1 resumes the experimental conditions carried out in the tests from this section. All experiments were conducted at a controlled temperature of 30°C where 40 mM of sodium acetate was chosen as substrate. Reactors were purged with nitrogen gas before polarization. In Test 5.1, SS microelectrodes were polarized at five-selected anode potentials, where acetate was regularly added into the reactors. After, in Test 5.2, the values of potentials that yielded the best performant anodes in Test 5.1 were selected. In this case, acetate was added in pulses.

V.2.1.1. Test 5.1: Effect of the anodic potential when acetate is added regularly

Figure V-1 shows the CA curves for each bioanode polarized at the five selected potentials. The best performing bioanode was the one for the EAB formed under an applied potential of 400 mV/SCE, reaching a maximum current value of 11.47 A/m^2. Decreasing the anode potential to 200 mV/SCE resulted in a drastic change in the results, where the maximum performance corresponded to 0.86 A/m^2. When polarizing at 0 mV/SCE, the trend was similar for the bioanode formed at 400 mV, yet with a longer lag phase and a maximum current value of 10.53 A/m^2. For polarization at -200 mV/SCE maximum current reached 3.15 A/m^2 and for -400 mV/SCE current started to increase by the end of the experiment to a final maximum value of 3.72 A/m^2.

CVs at the end of constant polarization could be grouped into three sets of results. For EABs formed under a polarization potential of 400 mV/SCE and 0 mV/SCE, the electroactivity seemed to be the same when the potential was scanned. For potentials of -200 mV/SCE and -400 mV/SCE, there was no current plateau when scanning to positive potentials. The CV curve for 200 mV/SCE presented the same shape than 0 mV and 400 mV but with considerably lower values.

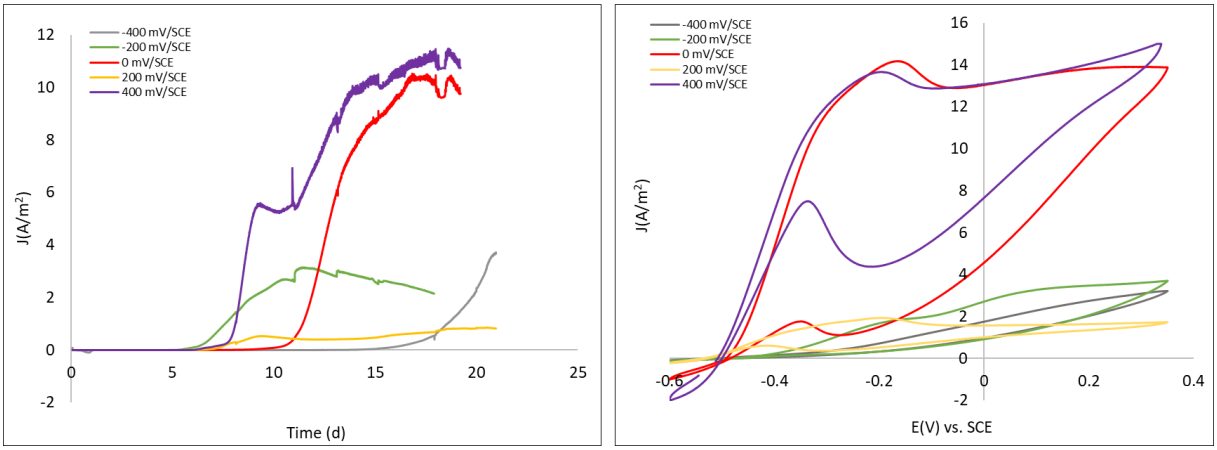

Figure V-1: (A) Evolution of current density versus time for salt marsh EABs formed over stainless steel microelectrodes at five different potentials. (B) CVs performed at a scanning rate of 1mV/s for bioanodes after the end of polarization.

The behavior observed for the bioanodes polarized at different potential values did not correspond to the one described in conventional electrochemical kinetics. From this point of view, it would have been expected that as higher the potential, current production should have increased. However, as seen in Figure V-1 (A), current density for the microelectrode polarized at 200 mV/SCE was lower than

expected. It is possible that the confidence given to this result was quite low. It would be necessary to repeat the experiment to check whether current values fall in the trend between those obtained for 0 and 400 mV/SCE. In addition, for a polarization potential of -400 mV/SCE, current production should have been the lowest of the test. This was not surprising as different trends have been observed with respect to the anode potential and current production in both multi-species EABs (Zhu et al., 2014; González-Muñoz et al., 2018; Guo et al., 2021) and single-species as well (Pinto et al., 2018; Yang et al., 2019).

In order to gain a deeper understanding of the effect of the anode potential in the electroactivity of the salt marsh EABs, after the final CV, microelectrodes were retrieved from the reactors. Each microelectrode was divided into two pieces, where one was dedicated to EPS observation by CLSM and the other to microbial population analysis by DNA extraction. In the case of the EAB formed at 200 mV/SCE, only a small part of the bioanode could be recovered, being the latter dedicated to EPS observation; therefore, the microbial population analysis was not performed in this case.

EPS composition was quantified from CLSM images and its abundance in each sample was summarized in Figure V-2 (A). The ratio of polysaccharides to proteins (PS/(Prot+PS)) was calculated and correlated to the final current value obtained in the CAs, as seen in Figure V-2 (B). A linear correlation was observed between current density and the PS/(Prot+PS) independently of the anode potential, where current was inversely proportional to the PS/(Prot+PS).

- The highest protein production was for anodes polarized at 400 mV and 0 mV, in addition to the lowest rate of PS/(Prot+PS). In addition, in these two cases, the bioanodes yielded the highest electroactivity of the set.
- For -400 mV and -200 mV, the composition in terms of proteins and polysaccharides was similar, yet a higher amount of total cells was observed for -200 mV.
- The highest PS/(Prot+PS) was for the anode polarized at 200 mV, which showed the lowest electroactivity of the group.

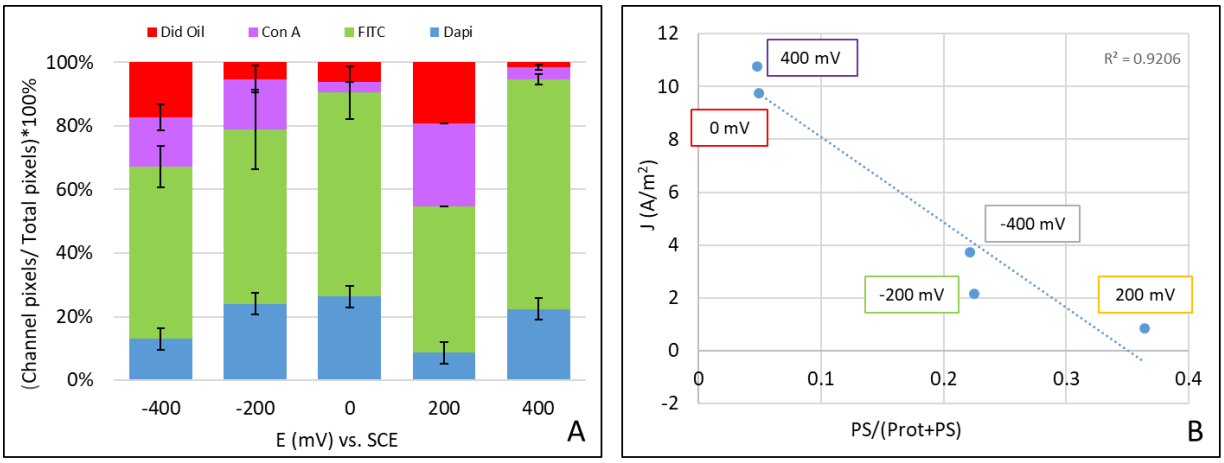

Figure V-2: (A) Determination of EPS components by pixel quantification in 2D images in ImageJ at different anode potentials. DiD Oil: Lipids, Con A: α-polysaccharides, FITC: Proteins, DAPI: Total cells. (B) Scattered plots of current density and PS/(Prot+PS) with their corresponding working electrode potential.

The relative abundance in terms of microbial population for each sample presented two main trends as seen in Figure V-3. EABs cultured at -400 and -200 mV/SCE showed a main abundance of *Marinobacterium* of 74.68 ±5.27 %, whereas for an applied potential of 0 and 400 mV/SCE the dominant genera was *Halomonas* with 54.06 ± 5.52 %. Another species belonging to order, family or genera already described in the previous chapters were present in the EAB, such as *Halanaerobium*, *Thermotalea*, *Acidaminobacteraceae* and *Desulfovibrio*, yet in small percentages. The slight presence of sulfate-reducing bacteria such as *Desulfuromonas* was not surprising due to the short duration of the experiment. As *Desulfuromonas* was found in the salt marsh EABs at the very late stages of biofilm formation when sulfur in the anolyte was depleted (Research Article 2), probably, in this experiment *Desulfuromonas* was still in a planktonic form.

Species from *Bacillus* and *Geotoga* genera as well as *Tissierellaceae* family were also detected. *Bacillus* species were found in bioanodes and their electroactivity was demonstrated (Yu et al., 2013, Islam et al., 2017). On the other hand, there were no hints for *Geotoga* species to be electroactive. They are sulfate-reducing bacteria that can participate in fermentative processes, therefore their role in bioanodes is unknown (Vigneron et al., 2016). In addition, *Tissierellaceae* family belongs to *Clostridiales* order, which are found to be present in bioanodes, yet their role seems to be related to scavenge byproducts generated by current production. As examples, species from this order can digest proteins, therefore they may feed on dead cells, while others are known to produce acetate from CO_2 and H_2 (Yuan et al., 2017).

It has already been described that anode potentials modulate the relative abundances of microbial population when using salt marsh as the inoculum source (Rousseau, 2016). In this case, the most efficient bioanodes (0 and 400 mV/SCE) seemed to be colonized by *Halomonas* and *Marinobacterium* genera. However, the correlation of the electroactivity with the population of the EAB was not straightforward.

It is worth noting that as in the previous chapter, the microbial population analysis for each biofilm can go to different phylogenetic levels. As in the case of Figure V-3, classification went up to family and genus level. However, there is no overlap between the phylogenetic levels.

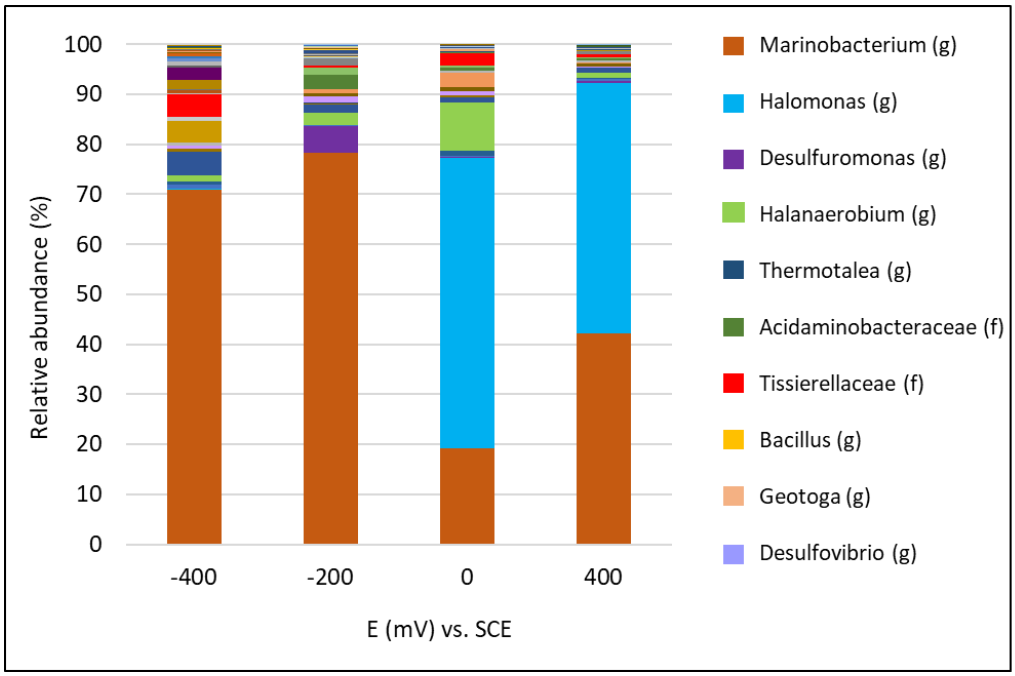

Figure V-3 : Relative abundances of microbial population in salt marsh EABs cultured at different potentials. Main abundances are resumed on the list on the right. (g) indicates that the DNA analysis classification went until the genus level, while (f) to the family level.

Subsequently, in order to gain more information, a second batch of reactors was launched, where the best performant anode potential values were selected from this set of experiments and acetate was added in pulses.

V.2.1.2. Test 5.2: Effect of the anodic potential when acetate is added in pulses

In the second part of this section, the following anode potentials were selected: -200 mV, 0 mV and 400 mV to continue with the experiments. In addition, the polarization potential value of 100 mV/SCE was added, as it corresponds to the potential typically applied to form salt marsh EABs in the rest of the experiments presented in this manuscript. The difference with Test 5.1 resides in the mode of acetate addition to the reactor. In this new batch of experiments, 40 mM of acetate were only added when electroactivity decreased to zero.

Figure V-4 shows the CA curves for the four pairs of duplicated tests of salt marsh bioanodes together with the profile of acetate concentration. In the lapse of 32 days of experiment, EABs formed under -200 mV and 0 mV generated three current cycles in response to three successive additions of 40 mM of acetate. For biofilms formed on SS microelectrodes polarized at 100 mV and 400 mV, only two current peaks were attained. For working electrode potential of 400 mV, one microelectrode of the two was

found to be broken inside the reactor after 11 days of polarization; therefore, only one a single set of data and a single colonized microelectrode was collected for this potential.

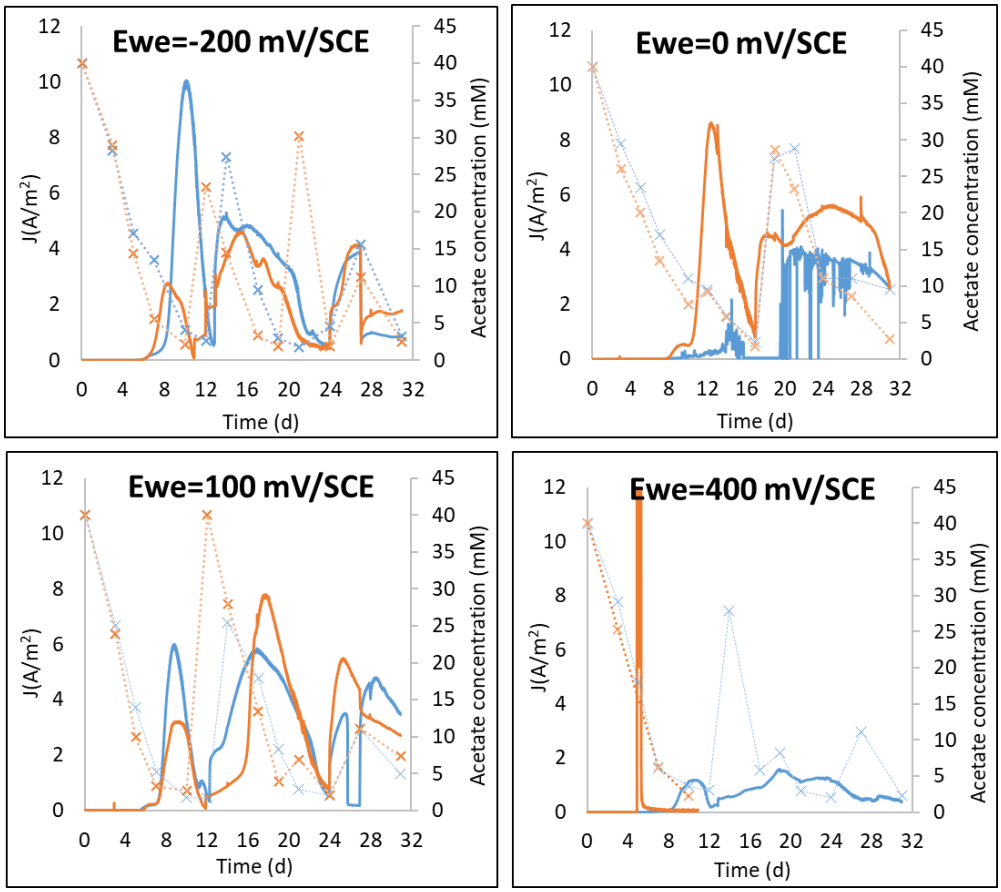

Figure V-4: Evolution of current density versus time and acetate concentration for salt marsh EABs formed on stainless steel microelectrodes when acetate was added in pulses. 'x' markers and dotted lines represent the acetate concentration (right axis) while the solid line represents current density (left axis).

The most reproducible current production curves were observed for a working electrode potential of 100 mV/SCE. In the case of -200 mV, there was a marked difference between current density in the first peak between duplicates, which then disappeared in the next two batches of acetate addition. For electrode potential of 0 mV/SCE, the trend was similar, yet in one duplicate current returned to zero intermittently, probably due to some electrical connection failures in the microelectrode.

Figure V-5 compares the results obtained with pulse and regularly addition of 40 mM of acetate at the anode potentials of -200, 0, 100 and 400 mV/SCE. For the potential of 100 mV/SCE, the curves for regular acetate addition were taken from Figure III-16 (A). For the rest of the potentials, CA curves from Figure V-1 and Figure V-4 were overlapped. As a first observation, the lag phase in both ways of managing the acetate addition conditions was similar. Therefore, whether acetate was added only once or regularly in this short period, it did not affect the electroactivity of the bioanode. However, excepting the case of -200 mV/SCE, acetate added regularly had a more positive impact in current production after the lag phase, since higher maximum current values were yielded for 0, 100 and 400 mV/SCE. This

would mean that even if the current density peak was reached sometime later in the experiment, better current densities could be obtained by adding acetate regularly than by adding it at the point of complete depletion.

As the potential of 100 mV/SCE was the only one where current production was recorded in both acetate addition conditions for a time of 32 days, it was also possible to compare the curves of current production after the current peak. Maximum current values attained in the reactors with acetate addition in pulses were within the values obtained for a regular addition of acetate. This would confirm that when polarizing at 100 mV/SCE, it would be preferable to add acetate regularly in order to obtain better performances in terms of current density values. Rousseau et al. (2013) also reported the same observation when working with the same inoculum yet implementing 2-cm^2 carbon felt electrodes as the anodes. It is believed that when substrate is depleted and a pulse of acetate is added, the EAB needs time to recover its electroactivity. In this reactivation period, acetate could be diverted to other metabolic pathways from planktonic bacteria, leaving the EAB with less amount of substrate than the expected one (Rimboud et al., 2014). This could explain why the performances for 100 mV/SCE were lower in the case of pulse addition than in the regular acetate addition.

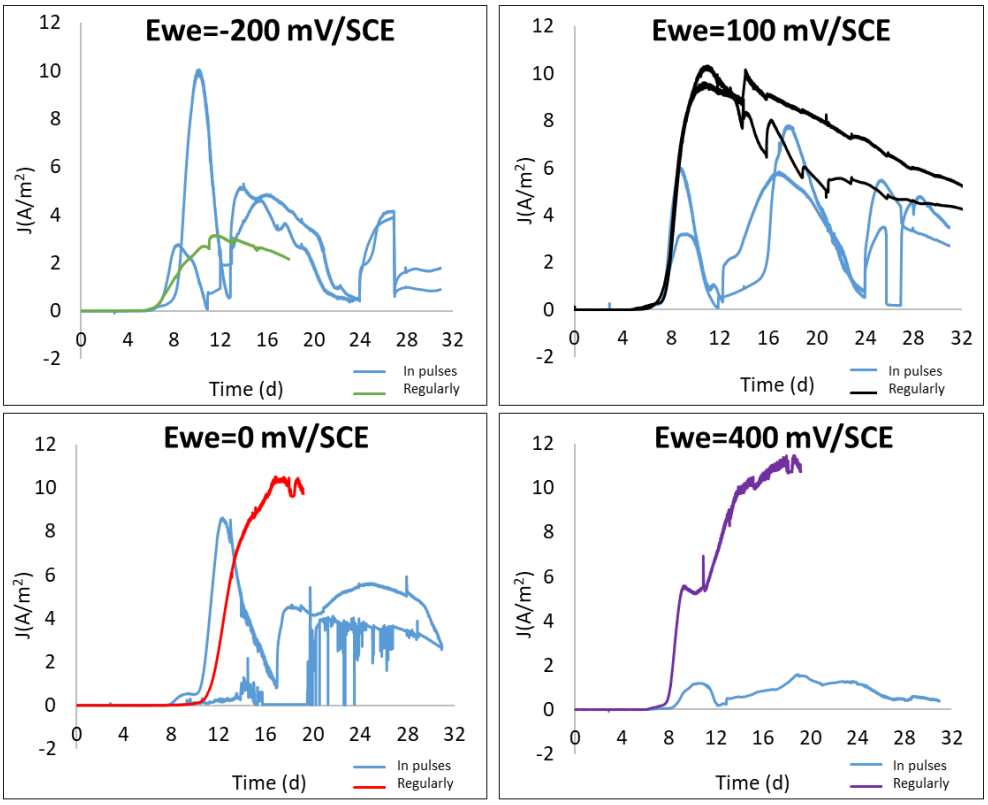

Figure V-5: Comparison between current densities obtained for salt marsh EABs at different polarization potentials when acetate was added whether in pulses (when current dropped to zero) or regularly.

After polarization, microelectrodes colonized with EABs were retrieved for EPS composition and microbial population analyses. EPS were quantified from CLSM images and their abundances in each sample was summarized in Figure V-6 (A). The (PS/(Prot+PS)) was calculated and correlated to the

final current value obtained in the CAs as seen in Figure V-6 (B). In this case, as there were duplicates for the potentials of -200, 0 and 400 mV/SCE, the error bars were calculated with the standard deviation both for current density and for the (PS/(Prot+PS)). For the potential of 400 mV/SCE, only a single value was presented.

The highest content of protein and the lowest (PS/(Prot+PS)) was again found out for EABs grown on anodes polarized at 0 and 400 mV/SCE; however, final current density values were not the highest of the set. The linearity that was determined in the previous experiment where current production increased with a lower (PS/(PS+Prot)) was not observed here. Nevertheless, comparison between Test 5.1 and this one does not make much sense since biofilms are from a different age. It was already demonstrated in Research Article 2 that together with the temporal evolution of the EAB there were shifts in the microbial abundance and the EPS composition. Polarization should have been stopped at the same time as in Test 5.1 in order to compare the effects acetate added in pulses or regularly in the EPS composition and the microbial abundance.

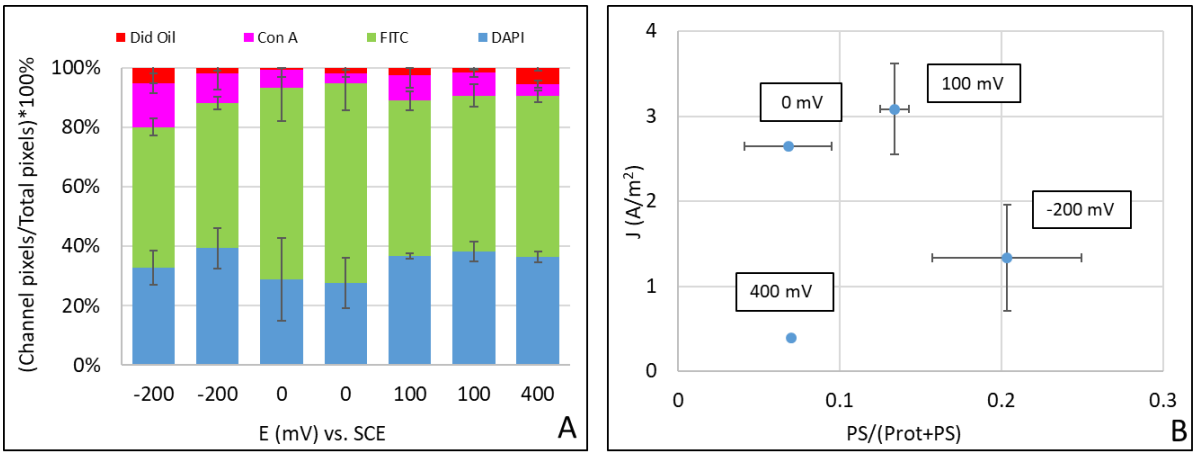

Figure V-6: (A) Determination of EPS components by pixel quantification in 2D images in ImageJ at different anodic potentials when acetate was added in pulses. DiD Oil: Lipids, Con A: α-polysaccharides, FITC: Proteins, DAPI: Total cells. (B) Scattered plots of current density and PS/(Prot+PS) with their corresponding working electrode potential.

Figure V-7 resumes the relative abundance of microbial population for each sample. The phylogenetic level went at some cases down to the species level, whether in others to either the order, family or genus. At glance, a much higher microbial diversity can be observed than in other sets of results, with the appearance of families and genera that were not detected before. Moreover, duplicates of EABs grown at the same potential presented a relative abundance that did not resemble each other, thus making it difficult to draw any conclusions.

- Species from the family *Idiomarinaceae*, comprising genus of *Pseudidiomarina* were present in all samples, and *Idiomarina* genus in the biofilm formed at 400 mV/SCE. These species were already detected in EABs formed from marine sediments (Erable et al., 2009). *Idiomarina* was found in the cathodic compartment of an MFC inoculated with the same SMS used in this work

(Rimboud et al., 2021). Species from this genus were found to use EET for respiration (Vinales et al., 2022).

- In biofilms formed at 0, 100 and 400 mV, species from the family *Flavobacteriaceae* were detected. The *Flavobacteriales* order contains gram negative halotolerant species (Gaffney et al., 2021), able to reduce nitrate (Mann et al., 2013). Species were also found to be present in bioanodes (Alatraktchi et al., 2014).
- *Exiguobacteraceae* family was detected in one EAB formed at 0 mV/SCE and in another at 100 mV/SCE. *Oceanobacillus profundus* specie was mainly identified in one bioanode at -200 mV/SCE. There is no record of electroactivity or presence in bioanodes of these bacteria.

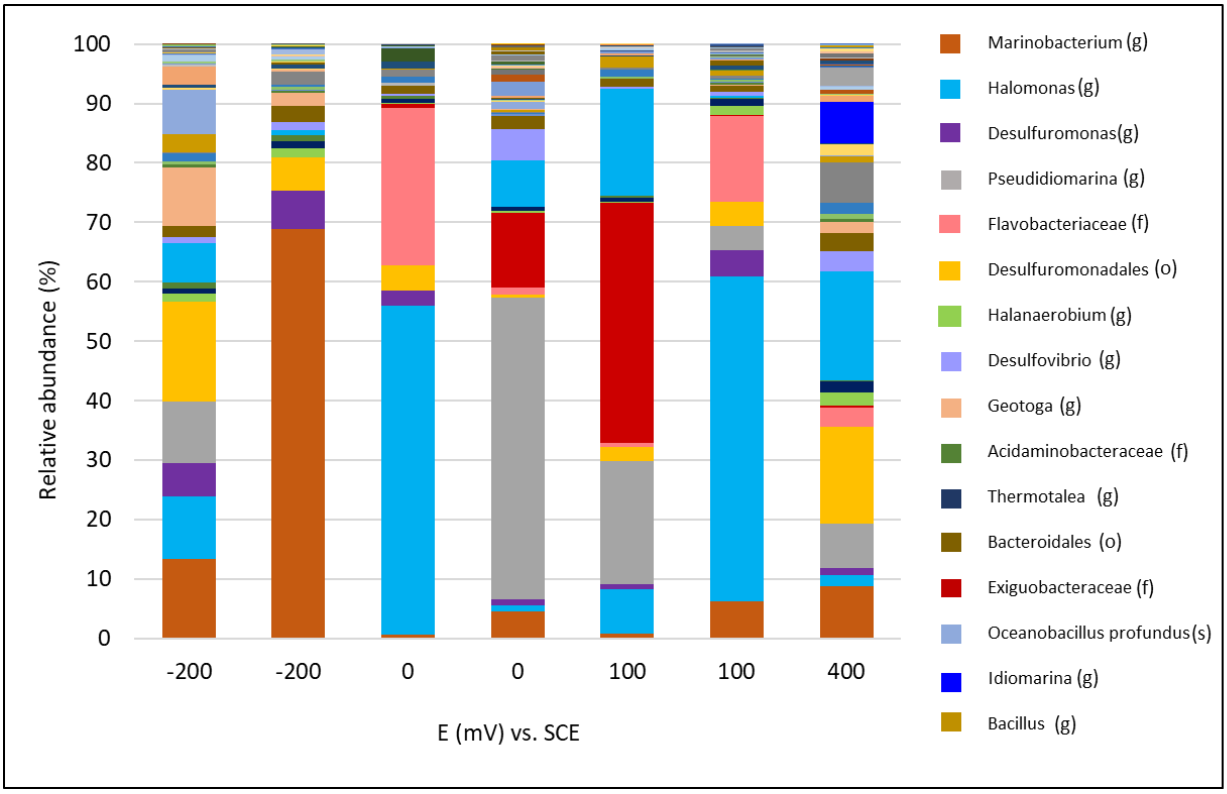

Figure V-7: Relative abundances of microbial population in salt marsh EABs cultured at different potentials when acetate was added in pulses. Main abundances are resumed on the list on the right. (s) indicates that the DNA analysis classification went until the species level, while (g) to the genera, (f) to the family and (o) to the order level.

It may be worthwhile to compare the microbial population of the EABs cultured under 100 mV/SCE of this test with those presented in the previous chapter. In both cases, the duration of the polarization was the same and the inoculum was taken from the same batch of SMS; what differed was the mode of acetate addition. When acetate was added regularly, the main species present in the salt marsh EABs were from *Desulfuromonas* and *Marinobacterium* genera. In this test, in one sample *Pseudidiomarina*, *Exiguobacteraceae* and *Halomonas* were dominant, whether in the other duplicate it was the case for *Halomonas* and *Flavobacteriaceae.* It is possible that acetate addition in pulses, where the biofilm was left at substrate starvation conditions, could have influenced the selection of other species to respire in

the anode. The same may have happened for the rest of polarization potentials, yet it is difficult to compare relative abundances since polarization was stopped at different moments.

V.2.1.3. Conclusions from Test 5.1 and 5.2

These two tests served, on one hand, to ratify the choice of polarizing the SS microelectrodes at 100 mV/SCE and adding 40 mM of acetate regularly to the reactors, as previously selected in Chapter III. Concerning the anode potential, it is true that by polarizing the anode at 0 and 400 mV/SCE, high current densities were also obtained. However, 400 mV/SCE was a rather high value to polarize the SS microelectrode and in some cases, as seen for the duplicate of Test 5.2, the microelectrode has broken in the course of polarization. A value of 0 mV/SCE could have been an alternative polarization potential to form salt marsh EABs.

On the other hand, an attempt was made to correlate the content of polysaccharides and proteins with the electroactivity of the EABs. For Test 5.1, the (PS/(Prot+PS)) seemed to increase with the decreasing final current, confirming what has been noted in bibliography. This was because the presence of proteins increased at higher currents in the biofilm matrix, whether the amount of polysaccharides decreased. Nevertheless, for Test 5.2, there was no clear trend between the (PS/(Prot+PS)) and final current density, as there was no trend for the individual components either. In the few bibliographic works for single species and multi-species EABs, the analysis has always been made by stopping the polarization at the maximum current value or when current reached stationary state (Yang et al., 2019; Guo et al. 2021). In those cases, they were young biofilms of three to nine days old. Regarding microbial diversity, in Test 5.1, *Marinobacterium* and *Halomonas* mainly colonized the biofilms that reached the highest current density values (polarized under 0 and 400 mV/SCE). For Test 5.2, results were more diverse in terms of relative abundance, probably due to the acetate added in pulses.

As a comparison between the two tests was not possible due to the polarization time and the conditions under which the biofilms were formed in both tests, other strategies to study the link between the EPS composition and the electroactivity of salt marsh EABs were developed. This will be presented in the following sections of this chapter.

V.2.2. Study of the role of EPS in the electroactivity of the biofilm by pixel quantification of CLSM images in MATLAB

So far, the post-processing of the images obtained from the CLSM analysis for EPS quantification presented certain particularities: it was a laborious process, where each image obtained from a z-scan was converted into a two-dimension projection. After, the application of threshold value to discriminate which pixels represented the biofilm matrix and which did not, was done manually. This implied that for a sample, as there were four acquisition channels for the different EPS components, this process had

to be repeated successively four times. The method could be performed for the treatment of a few stack of images, but it was non-manageable if a more massive analysis was needed.

This section includes the experiments carried out in the framework of Juan Diego Carvajalino Olave's Master 2 internship. One of his main tasks was to improve and to automatize the post-processing procedure of the image stacks obtained in CLSM. For this, a protocol explained in more detail in section II.4.1.2. was developed in MATLAB to treat images and to define the pixel threshold value automatically.

Again, the idea was to investigate the role of the EPS in the electroactivity of EABs. In addition, supplementary quantitative data on the thickness of the biofilm was also measured with the MATLAB protocol and included in the analysis. Here results were analyzed by applying the ANOVA method. This analysis of variance allows determining if the effect of the EPS components or the biofilm thickness were significant or not on the current density produced by the biofilm. This was easy translated into p-values, where variables that had a significant effect presented low p-values, under 0.05. Then, for the significant variables, a scattered plot graph allowed indicating whether the correlation had a positive or negative impact. This method has already been used to determine the influence of EPS components on stationary current and EPS redox properties in multi-species EABs (Guo et al., 2021)

In Test 5.2 belonging to the previous section, the effect of acetate addition at different polarization potentials was tested. In this section, to continue in the same line of work, the first experiment (Test 5.3) tested the effect of different acetate concentrations at the typically applied working electrode potential of 100 mV/SCE. Four different concentrations were considered: 10, 20, 40 and 100 mM and added in pulses. The aim of this experiment was to determine the impact of acetate concentration on the electroactivity and the influence in EPS production. In the next Test 5.4, formate, butyrate and glucose were added to the reactors as alternative substrates instead of acetate. This allowed to determine whether other substrates may be suitable for salt marsh EABs formation and to compare the performances of bioanodes formed from diverse substrates. A number of studies have tested different substrates in BES (Kan et al., 2011; Speers and Reguera, 2012, Flayac et al., 2018). However, to date, only the effects on bioanode current generation have been studied without considering the impact on EPS production.

Subsequently, maintaining acetate as the substrate, in Test 5.5, the influence of the aging of the anolyte was inspected. Some strategies, such as keeping the microelectrodes in open circuit potential (i.e. not connected) for a certain time and then polarizing the microelectrodes, or the introduction of clean microelectrodes at different times of the experiment were tested. This helped to corroborate certain hypotheses put forward in Chapter IV regarding the spatio-temporal evolution of the microbial population of the biofilm and the planktonic bacteria. Finally, in Test 5.6, salt marsh EABs were formed under the addition of commercial QS molecules of acyl homoserine lactose (AHL) type. This experiment

enabled an insight into the electroactivity of bioanodes formed under the influence of these molecules, which has been scarcely studied for multi-species biofilms.

Table V-2 : Summary of experimental conditions for section V.2.2. for comparison, 40 mM of acetate corresponds to 2560 mg of COD. C4 corresponds to N-Butyryl-DL-homoserine lactone, C6 to N-Hexanoyl-L-homoserine lactone and C12 to N-(3-Oxododecanoyl)-L-homoserine lactone.

Shared parameters				
Inoculum	Salt marsh			
Temperature	30 °C			
Culture medium	Starkey medium (45 g/L of NaCl)			
Inoculation size % V/V	5			
Operation mode	Batch			
WE material	Stainless steel (SS)			
Reactor type	Standard			
E_{we} (V) vs. SCE	0.1			
Individual parameters				
Tests	Test 5.3	Test 5.4	Test 5.5	Test 5.6
Date of inoculum sampling	October 2021	February 2022	February 2022	February 2022
N° of reactors	8	6	8	10
Substrate	Acetate	Formate, Butyrate, Glucose	Acetate	Acetate
Substrate concentration	10, 20, 40, 100 mM	2560 mg COD	40 mM	40 mM
QS molecules?	-	-	-	C4, C6, C12
Polarization time (d)	17 to 30	17 to 48	20 to 48	17 to 55

Table V-2 resumes the experimental conditions for this section. All reactors were maintained at a constant temperature of 30 °C and flushed with a gas stream of nitrogen for 20 minutes before the start of the polarization. Substrate, either acetate, formate, glucose or butyrate, was added in pulses. It was decided to proceed in this way since the current peak for acetate was usually obtained faster than when feeding regularly, as seen in Figure V-5. Substrate addition was done either when current decreased to zero, or when substrate concentration in the anolyte was less than 10% of the initial and wanted value. Unfortunately, in this section only the microbial population results were obtained for the bioanodes of Test 5.3 formed under different acetate concentrations.

V.2.2.1. Test 5.3: Effect of acetate concentration (added in pulses)

Acetate concentrations of 10, 20, 40 and 100 mM were tested as substrate. Figure V-8 shows current production for EABs cultured under the four acetate concentrations. Acetate at the concentrations of 10 mM and 20 mM was not sufficient to develop significant current in the anode, as it was successfully observed for the reactors fed at 40 mM and 100 mM. Although acetate concentration used was 2.5 times higher for 100 mM than for 40 mM, the maximum current achieved was in the same range. Duplicates for acetate at 40 mM reached a maximum of 6.75±0.13 A/m^2, yet this value was attained 10 days apart. For acetate concentration of 100 mM, CAs shapes were similar, yet after day 10 one duplicate yielded

higher current up to 7.43 A/m^2. The effect of acetate saturation in the performance of bioanodes has already been described. In general, a linear trend is observed between the current yielded and the concentration of acetate, but the slope decreases at higher concentration values, with current reaching a maximal plateau. This is probably related to a limit reached in the acetate conversion rate, which remains stable at higher substrate values (ter Heijne et al., 2015).

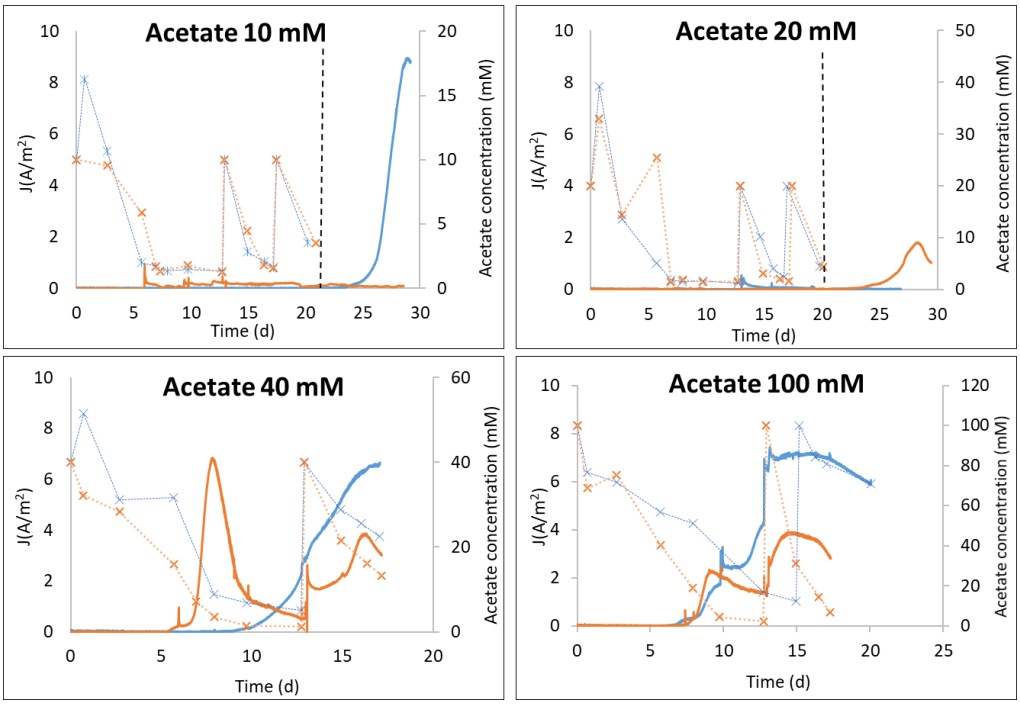

Figure V-8: Evolution of current density versus time and acetate concentration for salt marsh EABs grown at different acetate concentrations under constant polarization of 0.1 V/SCE. Dashed lines at 10 mM and 20 mM of acetate show the change of acetate addition from pulse to regular. 'x' markers and dotted lines represent the acetate concentration (right axis) while the solid line represents current density (left axis).

In an effort to produce current in reactors with 10 mM and 20 mM of acetate, after 20 days of polarization, their initial acetate concentration was replenished on a daily basis until the end of the experiment. In this acetate addition mode, only one each duplicate showed a current response. For reactors where acetate was added regularly to 10 mM, one duplicate reached 8.95 A/m^2 by the end of the polarization, whether for acetate concentration at 20 mM, one duplicate attained 1.81 A/m^2 at day 28. Probably, the constant input of substrate led to a faster recovery of the EABs electroactivity, serving the microelectrode as the electron sink.

CVs conducted at the end of polarization as seen in Figure V-9 showed that reactors with clear current response presented curves with redox peaks and hysteresis phenomena, something already observed for salt marsh biofilms fed with acetate. For duplicates that did not yield any current in the case of 10 mM and 20 mM, the CV scan yielded values close to zero thus confirming the sparse electroactivity of the bioanode.

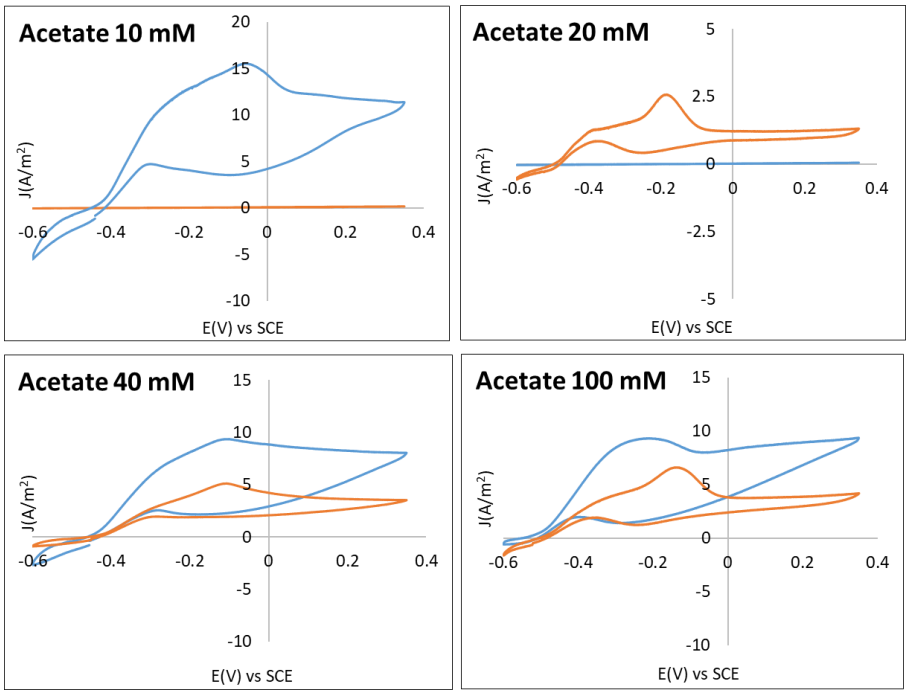

Figure V-9: Final CVs performed at a scanning rate of 1 mV/s for salt marsh biofilms formed over SS microelectrodes at different acetate concentrations.

Unfortunately, the low reproducibility between duplicates made it difficult to statistically conclude any link between the external variable tested (in this case, the concentration of acetate) with other response variables such as EPS composition and the bioanode J_{max}. For example, on duplicates that run at 100 mM of acetate, the difference in the current density peaks was almost double between samples. Nonetheless, the lag phase on current production for reactors at 40 mM and a 100 mM of acetate was similar (around 6-10 days), while acetate depletion in all cases for the first batch of acetate was achieved from 10 to 12 days. For this reason, it was decided to keep on correlating the final value of current density of the CAs, as done in the previous section, to the components of the polymeric matrix and the biofilm thickness.

After polarization, microelectrodes were retrieved and biofilms were stained for EPS observation. The scan of each microelectrode with CLSM and image processing with the new automatized protocol, allowed calculating the influence of the EPS components and biofilm thickness on current density, as seen in Table V-3.

Table V-3 : ANOVAs results from the effect of EPS components and biofilm thickness on current density at different acetate concentrations. Eight samples were analyzed. PS: α-polysaccharides. Prot: Proteins. Ratio refers to the proportion of the EPS component on the biofilm matrix.

EPS component	p-value
Total cells (DNA) ratio	0.111
Lipids ratio	0.378
Proteins ratio	0.024
α-polysaccharides ratio	0.627
PS/(Prot+PS)	0.100
Biofilm thickness	0.015

Significant correlations were found between the protein ratio and current density, and also between biofilm thickness and current density. For total cells, lipids, α-polysaccharides and (PS/(Prot+PS)), no significant correlation can be highlighted, either negative or positive since the p-values were higher than 0.05. Scattered plots of these two variables versus current density are shown in Figure V-10 where the correlation in both cases was positive. As CA were stopped after a second acetate addition and in most cases where reactors were at the maximum peak, a limiting biofilm thickness value was not observed, where beyond that value the correlation with current density would have been negative. This dual behavior could have been probably the case for results presented in Research Article 2, section 3.2, where current and biofilm thickness increased after the maximum current peak with the higher biofilm growth rate to a thickness of 32 µm after 11 days. Later biofilm kept on growing, yet current decreased, in order to reach a final thickness of 58 µm at day 55.

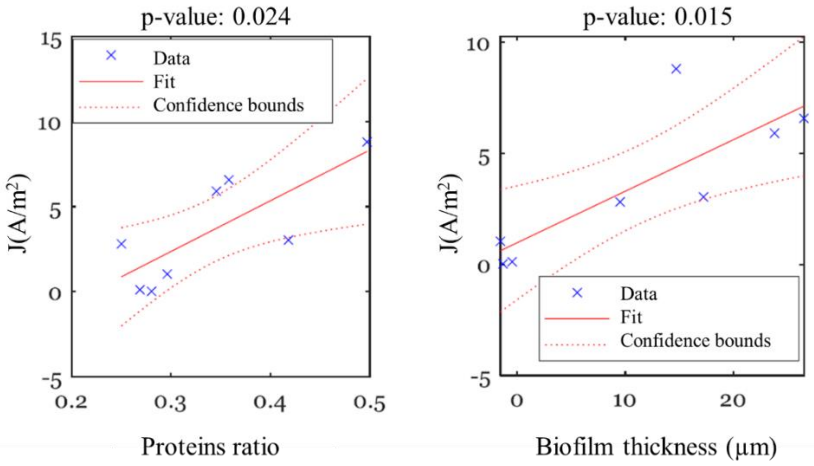

Figure V-10 : Scattered plot of proteins ratio and biofilm thickness vs. current production for the eight reactors of the Test 5.3.

Another portion of the microelectrode was devoted for microbial population analysis. Relative abundances of microbial population for duplicates are shown in Figure V-11. *Marinobacterium* was the dominant genus in all cases, with a presence between 33 to 59%. For acetate concentrations of 10 and 20 mM, in the bioanodes where current was not improved after the regular substrate addition, *Arcobacter* was detected with a 25% of abundance at 10 mM and 15% at 20 mM. *Arcobacter* was already present

in the bioanode formed at stage I in Research Article 2 at 9.7% of abundance, where there was no observable current density after 7 days of polarization. In addition, the presence of *Dethiosulfovibrio* was observed for the first time, yet in abundances ranging from 0.1% to 12.0%. Bacteria belonging to this order are sulfate-reducing microorganisms, strictly anaerobic, adaptable to a high-salinity environment and can reduce thiosulfate to hydrogen sulfide. They have been already detected in bioanodes of MFCs fed with food wastewater (Zhang et al., 2019).

The most remarkable observation from this set of experiments was clearly the increased presence of *Desulfuromonas* in anodes fed with elevated concentrations of acetate. In both reactors fed at 10 and 20 mM where current did improve when adding acetate regularly, the presence of *Desulfuromonas* in the bioanode was of 9.5% and 6.6%. At 40 mM of acetate, results were different. In one sample, the abundance was of 36.5%, while in the other it only reached to 4.6%. For reactors fed at 100 mM, *Desulfuromonas* incidence variated only slightly between 31.7% and 28.8%. It is known that this kind of bacteria grows by oxidizing simple organic compounds, such as acetate, using sulfate present in the liquid electrolyte providing from SMS as the electron acceptor. Thus, it is logical to observe an increase of *Desulfuromonas* at elevated acetate concentrations. Wang et al., (2022) corroborated the tendency of *Desulfuromonas* enrichment in BES specifically with acetate. They observed a selection in *Desulfuromonas* in acetate-fed MFCs, whether *Geobacter* species were mainly found in propionate-fed MFCs bioanodes.

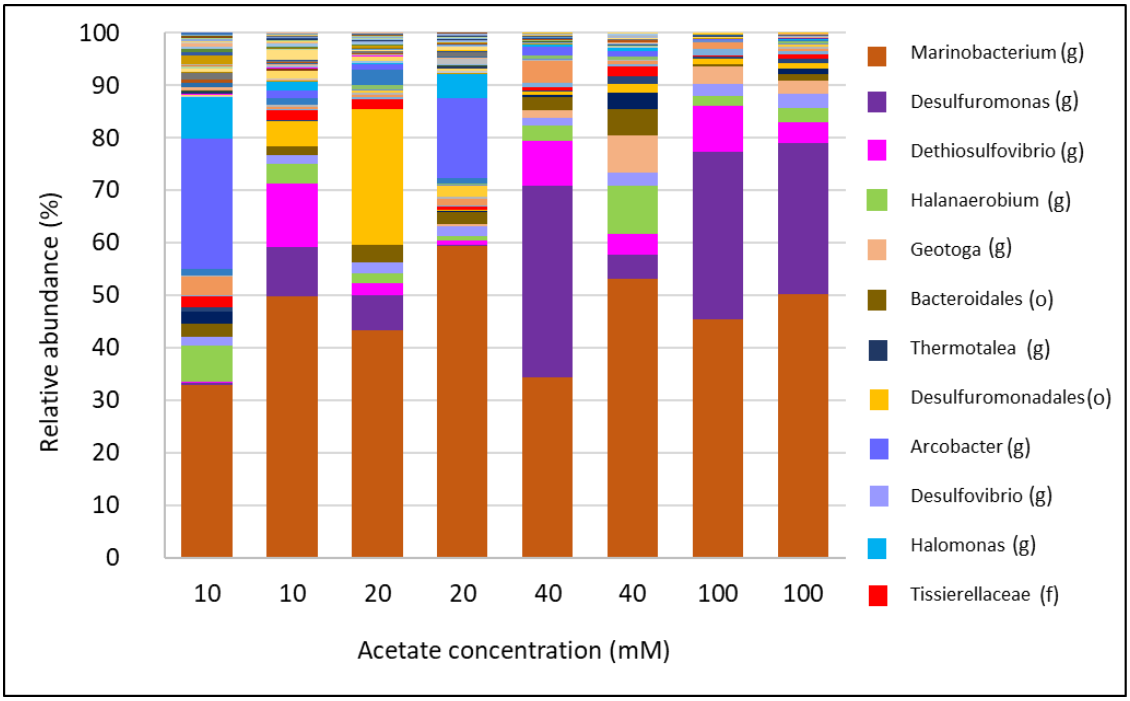

Figure V-11 : Relative abundances of microbial population in salt marsh EABs cultured at different acetate concentrations when the latter was added in pulses. Main abundances are resumed on the list on the right. (g) indicates that the DNA analysis classification went until to the genera level, (f) to the family and (o) to the order level.

V.2.2.2. Test 5.4: Effect of the nature of the substrate

In this set of experiments, reactors in duplicate were fed with glucose, butyrate and formate as substrates. The substrate concentration was equivalent to 40 mM of acetate in terms of electrons equivalence, corresponding to 2560 mg/L of COD.

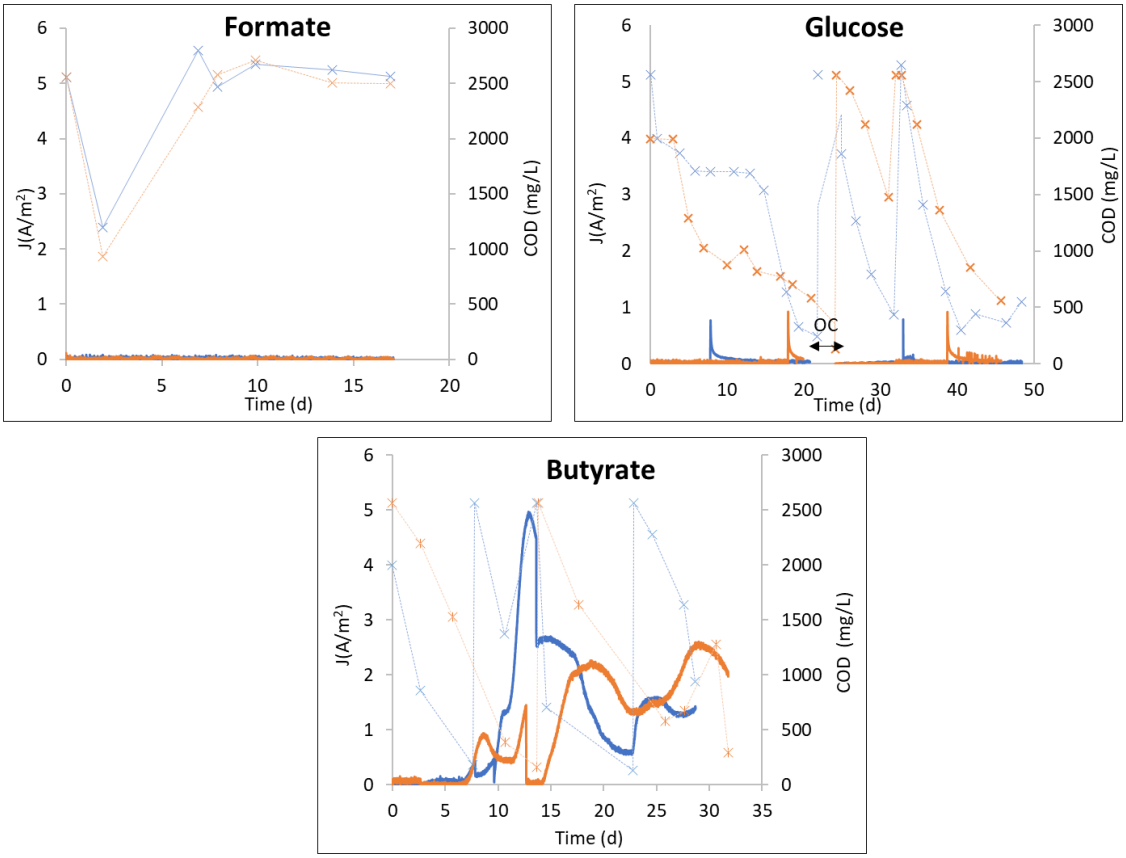

Figure V-12 : Evolution of current density versus time and COD consumption for salt marsh EABs grown with different substrates under constant polarization of 0.1 V/SCE. 'x' markers and dotted lines represent the COD concentration (right axis) while the solid line represents current density (left axis).

Figure V-12 shows current production for reactors fed with formate, butyrate and glucose, together with the COD evolution in time. For the case of formate, after 17 days of polarization, no electroactivity was observed for the bioanodes. The COD content decreased in the second COD measurement from 2560 mg/L COD to around 1000 mg/L of COD, but it was later reestablished to the initial value. This may have been a misreading; suggesting that even bacteria in planktonic state could not degrade and make use of formate as substrate. However, when looking at the shape of the CVs (Figure V-13) at the end of the polarization, a redox peak with a limited current density (~0.35 A/m^2) was observed for one of the formate-fed biofilm duplicates at a potential of -0.23 V/SCE. This might imply that there was an initial formation of the electroactive biofilm, but that the proportion of formate-degrading bacteria in the inoculum was low enough to drive an apparent change in the COD values. If the anode potential were set to -0.23 V/SCE, there would probably be an enhanced proliferation of formate oxidizing populations.

In contrast to formate, glucose was depleted in about 20 days; (approximately 2 times faster than acetate in the previous test) however, no current was recorded. After 20 days of constant polarization, other strategies were implemented to test whether the performance of glucose-fed reactors could be improved. Microelectrodes were left at open circuit potential for a period of 5 days and then polarization was resumed until a final time of 48 days. This strategy of working under periods of no polarization has proved to be a successful approach to improve the electroactivity of the anodic EAB (Pocaznoi et al., 2012c; Zhang et al., 2018). It would seem that electrons go to a process of storage when the circuit is open and they are later released when it is closed (ter Heijne et al., 2020). Nevertheless, it was not the case here for glucose-fed reactors, as the CVs performed on the biofilms after polarization showed almost no electroactivity.

Only in the reactors fed with butyrate current was produced. The first batch of butyrate was consumed in 5 to 15 days. The duplicate reactors reached maximum peaks of 4.97 and 2.60 A/m^2, which were lower than the peaks basically attained for acetate-fed reactors at the same COD concentration (6.78 and 6.58 A/m^2). Thus, it is possible that planktonic bacteria present in the culture medium were able to degrade the butyrate molecules into acetate, something already described when using wastewater as inoculum (Flayac et al., 2018). CVs showed positive oxidation rates starting from -0.5 V/SCE and -0.4 V/SCE in each duplicate.

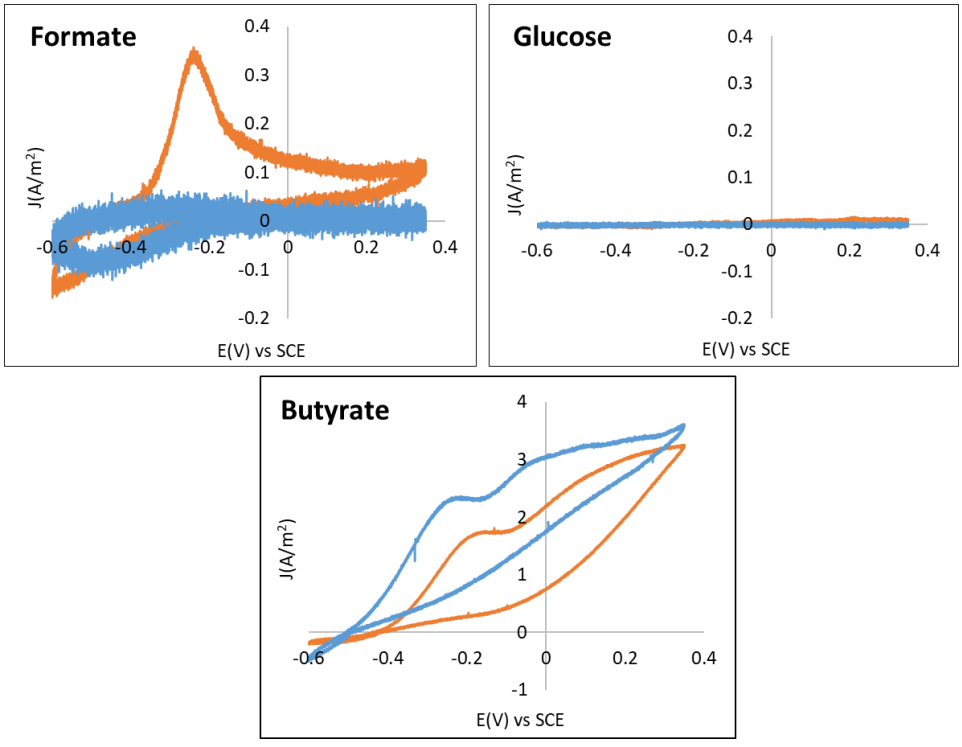

Figure V-13: Final CVs performed at a scanning rate of 1 mV/s for salt marsh EABs formed over SS microelectrodes in the presence of different substrates (formate, glucose and butyrate).

The use of glucose, formate and butyrate has been described several times in the literature to grow anodic EABs on electrode materials. In most of these studies, for glucose and formate, the anodic current

production was always lower than when using acetate as substrate (Lee et al., 2008; Kan et al., 2011; Speers and Reguera, 2012). One clear difference between glucose and formate fed reactors in this experiment was that in glucose reactors, there was a consumption of substrate over time and for formate-fed reactors there was not. This might mean that glucose molecules could have followed some fermentation pathways, possibly generating electrons acceptors that divert electron flow away from electroactive microorganisms (Freguia and Rabaey, 2008). This set of experiments made clear that acetate is the substrate that induces anodic EABs expressing the highest electroactivity when using SMS as the inoculum.

For the ANOVA analysis, only five of the microelectrodes were considered instead of six, since one microelectrode broke in one glucose-fed reactor by the end of the experience. Table V-4 shows that α-polysaccharides ratio, proteins ratio, (PS/(Prot+PS)) and biofilm thickness presented a significant correlation with current production ($p<0.05$). For the case of total cells and lipids, the correlation was not significant.

Table V-4: ANOVAs results from the effect of EPS components and biofilm thickness on current density at different substrate sources (formate, glucose and butyrate). Five samples were analyzed. PS: α-polysaccharides. Prot: Proteins. Ratio refers to the proportion of the EPS component on the biofilm matrix.

EPS component	p-value
Total cells (DNA) ratio	0.819
Lipids ratio	0.204
Proteins ratio	0.002
α-polysaccharides ratio	0.022
PS/(Prot+PS)	0.011
Biofilm thickness	0.015

The scattered plots from Figure V-14 indicated a positive correlation of current density with biofilm thickness and proteins ratio, whether a negative correlation with the α-polysaccharides ratio. As the p-value correlating current density with proteins ratio was the closest to zero, this correlation was the most significant one. It could be observed that in the case where butyrate was the substrate source, where final current ranged between 1 to 2 A/m^2, a biofilm was formed where the protein ratio was higher than in the case of formate and glucose, and the ratio of α-polysaccharides was lower. This confirms the conductive properties of the biofilm matrix extracellular proteins.

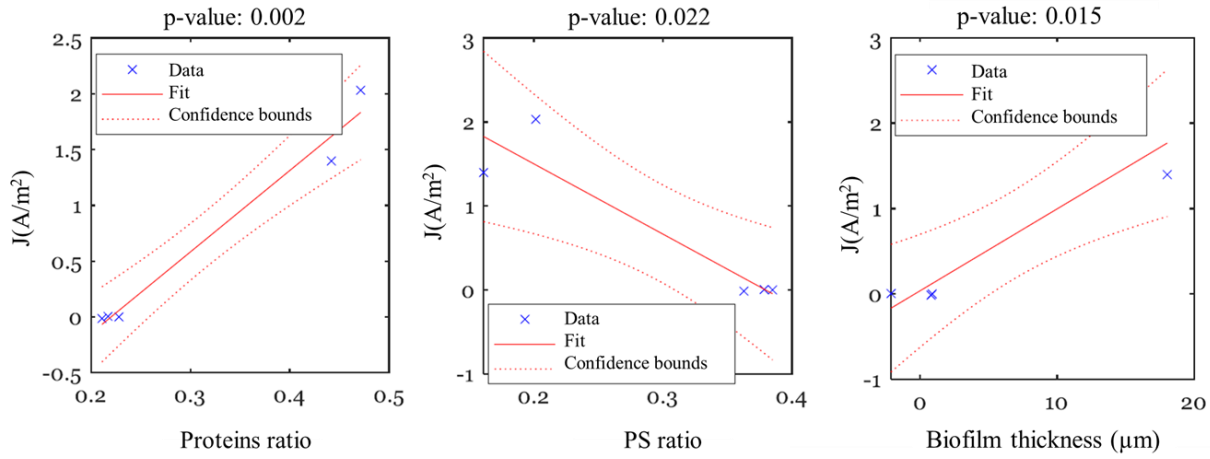

Figure V-14 : Scattered plots of proteins ratio, PS ratio and biofilm thickness vs. current production for different substrates (formate, glucose, butyrate). PS: α-polysaccharides.

These two consecutive experiments (Test 5.3 and Test 5.4) served to confirm that acetate was the most suitable substrate for the formation of salt marsh EABs on SS microelectrodes for high current generation. Choosing a concentration of 40 mM was still a right parameter, since at higher values current did not sharply increase. Butyrate could be also considered as an alternative substrate source, but for glucose and formate, it would appear that the salt marsh microbial consortium was not sufficiently adapted to use these organic molecules as fuel for electro-oxidation currents.

V.2.2.3. Test 5.5: Effect of the aging of the anolyte

In a previous experiment presented in Research Article 2, section 3.4, it was demonstrated that renewing the batch of anolyte with a fresh batch of Starkey medium and inoculum after ~ 30 days of polarization had no effect on the electroactivity of the salt marsh EABs formed over stainless steel microelectrodes. Starting from this premise, three strategies that can influence biofilm formation and current output were investigated. For this purpose, eight reactors were launched. The strategy in the first four reactors was to introduce clean microelectrodes as new anodes at different times of the experiment, always maintaining the same batch of anolyte, in order to evaluate current production in the new anodes with an aging anolyte. This was done for two cells operating at open circuit and two at a fixed potential of 0.1 V/SCE. In another two reactors, the anolyte was replaced twice in less than 20 days of experiment. In this case, the work was always done with the same microelectrodes. In the last two cells, the short effect of bioanode exposure to oxygen was investigated as to prove whether the bioanode air exposure when changing the anolyte had a negative effect on its electroactivity.

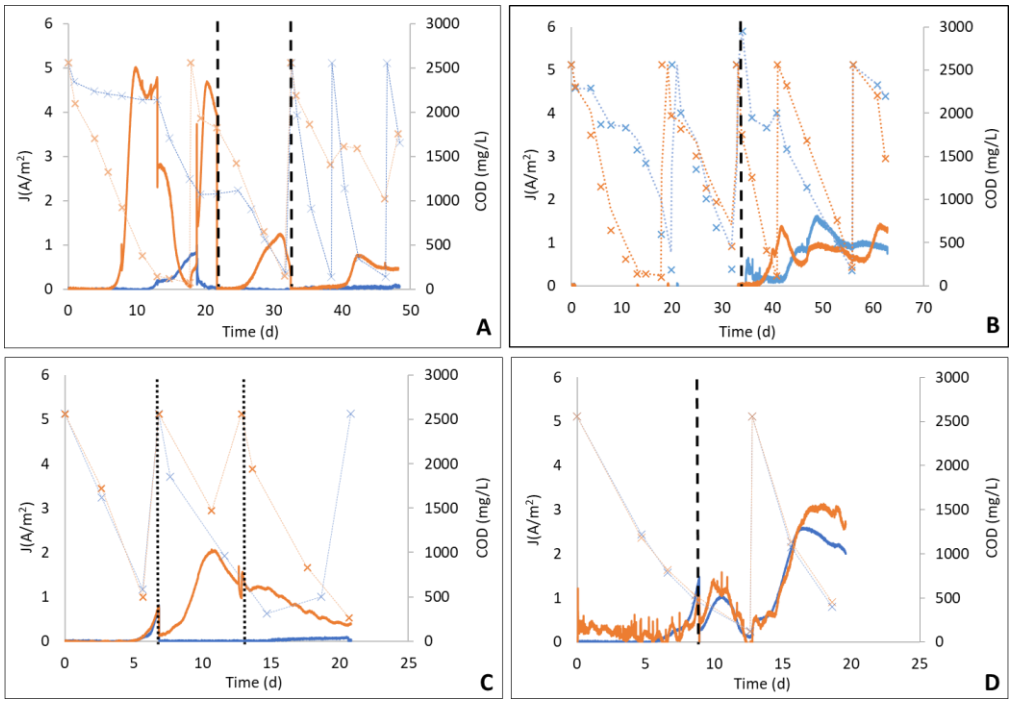

Figure V-15 : Evolution of current density versus time and COD consumption for salt marsh EABs cultured on SS microelectrodes. 'x' markers and dotted lines represent the COD concentration (right axis) while the solid line represents current density (left axis). Anodes polarized at 0.1 V/SCE (A) and open circuit potential (B) were replaced for new microelectrodes at the time indicated by the thick black dashed line. Similarly, fresh anolyte replaced the old one at the time points indicated by de black dotted line in (C). Microelectrodes from (D) were exposed to air for 1 minute to simulate the possible oxygen exposure during anolyte change in (C). All reactors were purged with nitrogen gas after having opened them for microelectrode replacement, anolyte change or microelectrode air exposure.

Figure V-15 shows the CA curves for salt marsh EABs polarized under a constant potential of 0.1 V/SCE and fed with 40 mM of acetate in pulses. For Figure V-15 (A), polarization with the microelectrodes inserted at time zero was performed up to day 22, where a new microelectrode was only replaced in the reactor corresponding to the orange curve. Polarization continued and at day 32, microelectrodes were replaced for new ones in both reactors until the end of the experiment. Current peak for the bioanode with the orange curve was 5.02 A/m^2 before the first microelectrode change. Later the peak decreased to 1.21 A/m^2 with the first new microelectrode, and to 0.75 A/m^2 with the second new one. No electroactivity was detected for the microelectrode replaced at day 32 corresponding to the blue curve. In Figure V-15 (B) microelectrodes were left at open circuit potential until day 32, where microelectrodes were replaced with new ones and polarization was launched for 30 more days. In this period with the new microelectrodes, maximum current of 1.53±0.13 A/m^2 was attained.

On one hand, what was described in Research Article 2, corresponding to the spatio-temporal evolution of the microbial population of the biofilm, may help to explain these results. As stated previously in the manuscript, the shift from *Marinobacterium* to *Desulfuromonas* in the EAB bacterial composition was probably due to a shift in the microbial composition of the planktonic bacteria suspended in the anolyte. As in the present experiment the medium was never replaced, for the first and second change of the microelectrode, the planktonic population in the medium had surely evolved. One hypothesis as to why

the new bioanodes did not have the same efficiency than the original one may have been because the consortium at day 22 and day 32 did not contain the same electroactive bacteria as in the start of the experiment. This can be corroborated by observing current production after day 32 for both pairs of reactors at closed and open circuit, where the order of current density was similar in both cases. In addition, as the microelectrode replacement was not performed in an anoxic atmosphere, it was also possible that during the brief time of the microelectrode change, the solubilization of oxygen in the media affected the electroactive anaerobic bacteria in planktonic state.

The following strategy was an essay to improve current production, yet at very early stages of anodic EAB formation, where the evolution of the microbial population was probably not as advanced. In Figure V-15 (C), medium was replaced in both reactors with no working electrode change. First, the medium was changed at the beginning of the exponential phase of current production at day 7, and later at day 13. After the first change, in one of the reactors current abruptly dropped to zero, whereas in the other, current recovered reaching a maximum of 2.07 A/m^2. After the second change of medium, the reactor that dropped to zero never recovered, yet in the other case, current production was not greatly affected as it was in the first media change. Current continued on decreasing from the final value it achieved before the second media change. It is very likely that the fast exposure to oxygen when changing the medium could have had affected the viability of the biofilm, with a higher impact when the bioanode was younger (thin biofilm). Probably oxygen diffusion was lower at an older and thicker biofilm and that might be the reason that after the second media change the current was not affected as in the first. This also could explain the results obtained in Research Article 2 when the anolyte was changed after ~ 30 days, where a thick biofilm was already developed. Another hypothesis could be due to a relatively premature change (6 to 7 days) of the anolyte, where certain nutrients, compounds and/or planktonic bacteria that would have evolved in the anolyte prior to its change and played a role in the augmentation of the EAB electroactivity, were eliminated.

To distinguish between the effect of the new batch of anolyte or of the exposure to oxygen in young biofilms, in Figure V-15 (D), microelectrodes were polarized, with the aim to reproduce the start of the exponential curve as seen in Figure V-15 (C). At the time of 9 days, microelectrodes were retrieved from the reactors, exposed to air for one minute and later reintroduced to the reactors. This time was selected, as this was approximately how long it takes in our experiment to change the total volume of 550 mL of anolyte. In both cases, current drastically dropped, then slightly recovered to a value of ~ 1 A/m^2 and dropped again reaching zero at day 12. Current later recovered to a final value of 2.33±0.47 A/m^2. It is clear that exposure to air affects the electroactivity of the EABs; however, in order to rule out the fact that air is the only factor affecting performance, the medium change operation should be repeated using a pumping system and in an anoxic atmosphere (i.e. in a glove box).

Lastly, the EPS components of the EABs were quantified together with the biofilm thickness and the correlation of each component with current production is shown in Table V-5. Theoretically, 13 bioanodes should have been analyzed:

- 5 from the reactors where microelectrodes were replaced (Figure V-15 (A)),
- 4 from the reactors where microelectrodes were initially at open circuit potential, then replaced and polarized at 0.1 V/SCE (Figure V-15 (B)),
- 2 from the reactors where the anolyte was changed (Figure V-15(C))
- And 2 from the reactors where the bioanodes were exposed to air (Figure V-15(D)).

However, biofilms exposed to air were not considered for the analysis, and the bioanode retrieved at day 22 from the reactor of Figure V-15 (A) corresponding to the CA orange curve was also not included.

Table V-5 : ANOVAs results from the effect of EPS components and biofilm thickness on current density at different reactor operational strategies. Ten samples were analyzed. PS: α-polysaccharides. Prot: Proteins. Ratio refers to the proportion of the EPS component on the biofilm matrix.

EPS component	p-value
Total cells (DNA) ratio	0.950
Lipids ratio	0.075
Proteins ratio	0.007
α-polysaccharides ratio	0.016
PS/(Prot+PS)	0.011
Biofilm thickness	0.018

As already seen in Test 5.4, here also the protein ratio was the most significant component impacting on current production, followed by the biofilm thickness and the α-polysaccharides ratio. The (PS/(Prot+PS)) also had a significant impact. The scattered plots of proteins ratio, α-polysaccharides ratio and biofilm thickness vs current production are shown in Figure V-16. Positive correlations of the protein ratio and the biofilm thickness were also obtained in this test, as well as the negative correlation with the α-polysaccharides ratio, supporting the theory and results obtained in Test 5.4.

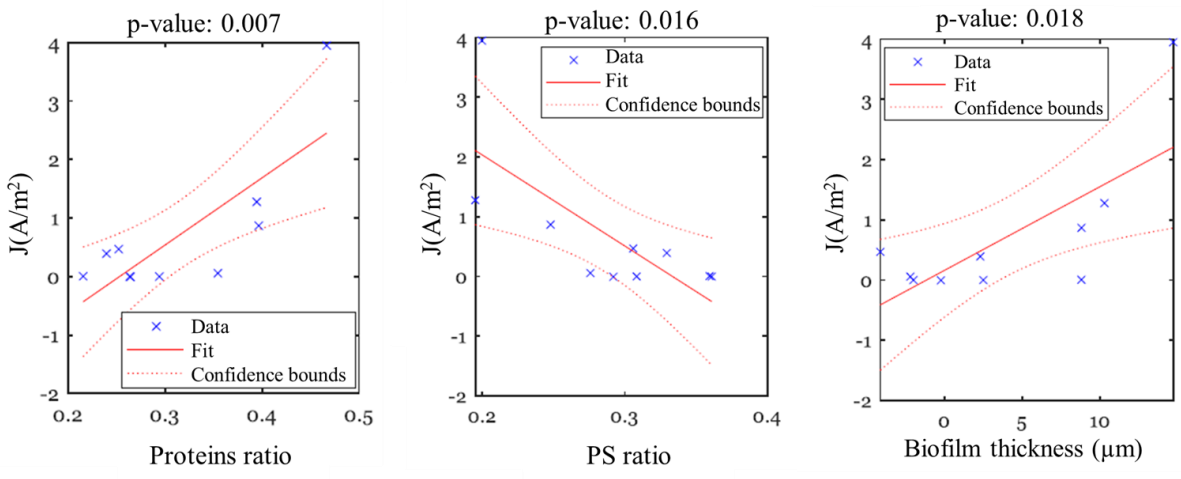

Figure V-16 : Scattered plots of proteins ratio, PS ratio and biofilm thickness vs. current production for different reactor operational strategies. PS: α-polysaccharides.

This meant that, regardless of the conditions under which the bioanodes were formed, when current was higher at the end of polarization, the amount of proteins was more elevated and the amount of polysaccharides was lower comparing with the bioanodes that yielded the lower current density. Moreover, the thicker biofilms were the ones that presented the highest electroactivity.

V.2.2.4. Test 5.6: Effect of the addition of quorum sensing (QS) molecules

In this last test, the addition of QS molecules to the reactors was tested. Three different types of molecules were selected, which were only added at the beginning of the experiment. N-(3-Oxododecanoyl)-L-homoserine lactone, N-Hexanoyl-L-homoserine lactone and N-Butyryl-DL-homoserine lactone were selected and they were referred as C12, C6 and C4 respectively due to the amount of carbon atoms in their structure. The interest in working with these molecules lay in investigating if the electroactivity of salt marsh EABs was improved when adding them into the reactors. As in some publications using the same QS molecules, concentration ranged between 0.1 µM to 10 µM (Monzon et al., 2016; Liu et al., 2021), an initial concentration of 5 µM was tested to start. Subsequently, another batch of reactors was launched with a concentration of 10 µM.

Figure V-17 shows current production for salt marsh EABs cultured in the presence of QS molecules. Firstly, for reactors where concentration of C12 was 5 µM, current density curves were quite similar in the course of the polarization with a maximum current value of 3.28±0.21 A/m^2. It is clear that current dropped due to acetate depletion; however, the trend in the CAs was different from that normally observed. Current peaks appeared to last longer between the additions of acetate, where current was sustained and did not fall abruptly. This effect was also observed for one duplicate in the case of C4 at 5 µM, where maximum current reached 3.26 A/m^2, yet current remained between 1.5 to 2 A/m^2 in the rest of the experiment. This was the reason those reactors were left running for a longer time, up to 55 days.

The other duplicate of C4 showed a completely different behavior that was more likely to bioanodes formed without the addition of QS molecules. The maximum current density reached in this case was of 6.88 A/m^2. Biofilm growth adding 5 μM of C6 led to completely different results, where no electroactivity was observed for one duplicate and a maximum of 4.64 A/m^2 was reached for the other. In these cases, polarization was stopped after 20 days.

As current density values were lower than usually obtained, it was decided to repeat the batch of experiments yet increasing the QS molecules concentration to 10 μM. Only C4 and C12 molecules were tested this time. As this second set of experiments was performed in July, few days before the summer closure of the laboratory, reactors only operated for 17 days. For C12, current trends were similar at the start of the polarization yet until at day 12, where there was a marked increase in the electroactivity in one of the duplicates up to 6.34 A/m^2 after the second addition of acetate. The other duplicate reached a maximum value of 2.76 A/m^2 by the end of polarization that would have probably dropped after acetate depletion. In the case of C4 at 10 μM, again, duplicates were despair as in the case of 5 μM, yet the polarization was too brief to have the possibility to observe the if current was sustained in time and did not fall abruptly, as seen in the reactors that run up to 55 days.

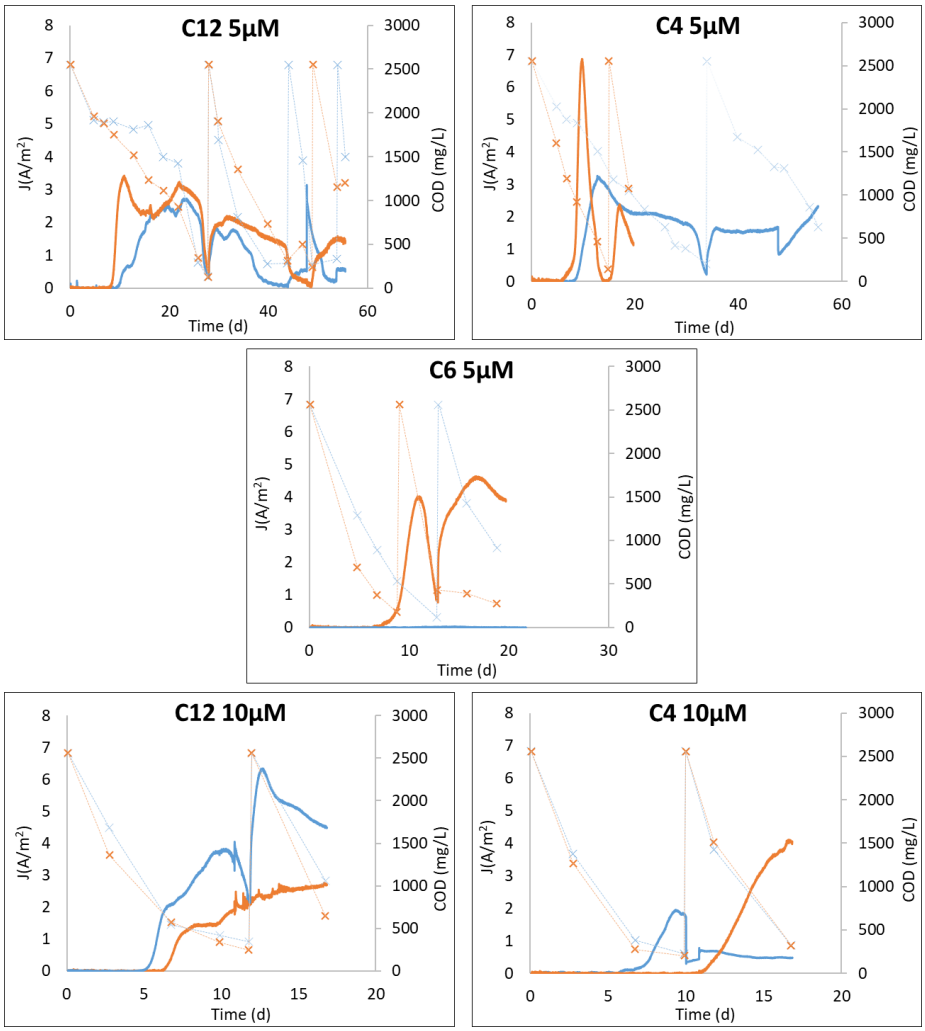

Figure V-17: Evolution of current density versus time and COD consumption for salt marsh EABs formed in the presence QS molecules (C4, C6 and C12) at 5 or 10 mM. 'x' markers and dotted lines represent the COD concentration (right axis) while the solid line represents current density (left axis).

EPS components and biofilm thickness were quantified at the end of microelectrode polarization as seen in Table V-6. Biofilms formed with C6 were not included in the analysis since the CLSM image quality was not proper for treatment. In this case, neither EPS components nor biofilm thickness showed a significant correlation with current density, as all p-values were found to be above 0.05.

Table V-6 : ANOVAs results from the effect of EPS components and biofilm thickness on current density for biofilms formed in the presence of QS molecules. Eight samples were analyzed. PS: α-polysaccharides. Prot: Proteins. Ratio refers to the proportion of the EPS component on the biofilm matrix.

EPS component	p-value
Total cells (DNA) ratio	0.739
Lipids ratio	0.223
Proteins ratio	0.670
α-polysaccharides ratio	0.942
PS/(Prot+PS)	0.942
Biofilm thickness	0.437

Figure V-18 shows the scattered plots for proteins ratio, α-polysaccharides ratio and biofilm thickness. The considerable dispersion between samples (blue crosses) explained the high p-values. One reason for this high dispersion may be that three of the four biofilms cultured at low concentrations of QS molecules were polarized to a final time of 55 days, whether for the EAB grown at C4 at 5 µM (orange CA curve) and for EABs grown at high concentrations, the polarization time was between 17 to 20 days.

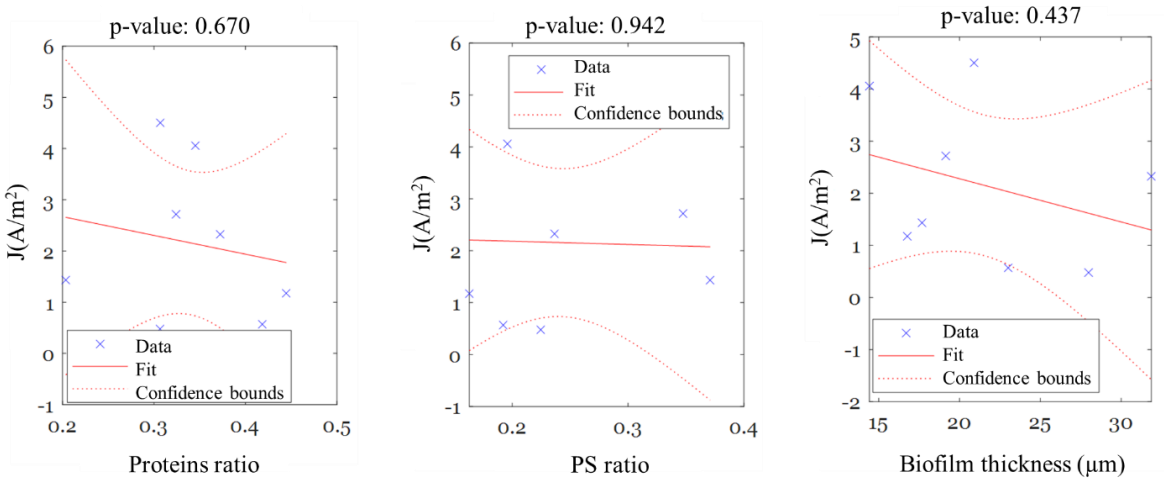

Figure V-18 : Scattered plots of proteins ratio, PS ratio and biofilm thickness vs. current production for biofilms formed in the presence of QS molecules. PS: α-polysaccharides.

Although in some studies from the literature, the addition of commercial QS molecules in a concentration range of 0.1 µM to 10 µM has improved the EABs electroactivity, such as PQS (Pseudomonas aeruginosa QS signal) and quinolones for *Halanaerobium* spp., (Monzon et al., 2016) or the same AHL molecules in activated sludge (Chen et al., 2017); here the electroactivity of the salt marsh EABs was no better than if no QS molecules had been used. Unfortunately, due to time constraints the same AHL molecules with higher concentrations or other type of QS signal molecules could not be tested.

To make it positive, it was interesting to note the effect seen in some cases where current was stable for long periods; nevertheless, more tests would be needed to confirm this behavior of bioanodes formed under the effect of QS mechanisms. It is unknown how the cell-to-cell communication is affected in order to have an impact in the biofilm electroactivity.

V.2.2.5. Combined EPS component analysis of Tests 5.3, 5.4, 5.5 and 5.6

EPS components, biofilm thickness and current production for the bioanodes analyzed by the ANOVA methodology in tests 5.3, 5.4, 5.5 and 5.6 were grouped here for a single ANOVA analysis. Correlation coefficients are shown in Table V-7. Even if the p-values in Test 5.4 were not significant, in this case correlation coefficients between proteins, polysaccharides, and biofilm thickness to current production showed a significance indeed. This could be explained by the size of the sample for Test 5.4, where from eight EABs three of them were approximately three times older than the remaining five, which

could have created a high dispersion in results. Nevertheless, when taking a larger number of samples, the variance seemed to decrease and more data felt into the confidence intervals, as seen in Figure V-19.

Table V-7 : ANOVAs results from the effect of EPS components and biofilm thickness on current density including all experimental tests (5.3, 5.4, 5.5, 5.6). Thirty-one samples were analyzed. PS: α-polysaccharides. Prot: Proteins. Ratio refers to the proportion of the EPS component on the biofilm matrix.

EPS component	p-value
Total cells (DNA) ratio	0.053
Lipids ratio	0.959
Proteins ratio	0.003
α-polysaccharides ratio	0.033
PS/(Prot+PS)	0.008
Biofilm thickness	0.001

As the biofilm thickness was the p-value closest to zero (p=0.001), it was the most significant parameter on current production. This linear correlation is valid in these four tests because all grown bioanodes achieved thickness values of maximum 30 µm. In general, reactors were stopped at or after the second maximum peak, and it could also happen that the addition of acetate in the form of pulses resulted in thinner biofilms than when adding acetate regularly, a phenomenon already seen in the works of Li et al. (2020) when acetate was added in lower concentrations.

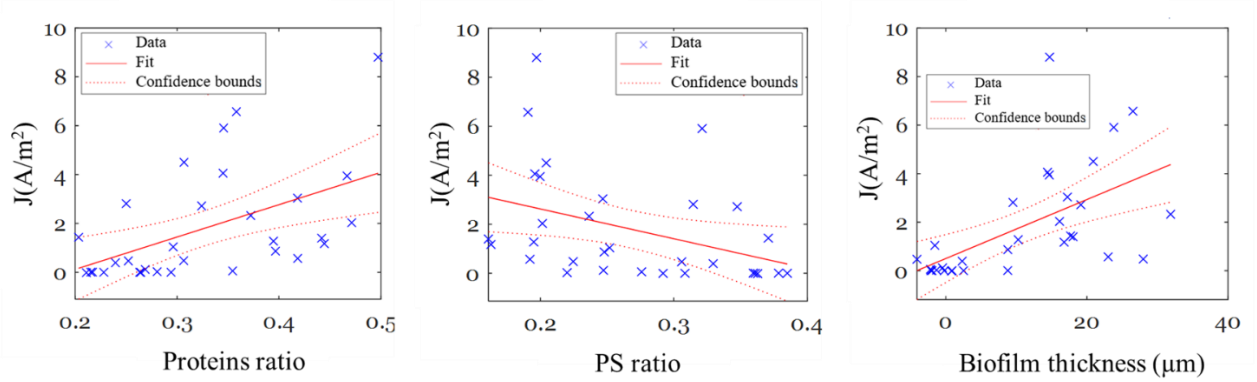

Figure V-19 : Scattered plots of significant EPS components on current density for tests 5.3, 5.4, 5.5 and 5.6. PS: α-polysaccharides.

From Tests 5.3, 5.4, 5.5 and 5.6, in general the protein and polysaccharide content correlation with current production was independent of the external factors like acetate concentration, substrate, anolyte age, since the same correlation was found in the combined EPS component analysis as well. Probably for the case of Test 5.3, the correlation with polysaccharides was not significant since the change of strategy at the end of the experiment, where acetate was added regularly for reactors fed at 10 mM and 20 mM, might have altered the polysaccharides content of the biofilm compared to reactors where acetate continued to be added in pulses.

In the experiments of this section, contrary to those presented in section V.2.1. of this chapter, the (PS/(Prot+PS)) was not considered for the scattered plots. By processing the images with MATLAB and then applying the ANOVA method, the advantage that this brought was to consider the weight of polysaccharides and proteins separately. In the cases where the (PS/(Prot+PS)) was not significant ($p>0.05$), it was either because one of the components was not significant, as in the case of Test 5.3 for α-polysaccharides, or both components were not significant, as in Test 5.6 for α-polysaccharides and proteins. This allows for a deeper insight than would be possible if only the relationship between both components were analyzed.

V.3. Conclusions of Chapter V

The tests carried out in this chapter allowed to study the influence of the following parameters on the salt marsh EABs electroactivity: anode potential, acetate addition mode and concentration, aging of the anolyte, substrate nature and the formation of EABs under the presence of QS molecules. In addition, the choice of the SS microelectrode potential at 100 mV/SCE and the regular addition of 40 mM of acetate into the reactors was reaffirmed. Furthermore, the impact of the described parameters was focused on the electroactivity of the biofilm, as well as on the production and composition of EPS, due to the development of image treatment protocols and the integration of statistical analysis methods.

At the beginning of the chapter, it was determined that the anode potential influenced the electroactivity as well as the microbial population of the biofilm. When acetate was added regularly on a daily basis, maintaining a constant concentration, microelectrodes polarized at 0 and 400 mV/SCE yielded the highest current density values, with a predominance of *Marinobacterium spp.* and *Halomonas spp.* on the EABs. When acetate was added in pulses, results were more despair in relation to the electroactivity and the diversity of microbial population. Therefore, a potential of 100 mV/SCE to form salt marsh EABs continued to be the most suitable option.

Concerning the choice of substrate to form salt marsh EABs on SS microelectrodes, acetate at a concentration of 40 mM lead to the biofilms that expressed the highest electroactivity. An increase in *Desulfuromonas* genera was observed with elevated acetate concentrations. Regular addition resulted in higher density current values yielded by the bioanode, yet by adding in pulses, the maximum peak was obtained earlier. Butyrate could be also used as substrate, despite bioanodes current production was lower than for acetate. Glucose and formate were discarded as possible substrates for this type of inoculum.

Furthermore, it was clear that the aging of the anolyte, probably related to a shift in the planktonic microbial population, played an essential role in the salt marsh EABs formation. The attempt to form bioanodes with an anolyte of 22 and 32 days-old, failed to reproduce the electroactivity of EABs such as those that can be observed when the anolyte is close to fresh. Various causes such as if electroactive bacteria are a minority at those times in the anolyte, or the presence of an already formed biofilm in the

microelectrode was necessary, or even if the chemical composition of the anolyte had already evolved and some key substances were depleted could be possible reasons to explain the phenomenon observed. At shorter times, when the anolyte was replaced at days 7 and 13, the exposure to air in thinner biofilms did not help to confirm that effectively the aging of the anolyte was the main reason why the expected performance of bioanodes could not be attained when culturing them in anolyte older than 22 days. Complementary experiments would be necessary to reach consistent conclusions, where it would be necessary to evaluate the microbial population of the suspended planktonic bacteria, as well as that of the biofilm, and the fact of being able to work in suitable anoxic conditions.

The use of AHL molecules, already identified for QS, did not improve the bioanode performances in terms of current density values, yet in some cases, the drop in current of more than 50% that is generally registered in bioanodes after reaching the peak was not observed here. It would have been interesting to continue with this line of research in order to see if it was possible to obtain more reproducible results by using QS molecules, and to understand better the mechanisms in the biofilm under the influence of these molecules.

Upgrading the protocol for EPS confocal microscope image post-processing with a MATLAB algorithm, together with the application of the ANOVA method, enabled a deeper understanding of the role of the EPS components in relation to the bioanode electroactivity. As proteins were the EPS component in salt marsh EABs that had the strongest effect in current production with a positive significance, followed by α-polysaccharides with a negative one, this supported the hypothesis of the involvement of these two components on the formation of an electron transfer network within the biofilm. In this conductive matrix, EPS proteins facilitate electron transfer between the biofilm and the anode, whether the polysaccharides seem to attenuate the electron path. More complex experiments could correlate the EPS components to their redox activity using UV/vis spectroscopy (Guo et al., 2021); however, for this type of analysis the extraction of the exopolymeric substances from the biofilm would be needed, somewhat laborious with such a small volume of biofilm formed over the microelectrode.

Chapter VI : In-situ real-time investigation of salt marsh EABs dynamics in MicroBES

VI.1. Introduction

This chapter is fully dedicated to the development of transparent microBES and their use to increase the knowledge of cell dynamics and EAB dynamics at the very close interface between the working microelectrode and the anolyte. The design of the transparent microBES is firstly based on the information capitalized in Chapter III. As a reminder, the use of Ag microelectrodes was discarded as a pseudo-electrode reference and the idea of working in a two electrode system in the microBES was raised. The experimental conditions that were defined at the end of Chapter III, such as SS microelectrode as the working electrode, polarization potential at 0.1 V/SCE, the composition of the anolyte of SMS, Starkey medium and 40 mM of acetate have been selected for the experiments in the microBES.

This chapter is then organized in two separate parts that address the two objectives:

- To obtain a transparent microBES that can be positioned under the objective of an optical microscope, where the electrochemical techniques can be applied simultaneously. The step-by-step methodology for achieving a properly functioning microBES prototype is developed in Part A: Development of a MicroBES.
- To form salt marsh EABs on the SS microelectrode in the microBES in a reproducible form and that their electroactivity is also reproducible to that usually observed in macroBES. In real time, the steps in the formation of EABs on the surface of the microelectrodes are studied in situ and correlated with the electroactivity of the EAB. In particular, the displacement of planktonic bacterial cells in the region of the SS microelectrode surface is monitored and quantified. These experiments are developed in Part B: Experiments in MicroBES.

VI.2. Part A: Development of a MicroBES

This first section of this chapter is devoted to the methodology developed, step by step, to obtain a microBES. This device must be suitable for fluidic and electrochemical operation, adaptable to work in simultaneous under the microscope while connected to a potentiostat. Figure VI-1 resumes the steps performed in a chronological order, which are described in full detail in this first part.

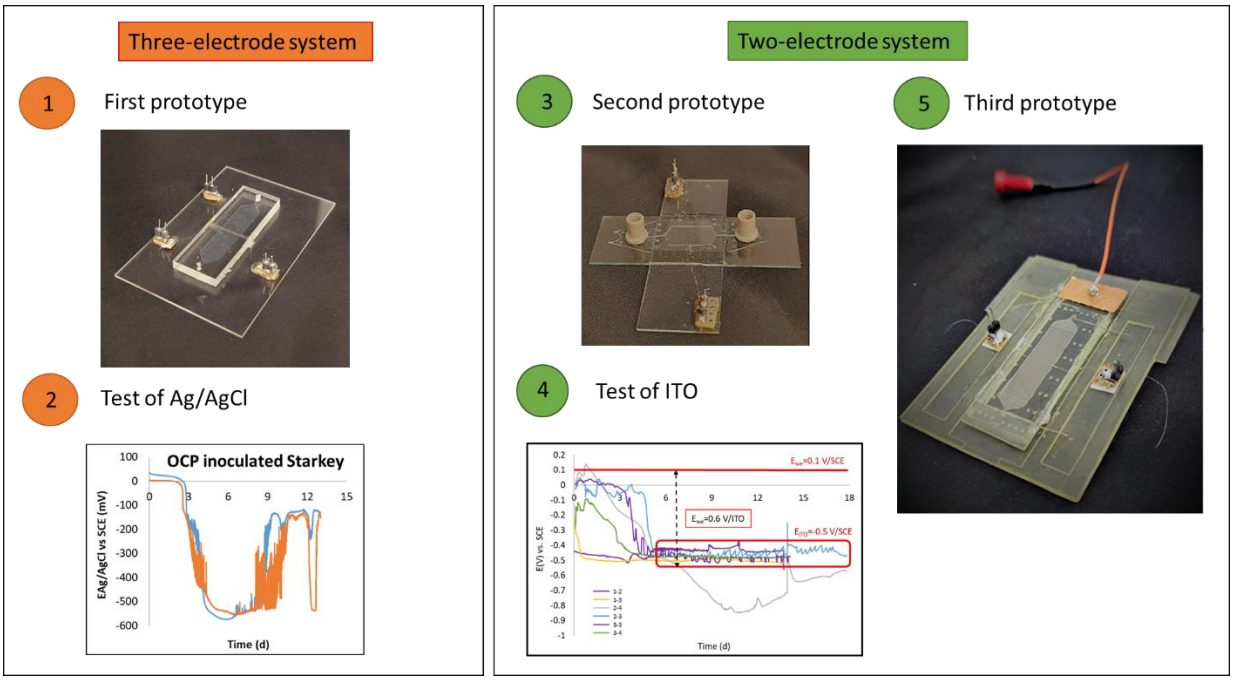

Figure VI-1: Description of the five main steps to obtain a microBES. The numbers correspond to the chronological order in which the steps were executed.

First, a three-electrode microfluidic cell (or three-electrode microBES) was developed using PDMS as the building material for the cell. The main bottleneck with this prototype resided in the difficulty of obtaining a stable reference electrode for a three-electrode electrochemical operation. It was already described in Chapter III that the potential of Ag microelectrodes was not stable for their use as pseudo-references; therefore, in this chapter it was decided to develop Ag/AgCl microelectrodes as an alternative option (Zhou et al., 2010). Ag/AgCl microelectrodes were successfully obtained, however their stability as reference electrodes when working with Starkey medium inoculated with salt marsh and acetate as substrate, deteriorated after three days of operation.

This led to adapt the microBES design from a three-electrode system to a two-electrode one. For this purpose, a transparent indium tin oxide (ITO) electrode was implemented as the reference and counter electrode, while the SS microelectrode remained as the working electrode. PDMS was discarded as the building material for the construction of the cell because we have found that it is not completely airtight. A more suitable polymer, OSTEMER, was used instead (Martin et al., 2016). The electrochemical performance of the second prototype of the micro-BES was verified, however, working with a two-electrode system required prior validation of the potential stability of the ITO electrode in order to use it as a pseudo-reference.

A serie of experiments using standard 550 mL MacroBES containing Starkey medium inoculated with SMS and fed with 40 mM acetate were launched. In these reactors, the evolution of the ITO potential in time was recorded versus a SCE reference electrode while the SS microelectrode was polarized at 0.1 V/SCE. The potential of the ITO electrode became very stable after six days of polarisation. Its potential

was fixed at -0.5 V/SCE, keeping this potential constant during 18 days of experiment (voluntary stop). Therefore, it was determined that the ITO electrode could be used as a pseudo-reference from day 6 of exposure in Starkey medium inoculated with SMS.

A first test aimed at forming a salt marsh EAB in the second prototype showed that there were deficiencies in the fluidic design of the reactor. This led to the third and final microBES prototype, in OSTEMER, which retained the two-electrode system while eliminating a typical microfluidic problem, namely the inclusion of air bubbles when filling the microvolume. The design of a cell holder was also included for the cell to be easily adapted to the microscope.

For a more detailed understanding of the approach just summarized, the microfluidic protocols and techniques for preparing and obtaining the different microBES are described in the Annexes. The step-by-step process of arriving at the final microBES prototype and its operational conditions in terms of stable reference electrode and microchannel design optimization are described here.

VI.2.1. Preliminary results for the microBES

VI.2.1.1. Micro-BES - First prototype: The three-electrode PDMS microfluidic cell

Cells of two different height were developed (50 and 100 µm), where a three-electrode system was implemented. Two Pt microelectrodes of 50 µm were used as working and counter electrode and an Ag microelectrode (50 µm) as the pseudo-reference electrode.

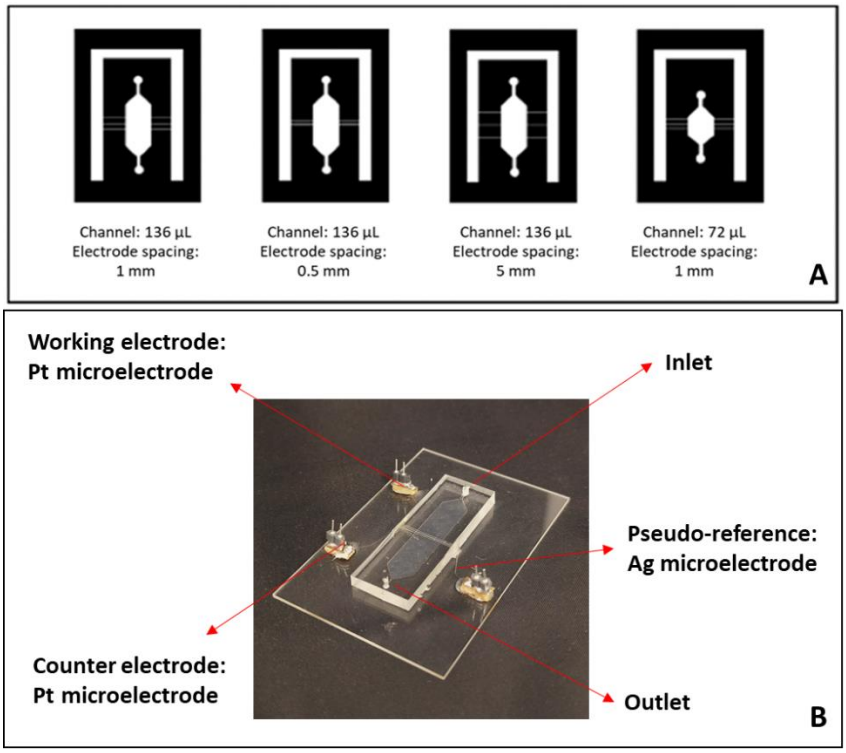

Figure VI-2: (A) Series of designed masks for the first prototype. (B) Finished three-electrode microBES of 100-µm height, 0.5 mm microelectrode spacing and 272 µL of volume with the electrical connections.

When the height of the channel was 50µm, the 50-µm diameter of the microelectrodes was not adequate for a cell of the same height. This deformed the PDMS walls to allow liquid flow, quite often causing leakage problems at the inlets and outlets of the system. In order to solve this problem, it was decided to double the height of the microBES to 100 µm, leading to more voluminous reactors of 144 and 272 µL. To keep the same reactor designs, an extra PDMS layer was created by the same protocol described in Annex Figure 1 yet using an extra mask without the microelectrode grooves. Once obtained, it was treated with plasma and glued to the main one containing the microelectrodes, thus forming the microchannel between the middle of the two PDMS layer. To finish, electric microconnectors were then glued to the glass support.

The main issue with this three-electrode microfluidic cell was the non-stability of the Ag pseudo-reference, as seen in III.2.1.1. As it was possible to electrochemically treat the Ag microelectrode inside the microBES to form an AgCl layer, it was decided to test the stability of Ag/AgCl microelectrodes in a larger reactor where their potential could be tracked against a SCE reference.

VI.2.1.1.1. Test of Ag/AgCl microelectrodes as pseudo-references

The aim of this study was to develop a homemade reference electrode with the following specifications already mentioned in Chapter III. The reference electrode must fit in the volume of the microBES, it must be able to measure without error the potential of the working electrode, and its potential must be stable (at least during two weeks) over time when in contact with the anolyte of study (Starkey medium + SMS + acetate).

Ag/AgCl electrodes are commercially available references electrodes, but several papers report that they can be made or designed in-lab (Polk et al., 2006; Zhou et al., 2010). As already seen in Chapter III, Ag exists in the form of microwire with the same design and diameter than Pt and SS microelectrodes. This opens up the possibility of manufacturing our own micro Ag/AgCl reference electrode starting from an Ag microwire insertable into a microBES.

Ag/AgCl microelectrodes were obtained by the application of the protocol described at the II.3.1.4. section. The thickness of the Ag/AgCl microelectrodes was measured by microscopic observation. In this experiment, 14 microelectrodes were developed where the average thickness was of 63.9±3.7 µm. The aim was not to exceed a thickness of 100 µm in order to further adapt the same protocol to form Ag/AgCl microelectrodes directly in the three-electrode PDMS microfluidic reactor.

The idea of this experiment was to measure the deviations in the potential of the Ag/AgCl microelectrodes in three different liquid media: KCl 1M, Starkey medium and inoculated Starkey medium (SMS 5%) with 40 mM of acetate. The potential of Ag/Ag microelectrodes was tested in four consecutive batches. In the three first batches, the potential of the Ag/AgCl microelectrode (four replicates in each batch) was tracked against a SCE by measuring the difference of potential with a

multimeter two times a day. A reactor of 150 mL was used to contain both electrodes. Temperature was kept constant at 30 °C with the exception of the first batch. The SCE was always the same in the three batches to ensure more accuracy in results:

- In the first batch, the potential of Ag/AgCl microelectrodes was tracked while both electrodes were submerged in a storage solution of KCl 1M for a period of 11 days. This experience was carried out at room temperature.
- In the second batch, the procedure was repeated with new Ag/AgCl microelectrodes, yet in this case, the Starkey medium was the anolyte. Measurements were taken in a period of 15 days.
- In the third batch, in order to mimic the real conditions of the anolyte, inoculated Starkey medium with SMS at 5% and 40 mM of acetate served as the anolyte where the electrodes were placed. Ag/AgCl microelectrode potential measurements were recorded over a period of 13 days.

A fourth batch was carried out in the same conditions of the third; yet, in this case, the evolution of the Ag/AgCl potential was followed by an open circuit potential (OCP) technique by means of the potentiostat.

A criterion was taken to determine how acceptable the Ag/AgCl microelectrode was as a pseudo-reference. When working with SCE in a three-electrode system, before launching an experiment, the potential of the SCE was always measured against a well-calibrated reference. The ideal value would be to obtain a delta of 0 mV between the two electrodes, yet the maximum deviation accepted was generally 50 mV in absolute value. This was justified as EAB can be formed in the range of -600 mV/SCE to 400 mV/SCE (Rimboud et al., 2014), therefore a shift of 50 mV in the working electrode should not prevent the formation of a EAB.

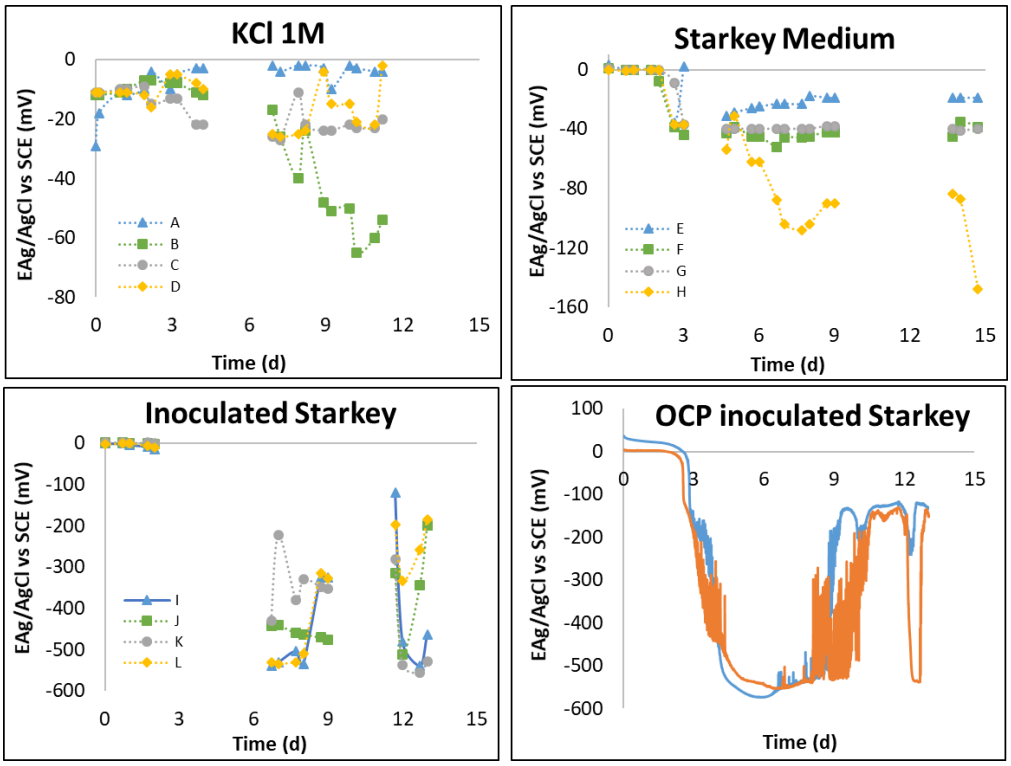

Figure VI-3 : Evolution of the Ag/AgCl microelectrodes in KCl, Starkey medium and inoculated Starkey medium. For inoculated Starkey medium, data was recovered with a multimeter (loose points) and with the potentiostat by launching an OCP technique.

The tracking of the Ag/AgCl microelectrodes potential is shown in Figure VI-3. For KCl 1M, microelectrodes A, C and D were in the defined range of 50 mV in the course of the experiment. However, for sample B, the potential of the Ag/AgCl microelectrode deviated after day 9 to a maximum delta of 65 mV. Subsequently, when using Starkey medium without inoculum, the temperature was maintained to 30°C in order to discard the influence of temperature with ion solubility and further changes in the potential. Microelectrodes E, F, G had a similar behavior where the potential remained under the 50 mV limit, yet sample H, presented a strong deviation towards the end of the experience to potentials lower than -160 mV/SCE.

When Starkey was inoculated with SMS, at the beginning of the experiment, potential values for all samples were similar and in the range of 0 to -20 mV/SCE, yet later, values oscillated between -120 mV/SCE to -560 mV/SCE. The experiment was repeated with two new Ag/AgCl microelectrodes, yet connected to the potentiostat as to corroborate the tendency already observed. It is clear that with the OCP technique, values remained in a range of a delta of 50 mV before the first two days of experience. Later, potential dropped to around -550 mV at day 5, and increased to around -150 mV at day 9.

For KCl and Starkey without inoculum, the shift in the potential after the first 3 days could have been due to the dissolution of the thin layer of AgCl formed over the silver microelectrode in a liquid volume of 150 ml. Clearly, in this type of pseudo-references, the reference electrode cannot be in equilibrium with a saturated KCl solution as would be the case in an Ag/AgCl commercial reference electrode for

large-scale reactors. The same phenomenon could have happened for the microelectrodes submerged in inoculated Starkey; however, the presence of bacteria seemed to have a significant impact in the potential. The drop to values around -550 mV could have been related to acetate oxidation, where the redox potential of the acetate/CO_2 couple occurs at -540 mV/SCE (Drake, 2006). Later, once acetate was consumed, the increase in potential to values around -150 mV could have been influenced due to bacterial activity over the microelectrodes, as seen after observing samples in inoculated Starkey medium under the epifluorescence microscope.

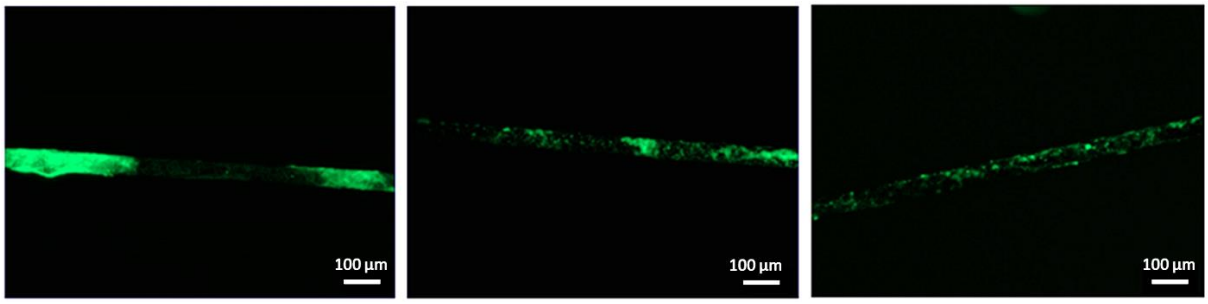

Figure VI-4 : Epifluorescence microscopic images of Ag/AgCl microelectrodes after 13 days of being exposed to Starkey medium inoculated with SMS.

After these consecutive tests, it was determined that the stability of Ag/AgCl microelectrodes as pseudo-references was deteriorated after two or three days of use. It is clear that the stability of the AgCl layer could have been ameliorated by increasing the time of electrodeposition, yet the thickness would have increased consequently. In addition, the volume of the reactor used here (150 ml) exceeded the volume the microBES, where surely in a smaller volume, the dissolution time of the AgCl layer would have been larger. However, it is not possible to measure the evolution of the potential of the AgCl microelectrode in the microBES.

On the other hand, the treatment for the Ag microelectrodes as to deposit Ag/AgCl was successful, and can be implemented directly in the microfluidic cell. Nevertheless, as it was proved, bacterial activity was the responsible for the significant changes in the microelectrode potential; the idea of working in a three-electrode system in the microfluidic reactor was now completely discarded. This was also supported by the results observed for Ag microelectrodes in Chapter III, which were not favorable for using Ag as a pseudo-reference.

VI.2.1.2. Micro-BES - Second prototype: The two-electrode OSTEMER + glass slide microfluidic cell

A typical microBES made of OSTEMER is presented in Figure VI-5 (B) by applying the fabrication protocol in Annex Figure 2. Nanoports were glued at the inlet and outlet of the microchannel with an epoxy adhesive. Once the adhesive was dry, a flow test was made by filling the microchannel with distilled water and observing if there was any leak in the system. Electrical microconnectors were glued

to the upper glass, and the microelectrode was welded at both sides of the cell. Electrical conductivity was checked with a multimeter in order to ensure that the connections were proper.

To first electrochemically test these chips, they were first filled with KCl 0.1 M and a CV technique was launched at a speed of 10 mV/s in a range of -1V/ITO to 1V/ITO. This was done simultaneously for four cells as seen in Figure VI-5 (C). The shapes showed the typical sigmoidal curve resulting from the electro reduction and electro oxidation of water, where no connection issues, such as a possible short-circuit between the microelectrode and the ITO glass or welding defects, were observed.

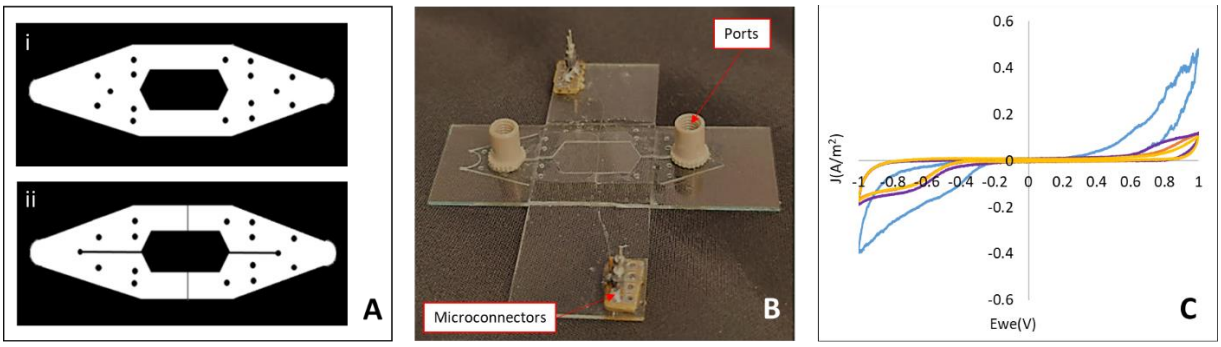

Figure VI-5 : (A) First (i) and second (ii) masks. The dots inside the white structure represent pillars for a better peel-off at the end of step three. The hexagonal shape of the microchannel was kept from the previous cell design. (B) Finished two-electrode microfluidic cell with ports and electric connections. (C) CVs performed with KCl 0.1 M at 10 mV/s for four different microBES.

VI.2.1.2.1. Test of ITO glass as a pseudo-reference electrode

As in the previous section, Ag/AgCl microelectrodes were discarded as pseudo-references for a three-electrode microBES, the idea of working with two electrodes at the microscale arose. In section III.2.4. the potential of the Pt grid as the counter electrode was tracked in time when functioning in a three-electrode 550 mL standard reactor. It was observed that starting from day 8, the potential of the Pt grid stabilized at a constant value of -0.8 V/SCE thus maintaining this value during the course of the experiment.

The aim of the following experiments was to still work in the standard 550 mL reactor yet using an ITO conductive transparent glass as the counter electrode. This allowed following the evolution of the ITO electrode versus a SCE when the working electrode (SS microelectrode) was polarized at a constant value of 0.1 V/SCE. This helped to determine if the ITO reached a fixed potential, as in the case of the Pt grid, which later could be correlated as a pseudo-reference electrode to normalize potential measurements in the SS microelectrode.

Three consecutive tests were launched, where main conditions are resumed in Table VI-1. All reactors were maintained at a temperature of 30 °C and bubbled with nitrogen for 20 minutes before the start of the polarization. 40 mM of acetate was added regularly into the reactors.

Table VI-1 : Summary of experimental conditions for testing ITO as a pseudo-reference.

Shared parameters			
Inoculum	SMS		
Temperature	30 °C		
Culture medium	Starkey medium (45 g/L of NaCl)		
Inoculation size % V/V	5		
Operation mode	Batch		
WE material	SS		
Reactor type	Standard		
E_{we} (V) vs. SCE	0.1		
Substrate	Sodium acetate 40 mM		
Material of CE	Pt grids, ITO		
Individual parameters			
Tests	Test 1	Test 2	Test 3
Date of inoculum sampling	October 2020	October 2020	January 2021
N° of reactors	3	3	4
Polarization time (d)	13	18	14

- Test 1:

In this first test, three identical reactors were launched, being the only difference the counter electrode. Reactor 1-1 used a Pt grid as a counter electrode, whether reactors 1-2 and 1-3 contained ITO glass electrode instead. The working electrode was left at OCP until the potential of the working and counter electrodes stabilized, meaning that no current was applied to the system, as seen in Figure VI-6 (A) and (B). After four days of OCP, a chronoamperometry (CA) was launched in the working electrode (Figure VI-6 (C)) while the potential of the counter electrode was continued to be tracked (Figure VI-6 (E)).

Since current density values were considerably lower to those expected, it was decided to switch from the CA to a CP technique. After 13 days of polarization (17 days of complete experiment), the applied potential to the working electrode was stopped, and a current of 0.03 mA was imposed to the SS microelectrode. The current value corresponded to a desired current anodic density of 10 A/m^2. Therefore, the potential of the SS microelectrode was not fixed from day 13 (Figure VI-6 (C)). In some cases, CP could work as an alternative strategy to form EABs besides CA technique.

Therefore, in order for the system to be able to produce the desired current of 10 A/m^2, the potentiostat raised the potential of the working electrode. In each SS microelectrode, the limit of potential of 10 V defined by the Ec-Lab software was quickly reached. Consequently, the SS microelectrodes were found to be broken. This probably occurred due to change in the reaction at the anodic surface, from acetate to water oxidation at high potentials. Because of the small microelectrode size, the presence of bubbles could have detached the microwire from the whole microelectrode structure.

Considering the stability of ITO potential as the counter electrode, after four days of OCP and the first two days of CA, where the potential was still dropping, an average potential value was calculated from day 6 to day 13. For reactor 1-2, the potential remained in an average value of -0.45±0.03 V/SCE,

whether for reactor 1-3, at a value of -0.50±0.01 V/SCE. However, as seen in the CAs, the current density values attained by the bioanodes were not high as expected. Therefore, the experiment was repeated in Test 2, where in this case, the OCP was skipped and SS microelectrodes were directly polarized at 0.1 V/SCE.

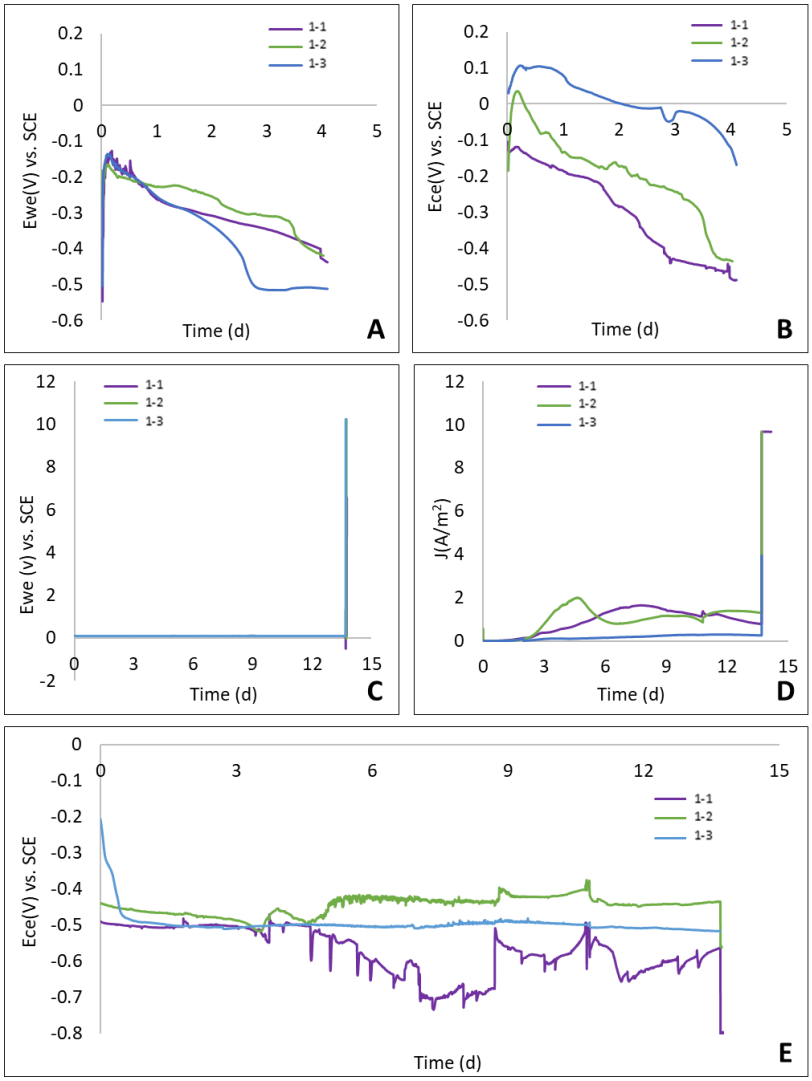

Figure VI-6 : OCP for SS microelectrodes (A) and counter electrodes (B) in the lapse of four days. (C) Tracking of the potential of SS microelectrodes after the first four days in OCP (while in CA and later CP). (D) Evolution of current density in time for salt marsh EABs in triplicates: in CA and subsequent CP at day 13. (E) Evolution of the potential of the counter electrode while in CA and later CP.

- Test 2:

Reactors 2-1 and 2-2 used a Pt grid as a counter electrode, while 2-3 and 2-4 contained an ITO glass electrode.

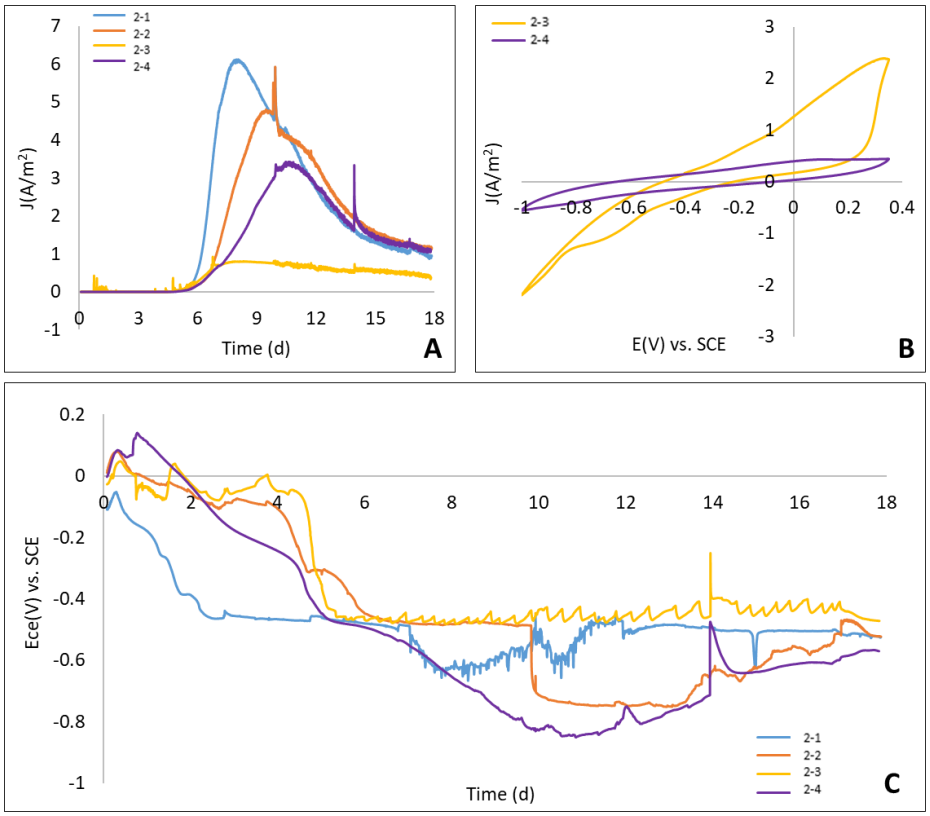

Figure VI-7 : (A) Evolution of current density in time for salt marsh EABs over SS microelectrodes polarized at 0.1 V/SCE for Test 2. (B) CVs for ITO electrodes at 10 mV/s. (C) Evolution of the potential of the counter electrode while in CA technique for Test 2.

Figure VI-7 (A) shows the current density produced by the SS microelectrodes. This same graph is found in Figure IV-2 (A), since after the CA, the samples were retrieved for microbial population analysis. The bioanodes performances were again not as high as expected, mainly in reactors 2-3 and 2-4, where the ITO worked as the CE.

At day 13, the polarization was temporarily stopped in reactors containing ITO as CE and a Pt grid was added in the fourth orifice of the reactors. With an auxiliary channel, the ITO was connected as the working electrode, the Pt grid as the counter electrode and the SCE already inside the reactor, as the reference. A CV was launched, Figure VI-7 (B), in order to detect any possible limitation from the ITO electrode that may have prevented the current production in the anode. The selected scanning rate ranged from -1 V to 0.35 V and the speed rate was of 10 mV/s. CV shapes did not suggest that the ITO electrode might have impeded current flow between it and the SS microelectrode. The CA was resumed after the ITO CVs until the end of the experiment.

For the tracking of the counter electrode potential, during the first days, the trend in the potential was similar to what was observed in Test 1, as seen in Figure VI-7 (C). This meant that the progression of the potential was the same whether the working electrode was polarized or not. Probably, the medium evolution at early times involved the reduction of oxygen traces, sulfates or nitrates, which could be translated into a cathodic current. Once all soluble electrons acceptors were consumed and acetate

started to be oxidized in the anode, proton reduction occurred in the counter electrode. The average value of the ITO potential was calculated starting from day 6, as considered in Test 1. For reactor 2-3, the value remained at -0.45±0.02 V/SCE between day 6 and the end of the experiment (day 18). For reactor 2-4, the variation of the potential was of -0.68±0.11 V/SCE in the same period. In this case, it appeared that the higher current production in the anode shifted the ITO potential to more negative values and then reestablished when current decreased. This same phenomenon was observed for reactor 2-2 using a Pt grid.

It was decided to perform a final and third test to determine whether the phenomenon observed in the ITO potential, where the value was considerably deviated to more negative potentials, was still repeated. A new batch of SMS was used and microelectrodes were polarized from the start of the experiment (January 2021).

It is worth noting that in Tests 1 and 2, the batch of sediments dated from October 2020. The analysis of low current density values yielded from the salt marsh EABs was described in chapter 4. For the reasons described above in Test 1, the microelectrodes were broken; therefore, they could not be retrieved for microbial analysis, and only those from Test 2 were recovered.

- Test 3:

Four reactors were launched as in Test 2, where reactors 3-1 and 3-2 contained Pt grids, and reactors 3-3 and 3-4 ITO glasses as counter electrodes. Figure VI-8 (A) shows the electrochemical performance for the SS microelectrodes, where again current density was not high as expected, regardless of the material of the counter electrode. In Figure VI-8 (B) the evolution of the potential of the counter electrodes presented the same tendence already seen in Test 1 and 2. After day 6, the potential of the ITO electrodes remained at an average value of -0.48±0.01 V/SCE for both reactor 3-3 and 3-4. Pt grids potential decreased to a range of -0.70 to -0.75 V/SCE.

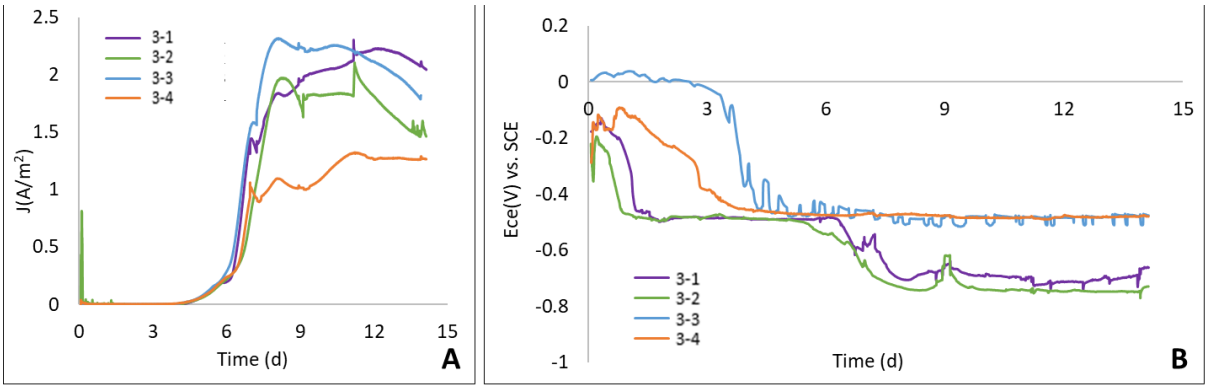

Figure VI-8: (A) Evolution of current density in time for salt marsh EABs formed over SS microelectrodes polarized at 0.1 V/SCE for Test 3. (B) Evolution of the potential of the counter electrode while in CA technique for Test 3.

As for the third time in the consecutive tests, the current density values yielded by the salt marsh EAB in the SS microelectrodes were not sufficiently high as compared to the expected; it was decided to switch to a chronopotentiometry technique after 14 days of CA. This was done for reactors containing ITO as counter electrode (3-3 and 3-4) as the aim was to determine if the potential of the ITO electrodes remained stable when rising the current in the working electrode. For reactors 3-1 and 3-2, the polarization kept on running. The complete curves of reactors 3-1 and 3-2 belong to Figure IV-3 (C), where the microbial population of the salt marsh bioanodes was analyzed.

Returning to reactors 3-3 and 3-4, as to avoid anode overloading in terms of potential, current was decided to be applied in consecutive steps. With a duration of one hour per step, the idea was to perform six steps: step 1 applying 0.01 mA, step 2: 0.014 mA, step 3: 0.018 mA, step 4: 0.022 mA, step 5: 0.026 mA and finally step 6: 0.03 mA, reaching the final value set in Test 1 of 10 A/m^2.

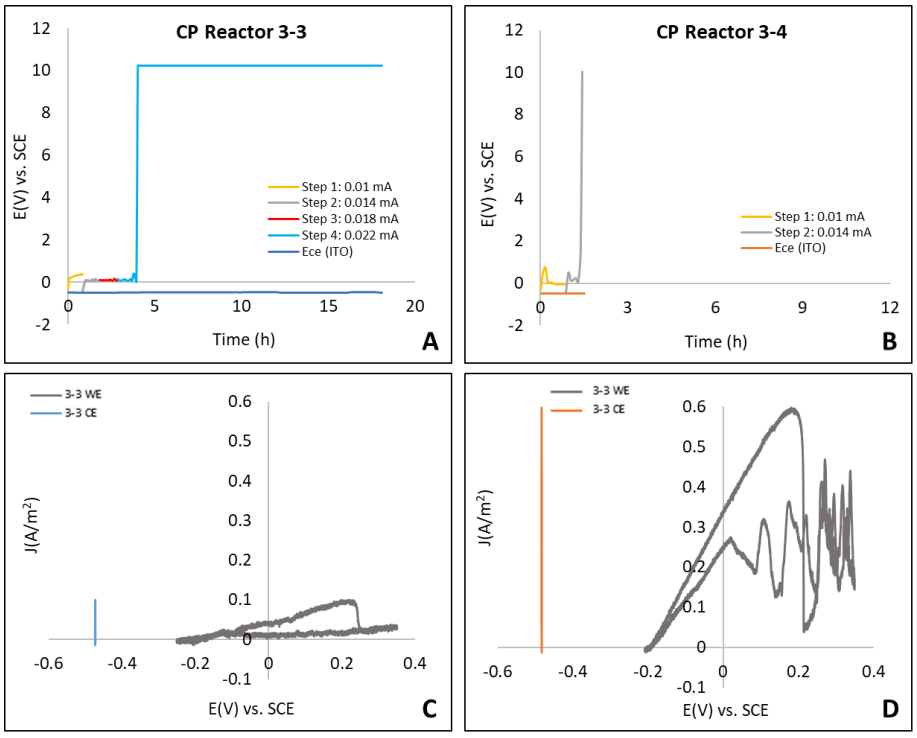

Figure VI-9 : (A) and (B): Evolution of the potential of the SS microelectrode and ITO electrode while applying steps of current in the SS microelectrode. (C) and (D): Final CV for SS microelectrodes together with the tracking of the ITO electrode potential.

Figure VI-9 shows the current steps applied. For reactor 3-4 (Figure VI-9 (B)), the potential steps were only applicable to step 2, where the potential of the SS microelectrode reached quickly the limit value of 10 V/SCE, therefore the CP was stopped. For reactor 3-3 (Figure VI-9(A)) the steps of potential were applicable just until step 4. The technique continued running for a longer time than in reactor 3-4 since it was decided to maintain this value of current during the night. When a current value of 0.022 mA was applied to the anode, its potential needed to be dramatically increased, reaching the 10 V/SCE limit.

What was remarkable of this CP strategy was that the potential of the ITO counter electrode remained constant in time despite the current steps applied to the anode. However, to determine the current limit value to be applied in the CP, the right procedure would have been to launch a CV as to determine the maximum current the salt marsh EAB could reach without shifting to other reaction, such as the oxidation of water into oxygen.

After the CP, a CV was launched in the bioanode, and the potential of the ITO was tracked. The low scanning limit was defined as the open circuit potential of the working electrode in order to prevent reduction reaction in the anode, and the high limit was 0.35 V/SCE. The scanning speed rate was of 1 mV/s. It was clear that current values were lower than the final value of the CA, since the augmentation of the potential in the anode might have produced oxygen which could have detached the biofilm and/or affect its viability. Again, the potential of the ITO electrode remained constant while the working electrode potential was being scanned.

- Strategy to use ITO glass as a pseudo-reference in the microfluidic system

After the three consecutive tests, the same trend in potential could be observed for the ITO electrodes starting from the sixth day of experiment. Table VI-2 gathers the potential values already presented above, where for the exception of the ITO electrode in reactor 2-4, the value remained close to -0.5 V/SCE. It was not very clear why the behavior of the ITO electrode in that case was not stable. The only difference within the rest of the reactors was that more current density was produced in the anode, which might have implied that the ITO potential had to shift.

Table VI-2 : Average potential for ITO as counter electrode between the period of 6 days and the end of each experiment.

Reactor	E_{ITO}(V) vs SCE
1-2	-0.45±0.03
1-3	-0.50±0.01
2-3	-0.45±0.02
2-4	-0.68±0.11
3-3	-0.48±0.01
3-4	-0.48±0.01

Therefore, a strategy was proposed when working on the microfluidic system. As seen in Figure VI-10, after 6 days where the potential of the ITO vs the SCE remained stable, the following calculation could be made:

$$E_{WE/ITO} = E_{\frac{WE}{SCE}} - E_{\frac{ITO}{SCE}} \qquad \text{Eq. VI-1}$$

$$E_{WE/ITO} = 0.1\,\frac{V}{SCE} - \frac{(-0.5)V}{SCE} \qquad \text{Eq. VI-2}$$

$$\boldsymbol{E_{WE/ITO} = 0.6\,\frac{V}{ITO}}$$

If a standard 550 mL reactor were launched, after at least six days, the anolyte composition would have evolved sufficiently for the ITO potential to stabilize at -0.5 V/SCE. It has already been seen that this happened whether the system was in OCP or CA (Test 1 vs. Tests 2 and 3). If at this point a sample of the anolyte was taken and introduced to the two-electrode microfluidic cell, the SS microelectrode could be polarized at 0.6 V/ITO, thus maintaining the equivalence with the 0.1 V/SCE potential. This will be the mode of operation in the following sections when working in the microBES.

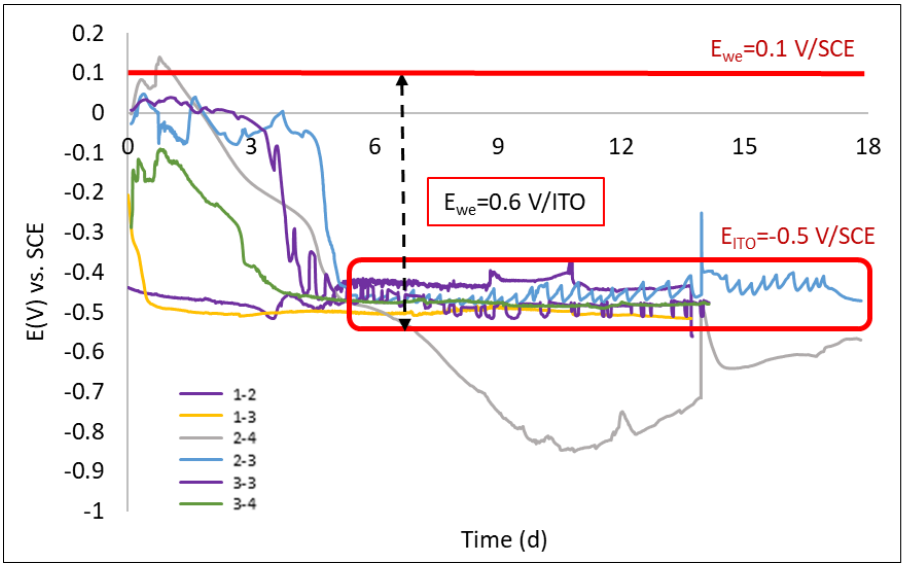

Figure VI-10 : Evolution of the ITO electrode potential for the three tests. Graphic representation of the calculated difference between the potential of the SS microelectrode fixed at 0.1 V/SCE and the stable ITO potential at around -0.5 V/SCE.

VI.2.1.2.2. First essay to form a salt marsh EAB in the two-electrode microBES

Once the electrochemical validation of the two-electrode microBES was successful, and considering the SS microelectrode polarization potential as 0.6 V/ITO, the first experiment was carried out in the microBES. The aim of this first test was to form a salt marsh EAB on the SS microelectrode inside the microBES. For this purpose, three different strategies were investigated:

- In the first case, one microBES was continuously fed with the anolyte of a 550 mL reactor that had been running from more than 6 days. The set flow rate was of 30 µL/min while the experiment was kept at a constant temperature of 30°C inside a stove. The SS microelectrode was polarized at 0.6 V/ITO throughout the whole duration of the experiment.

- Two other microBES were also kept in the stove at 30°C yet in fed batch mode with the same anolyte source as in the continuous reactor. The polarization potential was also 0.6 V/ITO and the medium was replaced when needed.
- Another cell was placed under the microscope at room temperature and connected to the potentiostat in order to work in batch mode. In this case, the initial potential was of 0.2 V/ITO and was later changed to 0.6 V/ITO.

The microBES were electrically connected to the potentiostat using crocodile clamps, as seen in Figure VI-12 (B). The counter and reference electrode electrical connections of the potentiostat channel were branched together and attached to the ITO glass, whether the working electrode was also attached with a crocodile clamp to the microconnector welded to the SS microelectrode

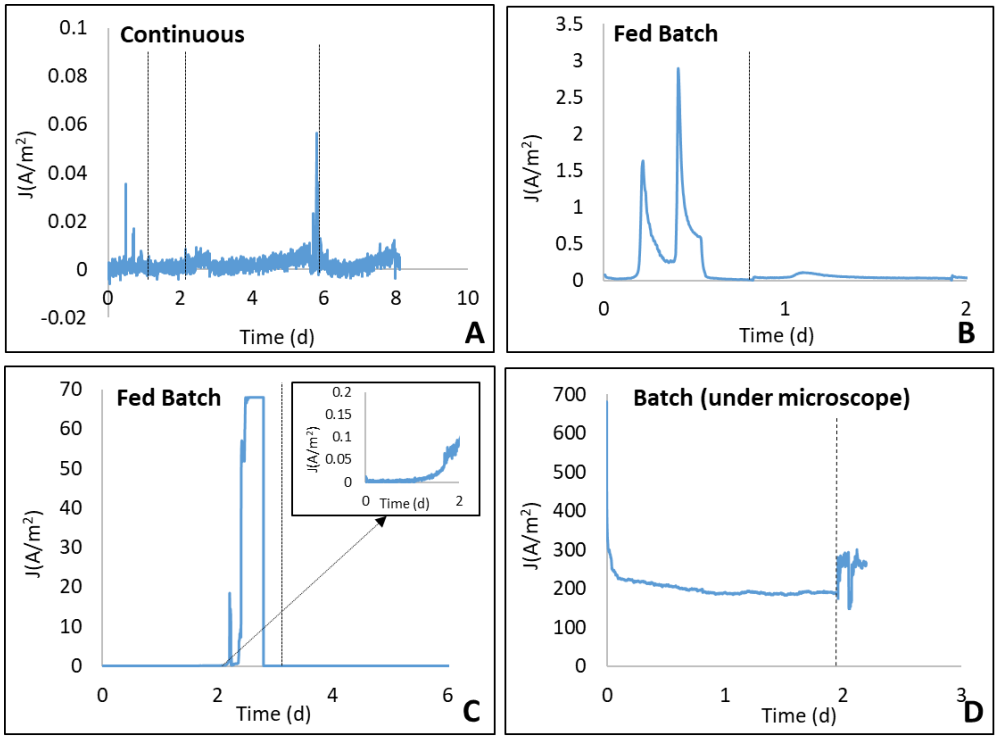

Figure VI-11 : Evolution of current density in time for SS microelectrodes in the two-electrode microBES. (A) In continuous feeding mode. Dotted lines show the shutdown of the fluid supply and cleaning of the cell (B) and (C) in fed batch feeding mode. Dotted lines show the media change. (D) Batch mode under the microscope. Dotted lines show the change in the polarization potential from 0.2 V/SCE to 0.6 V/SCE.

Figure VI-11 shows the CA curves for the SS microelectrodes. The microBES functioning in continuous mode presented several drawbacks. In the period of one day, white spots from salt deposits could be observed inside the reactor. In addition, despite circulating the anolyte through the filling tubes before entering the cell to avoid the insertion of air, bubbles were also found to be present. The combination of crystals and bubbles formation caused the appearance of dead volumes. This meant that at times the fluid did not cover the microelectrode area. These issues are shown in Figure VI-12. For this reason, it was decided to stop the polarization and fluid circulation at several times to clean the microBES with

water in order to remove the crystals. In Figure VI-11 (A), it can be seen that the bioanode performance was not successful. Most probably, the problems mentioned above together with the regular cleaning of the microBES hindered the formation of a biofilm or eliminated the few cells deposited on the microelectrode.

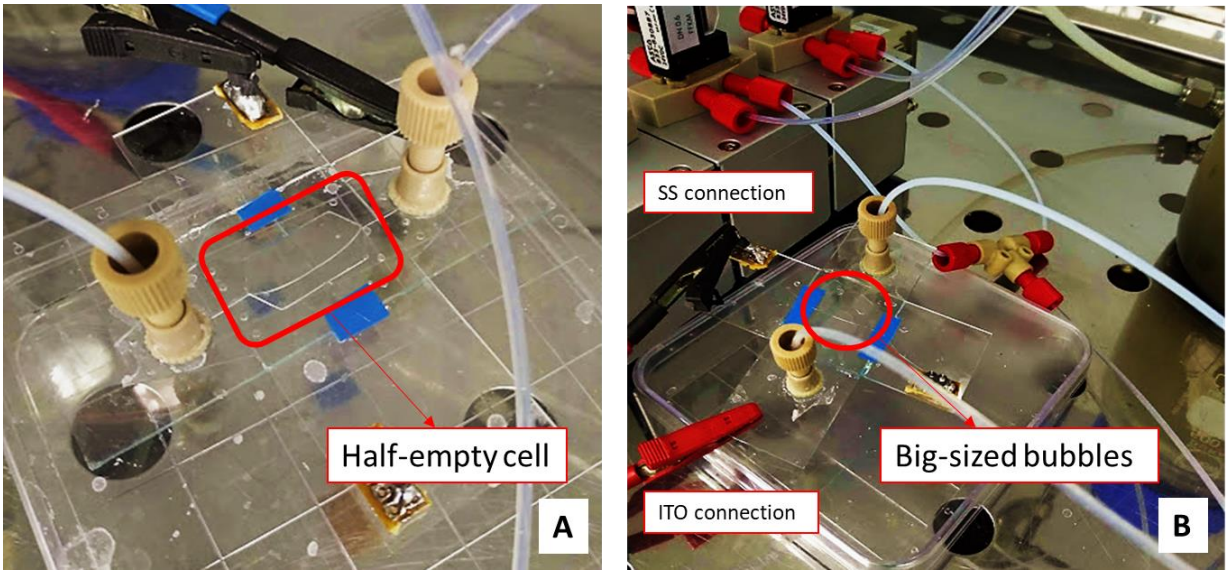

Figure VI-12 : Fluid issues encountered when working in continuous mode with the second prototype of the microBES. (A) microBES with less than half of the fluid. (B) Generation of large bubbles inside the microchannel. This example also illustrates the electrical connections to the potentiostat.

For the microBES working in fed-batch, results were despair. In Figure VI-11 (B), two current peaks were observed at 1.5 A/m^2 and 3 A/m^2 during the first day, and later and when the medium was replaced current production was zero. However, this experience not long enough to see the evolution in current. In Figure VI-11(C), it would seem that current started to increase at day 2, yet the value rose sharply to very high values of 70 A/m^2, giving signs of an electrical connection problem. Current finally dropped to zero at day 3, and even replacing the liquid medium, as in the other microBES, did not increase the current.

For the microBES placed under the microscope, current density values were extremely elevated compared to those typically expected. Nevertheless, Figure VI-13Figure VI-12 (A) and (B) gave a preliminary insight of what can be observed when forming a salt marsh EAB under the optical microscope. Figure VI-13 (A) shows the SS microelectrode at the start of the polarization surrounded by the anolyte containing the salt marsh inoculum. At this point, bacteria were swimming very close to the surface of the microelectrode. After two days, (Figure VI-13 (B)) bacterial concentration in the anolyte was lower than at time zero, and over the electrode, the early formation of a biofilm can be noticed.

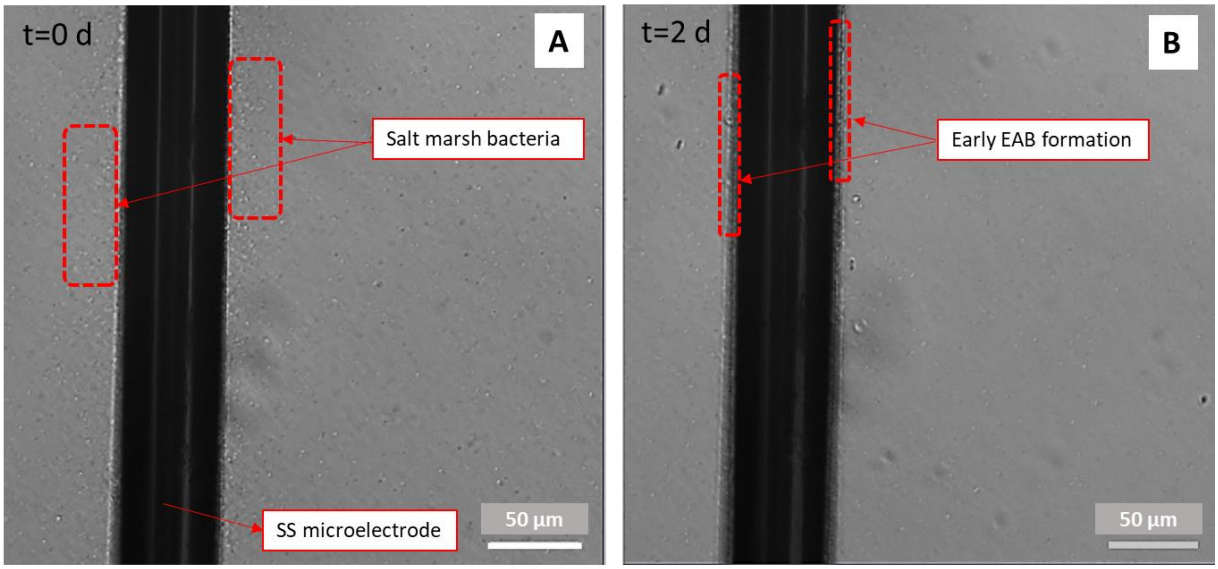

Figure VI-13 : DIC microscope images of the SS microelectrode polarized at 0.2 V/SCE while colonized by salt marsh bacteria. (A) at t=0 d. (B) at t=2 d.

However, regardless of working in continuous or batch mode of the anolyte supply, the electrochemical performances of the microBES were not very successful. Since no problem of electrical contact between the potentiostat channel and the electrodes was identified, our suspicions were rather focus on the design of the microfluidic shape, which may not have been the most appropriate. In our case, the sharp corners of the hexagonal shape and the perpendicular filling design (meaning that the filling of the microBES is perpendicular to the microchannel) were prone to create air pockets. In addition, air may also have been trapped inside the microchannel when closing the reactor with the upper glass slide (Pereiro et al., 2019). Eliminating the upper glass slide would avoid this problem as well as reducing the thickness of the microBES to allow better light transmission when using the microscope.

For the reasons just described, it was decided to redesign for a final time the shape of the microreactor but still maintaining the two-electrode electrochemical system including the SS microelectrode as the working electrode and the ITO glass slide as both the counter electrode and the pseudo-reference electrode.

VI.2.1.3. Micro-BES – Third prototype: The two-electrode OSTEMER microfluidic cell

Here it was proposed to soften the sharp edges, to lengthen the microchannel as to eliminate the hexagonal shape, and to arrange the fluids inlets and outlets in parallel to it as to avoid air pockets. Close to the inlet and to the outlet of the microchannel, phaseguides were added (Figure VI-14 (A-ii)). These small lines of material are helpful to build up capillary pressure and fill dead angles. This means that the region containing the phase guides is firstly completely filled and after that, the liquid can overflow to the rest of the microchannel. These modifications were useful to improve the uniform distribution of the liquid phase in the total, resulting in a microBES of 300 µL of volume.

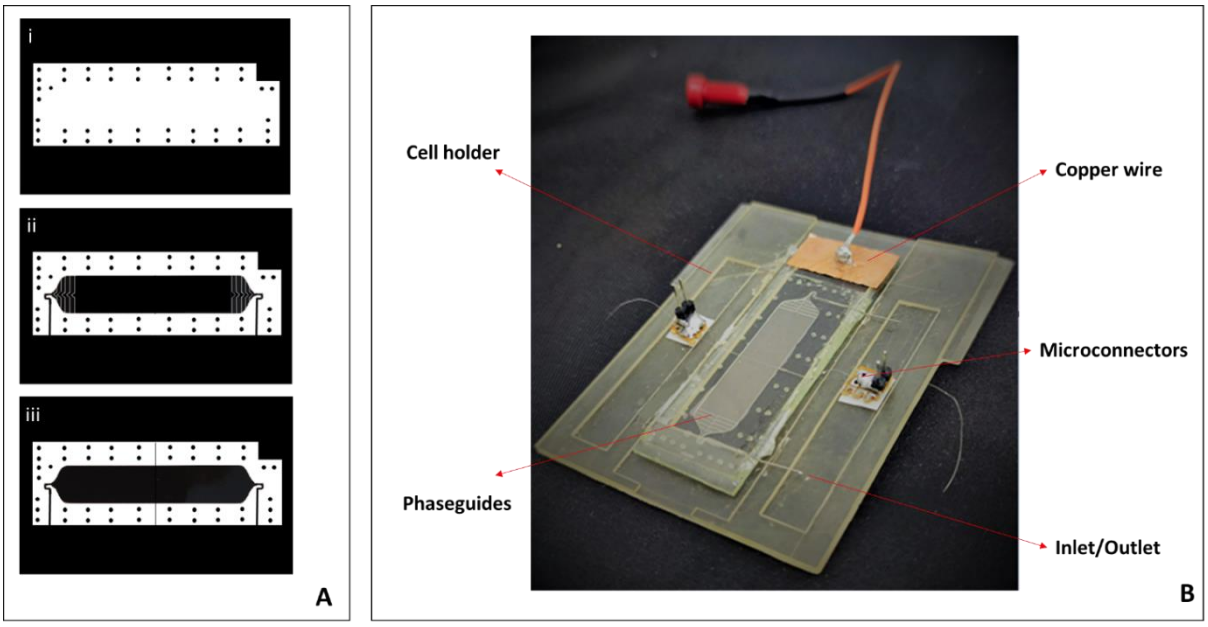

Figure VI-14 : (A) Designed masks for the third prototype of the microfluidic cell. (B) Final, ready-to-use two-electrode microfluidic cell.

The OSTEMER two-electrode microBES was developed with the chip fabrication protocol using Dupont WBR dry film by OSTEMER casting (see Annex Figure 2). Figure VI-14 (B) shows the final prototype of the microBES. SS needles with a diameter of 0.3 mm were placed at the inlet and outlet channels. They were glued with an epoxy adhesive. The microchannel was then filled with distilled water to test if there were any leaks. During filling, a bubble trap was connected to the inlet to prevent the injection of air bubbles from the outside. In addition, it was observed if the phaseguides fulfilled their function by observing whether the fluid first filled this region and no dead volumes were generated. Furthermore, a cell holder was designed to contain the microBES so it could be positioned in the microscope.

To ensure the electrical connections, a piece of conductive copper tape was bonded to the ITO glass slide at one end. On the conductive tape, a piece of copper wire was welded, containing a plug for the potentiostat, thus avoiding the use of a crocodile clamp for connecting the ITO glass. The microfluidic cell was then placed in the cell holder, where the SS microwire was welded to two microconnectors glued at each side of the cell holder. The electrical continuity of all connections was checked by measuring the resistance with a multimeter. After fabrication, before a new microBES is used in the experiments presented in Part B, an electrochemical test, i.e. a CV technique, is systematically performed to validate the electrochemical functioning of the two-electrode microBES.

VI.3. Part B: Experiments in MicroBES

Once the 2-electrode OSTEMER fabricated microBES was functional, experiments were conducted by filling the microBES microchannel with the 6-day anolyte from a 550 mL reactor. As explained in Part A, the 6-day anolyte is required to steadily polarize the SS microelectrode to a potential of 0.6 V/ITO (i.e. the equivalent of 0.1 V/SCE). The experimental platform used is the one described in Figure II-5, where the microBES is placed under the optical microscope objective and connected to a potentiostat for a simultaneous microscopic observation and application of electrochemical techniques.

Four tests were carried in this section in batch and in fed-batch mode. The operation in continuous mode was discarded due to its complexity for preliminary tests. Tests 6.1 and 6.2 had as objective to demonstrate the formation of a salt marsh EAB on the SS microelectrode present in the microBES by polarizing the microelectrode both in short and long times. In addition, this was possible by continuously measuring the current generated at the surface of the microelectrode and by imaging the SS microelectrode-salt marsh EAB-anolyte interfaces in the course of polarization.

Tests 6.3 and 6.4 aimed to investigate the displacement of salt marsh bacterial cells in the near-surface of the microelectrodes (for short times) and in the near-surface of the EABs during the temporal stages of salt marsh EAB formation on the microelectrode (for longer times). These two tests were performed at two different electrode potentials in order to study the displacement response of bacteria to a potential stimulus, in this case the so-called electrotaxis, when the microelectrode is polarized.

Table VI-3 resumes the experimental conditions for the tests in this section, making a distinction between the test conditions and those of the anolyte preparation in macroBES. Biofilm thickness was measured as indicated in section II.3.2.4.

Table VI-3 : Summary of experimental conditions for experiments in microBES.

MacroBES (only to prepare the anolyte to fill in the microBES)				
Inoculum	Salt marsh			
Temperature	30°C			
Substrate	Sodium acetate 40 mM			
Culture medium	Starkey medium (45 g/L of NaCl)			
Inoculation size % V/V	5			
Operation mode	Batch			
Reactor type	Standard			
OSTEMER two-electrode microBES				
Test	Test 6.1	Test 6.2	Test 6.3	Test 6.4
Temperature	Room			
E_{we} (V) vs. ITO	0.6	0.6	0.6	0.9
Operation mode	Batch	Fed-Batch	Fed-Batch	Fed-Batch
Polarization time (d)	7	48	48	73

VI.3.1. Formation of a salt marsh EAB in the microBES

VI.3.1.1. Test 6.1: Short-term experience (focus on stage I)

In this first experience, we tried to successfully form a salt marsh EAB over the SS working microelectrode in the two-electrode microBES. The microelectrode was polarized at 0.6 V/ITO during 7 days while the microBES was placed under the microscope objective at room temperature. Several times during the study, the optical field comprising the surface of the SS microelectrode and the liquid phase made of a bacterial suspension in the anolyte was imaged. Either a snapshot image was captured or a series of images were acquired as explained in II.3.2.4. in order to observe the movement of the bacteria in the optical field.

Figure VI-15 shows the progressive evolution of the electroactivity of the salt marsh EAB that forms on the SS microelectrode as well as the optical microscopy snapshots of the SS microelectrode in the microBES at days 0, 3 and 7. At days 0, when polarization started, the microelectrode surface was clean and free of bacteria. The bacteria moved all over the anolyte and in the immediate area of the microelectrode. Three days later, current density increased to 0.3 A/m^2. Over the SS microelectrode, cell aggreagates (forming a kind of roughness), corresponding to the colonization of salt marsh bacterial cells that iniciated the formation of an EAB, reached a thickness of 2.0±1.0 μm. Bacteria appeared more static in the surrounding anolyte. Current density kept on increasing, reaching a maximum of 0.71 A/m^2 at 6.3 days. The sharp drop in current after the maximum is related to an electrical connection problem or a potentiostat malfunction that was quickly resolved. The biofilm enlarged to a final thickness of 5.1±1.7 μm at day 7. At this point, bacterial displacement was only scarcely detected in the surroundings of the microelectrode.

When comparing the level of the current density values obtained here in microBES and the ones usually reached from the experiments carried out with SS microelectrodes in the macroBES at stage I (see Research Article 2) , the order of magnitude of the current density values produced by the bioanode was similar. The lag-phase was shorter in the microBES, probably due to an effect attributable to confinement. This first feasibility test was successful. It clearly demonstrated that it was possible to mimic the electroactivity of the salt marsh bioanodes at stage I in macroBES.

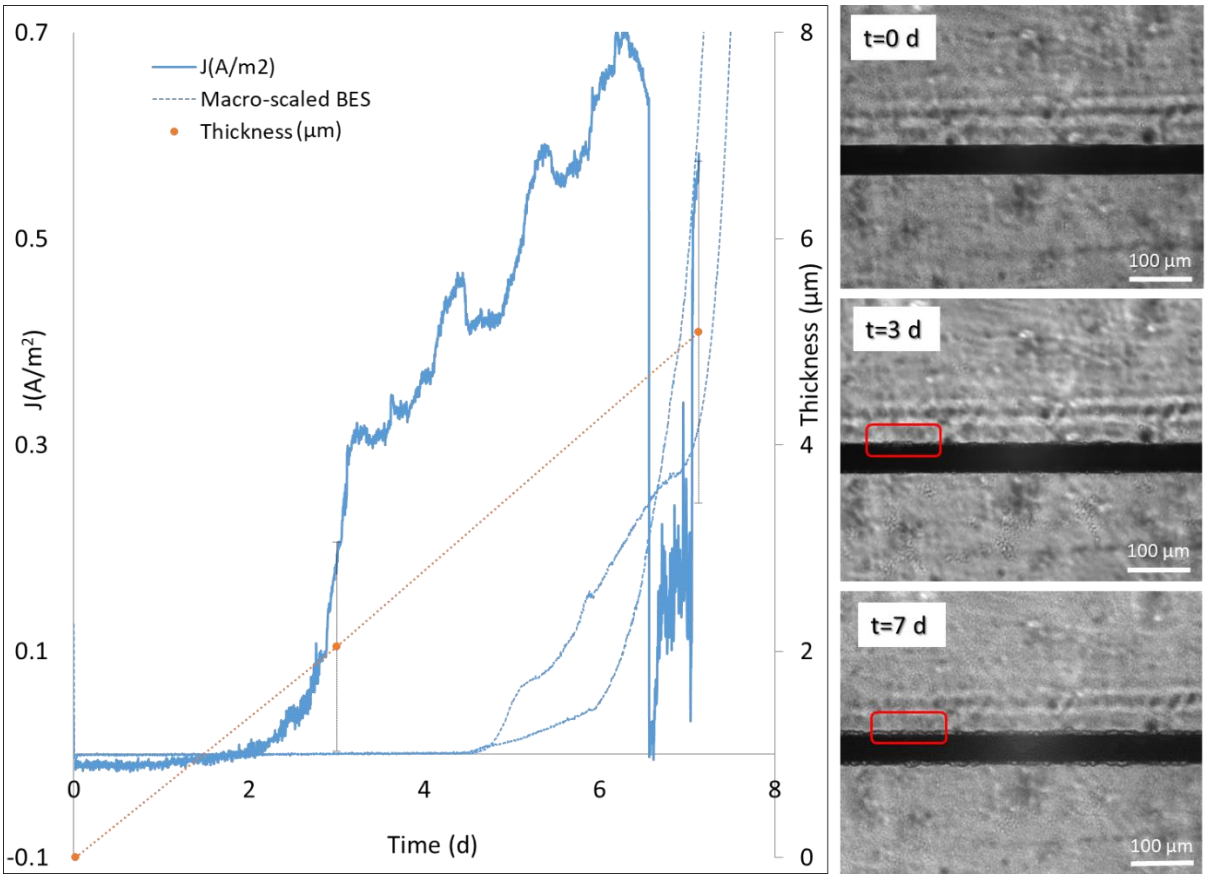

Figure VI-15 : Evolution of the current density in time for the salt marsh EAB formed on the SS microelectrode in the microBES (blue full line) and in the macroBES (blue dashed lines). Biofilm thickness values obtained from the DIC images at different days of the experiment. DIC Microscopy images on the right show the in situ and in real time formation of the salt marsh EAB in the microBES at different times of the experiment. The red panels highlight the bacterial cells constituing the biofilm that colonize the microelectrode.

VI.3.1.2. Test 6.2: Long-term experience

In this experiment, the SS microelectrode was polarized for a longer time of 48 days at 0.6 V/ITO. In addition, DIC light microscopy captures were performed at higher magnification (x2 and x4) to visualize the SS microelectrode-salt marsh EAB-anolyte interfaces in more detail.

The Figure VI-16 shows the current density produced by the salt marsh EAB together with microscope images obtained simultaneously during polarization. At day 0, the microelectrode was clean. One day after, bacterial density seemed to increase in the microelectrode surroundings. Current density started to increase at day 2, likewise in the previous experiment, but with a minor slope, probably because of the difference in the room temperature (the previous experiment was conducted in summer and this one in winter). At day 8, current reached a density value of 0.26 A/m^2 with a biofilm thickness of 6.6±0.6 µm. Current kept on increasing until reaching the maximum value of 0.50 A/m^2 at day 13, where the biofilm thickness attained a value of 10.5±1.4 µm. Current was fairly stable for a week (day 13 to day 20) and dropped drastically between days 20 and 33. In this case, current drop was most probably due to acetate depletion in the anolyte, as it was fed into the microBES only at the beginning of the polarization. This

was corroborated after injection on day 33 of a new batch of anolyte containing acetate, which resulted in a re-increase of the bioanode current. At day 48, polarization was stopped and biofilm thickness reached a value of 16.1±3.3 µm.

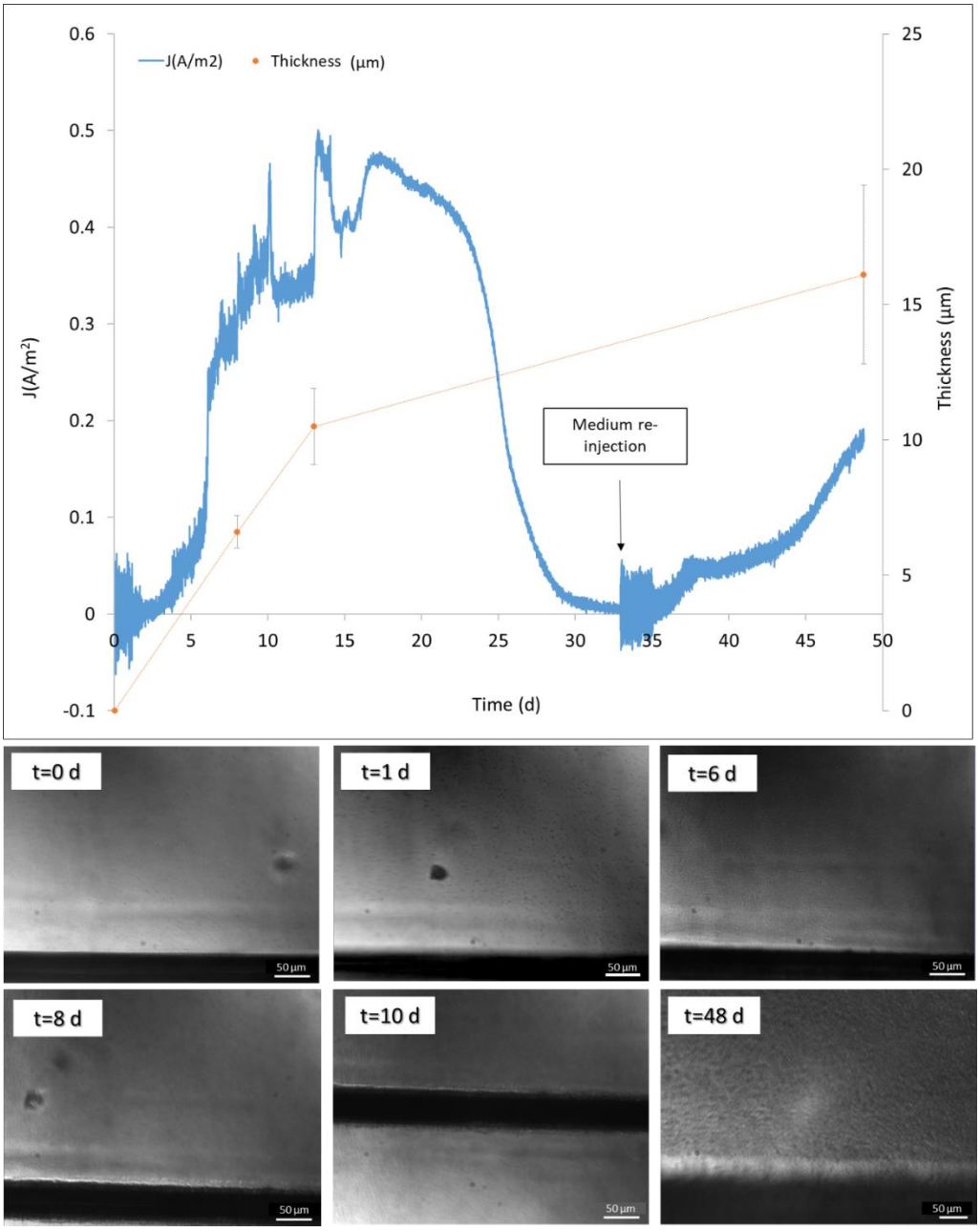

Figure VI-16: Evolution of the current density in time for the salt marsh EAB formed on the SS microelectrode of the microBES. Biofilm thickness values obtained from the DIC images at different days of the experiment. DIC Images below the CA show the in situ and real time formation of the salt marsh EAB in the microBES at different times of the experiment. All images were acquired with a 20x objective with the exception of the one at t=48 days, where a 40x objective was used.

As a result of these two experiments (test 6.1 and test 6.2), we can report that:

The formation of a salt marsh EAB on the SS microelectrode of a microBES was feasible, thus accomplishing one of the major demonstration of this PhD work. This was possible for short and long

term experiments (7 to 48 days), meaning that the microBES is suitable for biofilm formation over short and long periods.

The strategy for forming the EAB inside the microBES was to fill the microchannel with anolyte containing acetate substrate and salt marsh inoculum, wait until current dropped and re-add a batch of anolyte containing acetate, as seen for the long-term experiment. Managing the acetate supply is critical as discussed in Chapter V, but it is not possible for us to measure the concentration of acetate over time within the microBES. The method available to us required at least 2 mL of anolyte for the measurement. The volume of anolyte in the microBES is only 0.3 mL. As in Chapter V for the 550 mL macro BES, when acetate was added in pulses, salt marsh EABs were formed with maximum electroactivity comparable to that obtained when it was added regularly, a similar strategy was adapted for the microBES.

The trends in the electrochemical performance of EABs and the biofilm growth rate in the microBES were similar when comparing with macroBES still values were lower. In the short-term experience (7 days) current density seemed to show a similar behavior in terms of shape and values for salt marsh EABs formed on SS microelectrodes to that seen for the ones in macroBES. Nevertheless, the long-term experience showed that current density value reached a maximum of 0.50 A/m^2 and later dropped to zero due to acetate depletion. In macroBES where acetate was added in pulses, J_{max} peaks were between 6.00 to 8.00 A/m^2.

The evolution of biofilm thickness was similar for both microBES experiences in the first seven days. For the long-term experience, although there was no capture of the biofilm thickness between day 14 and 47 (the focus did not provide bright, clean images), a decline in biofilm thickening kinetics occurred between day 13 and day 48, although this finding is based on only two measurement points. It would seem that the biofilm grew faster in the first 13 days, with the increasing current density, and later the growth rate decreased. This trend in the growth rate was similar to what was observed for salt marsh EABs in 550 mL reactors described in article 2 (see table S2), where growth rate was higher when current increased and then it diminished with current drop and final stabilization. The main difference is that thicker biofilms were formed in macroBES (~57 μm at 55 days).

The change in scale between macroBES and microBES is certainly the cause of these discrepancies. In macroBES, the surface area of the SS microelectrode was only 2 or 4 times larger while the volume of anolyte was 2000 times larger than in microBES. Such a difference in volume for an electrode whose surface does not change much from one system to the other may have implied less colonization of the microelectrode. The substrate reservoir is much more limiting and the confinement effect in the microchannel may also have played a role. Another possible explanation is related to the fact that the anolyte was already 6 days old at the beginning of the experiments. As already shown in Chapter IV, the microbial population of the biofilm evolves over time, it is very likely that the microbial population

of the anolyte does too. Therefore, the amount of electroactive bacteria in the microBES may have been lower than in the macroBES.

From a technical point of view, in these two experiments, it was possible to couple in simultaneous the real-time spatio-temporal evolution of the SS microelectrode-salt marsh EAB-anolyte interfaces with the electroactivity of the EAB. However, improvements should be made in the microscope acquisition settings in order to obtain a better image quality allowing quantitative measurements. One of the most important constraints in this experimental set-up was that bacterial movement inside the microBES evolved in time together with biofilm formation. It is therefore difficult to automate acquisitions without manual readjustment of the focus.

VI.3.2. Study of bacterial cell displacement and stages of EAB formation in the microBES

Once the formation of a salt marsh EAB on the SS microelectrode of the microBES was demonstrated and its short and long-term operation was validated, the next step was to attempt to study bacterial cell displacement inside the microBES and EAB formation stages.

VI.3.2.1. Preliminary steps

As the optical flow method was used to quantify bacterial cell displacement, the latter should be short as to ensure constant pixel intensity between consecutive images and to avoid losing information about bacterial position; therefore, time between the acquisitions of each image (frequency) should be relatively low. Here, the lowest possible frequency to be set in the Blue Zen software controlling the microscope was of 0.4 seconds (time between images). The acquisition time for a stack of images (i.e. time frame) was set at 1 minute, obtaining a stack of 150 images.

Secondly, a procedure was tested to corroborate whether the optical flow algorithms could effectively process microscope image stacks (Figure VI-17). In step 1, the microBES was filled only with distilled water and placed under the microscope. A one-minute acquisition was launched with a frequency of 0.4 second per image. Without moving the cell, distilled water was replaced for the anolyte and the acquisition was repeated (step 2). Later, a MATLAB code produced a blank image (see Annexes: CalculMeanImage) and another MATLAB code performed the subtraction between the acquisition with the anolyte containing bacterial cells and the blank image generated (see Annexes: ImageSubstraction). This allowed obtaining a new stack of images where only bacterial cells were present and the background of the microelectrode and the liquid phase were eliminated. In step 3, MATLAB optical flow algorithms (see Annexes: OpticalFlow) were applied to the stack of images, thus obtaining the velocity vector fields. The field indicated as ‘A’ (see Figure VI-17) shows the displacement vectors between one image and the consecutive one. The axis in the right show the velocity values, which increase with color warmth. The field indicated as ‘B’ (see Figure VI-17) shows the average displacement vectors of the 150 images of the stack. In this test example, the average velocity field

showed that bacterial cells displaced themselves from the upper left corner to the electrode area, with a higher velocity values coming from the left side.

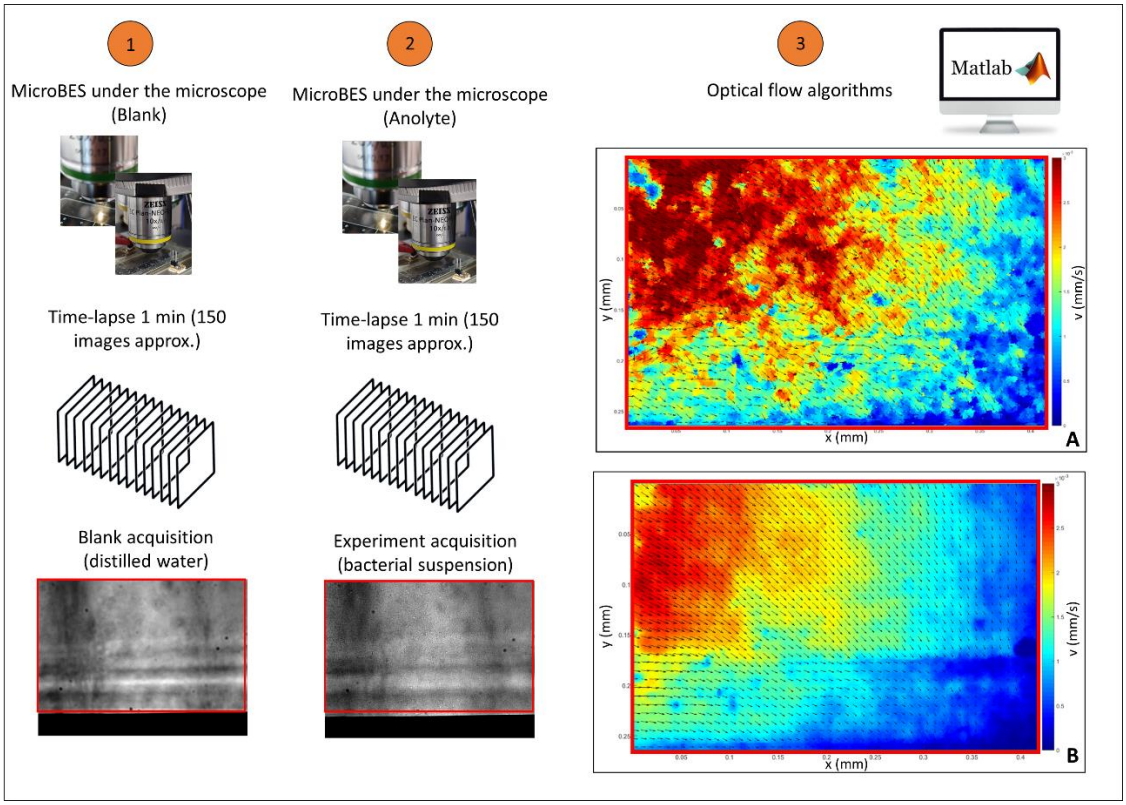

Figure VI-17 : Simplified procedure for post-processing of microscopic image stacks by applying optical flow algorithms. The area analyzed (red rectangle) excludes the part where the electrode is present (A) Velocity vector field between two consecutive images of the stack. (B) Average velocity field for all the images of the stack (150 images).

VI.3.2.2. Test 6.3: Experience at 0.6 V/ITO (fed-batch)

The microchannel of a new microBES was filled with the anolyte of a macroBES reactor that had been running for 6 days. The system was left at OCP for 24 hours. After, the SS microelectrode was constantly polarized at 0.6 V/ITO, where current density curves can be observed in Figure VI-18 (A). Total polarization time lasted for 48 days. The volume (0.3 mL) of the microchannel was changed four times in the course of the experiment:

- Day 13: First anolyte change (Starkey medium + inoculum + acetate)
- Day 27: Second anolyte change (Starkey medium + inoculum + acetate)
- Day 30: Only Starkey medium (No inoculum, no acetate)
- Day 34: Starkey medium with acetate (No inoculum)

The SS microelectrode-salt marsh EAB-anolyte interface was simultaneously imaged as seen in Figure VI-18. In addition, the thickness of the biofilm was also measured from the microscope images and

registered in Figure VI-18 (B). For an easier explanation, results are divided from days 0 to 15, and from days 16 to 48.

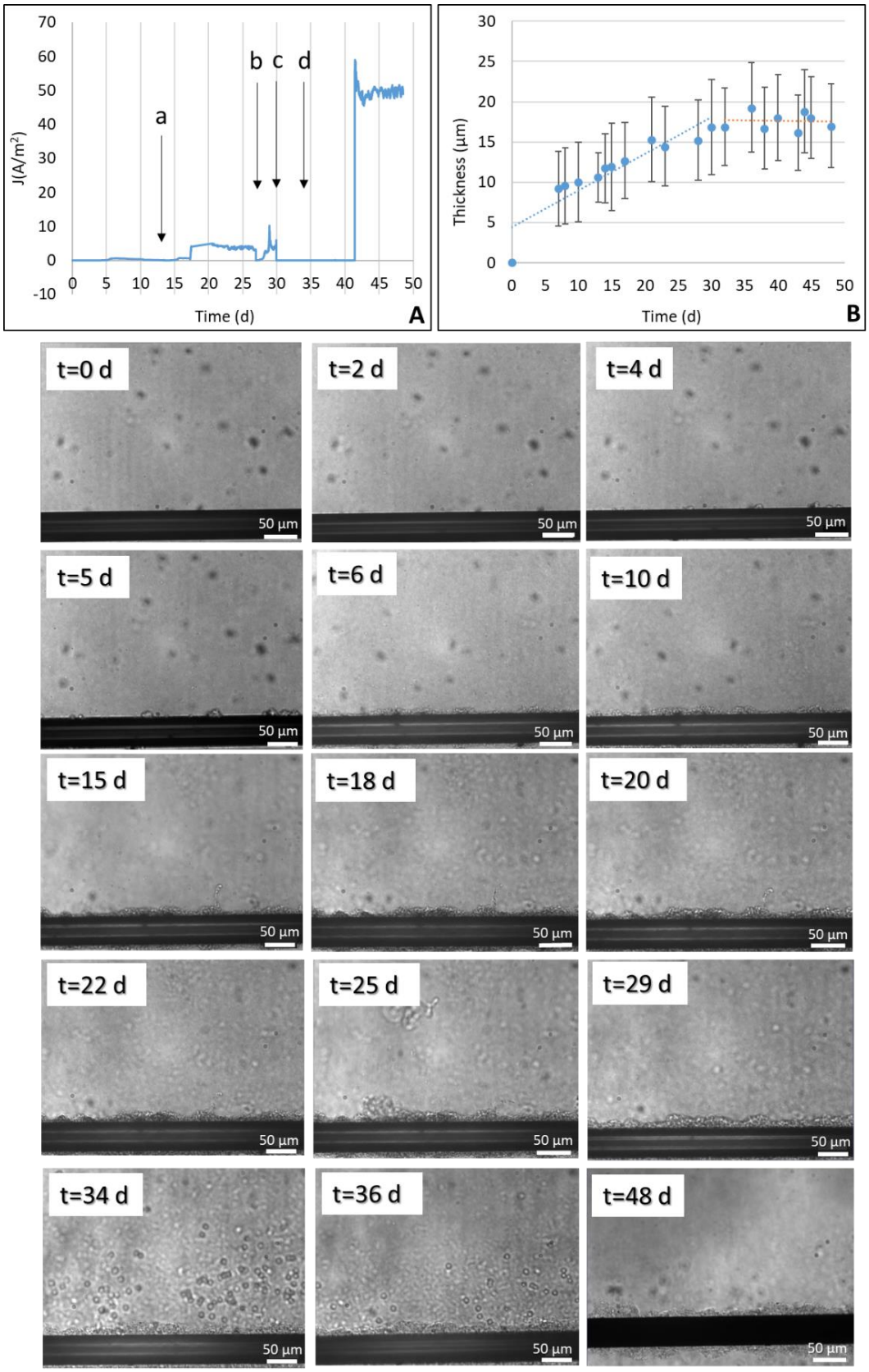

Figure VI-18 : On the top of the figure: (A) Evolution of the current density in time for the salt marsh EAB formed on the SS microelectrode of the microBES. Letters correspond to changes in the volume of the microBES: (a) first anolyte change, (b) second anolyte change, (c) Starkey medium with no acetate, (d) Starkey medium with acetate. (B) Biofilm thickness values obtained from the DIC images at different days of the experiment. Below (A) and (B): DIC microscope images for the SS microelectrode-salt marsh EAB-anolyte interfaces when the microelectrode was polarized at 0.6 V/ITO.

- Days 0 to 15

Figure VI-19 shows current density curves for the salt marsh EAB during the first 15 days, since in Figure VI-18 (A) it is not well visible due to the scale size. In this period, J_{max} was of 0.68 A/m^2 being within the range of values obtained for the two previous experiments. As expected, current dropped to zero, probably due to acetate consumption and it was restored when the anolyte was changed for the first time at day 13.

The DIC microscope images in Figure VI-18 show the spatio-temporal stages of biofilm formation on the microelectrode. The stages of EAB formation can be correlated with its electroactivity. At day 0 and 2, the microelectrode had a clean appearance; planktonic bacteria are only present in the anolyte. No current was produced at this point. Later, at day 4, the first clusters of microbial cells appeared over the microelectrode surface and continued to grow on day 5. At these days, current was increasing. At day 6, a more homogeneous biofilm was formed in the microelectrode and current reached its maximum. The important observation at this point was that in the region near the microelectrode, the bacterial density in the anolyte was greater than far from the electrode. In the time lapse videos generated from the image stacks (data not shown) it would appear that in this region of higher bacterial density, the cell displacement of planktonic bacteria was increased close to the bioanode. At day 10, current decreased to 0.35 A/m^2 with no change in the biofilm morphology. However, the region of higher bacterial density and displacement was no longer present (data not shown). At day 13, the anolyte was changed and current restarted. At day 15, the region of higher bacterial density and displacement was again present (data not shown).

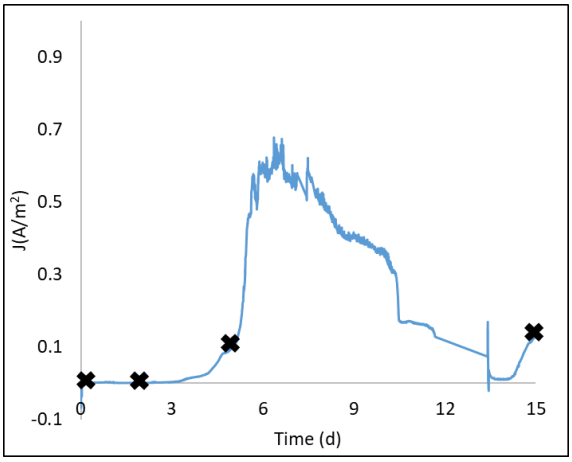

Figure VI-19 : Evolution of current density in time for the salt marsh EAB formed on the SS microelectrode of the microBES for the first 15 days. Black crosses indicate the days where the image stacks obtained with the optical microscope where post-treated with the optical flow algorithms.

To clearly demonstrate this cell densification and the general increase of the displacement rate in this area, time stacks of images from days 0, 2, 5 and 15 (indicated by black crosses in Figure VI-19) were treated with MATLAB optical flow algorithms with the protocol described in Figure VI-17. For image stacks of day 0 and 2, as no biofilm was still formed over the microelectrode, the image subtraction

performed before step 3 between the image stack and the blank with distilled water was done without any inconvenient. This means that the resultant stack of images for MATLAB treatment had only the bacterial cells in planktonic state and the electrode and background effects were eliminated. However, for days 5 and 15, when image subtraction was done with the initial blank with distilled water, the biofilm already formed at days 5 and 15 was not eliminated. This generated images with bacterial cells in planktonic state and the biofilm which, when treated with optical flow algorithms, generated non-convergent results due to the presence of static objects. Therefore, it was decided to use the concept of sliding average. This means that for the stack either at day 5 or 15, the blank image to subtract was the first image of the stack. This was done for the first 10 images of the stack of 150. Then image 11 was chosen as the blank for the second 10 images. Then image 21 was chosen as the blank for the third 10 images, and so on until the whole stack was completed.

Figure VI-20 shows the velocity vector fields (on the right side) at the four different days. Here, it was decided to calculate the maximum velocity of the whole stack of images, as when calculating the average, certain cell displacements were cancelled out and information about cell displacement was lost. At day 0, the maximum displacement velocity of bacterial cell was between 0 and 2 μm/s. The direction was mainly towards the SS microelectrode (down) and slightly to the right. At day 2, in some areas velocity was almost 0 μm/s. In that area, bacterial cells were not moving or there was no bacteria present. However, in other regions, velocity increased and was in the range of 2 to 4 μm/s. The direction seemed to be oriented to the right. At day 5, cell clusters started to form on the microelectrode surface. Velocity was of 2 to 4 μm/s in the area far from the microelectrode, and from 4 to 8 μm/s in the area closer to the microelectrode surface, as delimited by the red panels in Figure VI-20. The average direction was towards the microelectrode (down). Finally, at day 15, a biofilm was already formed on the microelectrode. The analysis of velocity vector fields still showed an area where velocity (4 to 8 μm/s) was increased in the proximity of the microelectrode as at day 5.

Therefore:

i) When biofilm started to form on the microelectrode, it matched to the time when current production was increasing and the area of high bacterial density and rapid displacement was present close to the bioanode.

ii) When the biofilm was already formed but current was decreasing, this area disappeared.

iii) When the anolyte was changed and a biofilm was already formed in the bioanode, current raised and the area of high bacterial density and rapid displacement close to the bioanode reappeared. This suggests that in order for the current to be produced by the bioanode, the presence of the bacterial high density layer in which cell displacement is accelerated is required in the anolyte near the bioanode.

However, a deeper explanation would need the development of more experiments. Is the area of increased bacterial density and displacement generated by an electrotaxis effect when the microelectrode is polarized? Would the same happen if the microelectrode was left at OCP (no potential applied)? Would the velocity have been higher at higher polarization potentials and lower at lower polarization potentials? Or should we attribute this observation to a chemotaxis effect? Is it possible that some kind of chemical gradient exists in the proximities of the bioanode? Kim et al., (2016) observed an enhanced displacement of *S.Oneidensis* cells under a riboflavin gradient using a microfluidic device, whether Harris et al., (2010) observed the complete reduction of MnO_2 particles in a 24-hours period also using *S.Oneidensis*. In this case, cell velocity was increased in the proximities of the particle as it was reduced. However, more experiments would be needed as to investigate a chemotaxis hypothesis.

The absolute necessity to maintain this active layer of planktonic bacterial cells can explain why continuous flow BES operates with difficulty. Rousseau (2013) observed a drastic decrease of the anodic current in a MEC when switching from batch operation to continuous supply of anolyte. The suggested hypothesis in his work was the dilution (washout) of some nutrients or redox mediators of the anolyte when operating in continuous mode. However, now considering our new finding, probably that it was the dense and active layer of planktonic bacteria that was removed by the continuous flow of anolyte.

As in the study of (Harris et al., 2010) with *S. Oneidensis* the bacterial displacement velocity increased at higher applied potentials, in the last experiment of this chapter it was decided to repeat the experiment but polarizing the SS microelectrode at 0.9 V/ITO, which corresponds to a potential of 0.4 V/SCE. This potential was selected as it was the maximum applied to form a salt marsh EAB on a SS microelectrode in this work.

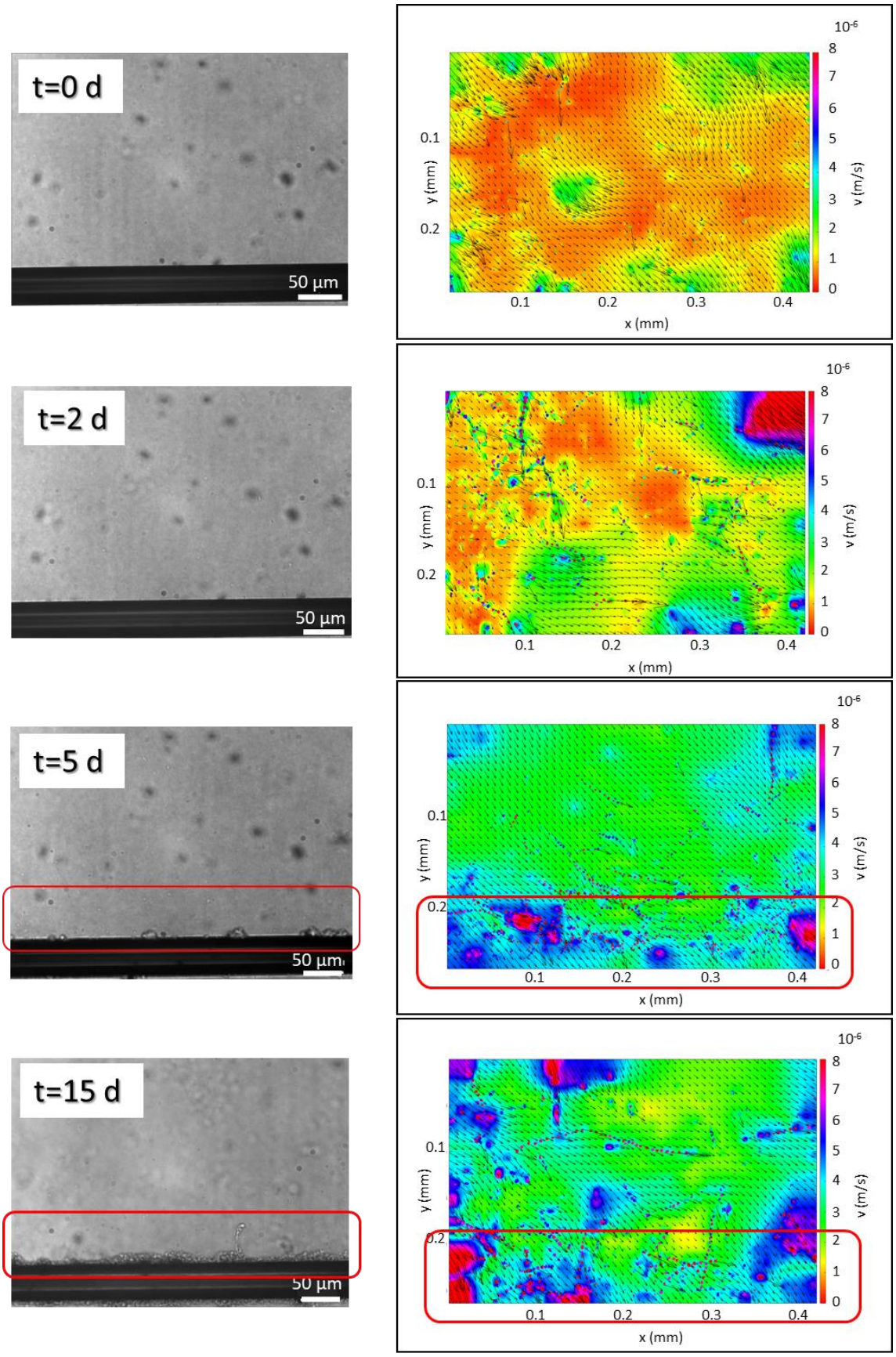

Figure VI-20: On the left: DIC microscope images for the SS microelectrode-salt marsh EAB-anolyte interfaces when the microelectrode was polarized at 0.6 V/ITO. On the right: Maximum velocity fields for the each stack of images on the left. Red panels show the equivalent area between DIC images and velocity fields.

- Day 15 to 48

After the first change of anolyte at day 13, current density increased to a value of 4.9 A/m^2 at day 20, which then oscillated between 3.0 and 4.0 A/m^2 until day 27. In this period (day 13 to 27) biofilm thickness increased from 10.6±3.1 to 15.3±5.0 µm. The biofilm enlargement can be observed in the images from Figure VI-18. When anolyte was changed for the second time at day 27, current raised to a J_{max} of 10.2 A/m^2. These high current density values were quite unusual, with respect to our first feasibility tests carried out in batch. As they were sustained over time, a problem with the connectors, a short circuit or something else was not expected at all.

At day 30, Starkey medium was added (acetate and salt marsh free) and no more current was produced. Thus confirming that in the absence of substrate or any possible oxidizable organic compound present in the inoculum, there was no current production in the bioanode. At day 34, Starkey with acetate was added (salt marsh free). Current was still zero until day 41, when current sharply increased to 57.9 A/m^2 and then oscillated between 48 to 50 A/m^2 until day 48. These values were even higher than after the first and second anolyte change. If the CE (see section II.3.1.3. is calculated between day 41 and 48 taking a current average value of 50 A/m^2 and also considering that from day 34 to day 41 no acetate was consumed as to be conservative in the calculation, CE value is of 500%. If all acetate (40 mM) was consumed starting at day 41 with a current density of 50 A/m^2, it would have taken 1.43 days to consume it, which does not explain the fact that current at 50 A/m^2 was sustained for 7 days. We do not have any concrete explanations but there may have been a problem with the connectors, an oxidation (corrosion) of a connector, a shift in the ITO potential due to the anolyte change (i.e. presence of oxygen). Moreover, we have not verified the evolution of the ITO potential in time in all the anolytes (with or without acetate, with or without salt marsh).

The average thickness of the EAB at day 30 was of 16.9±5.9 µm and 17.0±5.2 µm at day 48. The final thickness value was similar to the one obtained in the previous experiment at day 48 of 16.1±3.3 µm. By observing the trend in biofilm thickness values from day 0, it increased until day 30 and later the slope in the trend flattened. This means that when no source of electroactive microorganisms (inoculum) was added into the reactors, there was no increase in the biofilm mass. This may finally challenge some theories in which EABs grow on the electrodes in the manner of classical biofilms. It would seem here in our work that planktonic cells can perhaps also gradually associate and integrate EABs through the outer layers. This new hypothesis of growth "by external association" of additional planktonic cells really needs to be explored as it could put into question the current strategies developed by the scientific community for the optimization of the bioanode design. In a recent paper, the massive integration of planktonic bacteria in a model biofilm of *Bacillus* was mentioned (El-Khoury et al., 2021). This is not directly related to EABs but classical theories may be changing.

As there were no bacterial cells in the anolyte from day 30 until the end of the experiment, the stacks of images were not treated with MATLAB for this period.

VI.3.2.3. Test 6.4: Experience at 0.9 V/ITO

A final test was performed in a new microBES. In this experiment, the microelectrode was left at OCP for the first 24 hours and then it was constantly polarized at 0.9 V/ITO (0.4 V/SCE) for a total time of 73 days as seen in Figure VI-21 (A). The anolyte was changed at day 28. At day 47, the software that controlled the potentiostat reached a limit on the number of data acquisition and generated an error that resulted in the loss of data between days 28 to 47. For this period, however, a few additional trend points were added to the curve using a screen shot of the chronoamperometric graph that had been saved in the potentiostat software at the end of day 47 (see Annex Figure 6). Polarization, and data acquisition, were restarted until day 73. In addition, the thickness of the biofilm was also measured from the DIC microscope images, as observed in Figure VI-21 (B).

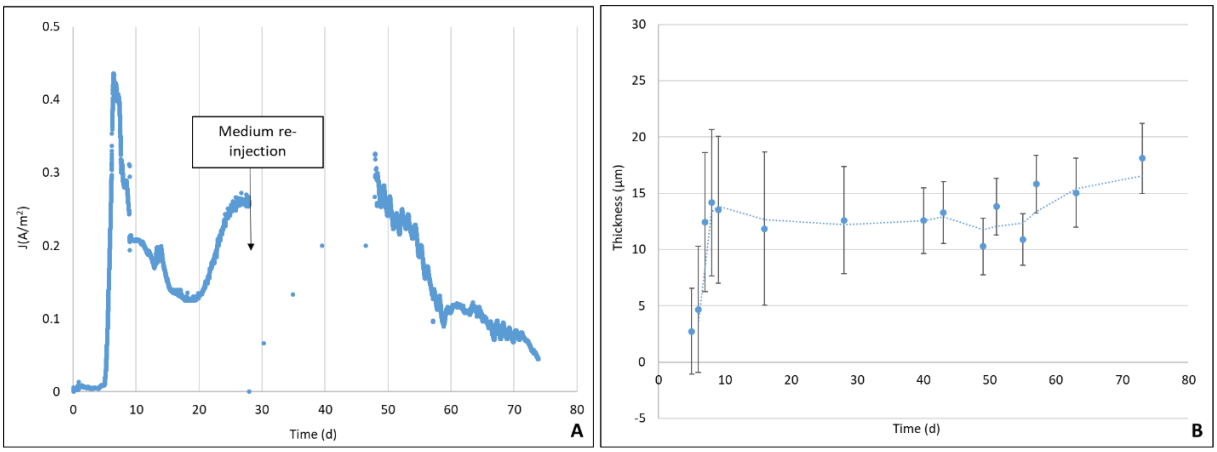

Figure VI-21 : (A) Evolution of the current density in time for the salt marsh EAB formed on the SS microelectrode of the microBES when polarized at 0.9 V/ITO. (B) Biofilm thickness values obtained from the DIC images at different days of the experiment.

As done in the previous experiments, the spatio-temporal stages of biofilm formation on the microelectrode were imaged simultaneously with the microelectrode polarization. The stages of EAB formation can be again here correlated with the electroactivity progressively expressed by the EAB. From day 0 to 5, no current was produced and the microelectrode surface had a clean appearance. However, later that day, current started to sharply increase and the first clusters of cells started to form on the microelectrode surface. In the time lapse videos generated from the image stacks (data not shown) a dense layer of highly mobile bacteria was present at day 5. Current kept on increasing until reaching J_{max} of 0.43 A/m^2 at day 7 where biofilm thickness increased up to 12.4±6.2 µm and a more homogeneous biofilm was formed on the SS microelectrode. Current then decreased until day 20 at a value of 0.13 A/m^2. Here, the presence or the absence of a clear layer where bacterial density and displacement was

higher was difficult to determine, since the presence of planktonic swimming bacteria in the anolyte remained stable throughout the time image stacks.

Anolyte was changed at day 28. As from day 28 to 43, the experiment kept on running while the laboratory was closed due to the summer holidays. In that period, as there was no human monitoring and control of the microscope, the images lost quality since the focus of the microscope shifted. For that reason, the images were not included for biofilm thickness measurement and they were not shown in Figure VI-22. Current started from zero on day 28, reaching a second maximum of 0.32 A/m^2 at day 48. After the second maximum, current started to decrease gradually until the experiment was stopped. In the time lapse videos from day 43 to 73, the bacterial density in the anolyte appeared lower that in the first 28 days (data not shown). The trend in biofilm thickness showed that it remained constant after day 28, with error bars decreasing in time (meaning that the biofilm morphology was less heterogeneous) until day 43 to a value of 13.3±2.8 μm. In the next measurements, the thickness values ranged between 10 and 13 μm. A thickness of 15.8±2.6 μm was registered at day 57 and a final biofilm thickness of 18.1±3.1 μm at day 73.

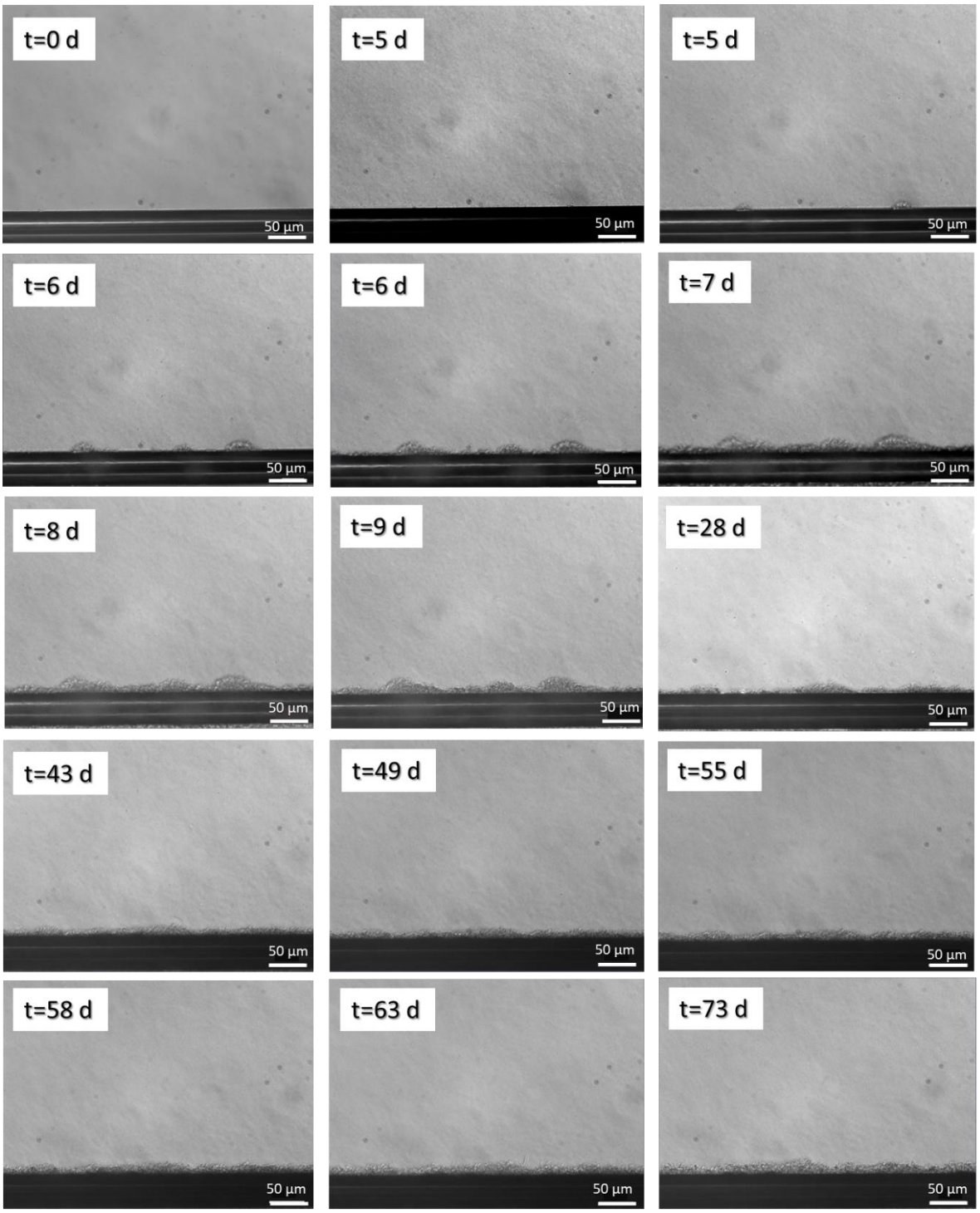

Figure VI-22 : DIC microscope images for the SS microelectrode-salt marsh EAB-anolyte interfaces when the microelectrode was polarized at 0.9 V/ITO.

For this experiment, it was not possible to treat the image stacks with the optical flow algorithms. The images obtained by DIC show a background relief, probably caused by the OSTEMER cross-linking when developing the microBES. This relief created zones of static objects, which led to non-convergent results when treating the stacks of images with MATLAB. The idea would have been to compare the displacement velocities of the bacterial cells with those of the previous experiment to find out whether

applying a higher potential to the SS microelectrode influenced the displacement velocity of the bacterial cells.

Comparing the values of J_{max} for Test 6.3 and Test 6.4, J_{max} was obtained at day 7 in both cases, yet J_{max} was higher for the microelectrode polarized at 0.6 V/ITO. However, the biofilm thickness was larger for the biofilm formed at 0.9 V/ITO: 12.4±6.2 µm against 9.2±4.6 µm for the EAB formed at 0.6 V/ITO. Current density seemed more stable for the bioanode at 0.9 V/ITO, since only one change in the anolyte was made and current was still being produced at day 73. However, as both tests were not executed at the same fed-batch conditions, it is difficult to make exact comparisons. All of this must demonstrate, as we see many differences in behaviour, that there is indeed an interest in observing locally how dense the layer of planktonic bacteria close to the bioanode evolves and behaves.

VI.4. Conclusions of chapter VI

The first part of this chapter (Part A) described the methodology step-by-step to obtain a microBES. First, a PDMS three-microelectrode microBES was developed, where Ag/AgCl microelectrodes were tested as a pseudo-reference. Since the stability in the potential of the Ag/AgCl microelectrodes was deteriorated after three days of being in direct contact with the anolyte containing salt marsh bacteria, it was decided to move into on to the design of a two-electrode microBES.

The final design of the microBES was a 0.3 mL OSTEMER two-electrode microfluidic cell with a SS microelectrode and an ITO glass electrode. This completely transparent microBES could be simultaneously coupled with a potentiostat for electroanalysis and to an optical microscope for in situ and real-time observation of the bacterial cells in the proximity and on the SS microelectrode. As to maintain the polarization potential of the SS microelectrode equivalent to 0.1 V/SCE in the two-electrode microBES, the latter can be polarized at 0.6 V/ITO with the condition that the microchannel was filled with an anolyte (Starkey medium + SMS + acetate) of at least 6 days old providing from a 550 mL reactor.

Once the construction of the OSTEMER two-electrode microBES has been both fluidic and electrochemically validated, experiments carried out in part B met the first objective to form a salt marsh EAB on the SS microelectrode of the microBES when polarized at 0.6 V/ITO. This was demonstrated at short (7 days) and at long polarization times (48 days). The application of electrochemical techniques (CA) was applied in simultaneous with the real-time observation of the interface between the SS microelectrode and the anolyte containing the salt marsh bacterial suspension using DIC microscopy.

The trend in salt marsh EAB electroactivity in micro BES was similar to what was observed for salt marsh EABs formed on SS microelectrodes in 550 mL reactors when acetate was added in pulses. First, a lag-phase followed by a sharp increase in current production until reaching J_{max} was followed by a gradual decrease in current that reached zero when acetate was depleted. The difference was in the J_{max}

values obtained. In macroBES J_{max} values were 10 times larger than in microBES. This was probably due to the very large difference in the anolyte volume, a very different acetate reservoir, a shift in the microbial population of the anolyte, and maybe also an effect of the confinement in the microchannel.

In order to study bacterial cell displacement and to observe in better detail the stages of EAB formation on the microelectrode, certain parameters of the optical microscope were set such as the x20 objective, the frequency (time between images) of 0.4 s and the total acquisition time of 1 minute. To treat the image stacks with optical flow algorithms, image subtraction for only obtaining the displacement of bacterial cells was sometimes done with the blank performed at the beginning of the experiment with distilled water, and in other cases, the sliding average concept was used. The velocity vector fields obtained in MATLAB showed the maximum velocity of the bacterial cells in the stack of images.

For the two experiments launched at 0.6 V/ITO and 0.9 V/ITO, only for the first one, it was possible to apply optical flow algorithms to the microscope image stacks at some strategic points during the first 15 days of polarization. Optical flow algorithms turned out to be a useful tool to put into numbers the phenomena observed under the microscope objective, allowing data transformation from qualitative to quantitative. The hypothesis that emerged from these results was that a dense layer of very mobile bacteria is present near the surface of the bioanode when current is produced. The question remains open whether this phenomenon is related to the polarization potential, whether it occurs in the presence of substrate, or what other factors may influence it.

From both experiments at 0.6 V/ITO and 0.9 V/ITO, it was possible to observe the spatio-temporal stages of biofilm formation, most likely the adhesion and growth phases. These observations allowed obtaining more insights of what occurs between stages I and II described in Research Article 2. What is clear is that biofilm microelectrode colonization goes in hand with the sharp increase in current up to $J_{max.}$

It was shown how microBES could be a useful tool to study the mechanisms of bacterial taxis, in this case of electrotaxis, when a potential was applied to the SS microelectrode. The advantages of using microfluidic devices for bacterial taxis have been already described in the literature (Li and Lin, 2011; Pérez-Rodríguez et al., 2022); however, as demonstrated throughout this chapter, the set-up to launch an experiment in the microBES and the post data processing requires several validation steps (i.e. construction of the microBES, proper microscope set-up, obtaining images with the appropriate quality, among others)

Conclusions

Throughout this thesis, the spatio-temporal evolution of multi-species EABs on microelectrodes was studied at different time scales and in two types of BES reactors with a difference volume size of three orders of magnitude. The correlation of the spatio-temporal dynamics of biofilm formation with their electrochemical performance had the objective of elucidating the processes of change that contribute with the gradual loss of its electroactivity.

State of the art in Chapter I described the possible causes or hypotheses for the limitations in the electroactivity of bioanodes and pointed out the methodological flaws in the approaches typically used to study the hypotheses put forward. In response, the advantages of using microelectrodes and microBES as tools to study multi-species EABs were thoroughly described. The access to biofilm-aggregated cells in the surface of the electrode and planktonic cells in the surroundings, the possibility of fine-tuning the anolyte conditions and the coupling with real-time analysis techniques showed the great potential of these technologies. Microelectrodes and microBES are useful to study mechanisms of multi-species EAB formation, bacterial taxis and bacterial interactions, EET mechanisms simultaneously with the evolution of the biofilm electroactivity.

Then, the manuscript was divided into two main sections according to the experimental set-up: i) experiments with a microelectrode as the working electrode in a macroBES and ii) experiments with a microelectrode as the working electrode in microBES.

In section i), the first milestone of this thesis was to form multi-species EABs on microelectrodes in a reproducible form and that their electroactivity is reproducible to that usually observed in macroelectrodes over a long period. These two conditions, successfully experimentally verified, have allowed the microelectrode to be adopted as a tool for the study of EAB. Results from Chapter III confirmed that SS microelectrodes (Ø=50µm) polarized at 0.1 V/SCE, an anolyte composition of SMS as the microbial inoculum, Starkey medium with 45 g/L of NaCl and 40 mM of acetate were the optimal experimental conditions. Salt marsh EABs on SS microelectrodes produced maximum current values of 10.00 ±0.50 A/m^2 when the microelectrode was constantly polarized for 55 days.

Once salt marsh EABs on microelectrodes proved to reproduce the expected electrochemical performance, hypotheses related to the gradual loss of electroactivity in bioanodes were tested. Results from Chapter IV showed that biofilm viability, EPS composition, microbial population and biofilm morphology evolved over time and were intrinsically related to the evolution of the EAB electroactivity. Maximum biofilm growth rate, high viability and high content of extracellular proteins in the EPS matrix promoted the increasing electroactivity from the early stages of biofilm colonization to the maximum peak of current production J_{max}. After the J_{max}, the loss of electroactivity became irreversible. A decrease in the biofilm growing rate, an accumulation of dead cells and an increase in the content of extracellular polysaccharides in the EPS matrix accompanied the gradual decrease in current to more than 50% of

J_{max}. In addition to the chemical, morphological and viability changes, the microbial community of the salt marsh EAB shifted from a majority of *Marinobacterium spp*. in the early stages to a predominance of *Desulfuromonas spp*. at the later stages, reflecting a microbial temporal evolution of the biofilm. As the chemical composition of the anolyte also evolved, this probably brought changes in the population at the planktonic level, which were then reflected at the biofilm level. Therefore, biofilm formation stages of most interest are those occurring between the early stages of EAB formation (start of stage I) and to when J_{max} is reached (end of stage II).

Despite the fact that the techniques applied were of a destructive nature (microscopy, cell staining, molecular biology), the importance of studying EABs with a temporal approach was highlighted. Furthermore, the use of microelectrodes was advantageous for the post-treatment of EABs. As mass transfer is enhanced in microelectrodes, a proper and rapid cell staining (especially for live dead cell viability assay) can be performed in preparation for epifluorescence microscopy and CLSM. In addition, their small size allowed microscopic observations without cross-cutting or other possible mechanical pre-working of the samples.

Additionally, the reliability of SMS as the inoculum source was also discussed. Batches of sediments collected at different seasons of the year, as well as the time between storage and inoculation in the laboratory were shown to introduce variability to the electroactivity and microbial population of EAB. Control over the microbial population and chemical composition of the inoculum batch would be advisable before usage.

Optimization of salt marsh EABs electroactivity was studied in Chapter V. Acetate at a concentration of 40 mM added regularly led to the biofilms that expressed the highest electroactivity. Butyrate also led to the formation of salt marsh EABs when it was used as a substrate; however, J_{max} was lower than for acetate. Glucose and formate were discarded as possible substrates for SMS. In addition, 0.1 V/SCE was the most suitable anode potential to polarize the SS microelectrodes. QS molecules did not improve the bioanode electroactivity in terms of current density values, but in some cases, the typical gradual decrease of the current to 50% of J_{max} was not observed at all.

In the experiments of Chapter V, extracellular proteins showed a positive correlation with salt marsh EABs electroactivity whereas extracellular polysaccharides showed a negative one, backing the results found in Chapter IV. This also supported the hypothesis that EPS conform a conductive network within the biofilm, where extracellular proteins seem to facilitate electron transfer between the biofilm and the anode, while polysaccharides seem to attenuate the electron path. The protocol upgrade for EPS confocal microscope image post-processing with MATLAB, together with the application of the ANOVA method, allowed the in-depth study of the EPS role in the biofilm electroactivity, something that to this day remains largely unexplored.

Section ii) was dedicated to experiments in microBES developed in Chapter 6. The first objective was to obtain a properly functioning microBES. The initial prototype of the PDMS three-microelectrode microBES was discarded since Ag and Ag/AgCl microelectrodes were not suitable as pseudo-reference microelectrodes. A 0.3 mL OSTEMER two-electrode transparent microBES with a SS microelectrode and an ITO glass constituted the final prototype. This microBES was positionable under the microscope objective where electrochemical techniques could be applied simultaneously.

Subsequently, salt marsh EABs were successfully formed on the SS microelectrode of the microBES at short (7 days) and long (48 days) polarization times. In addition, the trend in the salt marsh EABs electroactivity in microBES was similar to the one observed in macroBES when acetate was added in pulses but J_{max} values were 10 times lower. The hypotheses linked to the marked difference in J_{max} were due to the very large difference in the anolyte volume, a shift in the microbial population of the anolyte and also to a probable confinement effect in the microchannel. When the SS microelectrode was constantly polarized at 0.6 V/ITO (0.1 V/ITO) J_{max} was of 0.63 ± 0.11 A/m^2.

DIC microscopy allowed the real-time in situ imaging of planktonic bacterial cells in the anolyte and biofilm-aggregated cells on the surface of the SS microelectrode. Focusing in stages I and II of biofilm formation revealed that biofilm microelectrode colonization was consistent with the sharp current increase up to J_{max}. Implementation of optical flow algorithms for the post-processing of images suggested that a dense layer of very mobile bacteria is present near the bioanode surface when current is produced. This is an original result because for the first time to our knowledge it was possible to visualise in real time a phenomenon of bacterial electrotaxis in response to an electrode stimulus or the presence of an EAB. The presence of this dense layer of bacterial cells also opened up a new direction for biofilm growth by massive incorporation of planktonic cells.

To conclude, the research carried out in this thesis provides enough evidence that multi-species EABs can be studied at the microscale while exhibiting the same trend in electroactivity that at the macroscale. We hope to have sufficiently substantiated the hypotheses put forward as to show that the EAB is a constantly changing living system, therefore its study must definitively contemplate its spatio-temporal evolution, not only considering the biofilm-aggregated cells in the electrode surface but also considering planktonic cells in the bioanode surroundings.

The results of this thesis can also set the foundations for future research paths. The role of the EPS in the EAB electroactivity has been barely investigated until today, where most of the few studies are devoted to single-species EABs. To gain knowledge of the mechanisms behind EPS production in multi-species EABs may be the key to understanding how these biofilm-produced EPS either enhance or attenuate the electroactivity. Furthermore, focusing on the early stages of biofilm formation until current reaches its maximum, understanding how to control the phenomena that promotes current production and how to avoid the processes that subsequently adversely affect the biofilm electroactivity should be

a research priority to improve the long-term durability of bioanodes. The microBES platform results in an extremely useful tool for this purpose since it is not only limited to the work carried out in this thesis. The possibility of studying mutli-species EABs in the microscale opens up the field of investigation for complex natural or industrial media, i.e. soil sediments, marine sediments, wastewater or digester sludges.

The discovery of the active dense layer in the surroundings of the biofilm opens the research as to how the bacterial cells from the planktonic layer can be integrated to the biofilm and if they can exchange electrons with the biofilm bacterial cells, something that would change the already known mechanisms of biofilm formation and EET. In addition, polarizing the SS microelectrode at different potentials in the microBES and post-treatment of images with Optical Flow would allow to determine if the velocity of bacterial cells in the active dense layer is affected. It is important to highlight that the majority of the studies carried out in this work were done with a temporal approach rather with a spatial one. The use of Fluorescence in-situ hybridation (FISH) could be useful to confirm a spatial microbial stratification in the biofilm. This could determine if the observed shift in the biofilm microbial population from *Marinobacterium* to *Desulfuromonas* at the latest stages is occurring in the upper layers of the EAB.

Control and manipulation of other variables i.e. anolyte hydrodynamics and its composition (pH, substrate concentration, oxygen or any other molecule concentration), which allows the rapid creation of gradients in the bioanode surroundings, with the integration of real-time microscopic techniques could provide more hints that link the biofim dynamics with its electroactivity. For the study of EET mechanisms, it is possible to couple microBES with other techniques i.e. Raman spectroscopy as to determine the redox state of c-cytochromes of bacterial cells; however, the study of EET up to these days has been only performed for single species biofilms. On the other hand, the implementation and optimization of algorithms that determine bacterial movement, such as cell tracking or optical flow for post-image microscopic images, may still be a suitable alternative for investigating bacterial cells interactions with the electrode in the formation process of a multi-species EAB. Finally, we sincerely hope that this work as well as the perspectives contribute to continuing the investigation to develop more efficient and durable multi-species bioanodes in BES.

References

Adler, J., Shi, W., 1988. Galvanotaxis in bacteria.

Aghababaie, M., Farhadian, M., Jeihanipour, A., Biria, D., 2015. Effective factors on the performance of microbial fuel cells in wastewater treatment–a review. Environ. Technol. Rev. 4, 71–89. https://doi.org/10.1080/09593330.2015.1077896

Ahn, Y., Logan, B.E., 2010. Effectiveness of domestic wastewater treatment using microbial fuel cells at ambient and mesophilic temperatures. Bioresour. Technol. 101, 469–475. https://doi.org/10.1016/j.biortech.2009.07.039

AJ Torriero, A., 2019. Understanding the Differences between a Quasi-Reference Electrode and a Reference Electrode. Med. Anal. Chem. Int. J. 3, 2–4. https://doi.org/10.23880/macij-16000144

Alatraktchi, F.A.Z. a., Zhang, Y., Angelidaki, I., 2014. Nanomodification of the electrodes in microbial fuel cell: Impact of nanoparticle density on electricity production and microbial community. Appl. Energy 116, 216–222. https://doi.org/10.1016/j.apenergy.2013.11.058

Allen, R.M., Bennetto, H.P., 1993. Microbial fuel-cells - Electricity production from carbohydrates. Appl. Biochem. Biotechnol. 39–40, 27–40. https://doi.org/10.1007/BF02918975

Ape, F., Manini, E., Quero, G.M., Luna, G.M., Sarà, G., Vecchio, P., Brignoli, P., Ansferri, S., Mirto, S., 2019. Biostimulation of in situ microbial degradation processes in organically-enriched sediments mitigates the impact of aquaculture. Chemosphere 226, 715–725. https://doi.org/10.1016/j.chemosphere.2019.03.178

Askri, R., Erable, B., Neifar, M., Etcheverry, L., Masmoudi, A.S., Cherif, A., Chouchane, H., 2019. Understanding the cumulative effects of salinity, temperature and inoculation size for the design of optimal halothermotolerant bioanodes from hypersaline sediments. Bioelectrochemistry 129, 179–188. https://doi.org/10.1016/j.bioelechem.2019.05.015

Babauta, J.T., Nguyen, H.D., Beyenal, H., 2011. Redox and pH Microenvironments within Shewanella oneidensis MR-1 Biofilms Reveal an Electron Transfer Mechanism 6654–6660.

Babauta, J.T., Nguyen, H.D., Harrington, T.D., Renslow, R., Beyenal, H., 2013. pH, Redox Potential and Local Biofilm Potential Microenvironments Within Geobacter sulfurreducens Biofilms and Their Roles in Electron Transfer 109, 2651–2662. https://doi.org/10.1002/bit.24538.pH

Baudler, A., Schmidt, I., Langner, M., Greiner, A., Schröder, U., 2015. Does it have to be carbon? Metal anodes in microbial fuel cells and related bioelectrochemical systems. Energy Environ. Sci. 8, 2048–2055. https://doi.org/10.1039/c5ee00866b

Beule, L., Karlovsky, P., 2020. Improved normalization of species count data in ecology by scaling with ranked subsampling (SRS): Application to microbial communities. PeerJ 8. https://doi.org/10.7717/peerj.9593

Beyenal, H., Babauta, J.T., 2015. SYSTEMS BIOFILMS IN BIOELECTROCHEMICAL SYSTEMS From Laboratory Practice to Data.

Blanchet, E., Desmond, E., Erable, B., Bridier, A., Bouchez, T., Bergel, A., 2015. Comparison of synthetic medium and wastewater used as dilution medium to design scalable microbial anodes: Application to food waste treatment. Bioresour. Technol. 185, 106–115. https://doi.org/10.1016/j.biortech.2015.02.097

Blanchet, E., Erable, B., Solan, M. De, Bergel, A., 2016. Two-dimensional carbon cloth and three-dimensional carbon felt perform similarly to form bioanode fed with food waste 66, 38–41. https://doi.org/10.1016/j.elecom.2016.02.017

Blanchet, M.E., 2016. CONCEPTION D'UN PROCEDE D'ELECTROSYNTHESE MICROBIENNE.

Bolyen, E., Rideout, J.R., Dillon, M.R., Bokulich, N.A., Abnet, C.C., Al-Ghalith, G.A., Alexander, H., Alm, E.J., Arumugam, M., Asnicar, F., Bai, Y., Bisanz, J.E., Bittinger, K., Brejnrod, A., Brislawn, C.J., Brown, C.T., Callahan, B.J., Caraballo-Rodríguez, A.M., Chase, J., Cope, E.K., Da Silva, R., Diener, C., Dorrestein, P.C., Douglas, G.M., Durall, D.M., Duvallet, C., Edwardson, C.F., Ernst, M., Estaki, M., Fouquier, J., Gauglitz, J.M., Gibbons, S.M., Gibson, D.L., Gonzalez, A., Gorlick, K., Guo, J., Hillmann, B., Holmes, S., Holste, H., Huttenhower, C., Huttley, G.A., Janssen, S., Jarmusch, A.K., Jiang, L., Kaehler, B.D., Kang, K. Bin, Keefe, C.R., Keim, P., Kelley, S.T., Knights, D., Koester, I., Kosciolek, T., Kreps, J., Langille, M.G.I., Lee, J., Ley, R., Liu, Y.X., Loftfield, E., Lozupone, C., Maher, M., Marotz, C., Martin, B.D., McDonald, D., McIver, L.J., Melnik, A. V., Metcalf, J.L., Morgan, S.C., Morton, J.T., Naimey, A.T., Navas-Molina, J.A., Nothias, L.F., Orchanian, S.B., Pearson, T., Peoples, S.L., Petras, D., Preuss, M.L., Pruesse, E., Rasmussen, L.B., Rivers, A., Robeson, M.S., Rosenthal, P., Segata, N., Shaffer, M., Shiffer, A., Sinha, R., Song, S.J., Spear, J.R., Swafford, A.D., Thompson, L.R., Torres, P.J., Trinh, P., Tripathi, A., Turnbaugh, P.J., Ul-Hasan, S., van der Hooft, J.J.J., Vargas, F., Vázquez-Baeza, Y., Vogtmann, E., von Hippel, M., Walters, W., Wan, Y., Wang, M., Warren, J., Weber, K.C., Williamson, C.H.D., Willis, A.D., Xu, Z.Z., Zaneveld, J.R., Zhang, Y., Zhu, Q., Knight, R., Caporaso, J.G., 2019. Reproducible, interactive, scalable and extensible microbiome data science using QIIME 2. Nat. Biotechnol. 37, 852–857. https://doi.org/10.1038/s41587-019-0209-9

Bond, D.R., Holmes, D.E., Tender, L.M., Lovley, D.R., 2002. Electrode-reducing microorganisms that harvest energy from marine sediments. Science (80-.). 295, 483–485. https://doi.org/10.1126/science.1066771

Bond, D.R., Lovley, D.R., 2003. Electricity production by Geobacter sulfurreducens attached to electrodes. Appl. Environ. Microbiol. 69, 1548–1555. https://doi.org/10.1128/AEM.69.3.1548-1555.2003

Borole, A.P., Reguera, G., Ringeisen, B., Wang, Z.W., Feng, Y., Kim, B.H., 2011. Electroactive biofilms: Current status and future research needs. Energy Environ. Sci. 4, 4813–4834. https://doi.org/10.1039/c1ee02511b

Bourdakos, N., Marsili, E., Radhakrishnan, M., 2014. A defined co-culture of Geobacter sulfurreducens and Escherichia coli in a.pdf.

Busalmen, J.P., Esteve-Núñez, A., Berná, A., Feliu, J.M., 2008. C-type cytochromes wire electricity-producing bacteria to electrodes. Angew. Chemie - Int. Ed. 47, 4874–4877. https://doi.org/10.1002/anie.200801310

Cai, T., Zhang, Y., Wang, N., Zhang, Z., Lu, X., Zhen, G., 2022. Electrochemically active microorganisms sense charge transfer resistance for regulating biofilm electroactivity, spatio-temporal distribution, and catabolic pathway. Chem. Eng. J. 442, 136248. https://doi.org/10.1016/j.cej.2022.136248

Callahan, B.J., McMurdie, P.J., Rosen, M.J., Han, A.W., Johnson, A.J.A., Holmes, S.P., 2016. DADA2: High-resolution sample inference from Illumina amplicon data. Nat. Methods 13, 581–583. https://doi.org/10.1038/nmeth.3869

Cao, B., Shi, L., Brown, R.N., Xiong, Y., Fredrickson, J.K., Romine, M.F., Marshall, M.J., Lipton, M.S., Beyenal, H., 2011. Extracellular polymeric substances from Shewanella sp . HRCR-1 biofilms : characterization by infrared spectroscopy and proteomics 13, 1018–1031. https://doi.org/10.1111/j.1462-2920.2010.02407.x

Carmona-Martínez, A.A., Harnisch, F., Kuhlicke, U., Neu, T.R., Schröder, U., 2013. Electron transfer and biofilm formation of Shewanella putrefaciens as function of anode potential. Bioelectrochemistry 93, 23–29. https://doi.org/10.1016/j.bioelechem.2012.05.002

Cercado-Quezada, B., Delia, M.L., Bergel, A., 2011. Electrochemical micro-structuring of graphite felt electrodes for accelerated formation of electroactive biofilms on microbial anodes. Electrochem. commun. 13, 440–443. https://doi.org/10.1016/j.elecom.2011.02.015

Chabert, N., Amin Ali, O., Achouak, W., 2015. All ecosystems potentially host electrogenic bacteria. Bioelectrochemistry 106, 88–96. https://doi.org/10.1016/j.bioelechem.2015.07.004

Chadwick, G.L., Otero, F.J., Gralnick, J.A., Bond, D.R., Orphan, V.J., 2019. NanoSIMS imaging reveals metabolic stratification within current-producing biofilms. Proc. Natl. Acad. Sci. U. S. A. 116, 20716–20724. https://doi.org/10.1073/pnas.1912498116

Champigneux, P., Delia, M.L., Bergel, A., 2018. Impact of electrode micro- and nano-scale topography on the formation and performance of microbial electrodes. Biosens. Bioelectron. 118, 231–246. https://doi.org/10.1016/j.bios.2018.06.059

Chang, C.C., Chen, Y.C., Yu, C.P., 2022. Microbial community dynamics in electroactive biofilms across time under different applied anode potentials. Sustain. Environ. Res. 32. https://doi.org/10.1186/s42834-022-00128-9

Chen, M., Lee, D., Tay, J., 2007. Staining of extracellular polymeric substances and cells in bioaggregates 467–474. https://doi.org/10.1007/s00253-006-0816-5

Chen, S., Jing, X., Tang, J., Fang, Y., Zhou, S., 2017. Quorum sensing signals enhance the electrochemical activity and energy recovery of mixed-culture electroactive bio fi lms. Biosens. Bioelectron. 97, 369–376. https://doi.org/10.1016/j.bios.2017.06.024

Cho, E.J., Ellington, A.D., 2007. Optimization of the biological component of a bioelectrochemical cell. Bioelectrochemistry 70, 165–172. https://doi.org/10.1016/j.bioelechem.2006.03.031

Chong, P., 2018. Ingénierie électrochimique pour déchiffrer les mécanismes de formation des biofilms électroactifs. https://doi.org/10.13140/RG.2.2.18816.89609

Chong, P., Erable, B., Bergel, A., 2021. How bacteria use electric fields to reach surfaces 3. https://doi.org/10.1016/j.bioflm.2021.100048

Cordas, C.M., Guerra, L.T., Xavier, C., Moura, J.J.G., 2008. Electroactive biofilms of sulphate reducing bacteria. Electrochim. Acta 54, 29–34. https://doi.org/10.1016/j.electacta.2008.02.041

Córdova-Kreylos, A.L., Cao, Y., Green, P.G., Hwang, H.M., Kuivila, K.M., LaMontagne, M.G., Van De Werfhorst, L.C., Holden, P.A., Scow, K.M., 2006. Diversity, composition, and geographical distribution of microbial communities in California salt marsh sediments. Appl. Environ. Microbiol. 72, 3357–3366. https://doi.org/10.1128/AEM.72.5.3357-3366.2006

Costerton, J.W., 1999. Introduction to biofilm. Int. J. Antimicrob. Agents 11, 217–221. https://doi.org/10.1016/S0924-8579(99)00018-7

Davey, H.M., Hexley, P., 2011. Red but not dead ? Membranes of stressed Saccharomyces cerevisiae are permeable to propidium iodide 13, 163–171. https://doi.org/10.1111/j.1462-2920.2010.02317.x

Dennis, P.G., Virdis, B., Vanwonterghem, I., Hassan, A., Hugenholtz, P., Tyson, G.W., Rabaey, K., 2016. Anode potential influences the structure and function of anodic electrode and electrolyte-associated microbiomes. Sci. Rep. 6, 1–11. https://doi.org/10.1038/srep39114

Dong, Y., Sui, M., Wang, X., Zhang, P., Jiang, Y., Wu, J., 2021. Responses of electroactive biofilms to chronic chlorine exposure : Insights from the composition and spatial structure of extracellular polymeric substances. Bioelectrochemistry 142, 107894. https://doi.org/10.1016/j.bioelechem.2021.107894

Donlan, R.M., 2002. Biofilms: Microbial life on surfaces. Emerg. Infect. Dis. 8, 881–890. https://doi.org/10.3201/eid0809.020063

Dulon, S., Parot, S., Delia, M., Bergel, A., 2007. Electroactive biofilms : new means for electrochemistry 173–179. https://doi.org/10.1007/s10800-006-9250-8

Dumas, C., Basseguy, R., Bergel, A., 2008. Electrochemical activity of Geobacter sulfurreducens biofilms on stainless steel anodes. Electrochim. Acta 53, 5235–5241. https://doi.org/10.1016/j.electacta.2008.02.056

Eaktasang, N., Kang, C.S., Ryu, S.J., Suma, Y., Kim, H.S., 2013. Enhanced current production by electroactive biofilm of sulfate-reducing bacteria in the microbial fuel cell. Environ. Eng. Res. 18, 277–281. https://doi.org/10.4491/eer.2013.18.4.277

Edel, M., Sturm, G., Sturm-Richter, K., Wagner, M., Ducassou, J.N., Couté, Y., Horn, H., Gescher, J., 2021. Extracellular riboflavin induces anaerobic biofilm formation in Shewanella oneidensis. Biotechnol. Biofuels 14, 1–14. https://doi.org/10.1186/s13068-021-01981-3

El-Khoury, N., Bennaceur, I., Verplaetse, E., Aymerich, S., Lereclus, D., Kallassy, M., Gohar, M., 2021. Massive integration of planktonic cells within a developing biofilm. Microorganisms 9, 1–10. https://doi.org/10.3390/microorganisms9020298

Erable, B., Bergel, A., 2009. First air-tolerant effective stainless steel microbial anode obtained from a natural marine biofilm. Bioresour. Technol. 100, 3302–3307. https://doi.org/10.1016/j.biortech.2009.02.025

Erable, B., Duţeanua, N.M., Ghangrekar, M.M., Dumas, C., Scott, K., 2010. Application of electro-active biofilms. Biofouling 26, 57–71. https://doi.org/10.1080/08927010903161281

Erable, B., Roncato, M.-A., Achouak, W., Bergel, A., 2009. Sampling Natural Biofilms : A New Route to Build Efficient Microbial Anodes 43, 3194–3199.

Flayac, C., Trably, E., Bernet, N., 2018. Microbial anodic consortia fed with fermentable substrates in microbial electrolysis cells: Significance of microbial structures. Bioelectrochemistry 123, 219–226. https://doi.org/10.1016/j.bioelechem.2018.05.009

Flemming, H.C., Wingender, J., 2010. The biofilm matrix. Nat. Rev. Microbiol. 8, 623–633. https://doi.org/10.1038/nrmicro2415

Foladori, P., Bruni, L., Tamburini, S., Ziglio, G., 2010. Direct quantification of bacterial biomass in influent , effluent and activated sludge of wastewater treatment plants by using flow cytometry. Water Res. 44, 3807–3818. https://doi.org/10.1016/j.watres.2010.04.027

Forster, R.J., 1994. Microelectrodes : New Dimensions in Electrochemistry.

Freguia, S., Rabaey, K., 2008. Syntrophic Processes Drive the Conversion of Glucose in Microbial Fuel Cell Anodes 42, 7937–7943.

Gaffney, E.M., Simoska, O., Minteer, S.D., 2021. The Use of Electroactive Halophilic Bacteria for Improvements and Advancements in Environmental High Saline Biosensing. Biosensors 11. https://doi.org/10.3390/bios11020048

González-Muñoz, M., Dominguez-Benetton, X., Domínguez-Maldonado, J., Valdés-Lozano, D., Pacheco-Catalán, D., Ortega-Morales, O., Alzate-Gaviria, L., 2018. Polarization potential has no effect on maximum current density produced by halotolerant bioanodes. Energies 11, 1–13. https://doi.org/10.3390/en11030529

Grattieri, M., Minteer, S.D., 2020. Microbial fuel cells in saline and hypersaline environments : Advancements , challenges and future perspectives. Bioelectrochemistry 120, 127–137. https://doi.org/10.1016/j.bioelechem.2017.12.004

Guerrini, E., Grattieri, M., Trasatti, S.P., Bestetti, M., Cristiani, P., 2014. Performance explorations of single chamber microbial fuel cells by using various microelectrodes applied to biocathodes. Int. J. Hydrogen Energy 39, 21837–21846. https://doi.org/10.1016/j.ijhydene.2014.06.132

Guo, J., Yang, G., Zhuang, Z., Mai, Q., Zhuang, L., 2021. Redox potential-induced regulation of extracellular polymeric substances in an electroactive mixed community biofilm. Sci. Total

Environ. 797, 149207. https://doi.org/10.1016/j.scitotenv.2021.149207

Gupta, P., Sarkar, S., Das, B., Bhattacharjee, S., Tribedi, P., 2016. Biofilm, pathogenesis and prevention—a journey to break the wall: a review. Arch. Microbiol. 198, 1–15. https://doi.org/10.1007/s00203-015-1148-6

Harris, H.W., El-Naggarb, M.Y., Bretschgerc, O., Wardd, M.J., Rominee, M.F., Obraztsovad, A.Y., Nealson, K.H., 2010. Electrokinesis is a microbial behavior that requires extracellular electron transport. Proc. Natl. Acad. Sci. U. S. A. 107, 326–331. https://doi.org/10.1073/pnas.0907468107

Hoareau, M., Etcheverry, L., Erable, B., Bergel, A., 2021. Oxygen supply management to intensify wastewater treatment by a microbial electrochemical snorkel. Electrochim. Acta 394, 139103. https://doi.org/10.1016/j.electacta.2021.139103

Hu, Y., Wang, Y., Han, X., Shan, Y., Li, F., Shi, L., 2021. Biofilm Biology and Engineering of Geobacter and Shewanella spp . for Energy Applications 9, 1–13. https://doi.org/10.3389/fbioe.2021.786416

Ieropoulos, I.A., Greenman, J., Melhuish, C., Hart, J., 2005. Comparative study of three types of microbial fuel cell. Enzyme Microb. Technol. 37, 238–245. https://doi.org/10.1016/j.enzmictec.2005.03.006

Inoue, K., Leang, C., Franks, A.E., Woodard, T.L., Nevin, K.P., Lovley, D.R., 2011. Specific localization of the c -type cytochrome OmcZ at the anode surface in current-producing biofilms of Geobacter sulfurreducens 3, 211–217. https://doi.org/10.1111/j.1758-2229.2010.00210.x

Islam, M.A., Ethiraj, B., Cheng, C.K., Yousuf, A., Khan, M.M.R., 2017. Electrogenic and Antimethanogenic Properties of Bacillus cereus for Enhanced Power Generation in Anaerobic Sludge-Driven Microbial Fuel Cells. Energy and Fuels 31, 6132–6139. https://doi.org/10.1021/acs.energyfuels.7b00434

Jamal, M., Ahmad, W., Andleeb, S., Jalil, F., Imran, M., Nawaz, M.A., Hussain, T., Ali, M., Rafiq, M., Kamil, M.A., 2018. Bacterial biofilm and associated infections. J. Chinese Med. Assoc. 81, 7–11. https://doi.org/10.1016/j.jcma.2017.07.012

Jing, X., Liu, X., Deng, C., Chen, S., Zhou, S., 2019. Chemical signals stimulate Geobacter soli biofilm formation and electroactivity. Biosens. Bioelectron. 127, 1–9. https://doi.org/10.1016/j.bios.2018.11.051

Jung, S., Lee, J., Park, Y., Kwon, E.E., 2020. Bioelectrochemical systems for a circular bioeconomy. Bioresour. Technol. 300, 122748. https://doi.org/10.1016/j.biortech.2020.122748

Kan, J., Hsu, L., Cheung, A.C.M., Pirbazari, M., Nealson, K.H., 2011. Current production by bacterial communities in microbial fuel cells enriched from wastewater sludge with different electron donors. Environ. Sci. Technol. 45, 1139–1146. https://doi.org/10.1021/es102645v

Karygianni, L., Ren, Z., Koo, H., Thurnheer, T., 2020. Biofilm Matrixome: Extracellular Components in Structured Microbial Communities. Trends Microbiol. 28, 668–681. https://doi.org/10.1016/j.tim.2020.03.016

Katoh, K., Standley, D.M., 2013. MAFFT multiple sequence alignment software version 7: Improvements in performance and usability. Mol. Biol. Evol. 30, 772–780. https://doi.org/10.1093/molbev/mst010

Ketep, S.F., Bergel, A., Calmet, A., Erable, B., 2014. Stainless steel foam increases the current produced by microbial bioanodes in bioelectrochemical systems. Energy Environ. Sci. 7, 1633–1637. https://doi.org/10.1039/c3ee44114h

Ki, D., Popat, S.C., Rittmann, B.E., Torres, C.I., 2017. H2O2 Production in Microbial Electrochemical Cells Fed with Primary Sludge. Environ. Sci. Technol. 51, 6139–6145.

https://doi.org/10.1021/acs.est.7b00174

Kiely, P.D., Regan, J.M., Logan, B.E., 2011. The electric picnic : synergistic requirements for exoelectrogenic microbial communities. Curr. Opin. Biotechnol. 22, 378–385. https://doi.org/10.1016/j.copbio.2011.03.003

Kim, B.H., Ikeda, T., Park, H.S., Kim, H.J., Hyun, M.S., Kano, K., Takagi, K., Tatsumi, H., 1999. Electrochemical activity of an Fe (III) -reducing bacterium , Shewanella putrefaciens IR-1 , in the presence of alternative electron acceptors 200, 475–478.

Kim, B.J., Chu, I., Jusuf, S., Kuo, T., TerAvest, M.A., Angenent, L.T., Wu, M., 2016. Oxygen tension and riboflavin gradients cooperatively regulate the migration of Shewanella oneidensis MR-1 revealed by a hydrogel-based microfluidic device. Front. Microbiol. 7, 1–12. https://doi.org/10.3389/fmicb.2016.01438

Kirchho, C., Cypionka, H., 2017. Propidium ion enters viable cells with high membrane potential during live- dead staining 142, 79–82. https://doi.org/10.1016/j.mimet.2017.09.011

Kitayama, M., Koga, R., Kasai, T., Kouzuma, A., Watanabe, K., 2017. Structures, compositions, and activities of live Shewanella biofilms formed on graphite electrodes in electrochemical flow cells. Appl. Environ. Microbiol. 83. https://doi.org/10.1128/AEM.00903-17

Koch, C., Harnisch, F., 2016. Is there a Specific Ecological Niche for Electroactive Microorganisms ? 1282–1295. https://doi.org/10.1002/celc.201600079

Koretsky, C.M., Moore, C., Meile, C., Dichristina, T., Van Cappellen, P., 2002. Seasonal oscillations in microbial iron and sulfate reduction in saltmarsh sediments. Geochim. Cosmochim. Acta 66, A411–A411.

Lee, H.S., Parameswaran, P., Kato-Marcus, A., Torres, C.I., Rittmann, B.E., 2008. Evaluation of energy-conversion efficiencies in microbial fuel cells (MFCs) utilizing fermentable and non-fermentable substrates. Water Res. 42, 1501–1510. https://doi.org/10.1016/j.watres.2007.10.036

Leicester, D., Amezaga, J., Heidrich, E., 2020. Is bioelectrochemical energy production from wastewater a reality? Identifying and standardising the progress made in scaling up microbial electrolysis cells. Renew. Sustain. Energy Rev. 133, 110279. https://doi.org/10.1016/j.rser.2020.110279

Lewandowski, Z., Beyenal, H., 2013. Fundamentals of biofilm research.

Li, J., Lin, F., 2011. Microfluidic devices for studying chemotaxis and electrotaxis. Trends Cell Biol. 21, 489–497. https://doi.org/10.1016/j.tcb.2011.05.002

Li, L.H., Sun, Y.M., Yuan, Z.H., Kong, X.Y., Li, Y., 2013. Effect of temperature change on power generation of microbial fuel cell. Environ. Technol. (United Kingdom) 34, 1929–1934. https://doi.org/10.1080/09593330.2013.828101

Li, R., Tiedje, J.M., Chiu, C., Worden, R.M., 2012. Soluble Electron Shuttles Can Mediate Energy Taxis toward Insoluble Electron Acceptors.

Li, S.W., Sheng, G.P., Cheng, Y.Y., Yu, H.Q., 2016. Redox properties of extracellular polymeric substances (EPS) from electroactive bacteria. Sci. Rep. 6, 1–7. https://doi.org/10.1038/srep39098

Li, T., Zhou, Q., Zhou, L., Yan, Y., Liao, C., Wan, L., An, J., Li, N., Wang, X., 2020. Acetate limitation selects Geobacter from mixed inoculum and reduces polysaccharide in electroactive biofilm. Water Res. 177, 115776. https://doi.org/10.1016/j.watres.2020.115776

Liu, W., Wu, Y., 2021. Simultaneous nitrification, denitrification and electricity recovery of Halomonas strains in single chamber microbial fuel cells for seawater sewage treatment. J. Environ. Chem. Eng. 9, 106761. https://doi.org/10.1016/j.jece.2021.106761

Liu, Y., Deng, D., Lan, X., 2015. A highly Efficient mixed-culture biofilm as anodic catalyst and insights

into its enhancement through electrochemistry by comparison with G. sulfurreducens. Electrochim. Acta 155, 327–334. https://doi.org/10.1016/j.electacta.2014.12.152

Liu, Y., Harnisch, F., Fricke, K., Schröder, U., Climent, V., Feliu, J.M., 2010a. The study of electrochemically active microbial biofilms on different carbon-based anode materials in microbial fuel cells. Biosens. Bioelectron. 25, 2167–2171. https://doi.org/10.1016/j.bios.2010.01.016

Liu, Y., Harnisch, F., Fricke, K., Sietmann, R., Schröder, U., 2008. Improvement of the anodic bioelectrocatalytic activity of mixed culture biofilms by a simple consecutive electrochemical selection procedure. Biosens. Bioelectron. 24, 1006–1011. https://doi.org/10.1016/j.bios.2008.08.001

Liu, Y., Kim, H., Bond, D.R., 2010b. Gold line array electrodes increase substrate affinity and current density of electricity-producing G . sulfurreducens biofilms 1782–1788. https://doi.org/10.1039/c0ee00242a

Liu, Z., Zhou, A., Wang, S., Cheng, S., Yin, X., Yue, X., 2021. Quorum sensing shaped microbial consortia and enhanced hydrogen recovery from waste activated sludge electro-fermentation on basis of free nitrous acid treatment. Sci. Total Environ. 766, 144348. https://doi.org/10.1016/j.scitotenv.2020.144348

Llamas, I., Quesada, E., Martínez-Cánovas, M.J., Gronquist, M., Eberhard, A., González, J.E., 2005. Quorum sensing in halophilic bacteria: Detection of N-acyl-homoserine lactones in the exopolysaccharide-producing species of Halomonas. Extremophiles 9, 333–341. https://doi.org/10.1007/s00792-005-0448-1

Logan, B., Watson, V., Estadt, G., 2007. Graphite Fiber Brush Anodes for Increased Power Production in Air-Cathode Microbial Fuel Cells 41, 3341–3346.

Logan, B.E., Rossi, R., 2019. Electroactive microorganisms in bioelectrochemical systems 1. https://doi.org/10.1038/s41579-019-0173-x

Mann, A.J., Hahnke, R.L., Huang, S., Werner, J., Xing, P., Barbeyron, T., Huettel, B., Stüber, K., Reinhardt, R., Harder, J., Glöckner, F.O., Amann, R.I., Teeling, H., 2013. The genome of the alga-associated marine flavobacterium Formosa agariphila KMM 3901T reveals a broad potential for degradation of algal polysaccharides. Appl. Environ. Microbiol. 79, 6813–6822. https://doi.org/10.1128/AEM.01937-13

Marsili, E., Baron, D.B., Shikhare, I.D., Coursolle, D., Gralnick, J.A., Bond, D.R., 2008. Shewanella secretes flavins that mediate extracellular electron transfer. Proc. Natl. Acad. Sci. U. S. A. 105, 3968–3973. https://doi.org/10.1073/pnas.0710525105

McDonald, D., Price, M.N., Goodrich, J., Nawrocki, E.P., Desantis, T.Z., Probst, A., Andersen, G.L., Knight, R., Hugenholtz, P., 2012. An improved Greengenes taxonomy with explicit ranks for ecological and evolutionary analyses of bacteria and archaea. ISME J. 6, 610–618. https://doi.org/10.1038/ismej.2011.139

Michie, I.S., Kim, J.R., Dinsdale, R.M., Guwy, A.J., Premier, G.C., 2011. The influence of psychrophilic and mesophilic start-up temperature on microbial fuel cell system performance. Energy Environ. Sci. 4, 1011–1019. https://doi.org/10.1039/c0ee00483a

Mier, A.A., Olvera-Vargas, H., Mejía-López, M., Longoria, A., Verea, L., Sebastian, P.J., Arias, D.M., 2021. A review of recent advances in electrode materials for emerging bioelectrochemical systems: From biofilm-bearing anodes to specialized cathodes. Chemosphere 283. https://doi.org/10.1016/j.chemosphere.2021.131138

Min, X., Yu, K., Selvam, A., Wong, J.W.C., 2013. Bioelectricity production from acidic food waste leachate using microbial fuel cells : Effect of microbial inocula. Process Biochem. 48, 283–288. https://doi.org/10.1016/j.procbio.2012.10.001

Monzon, O., Yang, Y., Li, Q., Alvarez, P.J.J., 2016. Quorum sensing autoinducers enhance biofilm formation and power production in a hypersaline microbial fuel cell. Biochem. Eng. J. 109, 222–227. https://doi.org/10.1016/j.bej.2016.01.023

Nevin, K.P., Richter, H., Covalla, S.F., Johnson, J.P., Woodard, T.L., Orloff, A.L., Jia, H., Zhang, M., Lovley, D.R., 2008. Power output and columbic efficiencies from biofilms of Geobacter sulfurreducens comparable to mixed community microbial fuel cells. Environ. Microbiol. 10, 2505–2514. https://doi.org/10.1111/j.1462-2920.2008.01675.x

Ni, G., Christel, S., Roman, P., Wong, Z.L., Bijmans, M.F.M., Dopson, M., 2016. Electricity generation from an inorganic sulfur compound containing mining wastewater by acidophilic microorganisms. Res. Microbiol. 167, 568–575. https://doi.org/10.1016/j.resmic.2016.04.010

Oliot, M., Bergel, A., Délia, M.-L., 2017a. Bio-ingénierie pour les piles à combustible microbiennes.

Oliot, M., Chong, P., Erable, B., Bergel, A., 2017b. Influence of the electrode size on microbial anode performance. Chem. Eng. J. 327, 218–227. https://doi.org/10.1016/j.cej.2017.06.044

Oliot, M., Erable, B., Solan, M. De, Bergel, A., 2017c. Increasing the temperature is a relevant strategy to form microbial anodes intended to work at room temperature.

Oren, A., 2008. Microbial life at high salt concentrations: Phylogenetic and metabolic diversity. Saline Systems. https://doi.org/10.1186/1746-1448-4-2

Pandey, P., Shinde, V.N., Deopurkar, R.L., Kale, S.P., Patil, S.A., Pant, D., 2016. Recent advances in the use of different substrates in microbial fuel cells toward wastewater treatment and simultaneous energy recovery. Appl. Energy 168, 706–723. https://doi.org/10.1016/j.apenergy.2016.01.056

Pant, D., Bogaert, G. Van, Diels, L., Vanbroekhoven, K., 2010. A review of the substrates used in microbial fuel cells (MFCs) for sustainable energy production. Bioresour. Technol. 101, 1533–1543. https://doi.org/10.1016/j.biortech.2009.10.017

Paquete, C.M., Rosenbaum, M.A., Bañeras, L., Rotaru, A.E., Puig, S., 2022. Let's chat: Communication between electroactive microorganisms. Bioresour. Technol. 347. https://doi.org/10.1016/j.biortech.2022.126705

Parameswaran, P., Bry, T., Popat, S.C., Lusk, B.G., Rittmann, B.E., Torres, C.I., 2013. Kinetic, electrochemical, and microscopic characterization of the thermophilic, anode-respiring bacterium Thermincola ferriacetica. Environ. Sci. Technol. 47, 4934–4940. https://doi.org/10.1021/es400321c

Park, D.H., Laivenieks, M., Guettler, M. V, Jain, M.K., 1999. Microbial Utilization of Electrically Reduced Neutral Red as the Sole Electron Donor for Growth and Metabolite Production 65, 2912–2917.

Pepè Sciarria, T., Arioli, S., Gargari, G., Mora, D., Adani, F., 2019. Monitoring microbial communities' dynamics during the start-up of microbial fuel cells by high-throughput screening techniques. Biotechnol. Reports 21, e00310. https://doi.org/10.1016/j.btre.2019.e00310

Pérez-Rodríguez, S., García-Aznar, J.M., Gonzalo-Asensio, J., 2022. Microfluidic devices for studying bacterial taxis, drug testing and biofilm formation. Microb. Biotechnol. 15, 395–414. https://doi.org/10.1111/1751-7915.13775

Pfennig, N., Biebl, H., 1976. Desulfuromonas acetoxidans gen. nov. and sp. nov., a new anaerobic, sulfur-reducing, acetate-oxidizing bacterium. Arch. Microbiol. 110, 3–12. https://doi.org/10.1007/BF00416962

Pierra, M., Carmona-martínez, A.A., Trably, E., Godon, J., Bernet, N., 2015. Specific and efficient electrochemical selection of Geoalkalibacter subterraneus and Desulfuromonas acetoxidans in high current-producing biofilms 106, 221–225. https://doi.org/10.1016/j.bioelechem.2015.02.003

Pinck, S., Ostormujof, L.M., Teychené, S., Erable, B., 2020. Microfluidic Microbial Bioelectrochemical Systems : An Integrated Investigation Platform for a More Fundamental Understanding of Electroactive Bacterial Biofilms 1–23. https://doi.org/10.3390/microorganisms8111841

Pinto, D., Coradin, T., Laberty-Robert, C., 2018. Effect of anode polarization on biofilm formation and electron transfer in Shewanella oneidensis/graphite felt microbial fuel cells. Bioelectrochemistry 120, 1–9. https://doi.org/10.1016/j.bioelechem.2017.10.008

Pletcher, D., 1991. Why microelectrodes ? 3–16.

Pocaznoi, D., 2012. Optimisation d'anodes microbiennes à partir de lixiviat de sol pour la conception de piles à combustible microbiennes.

Pocaznoi, D., Calmet, A., Etcheverry, L., Erable, B., Bergel, A., 2012a. Stainless steel is a promising electrode material for anodes of microbial fuel cells. Energy Environ. Sci. 5, 9645–9652. https://doi.org/10.1039/c2ee22429a

Pocaznoi, D., Erable, B., Delia, M.L., Bergel, A., 2012b. Ultra microelectrodes increase the current density provided by electroactive biofilms by improving their electron transport ability. Energy Environ. Sci. 5, 5287–5296. https://doi.org/10.1039/c1ee01469b

Pocaznoi, D., Erable, B., Etcheverry, L., Delia, M., Bergel, A., 2012c. Forming microbial anodes under delayed polarisation modifies the electron transfer network and decreases the polarisation time required. Bioresour. Technol. 114, 334–341. https://doi.org/10.1016/j.biortech.2012.03.042

Pocaznoi, D., Erable, B., Etcheverry, L., Delia, M.L., Bergel, A., 2012d. Towards an engineering-oriented strategy for building microbial anodes for microbial fuel cells. Phys. Chem. Chem. Phys. 14, 13332–13343. https://doi.org/10.1039/c2cp42571h

Poehere Chong, Erable, B., Bergel, A., 2018. Microbial anodes: What actually occurs inside pores? 24–26.

Price, M.N., Dehal, P.S., Arkin, A.P., 2009. Fasttree: Computing large minimum evolution trees with profiles instead of a distance matrix. Mol. Biol. Evol. 26, 1641–1650. https://doi.org/10.1093/molbev/msp077

Rahimnejad, M., Najafpour, G., Ghoreyshi, A.A., Shakeri, M., 2011. Methylene blue as electron promoters in microbial fuel cell. https://doi.org/10.1016/j.ijhydene.2011.07.059

Ramírez-Vargas, C.A., Prado, A., Arias, C.A., Carvalho, P.N., Esteve-Núñez, A., Brix, H., 2018. Microbial electrochemical technologies for wastewater treatment: Principles and evolution from microbial fuel cells to bioelectrochemical-based constructed wetlands. Water (Switzerland) 10, 1–29. https://doi.org/10.3390/w10091128

Ranjan, B., Sim, J., Ryu, H., Ren, H., Santo, J.W., Chae, J., Lee, H., 2017. Microbial activity influences electrical conductivity of biofilm anode. Water Res. 127, 230–238. https://doi.org/10.1016/j.watres.2017.10.028

Read, S.T., Dutta, P., Bond, P.L., Keller, J., Rabaey, K., 2010. Initial development and structure of biofilms on microbial fuel cell anodes. BMC Microbiol. 10. https://doi.org/10.1186/1471-2180-10-98

Reguera, G., McCarthy, K.D., Mehta, T., Nicoll, J.S., Tuominen, M.T., Lovley, D.R., 2005. Extracellular electron transfer via microbial nanowires. Nature 435, 1098–1101. https://doi.org/10.1038/nature03661

Reguera, G., Nevin, K.P., Nicoll, J.S., Covalla, S.F., Woodard, T.L., Lovley, D.R., 2006. Biofilm and nanowire production leads to increased current in Geobacter sulfurreducens fuel cells. Appl. Environ. Microbiol. 72, 7345–7348. https://doi.org/10.1128/AEM.01444-06

Renslow, R., Babauta, J.T., Dohnalkova, A.C., Boyanov, M.I., Kemmer, K.M., Majors, P.D.,

Fredrickson, J.K., Beyenal, H., 2013. Metabolic spatial variability in electrode-respiring Geobacter Sulfurreducens biofilms. Bone 23, 1–7. https://doi.org/10.1039/C3EE40203G.METABOLIC

Rimboud, M., Etcheverry, L., Barakat, M., Achouak, W., Bergel, A., 2021. Hypersaline microbial fuel cell equipped with an oxygen-reducing microbial cathode 337. https://doi.org/10.1016/j.biortech.2021.125448

Rimboud, M., Pocaznoi, D., Erable, B., Bergel, A., 2014. Electroanalysis of microbial anodes for bioelectrochemical systems: Basics, progress and perspectives. Phys. Chem. Chem. Phys. 16, 16349–16366. https://doi.org/10.1039/c4cp01698j

Rollefson, J.B., Stephen, C.S., Tien, M., Bond, D.R., 2011. Identification of an extracellular polysaccharide network essential for cytochrome anchoring and biofilm formation in Geobacter sulfurreducens. J. Bacteriol. 193, 1023–1033. https://doi.org/10.1128/JB.01092-10

Roubaud, E., Lacroix, R., Da Silva, S., Bergel, A., Basséguy, R., Erable, B., 2018. Catalysis of the hydrogen evolution reaction by hydrogen carbonate to decrease the voltage of microbial electrolysis cell fed with domestic wastewater. Electrochim. Acta 275, 32–39. https://doi.org/10.1016/j.electacta.2018.04.135

Roubaud, E., Lacroix, R., Da Silva, S., Etcheverry, L., Bergel, A., Basséguy, R., Erable, B., 2019. Benchmarking of Industrial Synthetic Graphite Grades, Carbon Felt, and Carbon Cloth as Cost-Efficient Bioanode Materials for Domestic Wastewater Fed Microbial Electrolysis Cells. Front. Energy Res. 7. https://doi.org/10.3389/fenrg.2019.00106

Rousseau, R., 2016. Halotolerant bioanodes The applied potential modulates the electrochemical characteristics, the biofilm structure and the ratio of the two dominant genera.

Rousseau, R., 2013. Production de biohydrogène par électro-catalyse microbienne 208.

Rousseau, R., Dominguez-Benetton, X., Délia, M.L., Bergel, A., 2013. Microbial bioanodes with high salinity tolerance for microbial fuel cells and microbial electrolysis cells. Electrochem. commun. 33, 1–4. https://doi.org/10.1016/j.elecom.2013.04.002

Rousseau, R., Santaella, C., Achouak, W., Godon, J.J., Bonnafous, A., Bergel, A., Délia, M.L., 2014. Correlation of the Electrochemical Kinetics of High-Salinity-Tolerant Bioanodes with the Structure and Microbial Composition of the Biofilm. ChemElectroChem 1, 1966–1975. https://doi.org/10.1002/celc.201402153

Saidi, N., Erable, B., Saadaoui, S., Driouech, R., Zaouak, A., Jelassi, H., Neifar, M., Masmoudi, A.S., Cherif, A., Chouchane, H., 2022. Tunisian hypersaline sediments to set up suitable halotolerant microbial bioanodes for electrostimulated biodegradation of thiabendazole. Front. Energy Res. 10. https://doi.org/10.3389/fenrg.2022.981802

Salvatore, D., Bragato, C., 2014. From Macroelectrodes to Microelectrodes: Theory and Electrode Properties.

Santoro, C., Arbizzani, C., Erable, B., Ieropoulos, I., 2017. Microbial fuel cells: From fundamentals to applications. A review. J. Power Sources 356, 225–244. https://doi.org/10.1016/j.jpowsour.2017.03.109

Santoro, C., Babanova, S., Cristiani, P., Artyushkova, K., 2021. How Comparable are Microbial Electrochemical Systems around the Globe ? An Electrochemical and Microbiological Cross-Laboratory Study 14.

Schaetzle, O., Barrière, F., Baronian, K., 2008. Bacteria and yeasts as catalysts in microbial fuel cells: Electron transfer from micro-organisms to electrodes for green electricity. Energy Environ. Sci. 1, 607–620. https://doi.org/10.1039/b810642h

Schrott, G.D., Ordoñez, M.V., Robuschi, L., Busalmen, J.P., 2014. Physiological stratification in

electricity-producing biofilms of geobacter sulfurreducens. ChemSusChem 7, 598–603. https://doi.org/10.1002/cssc.201300605

Schweinitzer, T., Josenhans, C., 2010. Bacterial energy taxis : a global strategy ? 507–520. https://doi.org/10.1007/s00203-010-0575-7

Shah, S.T.H., Xuezhi, X., 2021. Traditional and modern strategies for optical flow: an investigation. SN Appl. Sci. 3, 1–14. https://doi.org/10.1007/s42452-021-04227-x

Shahid, K., Lakshmi, D., Haapasaari, S., 2021. Stainless steel and carbon brushes as high-performance anodes for energy production and nutrient recovery using the microbial nutrient recovery system 233. https://doi.org/10.1016/j.energy.2021.121213

Shen, H.B., Yong, X.Y., Chen, Y.L., Liao, Z.H., Si, R.W., Zhou, J., Wang, S.Y., Yong, Y.C., OuYang, P.K., Zheng, T., 2014. Enhanced bioelectricity generation by improving pyocyanin production and membrane permeability through sophorolipid addition in pseudomonas aeruginosa-inoculated microbial fuel cells. Bioresour. Technol. 167, 490–494. https://doi.org/10.1016/j.biortech.2014.05.093

Sheng, G.P., Yu, H.Q., Li, X.Y., 2010. Extracellular polymeric substances (EPS) of microbial aggregates in biological wastewater treatment systems: A review. Biotechnol. Adv. 28, 882–894. https://doi.org/10.1016/j.biotechadv.2010.08.001

Shi, W., Stocker, B.A.D., Adler, J., 1996. Effect of the surface composition of motile Escherichia coli and motile Salmonella species on the direction of galvanotaxis. J. Bacteriol. 178, 1113–1119. https://doi.org/10.1128/jb.178.4.1113-1119.1996

Sleutels, T.H.J.A., Darus, L., Hamelers, H.V.M., Buisman, C.J.N., 2011. Effect of operational parameters on Coulombic efficiency in bioelectrochemical systems. Bioresour. Technol. 102, 11172–11176. https://doi.org/10.1016/j.biortech.2011.09.078

Speers, A.M., Reguera, G., 2012. Electron donors supporting growth and electroactivity of geobacter sulfurreducens anode biofilms. Appl. Environ. Microbiol. 78, 437–444. https://doi.org/10.1128/AEM.06782-11

Steidl, R.J., Lampa-Pastirk, S., Reguera, G., 2016. Mechanistic stratification in electroactive biofilms of Geobacter sulfurreducens mediated by pilus nanowires. Nat. Commun. 7. https://doi.org/10.1038/ncomms12217

Stiefel, P., Schmidt-Emrich, S., Maniura-Weber, K., Ren, Q., 2015. Critical aspects of using bacterial cell viability assays with the fluorophores SYTO9 and propidium iodide. BMC Microbiol. 15, 1–9. https://doi.org/10.1186/s12866-015-0376-x

Sun, D., Chen, J., Huang, H., Liu, W., Ye, Y., Cheng, S., 2016. The effect of biofilm thickness on electrochemical activity of Geobacter sulfurreducens. Int. J. Hydrogen Energy 41, 16523–16528. https://doi.org/10.1016/j.ijhydene.2016.04.163

Sun, D., Cheng, S., Wang, A., Li, F., Logan, B.E., Cen, K., 2015. Temporal-spatial changes in viabilities and electrochemical properties of anode biofilms. Environ. Sci. Technol. 49, 5227–5235. https://doi.org/10.1021/acs.est.5b00175

Sun, D., Cheng, S., Zhang, F., Logan, B.E., 2017. Current density reversibly alters metabolic spatial structure of exoelectrogenic anode biofilms. J. Power Sources 356, 566–571. https://doi.org/10.1016/j.jpowsour.2016.11.115

Sun, D., Roth, S., Black, M., 2010. Secrets of Optical Flow Estimation and Their Principles Optical flow : motion of image pixels. Cvpr 2432–2439.

Sutherland, I.W., 2001. Biofilm exopolysaccharides: a strong and sticky framework. Microbiology 147, 3–9.

Tan, W.H., Chong, S., Fang, H.W., Pan, K.L., Mohamad, M., Lim, J.W., Tiong, T.J., Chan, Y.J., Huang, C.M., Yang, T.C.K., 2021. Microbial fuel cell technology—a critical review on scale-up issues. Processes 9, 1–13. https://doi.org/10.3390/pr9060985

Tapia-Tussell, R., Valle-Gough, R.E., Peraza-Baeza, I., Domínguez-Maldonado, J., Gonzalez-Muñoz, M., Cortes-Velazquez, A., Leal-Baustista, R.M., Alzate-Gaviria, L., 2019. Influence of two polarization potentials on a bioanode microbial community isolated from a hypersaline coastal lagoon of the Yucatan peninsula, in México. Sci. Total Environ. 681, 258–266. https://doi.org/10.1016/j.scitotenv.2019.05.120

Tejedor-Sanz, S., Fernández-Labrador, P., Hart, S., Torres, C.I., Esteve-Núñez, A., 2018. Geobacter dominates the inner layers of a stratified biofilm on a fluidized anode during brewery wastewater treatment. Front. Microbiol. 9, 1–12. https://doi.org/10.3389/fmicb.2018.00378

ter Heijne, A., Pereira, M.A., Pereira, J., Sleutels, T., 2020. Electron Storage in Electroactive Bio fi lms xx, 1–9. https://doi.org/10.1016/j.tibtech.2020.06.006

ter Heijne, A., Schaetzle, O., Gimenez, S., Navarro, L., Hamelers, B., Fabregat-Santiago, F., 2015. Analysis of bio-anode performance through electrochemical impedance spectroscopy. Bioelectrochemistry 106, 64–72. https://doi.org/10.1016/j.bioelechem.2015.04.002

Thormann, K.M., Saville, R.M., Shukla, S., Pelletier, D.A., Spormann, A.M., 2004. Initial phases of biofilm formation in Shewanella oneidensis MR-1. J. Bacteriol. 186, 8096–8104. https://doi.org/10.1128/JB.186.23.8096-8104.2004

Torres, C.I., Krajmalnik-Brown, R., Parameswaran, P., Marcus, A.K., Wanger, G., Gorby, Y.A., Rittmann, B.E., 2009. Selecting anode-respiring bacteria based on anode potential: Phylogenetic, electrochemical, and microscopic characterization. Environ. Sci. Technol. 43, 9519–9524. https://doi.org/10.1021/es902165y

Torres, C.I., Marcus, A.K., Rittmann, B.E., 2008. Proton Transport Inside the Biofilm Limits electrical current generation by anode-respiring bacteria.

Ueki, T., Lovley, D.R., 2022. Desulfovibrio vulgaris as a model microbe for the study of corrosion under sulfate-reducing conditions . mLife. https://doi.org/10.1002/mlf2.12018

Velasquez-Orta, S.B., Head, I.M., Curtis, T.P., Scott, K., 2011. Factors affecting current production in microbial fuel cells using different industrial wastewaters. Bioresour. Technol. 102, 5105–5112. https://doi.org/10.1016/j.biortech.2011.01.059

Venkataraman, A., Rosenbaum, M., Arends, J.B.A., Halitschke, R., Angenent, L.T., 2010. Quorum sensing regulates electric current generation of Pseudomonas aeruginosa PA14 in bioelectrochemical systems. Electrochem. commun. 12, 459–462. https://doi.org/10.1016/j.elecom.2010.01.019

Vigneron, A., Alsop, E.B., Chambers, B., Lomans, B.P., Head, I.M., Tsesmetzis, N., 2016. Complementary microorganisms in highly corrosive biofilms from an offshore oil production facility. Appl. Environ. Microbiol. 82, 2545–2554. https://doi.org/10.1128/AEM.03842-15

Vinales, J., Sackett, J., Trutschel, L., Amir, W., Norman, C., Leach, E., Wilbanks, E., Rowe, A., 2022. Physiologic, Genomic, and Electrochemical Characterization of Two Heterotrophic Marine Sediment Microbes from the Idiomarina Genus. Microorganisms 10. https://doi.org/10.3390/microorganisms10061219

Wang, G., Xing, Y., Liu, G., Chu, Y., Yao, G., Li, Q., Chen, R., 2022. Poorly conductive biochar boosting extracellular electron transfer for efficient volatile fatty acids oxidation via redox-mediated mechanism. Sci. Total Environ. 809, 151113. https://doi.org/10.1016/j.scitotenv.2021.151113

Wei, J., Liang, P., Huang, X., 2011. Recent progress in electrodes for microbial fuel cells. Bioresour.

Technol. 102, 9335–9344. https://doi.org/10.1016/j.biortech.2011.07.019

Wilms, R., Sass, H., Köpke, B., Köster, J., Cypionka, H., Engelen, B., 2006. Specific bacterial, archaeal, and eukaryotic communities in tidal-flat sediments along a vertical profile of several meters. Appl. Environ. Microbiol. 72, 2756–2764. https://doi.org/10.1128/AEM.72.4.2756-2764.2006

Xu, H., Zou, Y., Lee, H.Y., Ahn, J., 2010. Effect of NaCl on the Biofilm Formation by Foodborne Pathogens. J. Food Sci. 75, 580–585. https://doi.org/10.1111/j.1750-3841.2010.01865.x

Yang, G., Huang, L., Yu, Z., Liu, X., Chen, S., 2019. Anode potentials regulate Geobacter biofilms : New insights from the composition and spatial structure of extracellular polymeric substances. Water Res. 159, 294–301. https://doi.org/10.1016/j.watres.2019.05.027

Yang, G., Mai, Q., Zhuang, Z., Zhuang, L., 2021. Buffer capacity regulates the stratification of anode-respiring biofilm during brewery wastewater treatment. Environ. Res. 201, 111572. https://doi.org/10.1016/j.envres.2021.111572

Yang, L., Liu, Y., Wu, H., Høiby, N., Molin, S., Song, Z.J., 2011. Current understanding of multispecies biofilms. Int. J. Oral Sci. 3, 74–81. https://doi.org/10.4248/IJOS11027

Yilmazel, Y.D., Zhu, X., Kim, K.Y., Holmes, D.E., Logan, B.E., 2018. Electrical current generation in microbial electrolysis cells by hyperthermophilic archaea Ferroglobus placidus and Geoglobus ahangari. Bioelectrochemistry 119, 142–149. https://doi.org/10.1016/j.bioelechem.2017.09.012

Yoshizawa, T., Miyahara, M., Kouzuma, A., Watanabe, K., 2014. Conversion of activated-sludge reactors to microbial fuel cells for wastewater treatment coupled to electricity generation. J. Biosci. Bioeng. 118, 533–539. https://doi.org/10.1016/j.jbiosc.2014.04.009

Yu, J., Seon, J., Park, Y., Cho, S., Lee, T., 2012. Electricity generation and microbial community in a submerged-exchangeable microbial fuel cell system for low-strength domestic wastewater treatment. Bioresour. Technol. 117, 172–179. https://doi.org/10.1016/j.biortech.2012.04.078

Yu, Z., Wang, Y., Qin, D., Yang, G., Zhou, S., 2013. Bacillus sediminis sp. nov., isolated from an electroactive biofilm. Antonie van Leeuwenhoek, Int. J. Gen. Mol. Microbiol. 104, 1109–1116. https://doi.org/10.1007/s10482-013-0032-0

Yuan, H., Sun, S., Abu-Reesh, I.M., Badgley, B.D., He, Z., 2017. Unravelling and Reconstructing the Nexus of Salinity, Electricity, and Microbial Ecology for Bioelectrochemical Desalination. Environ. Sci. Technol. 51, 12672–12682. https://doi.org/10.1021/acs.est.7b03763

Zakaria, B.S., Dhar, B.R., 2020. Changes in syntrophic microbial communities , EPS matrix , and gene-expression patterns in bio fi lm anode in response to silver nanoparticles exposure. Sci. Total Environ. 734, 139395. https://doi.org/10.1016/j.scitotenv.2020.139395

Zhang, L., Fu, G., Zhang, Z., 2019. Electricity generation and microbial community in long-running microbial fuel cell for high-salinity mustard tuber wastewater treatment. Bioelectrochemistry 126, 20–28. https://doi.org/10.1016/j.bioelechem.2018.11.002

Zhang, X., Prévoteau, A., Louro, R.O., Paquete, C.M., Rabaey, K., 2018. Periodic polarization of electroactive biofilms increases current density and charge carriers concentration while modifying biofilm structure. Biosens. Bioelectron. 121, 183–191. https://doi.org/10.1016/j.bios.2018.08.045

Zhu, X., Yates, M.D., Hatzell, M.C., Rao, H.A., Saikaly, P.E., Logan, B.E., 2014. Microbial Community Composition Is Unaffected by Anode Potential. https://doi.org/10.1021/es404690q

Annexes

Microfluidic chip preparation

At the beginning, the microBES were built either with polydimethylsiloxane (PDMS) or with thiolene-epoxy resin (OSTEMER). The design of the microfluidic chips were drawn using Autocad and printed on high-resolution emulsion film (from JD photodata or Techphotogravure). Basically, all the microfluidic chips consist in an Hele Shaw flow cell with one inlet and one outlet, meaning that fluid flows between two parallel flat plates separated by a small gap. The microelectrodes are introduced perpendiculary to the flow in the edge of the chips. Typical drawing of the microBES developed during this study were presented on Figure VI-2 (A). From these printed masks, a series of molds were prepared using dry film, these molds were used to build the microfluidic chip. The detailed protocol of chip fabrication is described next.

- PDMS Chip fabrication protocol using DF-300 dry film or three-electrode microBES

The obtention of a PDMS three-electrode microfluidic chip is summarized in Annex Figure 1. The first step of this protocol consisted on laminating a series of photoresist resin films to a glass support. The DF-3000 series dry film (with thickness of 50µm or 20µm) was implemented in this occasion. The desired thickness of the mold (and thus the one of the microfluidic chip) were obtained by successive lamination of several layers of dry films. Lamination of the dry film was done in a hot rolling press at a 100 °C.

Later, a mask was chosen according to the design used for the cell and placed on top of the laminated films. The whole system was crossed linked with UV light (100% power for 5 seconds @ 40mJ) using an UV-KUB 3. In order to improve the dry film resolution and to speed up the reticulation of the dry film, a post bake process was applied at 100 °C for 10 minutes. The molds were then developed in a cyclohexane bath for 4-minute wash (under orbital mixing at 160 RPM). The molds integrity were visually inspected under microscope in order to be check that the thickness and the size of the main features are preserved.

From these molds, PDMS chips were prepared by a classical mold casting procedure. Briefly, PDMS prepolymer was carefully mixed with the curing agent with a ratio of 10:1 and degassed for 20 minutes, to remove air bubbles. Then PDMS was poured over the mold obtained in the first step and degassed again for another 20 minutes. The mold + PDMS was heated at 65°C for 2 hours in order to cross-link the PDMS thermally.

Once the PDMS was totally cured, it was peeled off from the mold, and inlet and outlet holes were punched with a 1.6 mm diameter punch. The structure PDMS and a glass slide were then exposed to plasma for 30 seconds. Three microelectrodes were placed by hand into the grooves created for that purpose. The structured PDMS and the glass slide were brought in contact to form the microfluidic cell.

To enhance the adhesion of the PDMS into the glass support, the system was left inside the stove overnight at 65°C.

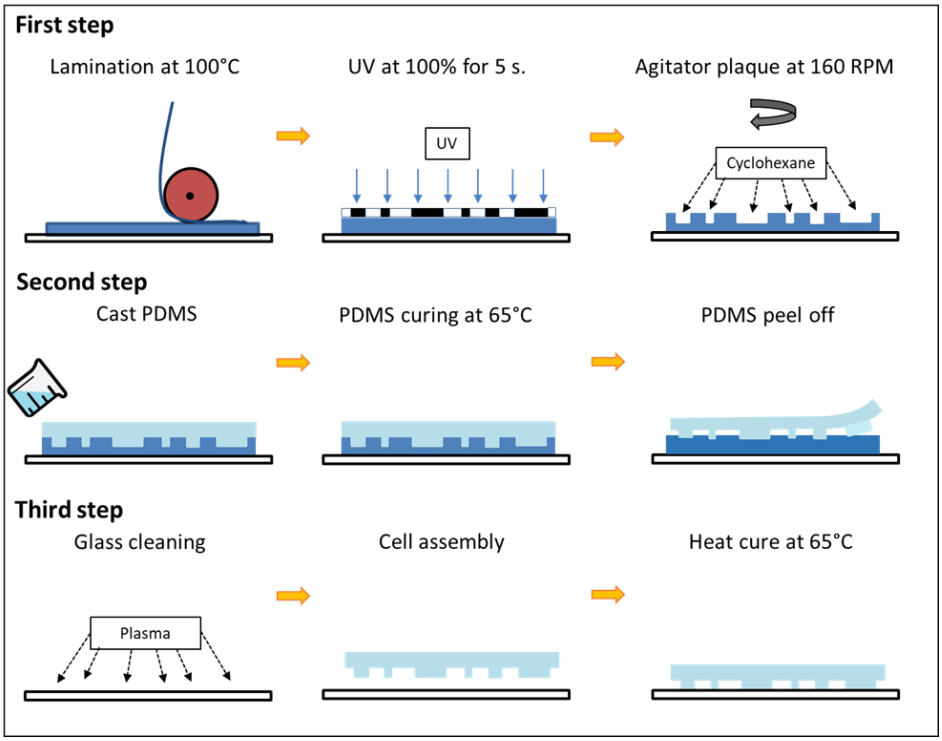

Annex Figure 1: Graphical step-by-step representation to obtain a PDMS chip using DF-300 dry film.

- OSTEMER Chip fabrication protocol using Dupont WBR dry film or two-electrode microBES

The next model of the microfluidic cell was aimed at changing from a three-electrode to a two-electrode system, while maintaining the transparency of the reactor. At this point of development, it had already been determined that the microelectrode material for the working electrode would be SS. For the counter and reference electrode, it was decided to implement an ITO conductive glass slide that could also work as the support of the microBES. Another modification from the first prototype was the change in the cell material. In this case, OSTEMER polymer was selected since it is less porous and less oxygen permeable compared to PDMS, allowing for very long experiments without water evaporation or oxygen transfer. The structure obtained was more rigid and it was also optically transparent. On the other hand, the use of OSTEMER made the microfluidic development process longer, since this polymer needed to be cured with UV light first and then thermally. Masks with a new cell pattern were designed (Figure VI-5). Some technical features that were added in this protocol were the use of more than one mask for a single cell design. This allowed the incorporation of the grooves for the microelectrode and the microchannel at different heights of the reactor. The final volume of the microfluidic cell was of 100 µL.

The step-by-step procedure to obtain a two-electrode OSTEMER microfluidic cell is summarized in Annex Figure 2. As it was decided to work with OSTEMER, this required the design of two successive molds: the first, a dry film mold, and the second, a PDMS mold.

The first step of this protocol was similar to the one described for the three-electrode PDMS microfluidic cell with the difference that in this case the WBR 2000 dry films were used. As two masks were needed to obtain the final cell structure, the lamination process was intercalated with the UV exposure. This means that the photoresist film was laminated into a glass support with a hot rolling press at a 100°C. Later, the mask was placed on the top of the laminated films and exposed with UV light at a power of 100% at 40 mJ/cm2. To get the final structure of the mold, the lamination procedure was repeated as well as the exposure with the second mask. As the exposure time depends of the thickness of the film, and this case the dry mold film had a final thickness of 550 μm, exposure times variated between 8 to 10 s. Consequently, the structure was developed with a solution of potassium carbonate for about 10 minutes using a homemade spin developer. After the development step, the dry film mold was immersed in NOVEC 1720 and left in the hot plate at a 100°C for 30 minutes. After this step, the mold is coated with a 10nm layer of fluorous nanoparticle, and made the mold hydro and lipophobic so that the PDMS can be easily peeled off after. The procedure for the preparation of the PDMS mold is the same as the one presented previously for preparing PDMS cells.

i) Chip preparation by injection molding

The microBES are prepared by injection molding. For this purpose, it was necessary to place the PDMS mold facing upwards on a glass support to close the structure. The mold was then covered with a thin PDMS film and on top of that, another glass was placed. Then, the OSTEMER was injected using a syringe between the PDMS mold and the PDMS thin film. The OSTEMER filled all the gap between the PDMS mold and the PDMS thin film. The first cure of the OSTEMER, was obtained by exposing the assembly to UV light (@360nm) for 27 s at a power of 100% at 40mJ/cm2. The PDMS thin film was peeled off together with the OSTEMER structure. This first curing step for the OSTEMER allowed obtaining a solid but flexible structure with a certain degree of adhesion.

In order to assembly the remaining components; the microelectrode was placed in the groove designed for that purpose. The PDMS + OSTEMER was stuck into an ITO conductive glass, and the PDMS thin film was removed. A glass slide was placed perpendicularly to the ITO glass on top of the OSTEMER structure in order to close it. The totally cure the OSTEMER and to provide a strong adhesion to the substrate, the resulting chip was cured at 65°C overnight.

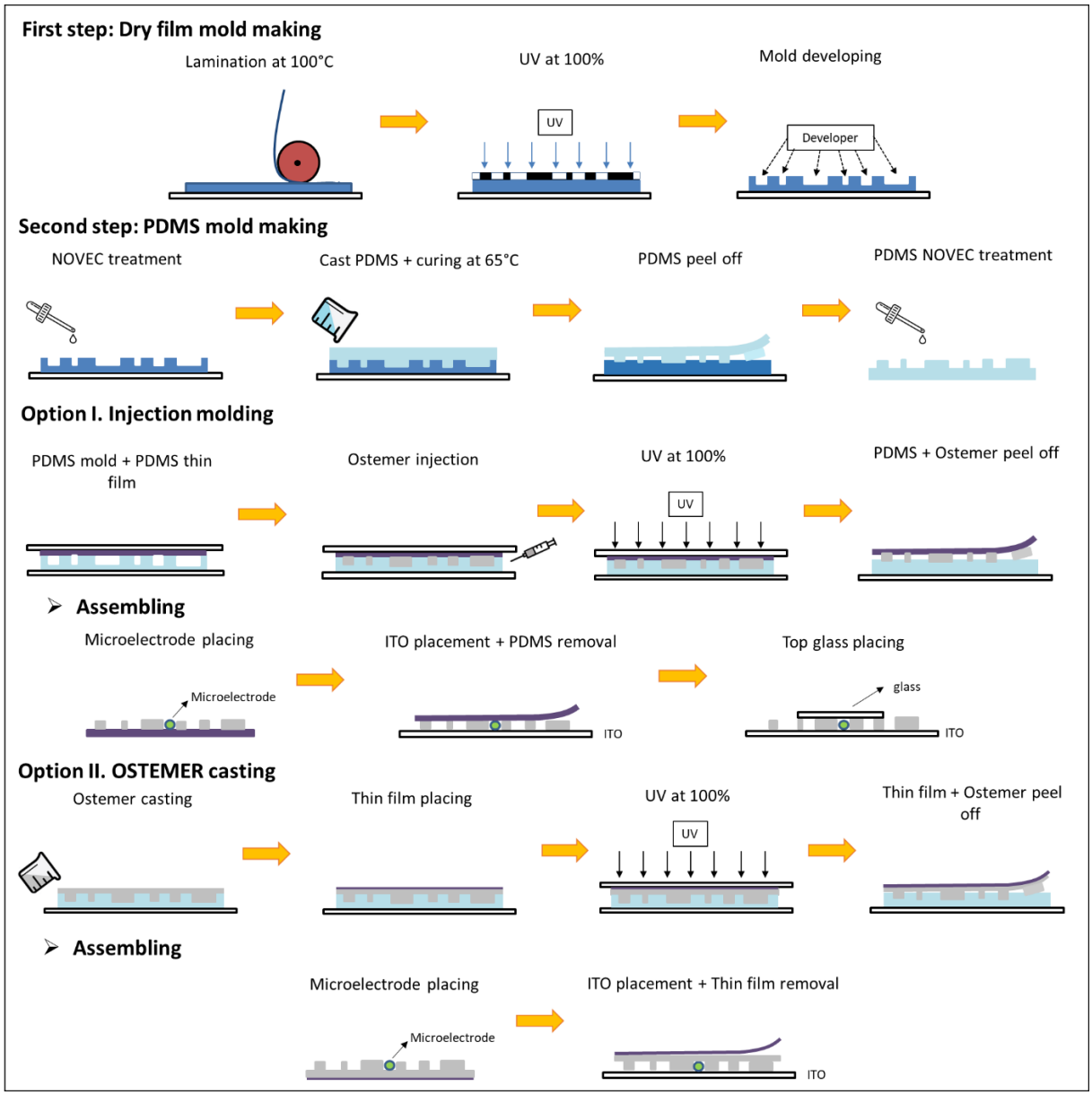

Annex Figure 2: Graphical step-by-step representation to obtain an OSTEMER chip fabrication using Dupont WBR dry film.

ii) Chip preparation by OSTEMER casting

As some cell design patterns were not suitable for injection molding, it that cases, OSTEMER chips were prepared by directly casting it on the PDMS mold. The PDMS mold + the liquid OSTEMER was degassed under vacuum until bubbles disappeared. A thin plastic film was placed on top of the liquid OSTEMER and the system was exposed for UV curing. The thin film together with the semi-cured OSTEMER structure were peeled off from the PDMS mold.

For the assembly, the microelectrode was placed in the groove designed for that purpose. The thin plastic film + the OSTEMER was then brought in contact to an ITO conductive glass, and the thin plastic film was removed. The assembly was thermally cured at 65°C overnight to obtain the final microfluidic chip.

Protocol for EPS staining

With the aim of staining in one-step cells and the different natures of the EPS of the biofilm, a staining protocol allowing the differentiation between nucleic acids, lipids, proteins and polysaccharides was designed. The basis for this protocol is that there is no superposition between the emission/excitation wavelengths of the stains. Consequently, two stains were proposed for polysaccharides, two for lipids, one for proteins and four for nucleic acids, as seen in Annex Table 1. The values were obtained from the Fluorescence SpectraViewer guide (*Thermofischer Scientific*), except for the values from Calcofluor White and Syto 63 (Chen et al., 2007).

Annex Table 1 : Stains with their corresponding EPS targets and wavelengths of excitation and emission in nanometers

Stain	EPS Target	Excitation Wavelength (nm)	Emission Wavelength (nm)
Calcofluor white	β-Polysaccharides	405	410-480
Concavalin A	α-polysaccharides	543	577
Nile Red	Lipids	507	582
DiD oil	Lipids	647	669
FITC	Proteins	490	525
Acridine orange	Nucleic Acids	502	527
DAPI	Nucleic Acids	358	461
Syto 9	Nucleic Acids	483	503
Syto 63	Nucleic Acids	633	650-700

To have a proper protocol, a single stain was selected for proteins. Nile Red, Acridine Orange and Syto 9 were firstly discarded from Annex Table 1 since they interfered with FITC as seen in the spectra diagrams of Annex Figure 3. For Syto 9, Annex Figure 3 (A) the excitation peaks were very close between Syto 9 and FITC and the emission spectrum were completely overlapped. Acridine orange and FITC spectrum were also very similar in the emission and excitation shapes (Annex Figure 3 (B)). The excitation spectrum of Nile Red overlapped the one of FITC (Annex Figure 3 (C)). This left only DiD oil as a lipid stain.

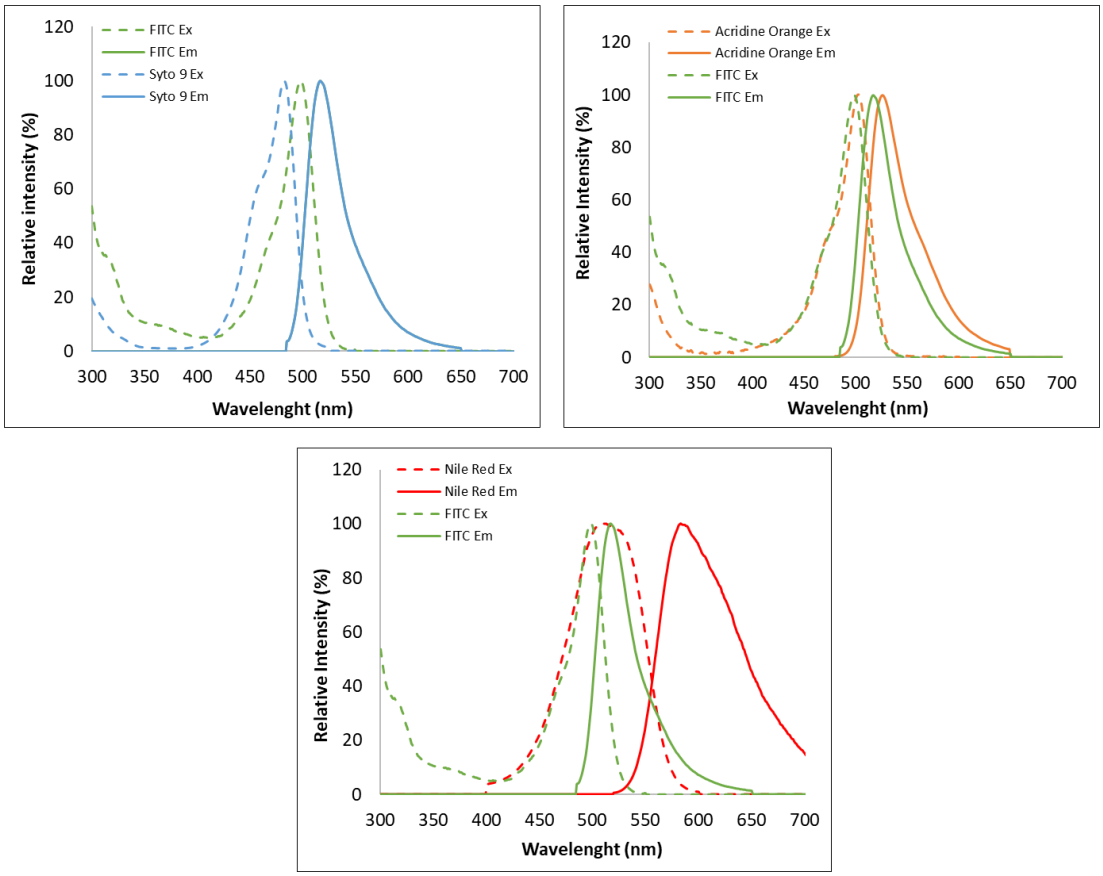

Annex Figure 3 : Emission and excitation spectral curves obtained from Fluorescence Spectraviewer (Thermofischer). (A) For FITC and Syto 9, (B) For FITC and Acridine Orange and (C) for Nile Red and FITC.

As DiD oil excitation wavelength and emission wavelength were very close to the values of Syto 63, the latter was discarded for nucleic acids, leaving DAPI as the most suitable option of the nucleic acids stain group. Finally, between the two options for polysaccharides, Calcofluor White wavelength values were close to DAPI values, therefore selecting Concavalin A as the option for polysaccharides. The comparison between DiD oil and Syto 63, and Calcofluor white and DAPI were not shown since there is not spectral curves in the Thermofischer *Fluorescence SpectraViewer* for exporting.

The final stain protocol for staining was formed by FITC for proteins, DID oil for lipids, DAPI for total cells and Concavalin A for polysaccharides, as seen in Annex Figure 4.

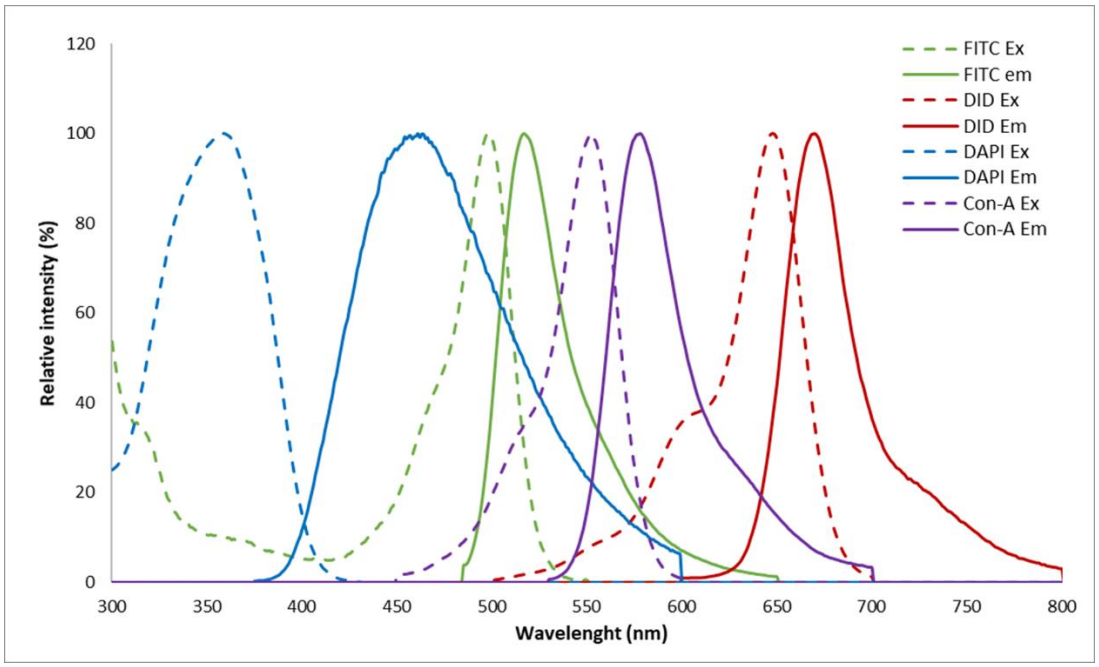

Annex Figure 4 : Excitation and emission spectral curves obtained from Fluorescence SpectraViewer (Thermofischer) for FITC, DiD oil, DAPI and Concavalin A.

MATLAB Routines

The following Matlab routine was developed by Juan Diego Carvajalino Olave.

- PixelQuantification

```
%function [pixT] =
CLSM(slicepath,bk_frac,bk_bin,gamma_lim,gamma_step,min_pk,adv,th_met
hod,th_frac)
function [pixT] =
CLSM(slicepath,bk_frac,bk_bin,gamma_lim,gamma_step,min_pk,adv,th_met
hod,th_frac)

 vec = linspace(0,2*pi(),120)';
 myPosition = [cos(vec) sin(vec) 0.2*ones(size(vec))];

dict_th = containers.Map({'peaks','iter','otsu'},[1,2,3]);
%DAPI = total cells - blue; DiD oil = Lipids - red; FITC = Proteins
-
%green; Con-A = alpha-PS - magenta
%quantitative analysis of projections is dangerous by itself,
specially when
        %comparing stacks with different number of slices. Moreover,
sum
        %projections are less appealing to the eye than max
projections but
        %more reliable for quantitative (or ratiometric) analysis.
% Rotation of images compresses and changes the information in
slices.
    % Rotation should be used only for publishing purposes, and only
used AFTER all analysis are
```

```
    % completed.
% For stratified samples, the intensity (emitted light) of a pixel
is
    % subestimated if in the same xy position, the laser has already
gone
    % through the sample. Ways to correct this loss of intensity: 1.
Ramp of
    % intensity in the laser (physical correction). 2. factor
correction for
    % deeper layers (post-processing correction)
[pname,folder,S,So,stacks] = get_stacks(slicepath); % GET STACKS OF
IMAGES FOR EACH CHANNEL OF A FILE
SS_wire = struct('Dim',50,'Unit','Âµm');
ch_bck = find(strcmp(S.ChannelColor,'white'));
stacks_original = stacks; % BACKUP ORIGINAL STACK
[Bwire] = removeBG(stacks,ch_bck,S.ZCount,S.ChannelCount); % GETS
THE LIMITS OF THE BIOFILM (ONLY USED IF REMOVING GLASS
AUTOMATICALLY)
zclean = not_glass(stacks,ch_bck,Bwire,folder); % FINDS THE SLICES
THAT ARE NOT AFFECTED BY THE GLASS
stacks = stacks(:,:,zclean(1):zclean(2),:); % REMOVES THE GLASSES
FROM THE STACKS
stacks_original = stacks_original(:,:,zclean(1):zclean(2),:);%
REMOVES THE GLASSES FROM THE STACKS
S.ZCount = size(stacks,3); % COUNTS HOW MANY SLICES ARE NOW AFTER
GLASS REMOVAL
[stacks,wire_edge,cmid,stacks_bk] =
removeBG(stacks,ch_bck,S.ZCount,S.ChannelCount); %BACKGROUND AND
FOREGROUND ARE SEPARATED
stacksbk_o = stacks_bk;
rotang = edge_slope(cmid);% ANGLE OF ROTATION IS FOUND
thick = get_thickness(wire_edge,rotang,S.Voxels,SS_wire,zclean);
%CALCULATION OF BIOFILM THICKNESS
th_slice = zeros(S.ZCount,S.ChannelCount,3);
th_glob = zeros(S.ChannelCount,3);
bwstacks = zeros(S.Pixels(1),S.Pixels(2),S.ZCount,S.ChannelCount);
pixelcount = zeros(S.ChannelCount,1);
compress_F = 0.5;
for ni = 1:S.ChannelCount
    if ni == ch_bck %SKIPS THE THRESHOLDING FOR THE CHANNEL WITH THE
WHITE LIGHT
        continue
    end
    fprintf('Channel %d: Thresholding...',ni)
     for zi = 1:S.ZCount
        slice = stacks(:,:,zi,ni);
        slice_bg = stacks_bk(:,:,zi,ni);
        [slice,slice_bg] =
adjust_bck(slice_bg,slice,bk_frac,bk_bin,gamma_lim,gamma_step);
%FINDS GAMMA FOR NOISE REMOVAL
       % [slice,slice_bg] = adjust_bck(slice_bg,slice,gamma_lim);
        stacks(:,:,zi,ni) = slice;
        stacks_bk(:,:,zi,ni) = slice_bg;
     end
```

```
    [th_glob(ni,1),th_glob(ni,2),th_glob(ni,3)] =
th_slices(stacks(:,:,:,ni),stacks_bk(:,:,:,ni),min_pk,adv); %FINDS
THRESHOLD PARAMETERS
    th = th_frac*th_glob(ni,dict_th(th_method));
    slices_ch = stacks(:,:,:,ni);
    slices_ch(slices_ch<=th) = 0; %APPLIES THRESHOLD OF ITERATIVE
METHOD ONLY
    slices_ch(slices_ch>th) = 1;%APPLIES THRESHOLD OF ITERATIVE
METHOD ONLY
    bwstacks(:,:,:,ni) = uint8(slices_ch);
    sumbk = sum(bwstacks(:,:,:,ni),3); %sum project
    pixelcount(ni) = sum(sumbk,'all'); %COUNTS PIXELS OF EACH
CHANNEL CORRESPONDING TO BIOFILM
    %sumbk = imscalebar(sumbk,S.Dimensions(2),50);
    fprintf('Done\n')
end
pixelcount(ch_bck) = [];
Xbar = S.ChannelColor;Xbar(ch_bck) = [];
pixT =
table([pixelcount;thick.BiofilmLength_XY],'VariableNames',{pname},'R
owNames',[Xbar;strcat('biofilm_',thick.LengthUnit)]); %STORES THE
PIXEL COUNTS
end
```

Some MATLAB functions were developed and included in the main code “PixelQuantification”

get_stacks

```
function [pname,folder,S,So,stacks] = get_stacks(slicepath)

    if isempty(slicepath)
        [pname,folder] = uigetfile('*.tif','Select one of the
slices...');
    else
        folder = slicepath{1};
        pname = slicepath{2};
    end
    list = dir([folder,'*.tif']);
    pname = extractBefore(pname,'_z');
    disp(pname)
    [S,So] = get_Metadata(folder,pname);
    stacks = zeros(S.Pixels(1),S.Pixels(2),S.ZCount,S.ChannelCount);
    Ntif = numel(list);
    fprintf('Getting Stacks...')
    for n = 1:Ntif
        filename = [folder list(n).name];
        nc = str2double(extractBetween(filename,'ch','.'));
        z = str2double(extractBetween(filename,'_z','_ch'));
        slice = imread(filename);
        stacks(:,:,z+1,nc+1) = slice;
    end
    fprintf('Done\n')
end
```

removeBG

```
Function [varargout] = removeBG(stacks,ch_bck,ZCount,ChannelCount)
    if nargout == 1
        fprintf('Finding Background mask...')
    else
        fprintf('Finding biofilm edges...')
    end
    if ZCount == 1
        bslide = 1;
    else
        bslide = round(ZCount/2);
    end
    Bwire = stacks(:,:,bslide,ch_bck);% channel with White/Bright
signal
    Bwire = rescale(Bwire,0,255);
    Bwire = imgaussfilt(Bwire,15);
    th_wire = 80;
    Bwire = Bwire <= th_wire;
    if nargout == 1
        varargout{1} = Bwire;
        fprintf('Done\n')
        return
    end
    stacks_bk = ones(size(stacks));
    move_edge = 0.3;
    wire_edge = edge(Bwire);

    if ZCount ~= 1
        [row,col] = find(wire_edge);
        cmid = false(size(Bwire,1));
        c_bg = cmid;
        coli = col(row == 1);
        if isempty(coli)
            row2 = col;
            col = row;
            row = row2;
        end
        for k = 1:size(Bwire,1)
            colk = col(row == k);
            left_edge = min(colk);
            right_edge = max(colk);
            if isempty(coli)
                cmid(round(mean([left_edge,right_edge])),k) = true;
                c_bg([1:round((1-
move_edge)*left_edge),round(right_edge+move_edge*(size(wire_edge,2)-
right_edge)):end],k) = true;
            else
                cmid(k,round(mean([left_edge,right_edge]))) = true;
                c_bg(k,[1:round((1-
move_edge)*left_edge),round(right_edge+move_edge*(size(wire_edge,2)-
right_edge)):end]) = true;
            end
        end
    else
        cmid = [];
    end
    for ni = 1:ChannelCount
```

```
        for zi = 1:ZCount
            slice = stacks(:,:,zi,ni);
            slice_bk = slice;
            slice(~Bwire) = NaN;
            stacks(:,:,zi,ni) = slice;
            if ZCount ~= 1
                slice_bk(~c_bg) = NaN;
            else
                slice_bk(Bwire) = NaN; %need to find real edge on
this case
            end
            stacks_bk(:,:,zi,ni) = slice_bk;
        end
    end
    varargout{1} = stacks;
    varargout{2} = wire_edge;
    varargout{3} = cmid;
    varargout{4} = stacks_bk;
    fprintf('Background removed\n')
end
```

not_glass

```
function zclean = not_glass(stacks,ch_bck,Bwire,folder)
    fprintf('Removing glass...')
    zload = [folder,'MetaData\','CropSlices.txt'];
    if isfile(zload)
       fileID = fopen(zload);
       zcell = textscan(fileID,'%d');
       fclose(fileID);
       fprintf('Glass loaded from file...')
       zclean = zcell{1};
       zclean = sort(zclean);
        fprintf('Done\n')
        return
    end
    stacks2 = stacks;
    stacks2(:,:,:,ch_bck)=[];
    Bwire = logical(Bwire);
    N = size(stacks2,3);
    Nch = size(stacks2,4);
    for n = 1:Nch
        for k = 1:N
            slice = stacks2(:,:,k,n);
            slice(Bwire) = 0;
            stacks2(:,:,k,n) = slice;
        end
    end
    N = size(stacks2,3);
    sum_ch = squeeze(sum(stacks2,[1,2]));
    [~,noisy_ch] = max(sum_ch(1,:),[],2);
    noisy_stack = stacks2(:,:,:,noisy_ch);
     suma =
1000*squeeze(sum(noisy_stack,[1,2]))/N/256/size(stacks2,2)/size(stac
ks2,1);
    figure(50)
```

```
    plot(suma)
    xlabel('Slice number')
    ylabel('Relative intensity')
    zglass = find(suma>1.1);
    zclean = zeros(1,2);
    M = numel(zglass);
    flag1 = true;
    flag2 = true;
    for n = 1:M
        if flag1 && n ~= zglass(n)
            if n == 1
                zclean(1) = 1;
                fprintf('Top glass not found...')
            else
                zclean(1) = zglass(n-1)+1;
            end
            flag1 = false;
        elseif flag1 && n == M
            zclean(1) = zglass(M)+1;
        end
        if flag2 && N-n+1 ~= zglass(end-n+1)
            if n == 1
                zclean(2) = N;
                fprintf('Bottom glass not found...')
            else
                zclean(2) = zglass(end-n+2)-1;
            end
            flag2 = false;
        elseif flag2 && n == M
            zclean(2) = zglass(1)-1;
        end
        if ~flag1 && ~flag2
            break
        end
    end
    fprintf('Done\n')
end
```

edge_slope

```
function ang = edge_slope(cmid)
    fprintf('Finding rotation...')
    [H,T,R] = hough(cmid);
    P  = houghpeaks(H);
    line = houghlines(cmid,T,R,P,'FillGap',10000);
    x = [line.point1(1),line.point2(1)];
    y = [line.point1(2),line.point2(2)];
    slope = diff(y)./diff(x);
    ang = atand(slope);
    fprintf('Done\n')
end
```

get_thickness

```
function thick = get_thickness(wire_edge,rotang,Vox,SS_wire,zclean)
```

```
    fprintf('Getting thickness...')
    thk_z = diff(zclean).*Vox(3);
    h_wire = imrotate(wire_edge,rotang);
    imshow(h_wire)
    [row,col] = find(h_wire);
    total = 0;
    pixels = 0;
    for k=1:numel(col)
        rowk = row(col == k);
        if numel(rowk)>1
            pixels = pixels + (max(rowk)-min(rowk));
            total = total+1;
        end
    end
    pixels = pixels/total;
    length = Vox(1)*(pixels);
    biolength = (Vox(1)*(pixels)-SS_wire.Dim)/2;
    thick =
struct('PixelsXY',pixels,'Length_XY',length,'BiofilmLength_XY',biole
ngth,'LengthUnit',SS_wire.Unit,...
        'PixelsZ',diff(zclean)+1,'Length_Z',thk_z);
    fprintf('Done\n')
end
```

th_slice

```
function [th_1,th_it,th_otsu] = th_slices(slice,slice_bg,min_pk,adv)
    [counts3,~] = histcounts(slice,0:255);
    th_it = th_iter_sel(counts3(2:end),0:255);
    th_otsu = otsuthresh(counts3)*255;
    th_1 = adv*th_it;
    if min_pk > th_1
        th_1 = min_pk;
    end
end
```

th_iter_sel

```
function th = th_iter_sel(counts,pix)
%%
    pix = pix';
    T_opt = zeros(numel(pix),2);
    for n = 1:pix(end)-1
        sumF = sum(counts(1:n));
        sumB = sum(counts(n+1:end));
        if all([sumF,sumB])
            t_fore = sum(pix(1:n).*counts(1:n))./sumF;
            t_back = sum(pix(n+1:end).*counts(n+1:end))./sumF;
            T_opt(n,1) = mean([t_fore,t_back]);
        else
            T_opt(n,1) = NaN;
        end
    end
    T_opt(:,2) = abs(pix-T_opt(:,1));
    [~,th] = min(T_opt(:,2));
```

```
end
```

adjust_bck

```
function [slice,slice_bg] =
adjust_bck(slice_bg,slice,bk_frac,bk_bin,gamma_lim,gamma_step)
%consider using fspecial and imfilter
    sg = slice;
    sb = slice_bg;
    if nargin == 3
        slice = double(imadjust(uint8(slice),[],[],bk_frac));
        slice_bg = double(imadjust(uint8(sb),[],[],bk_frac));
        slice(isnan(sg)) = NaN;
        slice_bg(isnan(sb)) = NaN;
        return
    end
    if gamma_lim <0
        flag1 = true;
        gamma_lim = -gamma_lim;
    else
        flag1 = false;
    end
    %slice = locallapfilt(uint8(slice),0.5,0.6);
    %slice_bg = locallapfilt(uint8(slice_bg),0.5,0.6);
    %slice_bg(isnan(sb)) = NaN;
    %slice_bg = slice_bg(1:300,:);
    slice_v = slice_bg;
    slice_v(isnan(slice_v)) = [];
    total_pix = numel(slice_v);
    [counts,~] = histcounts(slice_v,0:255);
    if sum(counts(1:bk_bin))/total_pix <= bk_frac
        for gamma = 1:gamma_step:gamma_lim
            if ~flag1
                new_slice = imadjust(uint8(slice_v),[],[],gamma);
            else
                new_slice = slice_v/gamma;
            end
            [counts,~] = histcounts(new_slice,0:255);
            if sum(counts(1:bk_bin))/total_pix >= bk_frac
                break
            end
        end
    else
        gamma = 1;
    end
    if flag1
        slice = slice/gamma;
        slice_bg = sb/gamma;
    else
        slice = double(imadjust(uint8(slice),[],[],gamma));
        slice_bg = double(imadjust(uint8(sb),[],[],gamma));
    end
    slice(isnan(sg)) = NaN;
    slice_bg(isnan(sb)) = NaN;
    fprintf('(%.1f)',gamma)
```

```
end
```

imscalebar

```
function stack = imscalebar(stack,width,widthbar)
    [hpix,wpix] = size(stack);
    stack(1:ceil(hpix/20),1:widthbar*wpix/width) =
max(stack,[],'all');
end
```

pixelcount

```
[xlsfile,xlspath] = uigetfile('*.xls*','Select the file with the
pixel count');
filename = strcat(xlspath,xlsfile);
sheets = sheetnames(filename);
flagstr = '-_-';
sheets = sheets(contains(sheets,flagstr));
Nsheets = length(sheets);
Tsheets = cell(Nsheets,1);
uifig =
uifigure('Name','Pixelcounts','Units','normalized','Position',[0.05,
0.05,0.92,0.92],'Resize','on');
tabgp = uitabgroup(uifig,'Units','normalized','Position',[0,0,1,1]);
uifig2 =
uifigure('Name','Graphs','Units','normalized','Position',[0.05,0.05,
0.8,0.8],'Resize','on');
tabgp2 =
uitabgroup(uifig2,'Units','normalized','Position',[0,0,1,1]);
yvars = {'Current','Biofilm thickness','Max current','Charge'};
dict_yvar = containers.Map({'Current','Max current','Biofilm
thickness','Charge'},{'Current density [A/m2]','Max
current','Biofilm thickness [µm]','Coulombs'});
dict_colors =
containers.Map({'green','blue','red','magenta'},{'Proteins','Total
cells','Lipids','alpha-Polysaccharides'});
fign = cell(Nsheets,1);
fign2 = cell(Nsheets,1);
xcolor = {'blue','red','green','magenta'};
xcomp = call_dict(dict_colors,xcolor);
xcat2 = categorical(xcomp);
xcat2 = reordercats(xcat2,xcomp);
for n=1:Nsheets
    fign2y = cell(numel(yvars),1);
    fign{n} = uitab(tabgp,'Title',erase(sheets{n},flagstr));
    fign2{n} = uitab(tabgp2,'Title',erase(sheets{n},flagstr));
    tabgpn2_2 =
uitabgroup(fign2{n},'Units','normalized','Position',[0,0,1,1]);
    Tsheets{n} =
readtable(filename,'Sheet',sheets{n},'ReadRowNames',true);
    Tsheets{n}{'Totalpix',:} =
sum(Tsheets{n}{{'blue','red','green','magenta'},:},1);
    Ncells = width(Tsheets{n});
    %t =
tiledlayout(fign{n},ceil(sqrt(Ncells)),round(sqrt(Ncells)));
```

```
       %ax = nexttile(t,m);
    t = tiledlayout(fign{n},1,2);
    xbar1 = Tsheets{n}.Properties.VariableNames;
    xcat1 = categorical(xbar1);
    xcat1 = reordercats(xcat1,xbar1);
    ax1 = nexttile(t,1);
    xvars = cell(6,2);
    xvars{5,1} =
Tsheets{n}{{'magenta'},:}./sum(Tsheets{n}{{'green','magenta'},:},1);
xvars{5,2} = 'PS/(Prot+PS)';
    xvars{6,1} = Tsheets{n}{{'Biofilm thickness'},:};xvars{6,2} =
'Biofilm thickness [µm]';
    xvars{1,1} =
Tsheets{n}{{'blue'},:}./sum(Tsheets{n}{{'blue','red','green','magent
a'},:},1);xvars{1,2} = 'Total cells ratio';
    xvars{2,1} =
Tsheets{n}{{'green'},:}./sum(Tsheets{n}{{'blue','red','green','magen
ta'},:},1);xvars{2,2} = 'Proteins ratio';
    xvars{3,1} =
Tsheets{n}{{'red'},:}./sum(Tsheets{n}{{'blue','red','green','magenta
'},:},1);xvars{3,2} = 'Lipids ratio';
    xvars{4,1} =
Tsheets{n}{{'magenta'},:}./sum(Tsheets{n}{{'blue','red','green','mag
enta'},:},1);xvars{4,2} = 'PS ratio';
    bar(ax1,xcat1,xvars{5,1});
    nameax1 = 'PS/(Prot+PS)';
    title(ax1,nameax1)
    ax1.YLim = [0 0.6];
    ax2 = nexttile(t,2);
    bar(ax2,xcat2,(Tsheets{n}{xcolor,:}./Tsheets{n}{{'Totalpix'},:})
');
    title(ax2,'Pixel Fraction')
    ax2.YLim = [0 0.7];
    legend(ax2,xbar1)
    t2 = cell(4,1);
    for yn = 1:numel(yvars)
        fign2y{yn} = uitab(tabgpn2_2,'Title',yvars{yn});
        t2{yn} =
tiledlayout(fign2y{yn},round(sqrt(size(xvars,1))),ceil(sqrt(size(xva
rs,1))));
        for xn=1:size(xvars,1)
            axy = nexttile(t2{yn},xn);
            [sort_x,idx] = sort(xvars{xn,1});
            %scatter(axy,sort_x,Tsheets{n}{yvars(yn),idx},'filled')
            mdl = fitlm(sort_x,Tsheets{n}{yvars(yn),idx});
            plot(axy,mdl)
            cd = 1*mean(mdl.Diagnostics.CooksDistance);
            axy.FontSize = 11;
            axy.FontName = 'Georgia';
            for k = 1:numel(sort_x)
                if mdl.Diagnostics.CooksDistance(k)>=0 %cd
                   %
text(axy,sort_x(k),Tsheets{n}{yvars(yn),idx(k)},xbar1{idx(k)},'Verti
calAlignment','bottom','FontSize',8)
                end
            end
```

```
            axy.XLabel.String = xvars{xn,2};
            axy.YLabel.String = dict_yvar(yvars{yn});
            %axy.Title.String = sprintf('R2-adj =
%.2f',mdl.Rsquared.Adjusted);
            axy.Title.String = sprintf('p-value =
%.3f',mdl.anova.pValue(1));
            %axy.Title.String = '';
        end
    end
    fprintf('%.1f%%\n',n*100/Nsheets)
end
```

Emmanuel Cid at LGC developed the following MATLAB routines:

- CalculMeanImage

```
clear all
close all

%lecture de l'image cam2 PLIF
[fnom1,fchemin1]=uigetfile('*.tif','fichier tif');
%[fnom1,fchemin1]=uigetfile('*.png','fichier png');
nomIm1=[fchemin1 fnom1];

%ImageA=im2double(imread(nomIm1));
ImageB=imread(nomIm1);
ImageA=ImageB(:,:,1);
DimA=size(ImageA);

cd(fchemin1);
rep1=dir(['*.tif']);
%rep1=dir(['*.png']);
fin=size(rep1);
%fin=150
cd ..

R=zeros(DimA(1),DimA(2),fin(1));


for nfich=1:fin; %boucle sur les fichiers image
    if mod(nfich,10)==0
        nfich
    end

    filename1=rep1(nfich).name;%affectation de rep(i).name dans
fichier
    nomIm1=[fchemin1 filename1];

    %ImageA=im2double(imread(nomIm1));
    ImageB=imread(nomIm1);
    ImageA=ImageB(:,:,1);

    R(:,:,nfich)=ImageA;
```

```
end
meanIm=mean(R,3);
figure
imagesc(meanIm)
axis image
colorbar
title('meanIM')

[fnom5, fchemin3]=uiputfile('*.tif','sauvegarder
meanimA','fchemin1/');
fspec=[fchemin3,fnom5];
imwrite(uint16(meanIm),fspec,'tif','Compression','none');
```

- ImageSubstraction

```
clear all;
close all;


[fnom1,fchemin1]=uigetfile('*.*','fichier imA tif ou bmp');
nomIm1=[fchemin1 fnom1];
Image=imread(nomIm1);
Dim=size(Image);
figure
imshow(Image);
title('Image1 de départ');

[fnom2,fchemin2]=uigetfile('*.*','fichier fond imA tif ou
bmp',fchemin1);
nomIm2=[fchemin2 fnom2];
Imagefond=imread(nomIm2);
Dim=size(Imagefond);
figure
imshow(uint8(Imagefond));
title('Image2 de fond');

IImagefond=Imagefond;
ndgfond=double(IImagefond);

[fnom5, fchemin3]=uiputfile('*.tif','sauvegarder imA-
fond',fchemin1);


cd(fchemin1);
rep1=dir(['*.tif']);
fin=size(rep1);
%fin=2
cd ..

for nfich=1:fin; %boucle sur les fichiers image
    if mod(nfich,10)==0
        nfich
    end
```

```
    filename1=rep1(nfich).name;%affectation de rep(i).name dans
fichier
    nomIm1=[fchemin1 filename1];

    Image=imread(nomIm1);

    IImage=Image;

    ndgim=double(IImage);

    %ajout d'un ofset à 80
    %ndgres=round(ndgim-ndgfond+80);
    %ajout d'un ofset basé sur la moyenne de l'image de fond
    ndgres=round(ndgim-ndgfond+mean(mean(ndgfond)));
    ndg=uint8(ndgres);

%     figure
%     imshow(uint8(ndg));
%     title('Image-fond');

    %[fnom5, fchemin3]=uiputfile('*.tif','sauvegarder imA-
fond',fchemin1);
    fspec=[fchemin3,filename1];
    imwrite(ndg,fspec,'tif');
end
```

- OpticalFlow

```
clear all
close all



%lecture du fichier imA brute
[fnom5,fchemin5]=uigetfile('*.tif','fichier image');
%[fnom5,fchemin5]=uigetfile('*.png','fichier image');
imgFilename=[fchemin5 fnom5];
I=imread(imgFilename);

occ=ones(size(I,1),size(I,2));
%xinterf=150;
%xinterf=15;
xinterf=5;
%occ(:,1:xinterf)=0;
occ(end-xinterf:end,:)=0;
for i=1:round(size(I,1)/2):size(I,1)
%     occ(i,1:xinterf)=1;%astuce pour que occ ne fasse pas boguer
jointWMF
    occ(end-xinterf:end,i)=1;%astuce pour que occ ne fasse pas
boguer jointWMF
end

cd(fchemin5);
rep=dir(['*.tif']);
%rep=dir(['*.png']);
%fin=size(rep);
```

```
fin=2;

%rect=[10 0 510-10 740];%pour manip schehinez 06/2014
%rect=[0 0 size(I,2) size(I,1)];%
rect=[0 0 size(I,2) 880];%pour manip Lucila

for nfich=1:fin-1; %boucle sur les fichiers image
%for nfich=1:2:fin-1; %boucle sur les fichiers image
%for nfich=1:3:fin-1; %boucle sur les fichiers image en sautant 1
image
    filename1=rep(nfich).name;%affectation de rep(i).name dans
fichier
    nfich

    filename2=rep(nfich+1).name;
    %filename2=rep(nfich+2).name;
    %filename2=[filename1(1:end-4) 'interp.tif'];

    %lecture image1
    %im1=double(imread(filename1));
    im1=imread(filename1);
    %filtrage im1
    %im1wmf = jointWMF(im1,im1,5,25.5,256,256,1,'exp',occ);
    %im1wmf = im1;
    %im1wmf = imadjust(im1);
    im1wmf = imadjust(im1(:,:,1));
    %on utilise pas le resultat WMF de 1 à xinterf
    %im1wmf(:,1:xinterf)=im1(:,1:xinterf);
    im1wmf(end-xinterf:end,:)=im1(end-xinterf:end,:,1);


    %lecture image2
    %im2=double(imread(filename2));
    im2=imread(filename2);
    %filtrage im1
    %im2wmf = jointWMF(im2,im2,5,25.5,256,256,1,'exp',occ);
    %im2wmf = im2;
    %im2wmf = imadjust(im2);
    im2wmf = imadjust(im2(:,:,1));
    %on utilise pas le resultat WMF de 1 à xinterf
    im2wmf(1:xinterf,:)=im2(1:xinterf,:,1);

     imcrop1=double(imcrop(im1wmf,rect));
     imcrop2=double(imcrop(im2wmf,rect));

     tic
     uv = estimate_flow_interface(imcrop1, imcrop2, 'classic+nl-
fast');
     toc

%      figure(1)
%      plotflow(uv);


     v.vx=uv(:,:,1);
     v.vy=uv(:,:,2);
```

```
      dimvx=size(v.vx);
      v.x=1:1:dimvx(2);
      v.y=1:1:dimvx(1);

      v.choice=[0,0,0,0,0,1];


      nomfichres=filename1(1:end-4);
      nomfichres=[nomfichres '.mat'];
      %save(nomfichres,'uv');
      save(nomfichres, '-struct', 'v');
      clear v
      clear uv
end
```

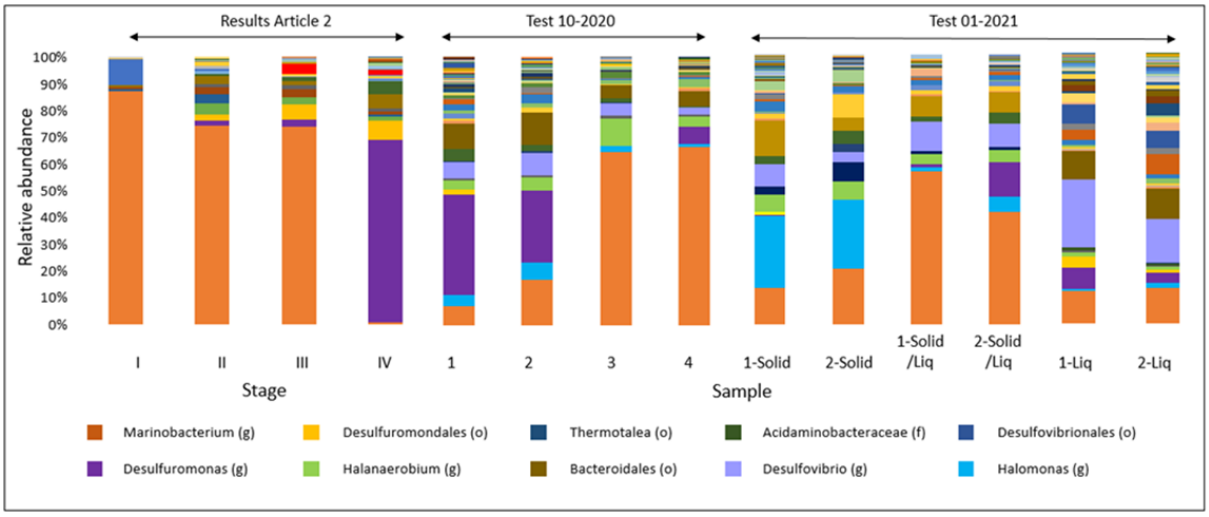

Annex Figure 5: Relative abundances of microbial population in salt marsh EABs for the pool of experiments performed in this chapter. Main abundances are resumed in the list on the bottom. (s) indicates that the DNA analysis classification went until the species level, while (g) to the genera, (f) to the family and (o) to the order level.

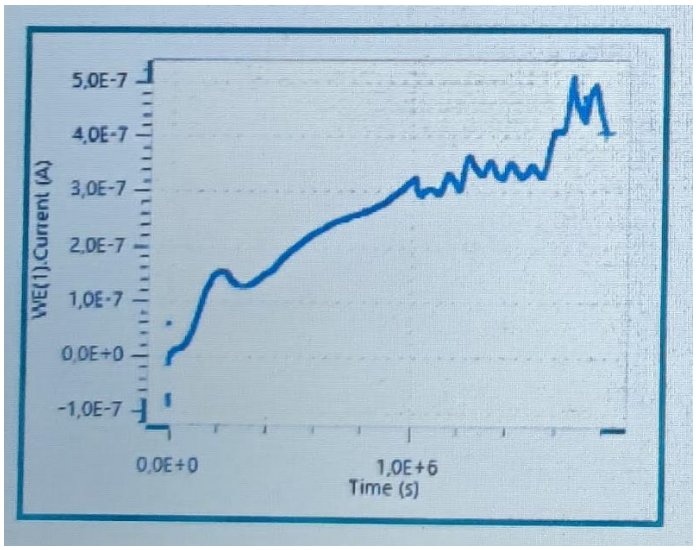

Annex Figure 6 : Screenshot of the NOVA acquisition software. The curve in blue shows the evolution of current (A) in time (s) for the salt marsh EAB formed on the SS microelectrode of the microBES between days 28 to 47.